Atom-to-photon quantum state transfer and teleportation
—
Experiments in the lab and over a metropolitan fibre

Dissertation
zur Erlangung des Grades
der Doktorin der Naturwissenschaften
der Naturwissenschaftlich-Technischen Fakultät
der Universität des Saarlandes
von

Elena Sina Arenskötter

Saarbrücken
– 2023 –

Tag des Kolloquiums:	28.04.2023
Dekan:	Prof. Dr. Ludger Santen
Berichterstatter:	Prof. Dr. Jürgen Eschner
	Dr. Florian Kaiser
Vorsitz:	Prof. Dr. Christoph Becher
Akad. Mitarbeiter:	Dr.-Ing. Steffen Recktenwald

Abstract

Single photon-pair sources are essential for future quantum networks. To be used effectively, the following requirements are essential: high photon rates, high-fidelity entanglement and light-matter interfaces to quantum memories.

This work describes the setup and characterisation of a single photon pair-source based on cavity-enhanced spontaneous parametric down conversion resonant to the $D_{5/2}$ to $P_{3/2}$ transition of a single $^{40}Ca^{+}$ quantum memory fulfilling the upper requirements. The main goal is the realisation of quantum state teleportation over a metropolitan fibre using the source as a resource of entanglement.

Our experiments demonstrate the preservation of high-fidelity entanglement during conversion to the low-loss, low-dispersion telecom wavelength range at 1550 nm and fibre transmission over a metropolitan fibre and up to 40 km of fibre spool, including back-conversion to the memory wavelength.

Further experiments show the excellent performance of our network protocols in transferring photon-photon entanglement to ion-photon entanglement and teleporting a spin qubit from the ion onto a polarisation qubit of a photon. Both protocols are based on the heralded absorption of one photon from a pair by the ion. The interface operations are also demonstrated with quantum frequency conversion and a metropolitan fibre of 14 km length.

Zusammenfassung

Einzelphotonen-Paarquellen sind für künftige Quantennetze unverzichtbar. Um effektiv nutzbar zu sein, müssen folgende Anforderungen erfüllt sein: hohe Photonenraten, hohe Verschränkungsgüte und Licht-Materie-Schnittstellen zu Quantenspeichern.

Diese Arbeit beschreibt den Aufbau und die Charakterisierung einer Einzelphotonen-Paarquelle auf der Basis resonatorverstärkter spontaner parametrischer Abwärtskonversion, die mit dem $D_{5/2}$ zu $P_{3/2}$-Übergang eines einzelnen $^{40}Ca^{+}$-Quantenspeichers resonant ist und die oberen Anforderungen erfüllt. Das Hauptziel ist die Realisierung einer Quantenzustands-Teleportation über eine städtische Faser unter Verwendung der Quelle als Ressource der Verschränkung.

Unsere Experimente demonstrieren die Erhaltung der Verschränkung mit hoher Güte während der Konversion in den verlust- und streuungsarmen Wellenlängenbereich bei 1550 nm und der Übertragung über eine städtische Faser und bis zu 40 km Faserspule, einschließlich der Rückkonversion zur Speicherwellenlänge.

Weitere Experimente zeigen die hervorragende Leistung unserer Netzwerkprotokolle bei der Übertragung von Photonen-Photonen-Verschränkung auf Ionen-Photonen-Verschränkung und bei Teleportation eines Spin-Qubits vom Ion auf ein Polarisations-Qubit eines Photons. Beide Protokolle beruhen auf der angekündigten Absorption eines Photons aus einem Paar durch das Ion. Die Schnittstellenoperationen werden auch mit Quantenfrequenzkonversion und einer 14 km langen städtischen Faser demonstriert.

Glossary

AOM Acousto-Optical Modulator. 16, 19, 39

APD Avalanche Photo Diode. 21, 34, 40, 47, 48, 59, 79, 89, 93, 100, 118, 123, 164

AR anti-reflective. 35, 36

AWG Arbitrary waveform generator. 20

BS non-polarising beamsplitter. 39, 40, 42, 159

BSM Bell state measurement. 2, 115, 118, 139

DFG Difference Frequency Conversion. 56

DIO Digital input/output. 20

DM dichroic mirror. 57

EMCCD Electron-Multiplying Charge-Coupled Device. 20, 21

FPI Fabry-Perot-Interferometer. 44, 46, 48, 58

FSR free spectral range. 18, 30, 31, 36, 43, 44, 46, 52

HALO High numerical Aperture Laser Objectiv. 10, 12–14, 73, 79, 81, 82, 84, 89

HOM Hong-Ou-Mandel. 3, 139

HR high reflection. 36, 38, 44

HT high transmission. 39

HTW University of Applied Science. 4, 5, 21, 65, 67, 71, 90, 105–109, 111, 129, 131–133

HVI Hard Virtual Instrument. 20

HWP half-wave plate. 33, 56, 159

JSA joint spectral amplitude. 29, 30

KTP Potassium titanyl phosphate ($KTiOPO_4$). 26, 29, 48

LST laser state transfer. 72, 77, 78, 86, 89, 90, 93, 94, 101, 162, 163

ML maximum-likelihood. 87, 120

MOT magneto-optical trap. 3

OTDR Optical Time Domain Reflectometry. 65, 66

PBS polarising beam splitter. 33, 38–43, 56, 57

PC physical contact. 82

PDH Pound-Drever-Hall. 16, 18, 35, 38

PID proportional-integral-derivative controller. 16

PLL Phase-Lock Loop. 18

PMT photo-multiplying tube. 21

ppKTP periodically poled potassium titanyl phosphate. 23, 24, 33, 35, 52

PPLN periodically poled Lithium-Niobate. 24, 56

QFC quantum frequency conversion. 3–5, 24, 52, 55, 58, 64, 71, 89, 90, 109, 111, 124, 133, 136

QKD quantum key distribution. 3, 4, 135

SBR signal-to-background ratio. 24, 50, 51, 60, 62, 64, 136, 137, 139

SHG second harmonic generation. 15, 24, 36, 39, 40, 160, 161

SM single-mode. 73

SPDC spontanous parametric down conversion. 4, 7, 21, 23, 24, 26–31, 33, 35, 38, 40, 43, 44, 48, 51, 52, 61, 133, 135, 138, 139, 159, 160

SPI Serial Peripheral Interface. 17

SSPD superconducting nanowire single-photon detector. 21, 59, 65, 90, 100, 106, 124, 129

TDC Time to digital converter. 20

TTL transistor-transistor logic. 40

UdS Saarland University. 4, 5, 66, 111

Contents

1 Introduction

Quantum networks [1, 2] with many different quantum systems are the backbone for various quantum technology applications. Networks based on entanglement are essential for distributed quantum computing [3, 4], quantum repeaters [5], quantum key distribution (QKD) with entangled photons [6], networks of quantum sensors [7], timekeeping [8] or are even discussed in the context of interstellar communication [9]. For all entanglement-based network applications, stationary nodes or quantum memories and links between them, i.e., flying qubits, are needed [10].

Several systems exist to realise a stationary node, e.g. single trapped atoms and ions, colour centres in diamonds, molecules, quantum dots, superconduction circuits, and clouds of atoms. Using single trapped ions as quantum network nodes has many appealing benefits. Trapped ions show good environmental protection, and their electrical and motional quantum state is under excellent control. Additionally, they offer well-controlled photonic interfaces with cavity enhancement [11, 12, 13] and without [14, 15, 16, 17, 18, 19]. Coherence times of up to 1 hour are reported [20, 21, 22, 23]. Furthermore, ion-based network nodes show high-fidelity quantum-gate operations on registers of tens of qubits [24, 25], which is especially important for quantum computing. Besides, they are excellent for sensing, and metrology [26, 27, 28].

Photons at optical wavelengths are the first choice for a flying qubit [29], as they can be transmitted through optical fibres or in free space and are as fast as possible. There are various possibilities to encode a qubit, e.g. in the polarisation degree of freedom, in the frequency- and spatial-mode [30], in different time bins [31], or in the orbital angular momentum [32].

Moreover, many experiments show the transmission of photons in free space over ever greater distances. Experiments using free-space links have transmitted a qubit across a lake (100 km) [33], between the Canary Island (143 km) [34] or even between a satellite and its ground station (1400 km) [35]. Free-space links are unbeaten when it comes to

losses, thus bridging large distances. Their drawbacks are the influence of atmospheric changes, e.g., weather, the need for an obstacle-free path between the nodes, and the beam divergence between two stations.

Another way of transmitting photons is through optical fibres, like in classical telecommunication. Fibres are not influenced by the atmosphere and do not need obstacle-fee paths. Additionally, a world-wide fibre infrastructure is already implemented, and fibre-optical components are optimised. The main limitation is the absorption of photons inside the fibre. Even at the optimal wavelength of 1550 nm the lowest reported loss is 0.1419 $\frac{\text{dB}}{\text{km}}$ [36], which means that after a distance of 21 km only 50 % of the input photons are available. Also, commercial products evolved, i.e. the ITU standard description G.654 specifies losses down to 0.15 $\frac{\text{dB}}{\text{km}}$ [37]. Nevertheless, the exponentially increasing loss with the travelled distance limits the communication range to a few hundred kilometres. In classical communication, this problem is solved by in-line fibre amplifiers and repeaters. This solution is not possible for a quantum channel due to the no-cloning theorem [38], which states that it is not possible to copy a qubit state perfectly from one system to another without modifying the initial one. A so-called quantum repeater [5] was proposed to overcome the limitation of fibre attenuation. The general idea is to divide the transmission channel into shorter segments, each consisting of two stationary qubits. The first step is to entangle these two stationary qubits, for example, by a Bell state measurement (BSM) between emitted photons [39]. This process transfers the atom-photon entanglement to an entanglement between the two stationary nodes and is therefore called entanglement-swapping [40, 41]. In the next step, several of these elementary building blocks are cascaded. With entanglement swapping between neighbouring stationary nodes, the entanglement is distributed over longer and longer distances until, finally, the two outer nodes are entangled. This technique reduces the distance the photons travel and breaks the exponential scaling loss. However, this is only true if the entanglement swapping runs asynchronously and successful entanglements are heralded. To ensure these prerequisites, the stationary qubit has to store the entanglement until the neighbouring node also reports the generation of entanglement with its partner. Without quantum memory, every entanglement-swapping attempt must succeed simultaneously. If only one attempt fails, the protocol has to start from the beginning. Such memoryless repeaters are called "quantum relays" [42] and do not help to overcome the problem of photon loss. Nevertheless, they can be helpful to facilitate other problems such as detector dark counts [43, 44].

Various repeater platforms have been proposed [45, 46]. Some of them include processing nodes capable of storing quantum information and performing quantum gates [47, 48],

which have significant advantages [49]. Ion-based platforms are good candidates for quantum repeaters, as discussed in [50]. They combine several essential capabilities: Interfaces between stationary qubit registers and telecom photons exist, the storage time is longer than the remote entanglement generation time, and deterministic quantum information processing is possible. Recently, such a repeater node was demonstrated [51]. The interface wavelength of the used ion in the experiment is 854 nm. This near-IR range wavelength limits the communication distance due to high fibre losses. The essential requirement of having an interface in the telecom wavelength range is only possible via quantum frequency conversion (QFC), which they used in their experiment.

The problem that the relevant optical transitions for the interface between photons and stationary nodes are in the visible or near-IR range is common to most platforms. Additionally, different quantum systems (ions, atoms, colour centres, ...) work with different characteristic wavelengths, making a direct photonic connection between them impossible. However, heterogeneous networks could take advantage of the different complementary strengths and functions of the different quantum systems, giving them advantages over networks of identical nodes. A solution to both problems is the modification of the spectral properties of the single photons via QFC in nonlinear optical crystals [52, 53]. In a recent experiment, [54], a complete quantum repeater node with kilometre-long fibres was demonstrated, which was only possible through QFC. The second mentioned advantage of QFC, the ability to connect different quantum systems, was shown in different experiments. There was a Hong-Ou-Mandel (HOM) experiment after frequency conversion between photons from two different quantum dots [55], and photons from an atomic ensemble and an ion [56]. In both cases, the wavelengths of the two systems are not compatible, and a HOM interference is not possible. However, through QFC, they are brought to the same wavelength, and the compatibility could be shown in a HOM experiment.

Once a link between stationary nodes is established, data can be transmitted. The channel is used to exchange a physically secure key via quantum key distribution (QKD). The exchanged key can subsequently be used to encrypt classical messages via a One-Time-pad, which is proven to be secure [57]. The channel can also be used to exchange quantum data directly via quantum state teleportation [58]. Several experiments report teleportation between two photons, like the mentioned free space experiments above [33, 34, 35]. Moreover, teleportation was also shown between a photon and a stationary node, for example, an atomic ensemble of caesium atoms [59], a rubidium magneto-optical trap (MOT) [60], and a colour-centre in diamond [61]. Also, the teleportation between two stationary nodes has been realised, for example, between two single-atom nodes [62, 63], between atomic

ensembles [64] or between two diamond-vacancy centres [65]. Additionally, the teleportation between two non-neighbouring diamond vacancy centre nodes has been demonstrated [66].

Several experiments have shown that quantum teleportation works in a lab environment. The next crucial step is to test the protocols under more realistic conditions, like standard communication fibres in metropolitan fibre networks. There already exists some metropolitan networks, in which, for example, QKD [67, 68] or a teleportation between two photons [69] has been implemented.

The central part of this work is the realisation of a small quantum network and the distribution of entanglement over long distances in a lab environment and over a metropolitan fibre. As discussed earlier, essential elements in quantum networks are quantum photonic interfaces between stationary quantum memories and photons. We present a photonic interface that connects a $^{40}Ca^{+}$ single-ion quantum memory to the telecom C-band. The interface is based on a memory-resonant, cavity-enhanced spontanous parametric down conversion (SPDC) photon pair source. Connecting the source with the telecom band is realised with bi-directional polarisation-conserving QFC. For the quantum frequency conversion, there is a collaboration with colleagues from the group of Christoph Becher [70, 71]. The converter is located in the same building on another floor. A 90 m long optical fibre connects both labs. We prove the functionality of the interface by demonstrating high-fidelity entanglement preservation during conversion, fibre transmission over up to 40 km and back-conversion to the memory wavelength. Furthermore, we present two interface protocols between a single trapped $^{40}Ca^{+}$ ion and single photons from the entangled-pair source, the quantum teleportation of a qubit from the ion onto a single photon and the entanglement transfer from photon-photon entanglement to ion-photon entanglement. Both protocols are based on the heralded absorption of one photon of the polarisation-entangled pair. In the case of the teleportation protocol, it allows us to identify all four Bell states. Finally, we combine the protocol with the interface above to connect the quantum memory with the telecom wavelength range, which allows for transmission in metropolitan fibre networks. Thanks to a collaboration with a local fibre provider, we have access to two 14 km long metropolitan fibres between the Saarland University (UdS) and the University of Applied Science (HTW) in Alt-Saarbrücken. These are standard telecommunications fibres laid above and below ground, including several patches and splices. These fibres enable us to test the developed network protocols and the entanglement distribution in a non-laboratory environment. We show control over

the polarisation drifts of the fibre. Finally, we demonstrate full quantum teleportation between an ion and a photon over this metropolitan fibre.

Structure of this thesis

In chapter 2, we summarise the basics of the ion experiment and our lab infrastructure. In the next chapter (chapter 3), we present the latest implementation of the photon-pair source and characterise its properties.

The experiments discussed in chapter 4 were performed without the ion and used the converter to distribute entanglement over various distances. In the first experiment, we show the preservation of entanglement in the conversion process. Afterwards, we include 20 km of optical fibre and measure the entanglement after this distance. In the following experiment, we terminate this fibre with a retro reflector and use the bidirectional capabilities of the converter to convert the photons back to the initial wavelength, thus bridging a distance of 40 km. We also demonstrate entanglement between photons detected at the UdS and the HTW after 14 km of metropolitan fibre.

In chapter 5, we describe the experiments in which we include the $^{40}Ca^{+}$ ion as a stationary quantum node. We show the entanglement transfer from photon-photon to atom-photon entanglement, a measurement similar to [72]. Additionally, we provide an improved protocol for teleporting a spin qubit from the ion to a polarisation qubit of a photon. The Bell measurement is based on the heralded absorption of one photon of the polarisation-entangled pair and allows us to identify all four Bell states. Moreover, we extend the protocol further by including the QFC, which connects our interface to the telecom wavelength range. Finally, we show teleportation between the ion and a photon detected at the HTW, 14 km apart.

The last chapter then summarises the work of this thesis and gives an outlook on further improvements and experiments planned in the future.

List of publications

During the time of this thesis, the following scientific articles were published:

- Polarisation-entangled photon pairs from a cavity-enhanced down-conversion source in Sagnac configuration [73]
- Quantum State Teleportation from a Single Ion to a Single Photon by Heralded Absorption [74]
- Telecom Quantum Photonic Interface for a $^{40}Ca^{+}$ Single-Ion Quantum Memory [75]
- Quantum teleportation with full Bell-basis detection between a $^{40}Ca^{+}$ ion and a single photon [76]

2 The $^{40}Ca^{+}$ ion as a quantum node

The fundamental unit for quantum information processing and communication is called a qubit. All experiments in this field need a physical system that stores and processes this information. One of the most straightforward systems is the polarisation state of a single photon. The problem is that photons always travel at the speed of light, which makes information storage very challenging. A suitable system for stationary operations, such as storing and processing, is a single trapped ion. The experimental control over the internal dynamics, as well as the motion of the particle, has been developed and refined over many years [77]. Furthermore, such a system is well isolated from the environment. There are many different ions available, all with their advantages and disadvantages.

In our group, we are using the singly ionised calcium isotope 40. Because of the single valence electron, the ion can be treated as a hydrogen-like system, simplifying its theoretical description. As shown in figure 2.1, the transitions between the relevant electronic levels are well addressable by available laser systems. The figure also includes the Landé factors of the energy levels and the Einstein coefficients of the transitions. The exact wavelengths and line widths of the transitions and the lifetimes of the excited states are compiled in table 2.1.

We can divide the level scheme into two so-called lambda schemes, $S_{1/2} - P_{1/2} - D_{3/2}$ and $S_{1/2} - P_{3/2} - D_{5/2}$. We use the first for laser cooling, which is necessary for long storage times, and the second for quantum logic. Especially the Zeeman sublevels of the $S_{1/2}$ ground state and the metastable $D_{5/2}$ state are of interest in defining a qubit. Furthermore, the $P_{3/2} - D_{5/2}$ transition at 854 nm is well suited for addressing by single photons from a SPDC source or the creation of single photons.

This chapter will lay out the essential technical facts about the ion experiment. Detailed descriptions of the entire toolkit, including cooling and pumping schemes, state detection and the coherent manipulation possibilities, are given in the theses of Jan Huwer [81] and Christoph Kurz [82]. Details about the spectrum of emitted photons are found in the

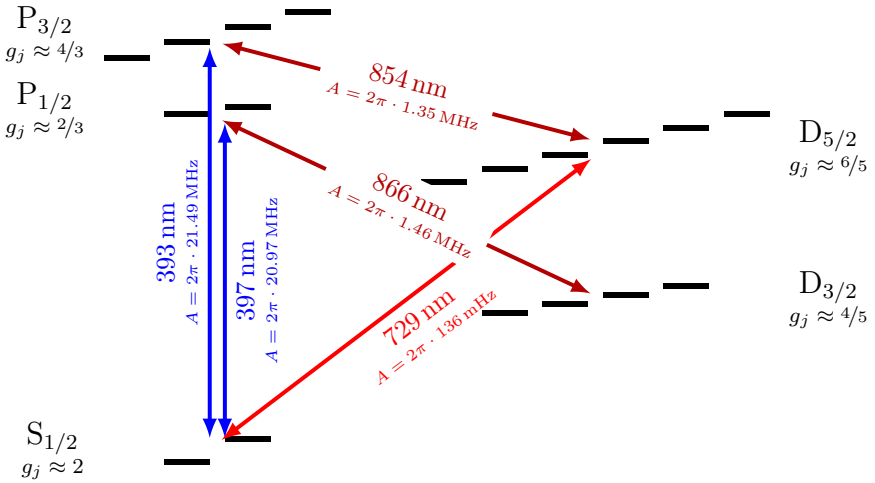

Figure 2.1: Relevant energy level scheme for the $^{40}Ca^{+}$-ion. The black bars represent the Zeeman sub-levels, and the arrows between the levels indicate the optical transitions with their wavelengths and Einstein A-coefficients. The Landé factors of the levels are also displayed.

Table 2.1: Summary of the relevant data of the calcium ion. The wavelengths were measured with a wavelength meter WS7-60 from HighFinesse GmbH. [78]

level	lifetime τ	transition	wavelength	$A_i/2\pi$
$S_{1/2}$	stable			
$P_{1/2}$	7.098(20) ns[79]	$\rightarrow D_{3/2}$	866.452 11(15) nm	1.44(7) MHz [79]
		$\rightarrow S_{1/2}$	396.959 15(3) nm	20.97(7) MHz [79]
$P_{3/2}$	6.924(19) ns[79]	$\rightarrow D_{5/2}$	854.443 37(15) nm	1.350(6) MHz [79]
		$\rightarrow D_{3/2}$	850.035 61(14) nm	0.1520(9) MHz [79]
		$\rightarrow S_{1/2}$	393.480 75(3) nm	21.49(6) MHz [79]
$D_{3/2}$	1.168(9) s[80]	$\rightarrow S_{1/2}$	732.5905(2) nm	0.1353(13) Hz [80]
$D_{5/2}$	1.176(11) s[80]	$\rightarrow S_{1/2}$	729.347 65(11) nm	0.1363(10) Hz [80]

thesis of Matthias Kreis [83]. We will refer to further theses conducted in the group, such as the ones of Stephan Kucera [72], Pascal Eich [84], Christoph Kurz [82], Philipp Müller [85], Hubert Lam [86] and Omar Elshehy [87].

2.1 The ion trap setup

The ion trap setup consists of a vacuum vessel containing the Paul trap (see section 2.1.1). An μ-metal box surrounds the vacuum vessel for shielding magnetic fields [86]. A picture of the current setup is shown in figure 2.2 (a) and (b). Directly mounted at the vacuum vessel is a pair of Helmholtz coils on each axis to compensate for the magnetic field of the earth and define a quantisation axis. If the μ-metal box is closed, no compensation is needed. Additionally, we have permanent magnets mounted on a ring holder, like in [22]. We use these to generate the magnetic field for the Zeeman splitting. In good approximation, the field is homogeneous around the trap centre, and comparable to one of the coils [87]. Also on the ion table is a strong pulsed laser at 535 nm, which is used to load the trap via ablation. This loading technique is not yet fully implemented. For loading single ions, we use ovens attached to the Paul trap (see section 2.1.3). Around the vessel are also several optical elements needed to address the ion under different angles with different lasers and collect the emitted light of the ion.

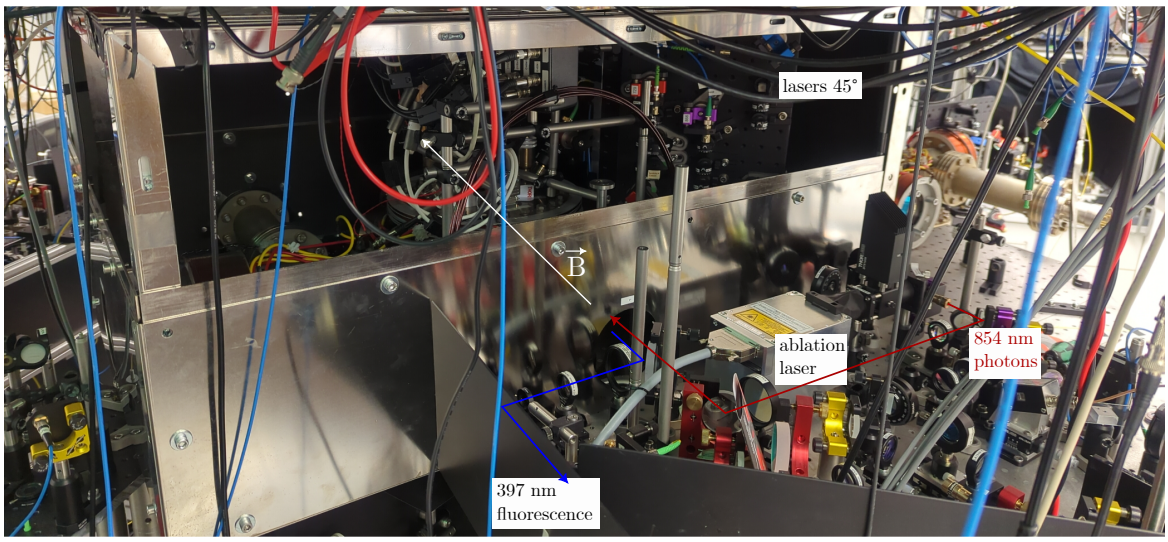

(a) Picture of the ion trap table with opened μ-metal box.

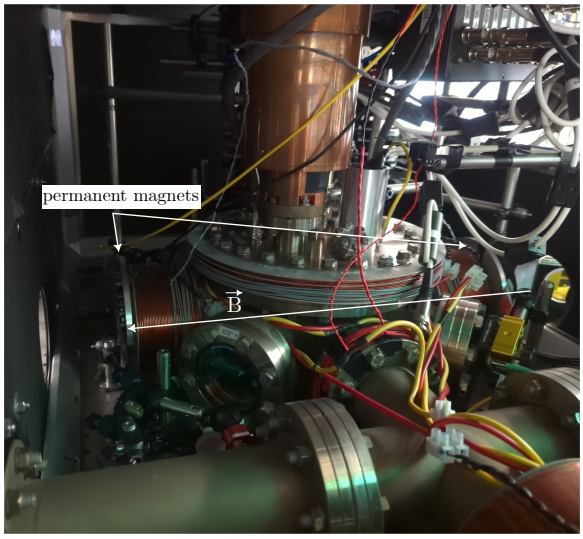

(b) View into the μ-metal box with the vacuum vessel.

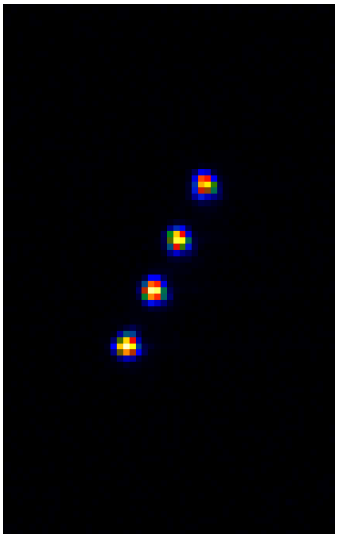

(c) A string of ions.

Figure 2.2: Picture of the ion trap table and a camera picture of an ion string. (a) View along the High numerical Aperture Laser Objectiv (HALO) axis. The vacuum vessel with the trap is placed inside the μ-metal box. The fibre couplers for the lasers under 45° and 90° (not visible in the picture) are mounted on a vertical breadboard. In red, we show the beam path of the photons, and in blue, the beam path of the 397 nm fluorescence. (b) Vacuum vessel with Helmholtz coils inside the μ-metal box. The view is perpendicular to (a). (c) Camera picture of a string of ions.

2.1.1 Linear Paul trap

When using single ions as quantum memories, it is essential to confine them in every dimension. Earnshaw's theorem [88] states that it is impossible to trap a charge in a static electrical field. So-called radio-frequency traps, which use dynamic electrical fields, solve this problem. Wolfgang Paul and Hans G. Dehmelt received the Nobel Prize for developing and applying this ion trap technique. Therefore, such traps are also called Paul traps.

The linear trap used in our experiment consists of four longitudinal electrodes in the form of a blade (see figure 2.3). These electrodes form the edge of a cuboid. The diagonally opposed electrodes are electrically connected and share the same potential U_{RF}. The voltage oscillates with the frequency ω_{RF} between its positive and negative maximum, with frequencies typically in the radio frequency range. This electric field confines the particle in two dimensions. The confinement in the last dimension, along the centre axis of the cuboid, is facilitated by a static electric field U_{tip}. Depending on the resulting force on this axis, the particles align in a string (see figure 2.2 (c)).

The electric potential in the centre of the trap is written as

$$\Phi(x,y,z) = \frac{\alpha U_{\mathrm{tip}}}{2l_0^2}\left(2z^2 - x^2 - y^2\right) + \frac{U_{\mathrm{RF}}}{2r_0^2}\cos\left(\omega_{\mathrm{RF}}t\right)\left(x^2 - y^2\right) \tag{2.1}$$

Here l_0 and r_0 are the minimum distance between the trap centre and the end tips or longitudinal electrodes. Due to the geometry of the trap, some shielding effects come in, which reduce the effective size of the end tip potential and are denoted by a numerical factor of $\alpha < 1$.

From the potential (equation (2.1)), we derive the equation of motion for a particle with charge e and mass m:

$$F_x = -e\frac{\partial\Phi(x,y,z)}{\partial x} = -e\left(\frac{U_{\mathrm{RF}}}{r_0^2}\cos\left(\omega_{\mathrm{RF}}t\right) - \frac{\alpha U_{\mathrm{tip}}}{l_0^2}x\right) = m\ddot{x} \tag{2.2}$$

$$F_y = -e\frac{\partial\Phi(x,y,z)}{\partial y} = -e\left(\frac{U_{\mathrm{RF}}}{r_0^2}\cos\left(\omega_{\mathrm{RF}}t\right) - \frac{\alpha U_{\mathrm{tip}}}{l_0^2}y\right) = m\ddot{y} \tag{2.3}$$

$$F_z = -e\frac{\partial\Phi(x,y,z)}{\partial z} = -e\left(2\frac{\alpha U_{\mathrm{tip}}}{l_0^2}z\right) = m\ddot{z} \tag{2.4}$$

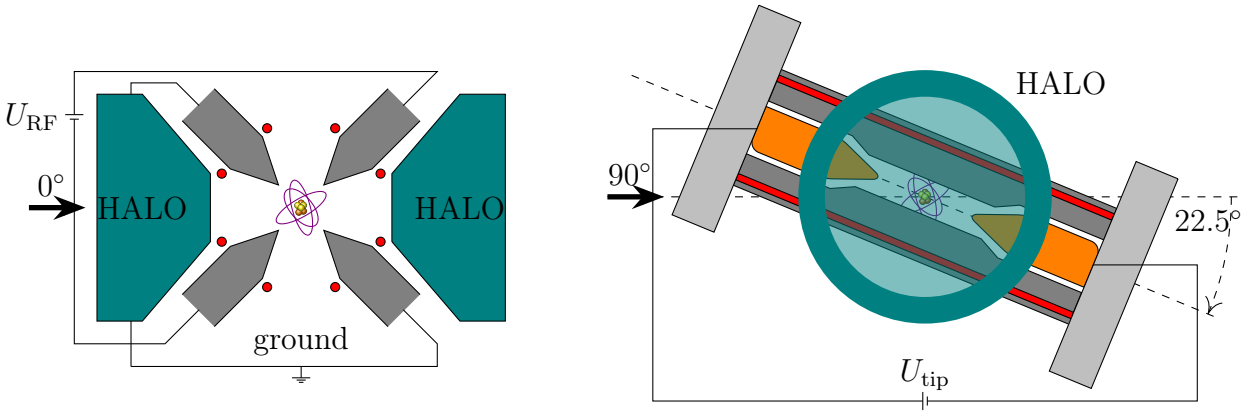

(a) View along trap axis. (b) Side view

Figure 2.3: Schematic of a linear Paul trap. The dark grey edges in (a) are the blade electrodes of the trap. The teal-coloured parts are the two HALOs. The red points and lines represent the compensation electrodes. The orange parts in (b) are the end-tip electrodes.

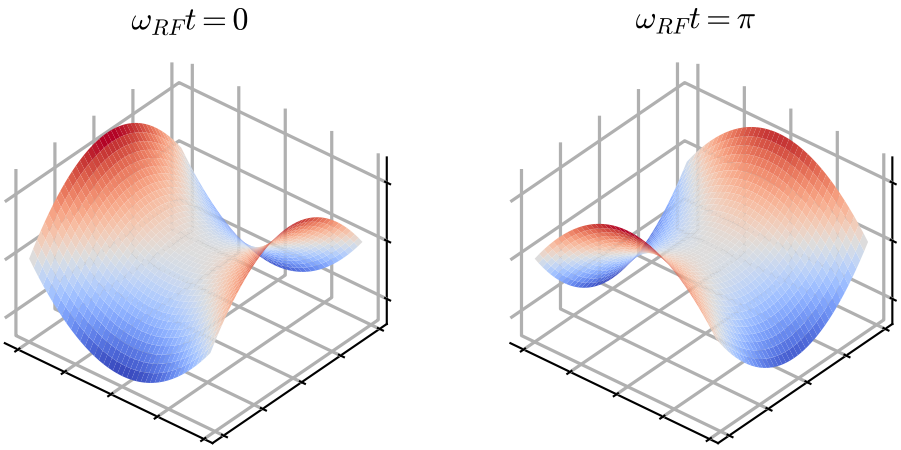

Figure 2.4: Oscillation saddle potential (radial term) according to equation (2.1) for two instances. The trapped particle would sit in the middle of the potential. If the particle moves away from the centre, it experiences an oscillating force.

With the substitutions

$$a_x = a_y = -\frac{1}{2}a_z = -\frac{4e\alpha U_{\mathrm{tip}}}{ml_0^2\omega_{\mathrm{RF}}^2} \tag{2.5}$$

$$q_y = -q_x = \frac{2eU_{\mathrm{RF}}}{mr_0^2\omega_{\mathrm{RF}}^2}, \qquad q_z = 0 \tag{2.6}$$

these equations transform into a Mathieu differential equation

$$\frac{\mathrm{d}^2 x_i}{\mathrm{d}t^2} + \left(a_i - 2q_i \cos\left(\omega_{\mathrm{RF}} t\right)\right) \frac{\omega_{\mathrm{RF}}}{4} x_i = 0 \tag{2.7}$$

Under the condition $|a_i|, q_i^2 \ll 1$ the Mathieu equation have a stable solution

$$x_i(t) \approx \cos\left(\omega_i t\right) \left(1 - \frac{q_i}{2} \cos\left(\omega_{\mathrm{RF}} t\right)\right) \tag{2.8}$$

with

$$\omega_i = \frac{\omega_{\mathrm{RF}}}{2} \sqrt{a_i + \frac{q_i^2}{2}} \tag{2.9}$$

This term for the frequency is a superposition of two oscillations, a *fast* one and a *slow* one. The *fast* motion oscillates with the driving radio frequency and is called micromotion. The *slow* motion is orientated in the radial direction and is called secular motion.

The parameter for the current trap setup are $r_0 = 0.8\,\mathrm{mm}$, $l_0 = 2.5\,\mathrm{mm}$, $\alpha = 0.183$ [82, 89], $U_{\mathrm{tip}} = 400\,\mathrm{V}$, $U_{\mathrm{RF}} \approx 1.5\,\mathrm{kV}$, $\omega_{\mathrm{RF}} = 2\pi \times 25.890\,\mathrm{MHz}$.

Additionally, there are four compensation electrodes beside the blades of the trap (see figure 2.3). Electric stray fields and imperfections of the trap lead to additional forces on the ion and displace it from the equilibrium position. We use the electrodes to move the ion inside the trap potential. The improved alignment in the trap potential minimises the micromotion of the trapped particle, which is important for optimising the cooling and the coherent manipulations.

2.1.2 Optical access: HALO

The Paul trap and a pair of HALOs are connected to the top flange of the vacuum vessel. For sub-micrometre positioning of the objectives, these are mounted on xyz translation stages[1]. The objective consists of four lenses to reach the diffraction limit for the relevant wavelength range between 400 nm and 870 nm. The design reaches a numerical aperture of 0.4, resulting in an opening angle of 47.2° and coverage of a solid angle of 4.17 %. The key facts for the upper and lower limit of the wavelength range are written in table 2.2. More detail is found in [90].

[1] Attocube: ANPx100, ANPz100

Table 2.2: Key facts of the HALOs.

	397 nm	866 nm
transmission	95.7 %	98.8 %
back focal length	13.7 mm	15.1 mm
focal spot size	1.2 µm	2.6 µm
working distance	11.8 mm	

The focal spot size in the centre of the trap enables addressing individual ions and collecting their fluorescence. In the experiments of this thesis, one HALO is aligned for optimal coupling of single photons at 854 nm. We use the same HALO for collecting the fluorescence of the ion at 397 nm. For this wavelength, the HALO is too far from the ion, resulting in a focused beam. The other HALO is set for optimal collection of the fluorescent light at 393 nm. Light at 854 nm, transmitted through both HALOs, is thus divergent.

2.1.3 Photo-ionisation & ion loading

Inside the vacuum chamber, in the direction of the trap centre, there are two resistive-heater tube ovens with metallic granules. It releases a beam of neutral Ca atoms through the trap by heating them. In order to trap a particle, at least one of the neutral atoms has to be ionised. A two-photon resonance-enhanced photoionisation process does this. A first beam excites the $4s^2\,{}^1S_0 \rightarrow 4s4p^1P_1$ transition at 422.67 nm. A second beam at 370 nm excites the $4s4p^1P_1$ state to a high Rydberg state. The remaining energy for releasing the electron comes from the strong electric field of the Paul trap. Although this process takes only nanoseconds, capturing a single ion takes about 5 min - 10 min. An increased waiting time leads to an arbitrary number of trapped ions. More details are found in [90]. For lowering the trapping time, there is also a calcium target for ablation loading [91] inside the trap, but the technique still needs to be fully implemented.

2.2 Laser system

We use laser systems for the 393 nm, 397 nm, 729 nm, 850 nm, 854 nm and 866 nm transitions, as well as a 375 nm and 422 nm laser for photoionisation. A laser at 852 nm

serves as a reference laser. Besides the laser at 729 nm, all others come from "Toptica Photonics AG" and are extended-cavity diode lasers with a Littrow configuration for optical feedback. All lasers have a free-running spectral linewidth of about 150 kHz. In the following, we compile the main facts of the different laser systems:

- 423 nm Step 1 of photoionization. The laser is free-running.
- 375 nm Step 2 of photoionization. The laser is free-running at a fixed wavelength.
- 852 nm Toptica DL pro. Cs resonant fundamental laser [92] for transfer locking scheme. Locked to the $S_{1/2} - P_{3/2}$ transition of Cs via saturated absorption spectroscopy in a vapour cell.
- 393 nm Toptica DL pro. Excites $S_{1/2} \rightarrow P_{3/2}$ transition. Stabilised by transfer lock to the 397 nm laser.
- 794 nm Toptica TA-SHG pro.Frequency doubled to 397 nm by second harmonic generation (SHG) in a bow-tie resonator. The laser excites the $S_{1/2} \rightarrow P_{1/2}$ transition. Used as a cooling laser for pumping and fluorescence detection. Transfer-locked to the 852-nm reference laser.
- 866 nm Toptica DL pro. Excites $S_{1/2} \rightarrow D_{3/2}$ transition. Used as repump laser in the cooling scheme. Transfer-locked.
- 850 nm Toptica DL pro. Resonant to the $P_{3/2} \rightarrow D_{3/2}$ transition. Mainly in use before the purchase of the 393 nm laser. Transfer-locked.
- 854 nm Toptica TA-SHG pro. Resonant to the $P_{3/2} \rightarrow D_{5/2}$ transition. Transfer-locked. It is also frequency doubled to 427 nm. This wavelength is used as a pump for the photon pair source.
- 729 nm M^2 Solstis. Resonant to the $S_{1/2} \rightarrow D_{5/2}$ quadrupole transition. Stabilised to an ultra-high finesse cavity, resulting in a linewidth below 32(2) Hz. More details are below and in [81]. Much cleaner spectrum compared to the Diode laser below. Unfortunately, we could not operate this laser reliably over long periods due to several technical deficiencies.
- 729 nm Toptica TA pro. Resonant to the $S_{1/2} \rightarrow D_{5/2}$ quadrupole transition. Stabilised to an ultra-high finesse cavity, as explained above. Most measurements with the ion are performed with this laser.

We use Acousto-Optical Modulators (AOMs) to fine-tune the laser frequencies in the MHz range, stabilise the laser powers, and switch the light. For monitoring the wavelengths, we use a HighFinesse WS7 wavemeter.

2.2.1 Transfer lock

Addressing individual transitions in the Ca^{+} ion requires a laser linewidth below the natural linewidth and a stable absolute frequency. A transfer-locking scheme fulfils both needs. We reach a low linewidth by locking the laser to a Fabry-Pérot resonator and the long-term stability to a fixed frequency by locking the resonator to another laser that in turn is stabilised to a resonance in Cs with the help of a Cs vapour cell as a stable reference. Figure 2.5 shows a schematic overview of the schema.

The first step in the locking scheme is stabilising the 852 nm laser to the mentioned Cs vapour cell. Next, we transfer the stability of this laser to a Fabry-Pérot resonator ($\mathcal{F} \approx 500$, $\nu_{\mathrm{FSR}} = 1\,\mathrm{GHz}$, $\Delta\nu \approx 2\,\mathrm{MHz}$) by stabilising its length using the Pound-Drever-Hall (PDH) technique [93]. Finally, we lock another laser to this resonator. For each laser, we have a separate transfer resonator.

Setting up the Fabry-Pérot resonators in a confocal configuration allows easy coupling under different angles and reduces coupling overhead [92]. However, the obtained PDH signal is insufficient for some lasers. In the confocal configuration, we observe changes in the resonance frequency and changes in the shape and offset of the PDH signal depending on the angle of incidence. A single-mode configuration solves this problem and gives a cleaner PDH signal [83].

A combination of a fast piezo-actuator and the slow thermal expansion of a spacer achieve the stabilisation of the resonator length. Using thermal expansion guarantees long-term operation and makes it possible to compensate for air pressure changes and hold the piezo around its zero position.

Additionally, the 393nm and the 794nm cavity are in a vacuum to prevent changes in the optical path length caused by air pressure changes on the timescale of days. The observed pressure change is around 0.1 mbar per day [83].

For the generation of an error signal for the proportional-integral-derivative controller (PID), we use the PDH technique [93]. The regulation is performed via self-build hardware, the ”cavity locker“, consisting of a microcontroller and a Raspberry Pi, communi-

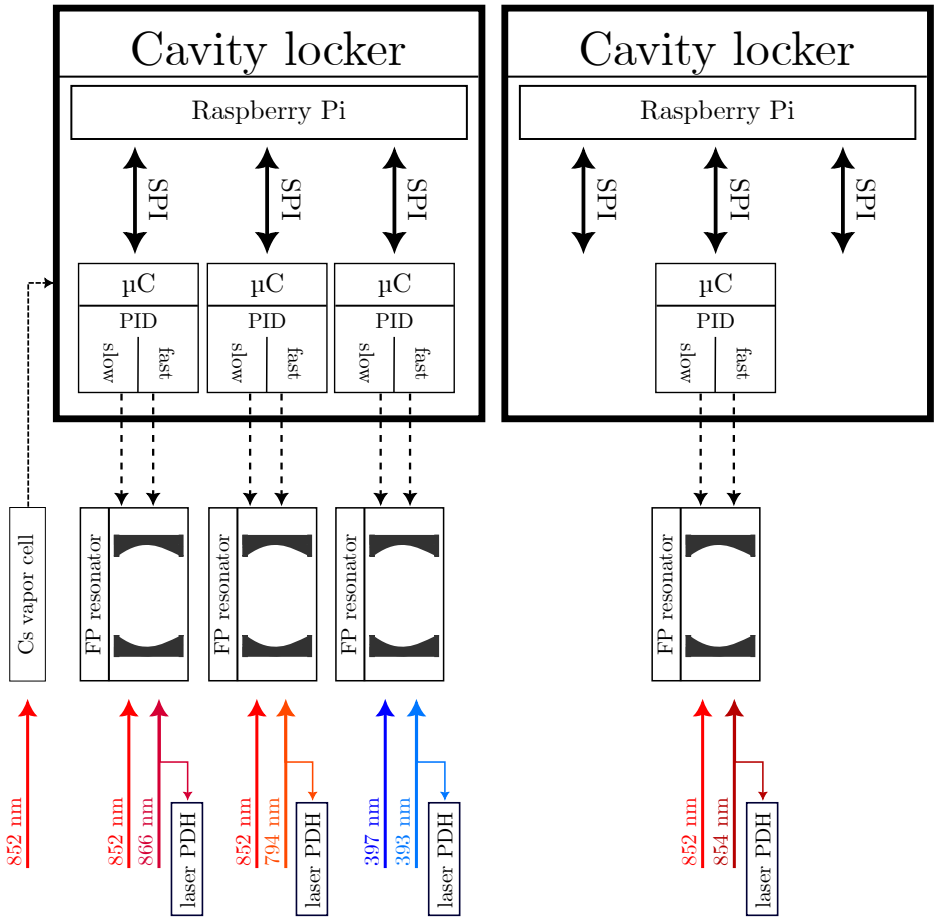

Figure 2.5: Schematic overview of the transfer-locking scheme. The resonators are stabilised to the 852 nm laser via the "cavity locker". The 852 nm reference is stabilised with the help of a Cs vapour cell. The individual lasers are then stabilised to the corresponding resonator.

cating via the Serial Peripheral Interface (SPI) protocol. The microcontroller runs two feedback loops—one for the slow thermal expansion and one for the piezo. The user interface runs on the Raspberry Pi, which is accessible over the network. More details are shown in the thesis of Matthias Kreis, who built the device [83]. With the presented technique, the resulting linewidth of the lasers is in the range of 100 kHz-300 kHz. More details on the locking scheme are found in [92, 94].

2.2.2 Qubit laser at 729 nm

Due to the high demands on the linewidth and stability of the qubit laser, which addresses the $S_{1/2} \rightarrow D_{5/2}$ quadrupole transition, the laser uses another stabilisation scheme. We

lock the laser directly to a passively stable ultra-high finesse resonator ($\mathcal{F} \approx 480\,000$). The spacer between the two mirrors is made of ultra-low-expansion glass. The whole cavity is mounted in an ultra-high vacuum to reach the best isolation from the environment. The whole chamber is additionally temperature-stabilised. The setup features a linewidth of 4 kHz and a free spectral range (FSR) $\nu_{\mathrm{FSR}} \approx 1.9\,\mathrm{GHz}$. The locking is realised by the PDH technique and a fast feedback loop module from Toptica (FALC 110). The drift due to the ageing of the spacer material is measured to be $80\,\mathrm{mHz\,s^{-1}}$ and the laser linewidth is below 32(2) Hz.[81].

2.3 Magnetic field

Good control over the magnetic fields and dynamic stray fields at the position of the ion is mandatory for all our experiments. Initially, the static field was produced by three pairs of coils, one on each axis. These coils are driven by an "Aim TTi QL 355" power supply. The long term stability is below 100 µA at 3 A[82]. Therefore, the expected magnetic field noise should be below 10 nT.

Three additional techniques are used to decrease magnetic field fluctuations and compensate for dynamic stray fields.

Feed-forward optimization. The main contribution of the dynamic stray fields comes from the power line and therefore shows oscillations at 50 Hz and its harmonics. Additional smaller coils ($\approx$ 20 windings) are added to the main field coils for compensation. These superimpose a specific *ac* magnetic field onto the *dc*-field of the main coils. A computer-controlled analogue output generates the signal for the compensations coils. A power line-locked Phase-Lock Loop (PLL) generates the triggers for the waveform generation. The parameter for amplitude and phase are measured in a Ramsey-type experiment (see section 5.2). For more details, see [95].

Permanent magnets. We now use permanent magnets to reduce external noise and the noise from the coils. A pair of rings is placed on both sides of the vacuum chamber with several small permanent magnets inside. These small magnets produce a homogenous field comparable to the field from the coils. Details are found in [87].

Magnetic shielding. A suitable way to increase the coherence time of the stored qubits is to suppress ambient magnetic fields. We archived this by an enclosure ($1000 \times 655 \times 470$ mm^3) out of heat-treated μ-metal, which surrounds the whole trap apparatus. The walls

consist of two layers of 1 mm μ-metal and an air gap of 2 mm. This cuboid is placed on the optical breadboard around the trap. For optical and electrical access, there are some holes in the box. Details are found in [86]

The setup for the measurements of this thesis uses magnetic shielding with permanent magnets to produce the quantisation fields. The coils, excluding the active compensation coils, are switched off. With the described setup, we reach an significant improvement in decoherence time. We reach an coherence time in the $S_{1/2}$ ground state of about 20 ms and in the $D_{5/2}$ state of about 3.5 ms. This is an improvement of 18 dB / 13 dB, compared to the old setup without magnet shielding but feed-forward optimisation.

2.4 RF coil

Additionally to the lasers, which drive the optical transitions, there is a magnetic field coil under the vacuum chamber to directly manipulate the Zeeman sublevels of the $S_{1/2}$ state. The coils have a diameter of 16 cm with two windings. An additional capacitor is installed for resonant enhancement, forming an LC circuit. By tuning the capacitance, the resonance is tuned to match the atomic resonance of $2\pi \times 8$ MHz at approximately 0.28 mT of static magnetic field produced by the permanent magnets. The realized Rabi frequency is $\approx 2\pi \times 100$ kHz. More details are found in [82].

2.5 Control unit

The experiments done with the ion consist of complex sequences of laser and RF pulses. Therefore complete control over the frequency, amplitude and phase of the RF signals is needed. The switching of the lasers is realised via AOMs, with a centre frequency between 100 MHz and 300 MHz. Additionally, it must be possible to react in nearly real-time to events, like detecting a photon.

A commercially available system called HYDRA fulfils these requirements. The system is produced by "Signadyne" (now part of Keysight), a spin-off of Marc Almendros, a former group member, who built the initial control unit in his thesis [96].

A PXI rack with various available cards is the basis of this system, making it easily expandable. An external Rubidium atomic clock[2] synchronises all RFs signals and serves as the time base for HYDRA. Programming and interaction with the device happen in two parts. The sequence itself, meaning the programming of the timing of the pulses, is done with a GUI program from Signadyne, which uses a flow-chart-like programming language. This program generates an Hard Virtual Instrument (HVI), which is run directly on a PXI card. A PC connected to HYDRA acts as an interface and processes the data. The interaction happens via a GUI. The scripts are written in Matlab by our group. Therefore, variables and results are stored in the Matlab environment and are available for the following sequences. The current configuration has the following specifications:

- Arbitrary waveform generator (AWG)
  - 1x Signadyne SD-PXE-AOU-H0002-1G / Keysight M3202A: in total 4 channels with 1 GSa/s, 400 MHz bandwidth
  - 2x Signadyne SD-PXE-AOU-H3344-1G: in total 8 channels with 500 MSa/s, 200 MHz bandwidth
- Time to digital converter (TDC)
  - Signadyne SD-PXE-TDC-H3345-1G: 8 channels: 320 ps time resolution
- Digital input/output (DIO)
  - Signadyne SD-PXE-DIO-H0002-1G: 64 digital I/O channels, 800 MBit/s

Attached to HYDRA are two additional devices. A microcontroller reads out the Electron-Multiplying Charge-Coupled Device (EMCCD) camera to discriminate the different ions in a string and processes the information in a sequence. The second device is a custom-made analogue input card that reads the signals from various photodiodes. These photodiodes are necessary to stabilise the different laser light amplitudes. The diploma thesis of Stephan Kucera [97] shows more details.

[2]Stanford Research Systems, FS725

2.6 Single-photon detection

Single-photon detection is a crucial point in all the experiments of this thesis. There are different types of detectors involved.

We use a photo-multiplying tube (PMT)[3] to detect the fluorescence counts. A multi-mode fibre first collects the light and guides it to the detectors. The quantum efficiency of the tube used is around 25 %. The timing resolution is around 280 ps.

To detect the emitted 393 nm photons, we use Avalanche Photo Diodes (APDs) [4]. These are coupled free space and are specified to have a quantum efficiency of 50 %. The timing resolution is around 1 ns.

The detection of the photons at 854 nm generated by the SPDC source (chapter 3) is also realised using APDs[5]. These have a specified quantum efficiency of 40 % at 854 nm and are free-spaced coupled. The timing resolution is around 1 ns.

For the detection of converted photons at 1550 nm, we use superconducting nanowire single-photon detectors (SSPDs). The detectors in the labs of AG Becher[6] have a quantum efficiency of 75 %, the ones installed at the HTW[7] show a quantum efficiency of 85 %. The timing resolution is below 90 ps.

For imaging the ion, there is an EMCCD[8], a low light level camera, to image the ion. Such a picture from a string of ions is shown in figure 2.2 b). The pixel size of the camera is 16 µm. The optics between the ion and the camera lead to a magnification of about 20. Together we reach a spatial resolution of 800 nm.

[3]Hamamatsu Photonics K.K. 7422P-30 SEL
[4]Laser Components COUNT-10B
[5]Excelitas SPCM-AQRH
[6]Single Quantum EOS
[7]Quantum Opus One
[8]Andor iXon DV887DCS-BV

3 Photon-pair source

Single photon-pair sources are a fundamental resource in quantum communication systems. They require on-demand photon creation, high photon rates, low transmission losses, pure entangled quantum states, and tunable spectral and polarisation properties to match any quantum-network technology. Most of these requirements have already been realised in separate systems. The current work is to combine as many of these points in a single device as possible.

The main goal of our approach is to interface a single $^{40}Ca^{+}$ ion as a quantum node with single photons as quantum information carriers. We present a source based on SPDC in a nonlinear crystal. In this process, a single pump photon decays into two photons, highly correlated in time, energy and polarisation. The available and addressable transitions in the ion and the choice of pump lasers and conversion crystals limit the wavelength range of the SPDC photons to the near IR. Already in the predecessors of the source presented here [98, 72] , a wavelength of 854 nm was chosen, which addresses the $P_{3/2}$ to $D_{5/2}$ transition in the $^{40}Ca^{+}$ ion. This choice has some benefits in transmission in optical fibres, and in the properties of the Zeeman sub-structure of the Ca^{+} ion [99].

The starting point for the source design of this thesis is the source described in [72]. It already implemented state-of-the-art features to reach high purity states and spectral brightness. The nonlinear crystal is placed inside a macroscopic resonator. This configuration leads to a spectral redistribution of the emission into the resonator modes, simplifying the filtering to a single mode and increasing the brightness. With a spectral brightness of 4.5×10^4 pairs/(s mW MHz), it was one of the brightness photon-pair sources published [100, 101, 102]. Additionally, the resonator was placed inside an interferometer, which guarantees high entanglement purity and fidelity in the range $> 98\,\%$, comparable to other interferometric sources like [103, 104, 105].

This chapter describes our new photon-pair source, which is based on type-II conversion in a periodically poled potassium titanyl phosphate (ppKTP) crystal, and highlights the

improvements made to the previous source version and the characterisation. We start in section 3.1 by calculating the quantum state of the SPDC source. In section 3.2.10, we show the calculation of the signal-to-background ratio (SBR) and discuss the background correction applied in the experiments presented in the following chapters. The last section (3.2) shows the new design and its characterisation.

3.1 SPDC quantum state

Generally defined, the dielectric polarisation **P** is the sum of material responses to different electric field orders. Higher order effects are mainly present in nonlinear optical media, such as ppKTP or periodically poled Lithium-Niobate (PPLN). The general expression for the polarisation is

$$\vec{P} = \varepsilon_0 \sum_{i=1}^{n} \chi^{(n)} \vec{E}^n = \varepsilon_0 \left[\underbrace{\chi^{(1)} \vec{E}}_{P_\mathrm{L}} + \underbrace{\chi^{(2)} \vec{E}^2 + \chi^{(3)} \vec{E}^3 + \ldots}_{P_\mathrm{NL}} \right] \tag{3.1}$$

wherein $\chi^{(n)}$ is the electric susceptibility, a tensor of $(n+1)$-th order. Here we are interested in the terms P_NL, and more specifically, in second-order terms, as these describe two-photon processes, such as SPDC, SHG or QFC. SPDC is the process in which a pump photon spontaneously splits into two photons inside a nonlinear medium. The generated photons show strong correlations in time, energy and polarisation. In QFC, a classical pump field is mixed with single photons to convert it to the sum or difference frequency. Lastly, in a SHG process, two photons of the same frequency interact with the nonlinear material to generate a new photon with twice the energy/frequency of the initial photons.

Here, we will focus on SPDC. We apply some simplification to the $\chi^{(2)}$-tensor and then derive an expression for the quantum state via perturbation theory. We start with an expression for the t-th component of the second-order polarisation in the Einstein sum convention.

$$P_i^{(2)}\left(\omega_n + \omega_m\right) = \varepsilon_0 \sum_{n,m} \chi_{ijk}^{(2)}\left(\omega_n + \omega_m, \omega_n, \omega_m\right) E_j\left(\omega_n\right) E_k\left(\omega_m\right) \exp\left(-\mathrm{i}\left(\omega_n + \omega_m\right) t\right) \tag{3.2}$$

Then we are going to reduce the number of independent components. We use the fact that the susceptibility describes all properties of the medium. Hence, the tensor reflects the structural symmetries of the medium. We use the following three symmetries:

- **Intrinsic permutation symmetry.** We can interchange the indices of the two frequencies and the corresponding indices of the tensor [106]

$$\chi^{(2)}_{ijk}\left(\omega_n+\omega_m,\omega_n,\omega_m\right)=\chi^{(2)}_{ikj}\left(\omega_n+\omega_m,\omega_m,\omega_n\right) \tag{3.3}$$

- Lossless optical media fulfil **full permutation symmetry**

$$\chi^{(2)}_{ijk}\left(\omega_n+\omega_m,\omega_n,\omega_m\right)=\chi^{(2)}_{jki}\left(\omega_n,-\omega_m,\omega_n+\omega_m\right)=\chi^{(2)}_{kij}\left(\omega_m,\omega_n+\omega_m,-\omega_n\right) \tag{3.4}$$

- If the frequencies of the involved fields are much smaller than the resonance frequency of the medium, the **Kleinman-symmetry** [107] is valid, meaning $\chi^{(2)}$ is independent of the frequency.

We therefore define a new 3×6-matrix

$$d_{ijk}=\frac{1}{2}\chi^{(2)}_{ijk} \tag{3.5}$$

with the remaining indices

jk	11	22	33	23,32	31,31	12,21
l	1	2	3	4	5	6

The nonlinear polarisation is then expressed as a simple matrix product

$$P_{\mathrm{NL}}\left(\omega_n+\omega_m\right)=4\varepsilon_0\begin{pmatrix} d_{11} & d_{12} & d_{13} & d_{14} & d_{15} & d_{16}\\ d_{16} & d_{22} & d_{23} & d_{24} & d_{14} & d_{12}\\ d_{15} & d_{24} & d_{33} & d_{23} & d_{13} & d_{36}\end{pmatrix}\begin{pmatrix} E_x\left(\omega_n\right)E_x\left(\omega_m\right)\\ E_y\left(\omega_n\right)E_y\left(\omega_m\right)\\ E_z\left(\omega_n\right)E_z\left(\omega_m\right)\\ E_y\left(\omega_n\right)E_z\left(\omega_m\right)+E_z\left(\omega_n\right)E_y\left(\omega_m\right)\\ E_x\left(\omega_n\right)E_z\left(\omega_m\right)+E_z\left(\omega_n\right)E_x\left(\omega_m\right)\\ E_x\left(\omega_n\right)E_y\left(\omega_m\right)+E_y\left(\omega_n\right)E_x\left(\omega_m\right)\end{pmatrix} \tag{3.6}$$

The phase-matching conditions

$$\hbar\omega_{\mathrm{p}}=\hbar\omega_{\mathrm{s}}+\hbar\omega_{\mathrm{i}}\qquad\text{and}\qquad\hbar\vec{k}_{\mathrm{p}}=\hbar\vec{k}_{\mathrm{s}}+\hbar\vec{k}_{\mathrm{i}} \tag{3.7}$$

represent the conservation of energy and momentum that must be fulfilled.

By fixing the geometry of the described system, this expression is written as a scalar equation

$$P_{\mathrm{NL}}\left(\omega_n + \omega_m\right) = 4\varepsilon_0 d_{\mathrm{eff}} E\left(\omega_n\right) E\left(\omega_m\right) \tag{3.8}$$

with the effective susceptibility d_{eff}.

As an example, we look at the susceptibility for Potassium titanyl phosphate ($KTiOPO_4$) (KTP) [108]

$$d = \begin{pmatrix} 0 & 0 & 0 & 0 & d_{15} & 0 \\ 0 & 0 & 0 & d_{24} & 0 & 0 \\ d_{31} & d_{32} & d_{33} & 0 & 0 & 0 \end{pmatrix} = \begin{pmatrix} 0 & 0 & 0 & 0 & 6.1 & 0 \\ 0 & 0 & 0 & 7.6 & 0 & 0 \\ 2.4 & 4.4 & 16.9 & 0 & 0 & 0 \end{pmatrix} \frac{\mathrm{pm}}{\mathrm{V}} . \tag{3.9}$$

Depending on the polarisation of the three light fields, the SPDC process is categorised into three groups

- type-0: The three light waves have the same polarisation.
- type-1: The pump light has orthogonal polarisation to the two generated fields.
- type-2: The polarisation of the generated waves are orthogonal.

3.1.1 Quantum state

We use the time-dependent perturbation theory to derive the quantum state of the SPDC source. The derivations of this chapter follow the explanations given in [109, 110, 111]. We start with the Hamilton operator for the electric field

$$\hat{H} = \underbrace{\frac{1}{2}\int_V \mathrm{d}^3 r \left(\vec{\varepsilon}_0 \vec{E}\cdot\vec{E} + \vec{B}\cdot\vec{H}\right)}_{\hat{H}_0} + \underbrace{\frac{1}{2}\int_V \mathrm{d}^3 r \vec{P}\cdot\vec{E}}_{\hat{H}_{\mathrm{I}}} . \tag{3.10}$$

We divide the Hamilton operator into a part $\hat{H}_0$, which represents the electromagnetic field in free space, and a part $\hat{H}_{\mathrm{I}}$, which describes the interaction with the dielectric medium.

For the SPDC process, we have to look at the interaction Hamiltonian and second-order terms for the susceptibility. Again in Einstein's sum convention, we get

$$\hat{H}_{\mathrm{I}} = \frac{\varepsilon_0}{2} \int\limits_V \mathrm{d}^3 r \chi^{(2)}_{ijk} E_i(\omega_1) E_j(\omega_2) E_k(\omega_3) \tag{3.11}$$

In the frame of the second quantisation, we replace the classical electrical field with the following operator

$$\mathbf{E}\left(\mathbf{r}, t\right) = \mathrm{i} \sum_{\mathbf{k}} \sqrt{\frac{\hbar \omega_{\mathbf{k}}}{2 \varepsilon_0 V}} \left(\hat{a}_{\mathbf{k}} \exp\left(\mathrm{i}\left(\mathbf{k} \cdot \mathbf{r} - \omega_{\mathbf{k}} t\right)\right) - \mathrm{h.c} \right) \mathbf{u}_{\mathbf{k}} \tag{3.12}$$

where V is the quantisation volume, $\mathbf{u}_{\mathbf{k}}$ is the polarisation vector for the mode with wave vector $\mathbf{k}$, and $\hat{a}_{\mathbf{k}}$ is the annihilation operator. We transform the sum into integrals over the quantisation volume for a big quantisation volume. Furthermore, we will take

$$\left|\Psi(t')\right\rangle = \left|\alpha_{\mathrm{P}}(\omega)\right\rangle \left|0_{k_2}, 0_{k_3}\right\rangle \tag{3.13}$$

as the ground state of the perturbation calculation. We have the coherent state of the pump $\left|\alpha_{\mathrm{P}}(\omega)\right\rangle$ and the vacuum state for the so-called signal- and idler photon $\left|0_{k_2}, 0_{k_3}\right\rangle$.

Additionally, we make the following assumptions, the pump field has a fixed polarisation along the z-axis, and the propagation direction is also along the z-axis. Therefore, we get the simplified Hamiltonian

$$\begin{aligned} \hat{H}_{\mathrm{I}} = -\frac{\mathrm{i}}{32\pi^3} \sqrt{\frac{\hbar^3 L^3}{2\varepsilon_0}} \int\limits_{-L}^{0} \mathrm{d}z \iiint \mathrm{d}k_1 \, \mathrm{d}k_2 \, \mathrm{d}k_3 \sqrt{\omega_{k_1} \omega_{k_2} \omega_{k_3}} \chi^{(2)}_{ijk}(\omega_{k_1}, \omega_{k_2}, \omega_{k_3}) \\ \times \hat{a}_{k_1} \hat{a}^{\dagger}_{k_2} \hat{a}^{\dagger}_{k_3} \exp\left(\mathrm{i}\left(k_1 - k_2 - k_3\right) z\right) \exp\left(-\mathrm{i}\left(\omega_{k_1} - \omega_{k_2} - \omega_{k_3}\right) t\right) \end{aligned} \tag{3.14}$$

Finally, we perform the integration over the length of the crystal L and get

$$\int\limits_{-L}^{0} \mathrm{d}z \exp\left(\mathrm{i}\Delta k z\right) = \frac{L}{2} \exp\left(-\frac{\mathrm{i}\Delta k L}{2}\right) \operatorname{sinc}\left(\frac{\Delta k L}{2}\right) . \tag{3.15}$$

with the quasi-phase-matching with poling period Λ

$$\Delta k = k_1 - k_2 - k_3 - \frac{2\pi}{\Lambda} \tag{3.16}$$

The time-dependent SPDC state is given as

$$|\Psi(t)\rangle_{\mathrm{SPDC}} = \hat{U}(t,t')\,|\Psi(t')\rangle \tag{3.17}$$

with the time evolution operator in first order

$$\hat{U}(t,t') = 1 + \frac{1}{\mathrm{i}\hbar}\int_{t'}^{t} \mathrm{d}\tau \hat{H}_{\mathrm{I}}(\tau) + \ldots \tag{3.18}$$

By using the Fourier transformation for the δ-function, representing the conservation of energy

$$\Delta\omega = \omega_1 - \omega_2 - \omega_3 \tag{3.19}$$

and performing the integration over the frequencies of the pump field, we get the first-order time evolution operator

$$\hat{U} = 1 - \frac{1}{32\pi^2 c^3}\sqrt{\frac{\hbar L^5}{2\varepsilon_0}} \iint \mathrm{d}\omega_2\,\mathrm{d}\omega_3 \sqrt{(\omega_{k_2}+\omega_{k_3})\,\omega_{k_2}\omega_{k_3}}\,\chi^{(2)}_{ijk}(\omega_{k_2}+\omega_{k_3},\omega_{k_2},\omega_{k_3}) \times \hat{a}_{k_1}\hat{a}^{\dagger}_{k_2}\hat{a}^{\dagger}_{k_3} \exp\left(-\frac{\mathrm{i}\Delta kL}{2}\right)\mathrm{sinc}\left(\frac{\Delta kL}{2}\right). \tag{3.20}$$

If the pump beam is a bright laser, the effect of the annihilation operator a_{k_1} on the corresponding initial state is given by

$$a_{\omega_1}\,|\alpha_{\mathrm{P}}(\omega)\rangle = \alpha_{\mathrm{P}}(\omega_1)\,|\alpha_{\mathrm{P}}(\omega)\rangle\ . \tag{3.21}$$

The function $\alpha_{\mathrm{P}}(\omega)$ describes the spectral amplitude distribution of the pump. The corresponding pump spectral density $\left|\alpha_{\mathrm{P}}(\omega)\right|^2$ is normalized to 1. The pump spectral amplitude can be approximated by a delta distribution, if the spectral width of the pump is much smaller than the bandwidth of the generated photons [112].

We then evaluate the SPDC state via equation (3.17) and get

$$|\Psi(t)\rangle_{\mathrm{SPDC}} = |0,0\rangle + \eta\int_0^{\infty}\mathrm{d}\omega_s \int_0^{\infty}\mathrm{d}\omega_i \alpha_{\mathrm{P}}\left(\omega_i+\omega_s\right)\sqrt{(\omega_i+\omega_s)\,\omega_i\omega_s} \times \exp\left(-\frac{\mathrm{i}\Delta kL}{2}\right)\mathrm{sinc}\left(\frac{\Delta kL}{2}\right)\hat{a}^{\dagger}_s\left(\omega_s\right)\hat{a}^{\dagger}_i\left(\omega_i\right)|0,0\rangle \tag{3.22}$$

$$= |0,0\rangle + \int_0^\infty \mathrm{d}\omega_s \int_0^\infty \mathrm{d}\omega_i \Psi(\omega_i, \omega_s)\, \hat{a}_s^\dagger(\omega_s)\, \hat{a}_i^\dagger(\omega_i)\, |0,0\rangle \tag{3.23}$$

where η summarises all prefactors and $\Psi(\omega_i, \omega_s)$ is the joint spectral amplitude (JSA) of the signal and idler photon. This function determines the essential properties of the SPDC process, like the spectra of signal and idler photons and the spectral correlations between them. As seen from equation (3.22), the JSA is the product of the pump spectral amplitude and a phase-matching function $f(\omega_i, \omega_s)$. The phase-matching function is

$$f(\omega_i, \omega_s) \propto \mathrm{sinc}\left(\frac{\Delta k L}{2}\right) \exp\left(-\frac{\mathrm{i}\Delta k L}{2}\right) . \tag{3.24}$$

The modulus squared of this phase-matching function

$$\left|f(\omega_i, \omega_s)\right|^2 \propto \mathrm{sinc}\left(\frac{\Delta k L}{2}\right)^2 \tag{3.25}$$

defines the spectrum of signal and idler photon. For a typical source with a KTP crystal length of around 2 cm, the spectral width is therefore 200 GHz. One problem is that the atomic transitions are in the order of a few MHz. Thus, the atom acts as a narrow filter, resulting in low photon rates. In order to improve the rate, one can modify the spectrum with an optical resonator.

3.1.2 Resonant SPDC

This section will briefly examine the modification of the JSA if we place the conversion crystal inside a two mirror resonator. The extension to any other resonator configuration works the same way. We start with the amplitude U of a wave inside an ideal resonator consisting of two planar mirrors with distance d and a medium with refractive index n. The amplitude U is the superposition of all the single amplitudes U_k, where k is the round trip number

$$U = \sum_{k=1}^{n} U_k \,. \tag{3.26}$$

In each round trip, a wave with frequency ω collects a phase

$$\phi = \frac{2\omega n d}{c} + \Delta\Phi \,, \tag{3.27}$$

where the factor $\Delta\Phi$ incorporates the phase jump at the mirrors. So a single amplitude is written as

$$U_l = e^{\mathrm{i}\phi} U_{l-1}\,. \tag{3.28}$$

If we take losses $\alpha_{s,i}$ inside the crystal with length d into account, the wave is attenuated by a factor of $\exp\left(-\alpha_{s,i} d\right)$ per round trip. Together with losses at the two mirrors, we rewrite this term to

$$U_l = \sqrt{R_1(\omega) R_2(\omega)} e^{-\alpha_{s,i} d} e^{\mathrm{i}\phi} U_{l-1}\,. \tag{3.29}$$

Here $R_1(\omega)$, $R_2(\omega)$ are the reflectivities of the first and second mirrors, respectively.

For a sufficiently large number of round trips, equation (3.26) is interpreted as geometrical series, and we get [113]

$$U = U_{\mathrm{s,i}} = \frac{\sqrt{\left(1 - R_{1\mathrm{s,i}}\right)\left(1 - R_{2\mathrm{s,i}}\right)} \exp\left(-\frac{\alpha_{\mathrm{s,i}} d}{2}\right)}{1 - \sqrt{R_{1\mathrm{s,i}} R_{2\mathrm{s,i}}} \exp\left(-\alpha_{\mathrm{s,i}} d\right) \exp\left(\frac{2\mathrm{i}\omega_{\mathrm{s,i}} n\left(\omega_{\mathrm{s,i}}\right) d}{c}\right)} \tag{3.30}$$

for the intensity.

For a SPDC process, where the crystal resides inside a resonator, we have to modify the JSA correspondingly

$$\Psi\left(\omega_i, \omega_s\right) = U_s(\omega_s) U_i(\omega_i) \alpha_{\mathrm{P}}(\omega_s + \omega_i) \sqrt{(\omega_i + \omega_s)\omega_i \omega_s} e^{-\frac{\mathrm{i}\Delta k L}{2}} \operatorname{sinc}\left(\frac{\Delta k L}{2}\right)\,. \tag{3.31}$$

The resonator modifies the spectrum of the source and can therefore be used to match the linewidth to the atomic transitions.

We describe the resonator by the finesse

$$\mathcal{F} = \frac{\pi \sqrt{R_1(\omega) R_2(\omega)}}{1 - R_1(\omega) R_2(\omega)}\,, \tag{3.32}$$

the FSR

$$\omega_F = \frac{2\pi c}{L_{\mathrm{eff}}}\,, \tag{3.33}$$

and the linewidth

$$\delta\omega = \frac{\omega_F}{\mathcal{F}}\,. \tag{3.34}$$

3.1.3 Cluster effect

The modified spectrum (3.31) results in a comb-like structure for signal- and idler photons within the phase-matching bandwidth of the crystal. Both photons are generated simultaneously, so they must fulfil energy conservation.

The generated photons have orthogonal polarisation in the type-II SPDC process. Together with the birefringence properties of the crystal, this results in a slightly different FSR for the two photons. Hence, only for specific frequencies both photons have a resonance (see figure 3.1a) and b)) and therefore experience a resonant enhancement. For other frequencies only the signal or the idler photon has a resonance, due to energy conservation. The generation of these photon-pairs is suppressed. This effect is called a cluster[114, 115]. The distance between two clusters is given as

$$\Delta\nu_{\text{cluster}} = \frac{\omega_F}{\left|\omega_{F,s} - \omega_{F,i}\right|}\omega_F = \frac{1}{|n_i - n_s|}\omega_F \tag{3.35}$$

where ω_F is the mean FSR of the modes. The phase-matching bandwidth of the crystal further influences the photon-pair generation (see figure 3.1 d)). Thus, it is possible that only a single cluster is supported, with little impact on the central mode. In our experiment, the cluster effect is useful to suppress the generation of photons in non-ion-resonant modes. The ideal case would be that only one cluster mode is supported, as then filtering would no longer be necessary.

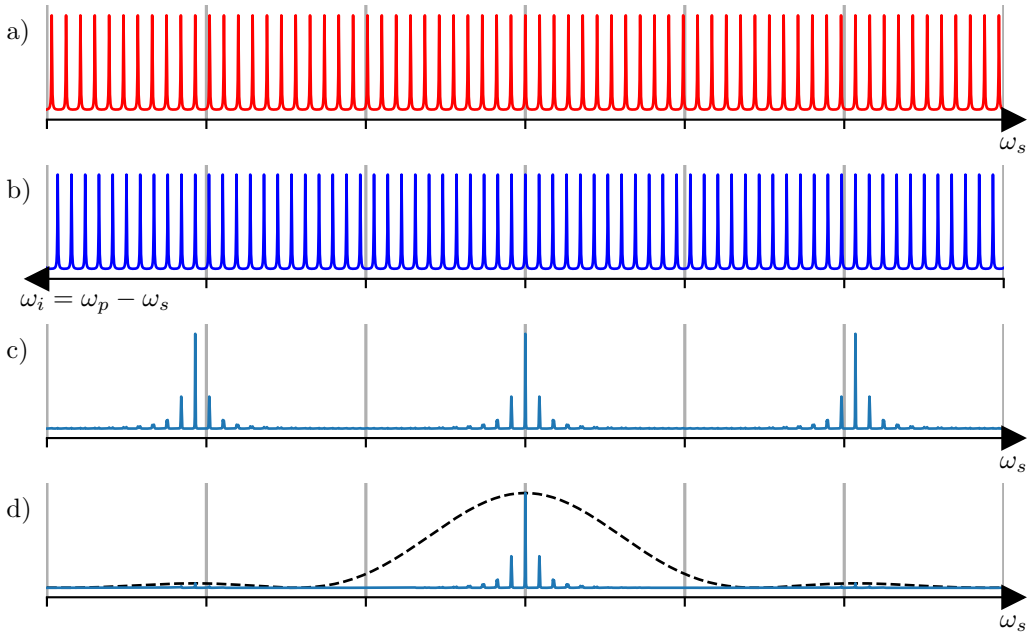

Figure 3.1: a): Resonator mode structure for the signal photon. b): Resonator mode structure of the idler photon. c): Combined resonator mode structure for both photons. The conservation of energy results in forming a cluster where both photons are resonant. d): Combined resonator mode structure with the conversion bandwidth of the crystal added, resulting in just one cluster within the bandwidth.

3.2 Setup and characterisation of the photon pair source

This section describes the design of the photon pair source and shows the characterisation of the generated photon pairs. As in [72], we aim to generate orthogonal linear polarised photon pairs that address the $D_{5/2} - P_{3/2}$ transition in the $^{40}Ca^{+}$ ion at 854 nm. Therefore, we choose type-II phase-matching conditions and use a ppKTP crystal for the conversion. For pumping the crystal, we choose a wavelength of 427 nm. The crystal is placed inside a 3-mirror-ring resonator, resonant for the signal and idler photons. This setup enhances the conversion and tailors the spectral properties to fit the atomic transition. Due to the cluster effect, the spectrum contains only a few modes, making single-mode filtering much more effortless.

3.2.1 Photon-pair source

A schematic and a picture of the source is shown in figure 3.2. We use a non-polarising 50:50 beam splitter to split the polarised pump light into two beams with approximately the same power. The ppKTP crystal converts only one polarisation, so we fine-tune the converted power with an additional half-wave plate (HWP) in one arm. The beams are aligned so that they counterpropagate through the nonlinear crystal, forming an interferometer. For focusing the beams, we use an $f = 250$ mm lens in each arm, resulting in a beam waist of 95 µm (see figure 3.4(b)). As mentioned above and explained in more detail in the next section, the crystal sits inside a signal- and idler-resonant 3-mirror ring resonator (see also figure 3.3). One mirror (M_{out}) is designed as output; therefore, the generated photon-pairs from both pump directions leave the resonator at this mirror but under different angles, 0° and 30°. The two directions have different beam waists at the position of the outcoupling mirror, leading to different beam waists of the output photons (see figure 3.4). Therefore, we place a telescope with two lenses in the 30° beam to achieve approximately the same beam waists. In this output, the polarisation of signal- and idler photon gets interchanged by an HWP. Finally, we overlap the photons from both outputs on a polarising beam splitter (PBS). The setup erases all distinguishability between the photons [103, 104] and avoids the background of unsplit pairs inherent in single-direction SPDC generation [98, 72, 116].

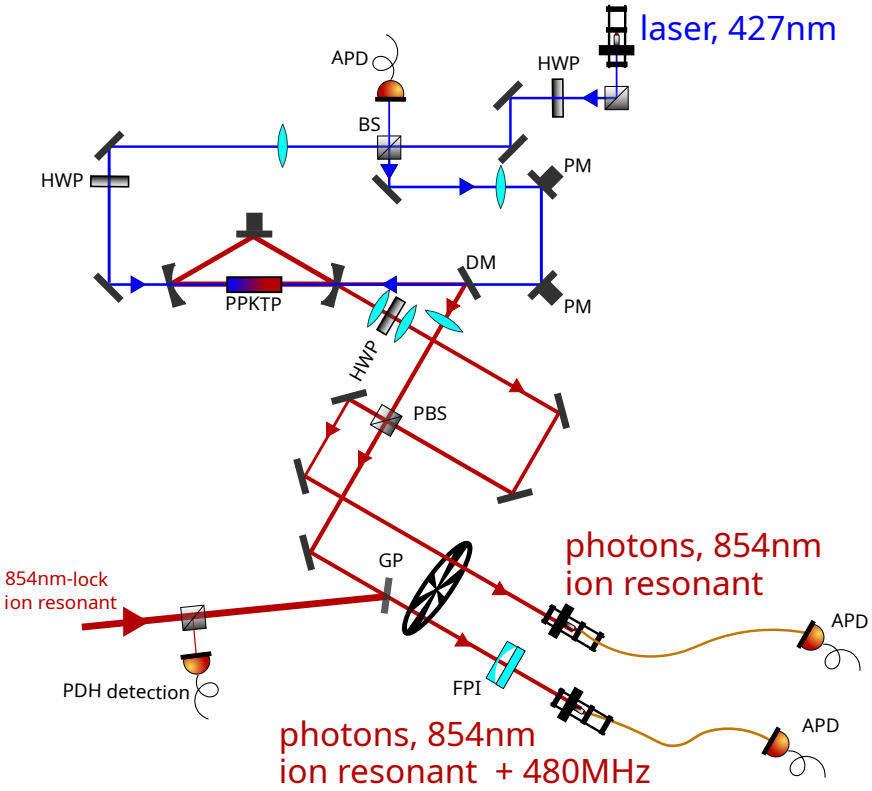

(a) Schematic of the source

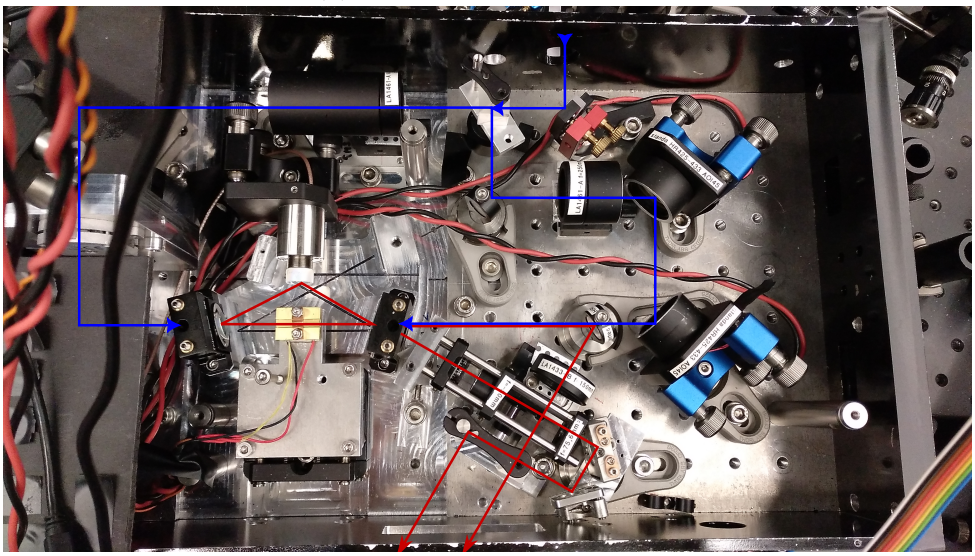

(b) Picture of the source

Figure 3.2: Schematic and picture of the source. The blue lines indicate the path of the pump beam, whereas the red lines show the beam path of the photons. (a) The stabilisation of the resonator and the interferometer is achieved by piezo-driven mirrors (PM). During the stabilisation runs, the photons are switched off by an optical chopper. We use two APD for the detection of single photons and another one for detecting the interferometer fringes. HWP/QWP: half-/quarter-wave plate, PBS: polarising beamsplitter, BS: non-polarising beamsplitter, DM: dichroic mirror, GP: glass plate, FPI: frequency filter.

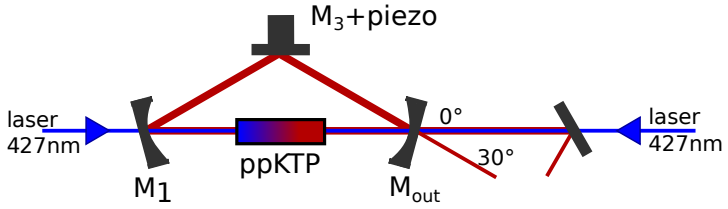

Figure 3.3: Schematic of the 3-mirror-ring resonator. We pump the ppKTP crystal inside the resonator from two counter-propagation beams at 427 nm. Photons are outcoupled at mirror M_{out} under different angles (0° and 30°). The stabilisation is achieved by a piezo-driven mirror (M_3) and the PDH technique (see section 3.2.3).

3.2.2 Resonator design

ppKTP crystal The most crucial part of the source is a ppKTP crystal designed for the SPDC process from 427 nm to 854 nm. The crystal has the dimensions 3.5 mm × 1 mm × 20 mm (y, z, x) and is grown with two different poling periods (14.575 µm and 14.45 µm), each 1 mm wide.

The poling period originates from a periodic poling fabrication technique that matches the phases of all three waves inside the crystal. During the growth of the crystal, strong electric fields are induced to control the direction of the ferroelectric dipoles. The direction of the dipoles results in a periodic inversion of the nonlinear coefficient and a structure with periodicity Λ, the so-called poling length.

The crystal fulfils quasi-phasematching at $\approx 24\,^{\circ}\mathrm{C}$ and $\approx 58\,^{\circ}\mathrm{C}$. The crystal facets are coated with an anti-reflective (AR) coating for 854nm to reduce photon losses. We tune and stabilise the temperature of the crystal with a Peltier element in the range between 15 °C and 80 °C. Positioning of the crystal inside the resonator and relative to the coupling lenses is possible with a 5-axis translation stage[1] (pitch, yaw, x, y, and z). S. Kucera used and characterised the crystal in a previous version of the source; hence further details are found in his PhD thesis [72]. For the work of this thesis, we use the bigger poling period at an operation temperature of $T = 22.5310\,^{\circ}\mathrm{C}$.

Resonator The resonator consists of two curved mirrors (M_1, M_{out}; $R = 50\,\mathrm{mm}$) and a flat mirror (M_3) attached to a piezo actuator[2]. One curved mirror (M_{out}) is partially

[1] Thorlabs PY005/M
[2] Piezomechanik, HPSt 150/14-10/12 VS22

reflective ($R_H = 95.8\,\%$, $R_V = 96.7\,\%$) and acts as outcoupling mirror. The other mirrors have a high reflection (HR) coating with a specified reflectivity of $> 99.9\,\%$. Additionally, the curved mirrors have an AR coating for the pump wavelength at 427 nm, reducing pump losses.

A design goal is to minimise the optical path length because it maximises the FSR and the spacing of the cluster modes. We like to recycle most parts of the previous version of the source. For that reason, we stay with the machined monolithic base plate to achieve sufficient mechanical stability and the commercially available mirror holders[3] of the previous setup. The distance between the curved mirrors stays the same, and the flat mirror is placed as close as possible to the crystal without cutting off the spatial resonator modes. Together this results in the following lengths:

$$|M_1 - M_{\text{out}}| = 69\,\text{mm}$$
$$|M_1 - M_3| = 39.1\,\text{mm}$$

We simulated the $1/e$ beam radius inside the resonator and crystal for the two polarisations in the sagittal and tangential plane using the ray matrix formalism for Gaussian beams [117]. The results are shown in figure 3.4(a). We achieve a beam waist for the signal and idler photon of 62 µm. The beam waist is slightly larger than in the previous resonator. Unwanted effects such as grey-tracking and thermal lensing [118, 119] should, therefore, not play a role in our setup [120].

To determine the optimal beam waist for the pump beam, we first measure the beam waist of the SHG light, if we pump the source with the lock light. From this measurement we conclude that the optimal beam waist is approximately twice the the waist of the produced photons. Further criteria that determine the beam waist are enough room to place the lens on the base plate and a commercially available lens with proper focal length. With these boundary conditions, we decided for a lens with a focal length of $f = 250\,\text{mm}$ in each pump beam and reach a beam waist of 96µm inside the crystal. The simulation of the pump beam path for both directions is shown in figure 3.4(b).

[3] M_1, M_{out}: Newport 9810-5-K; M3: Liop-Tec SR100-HS-100-3

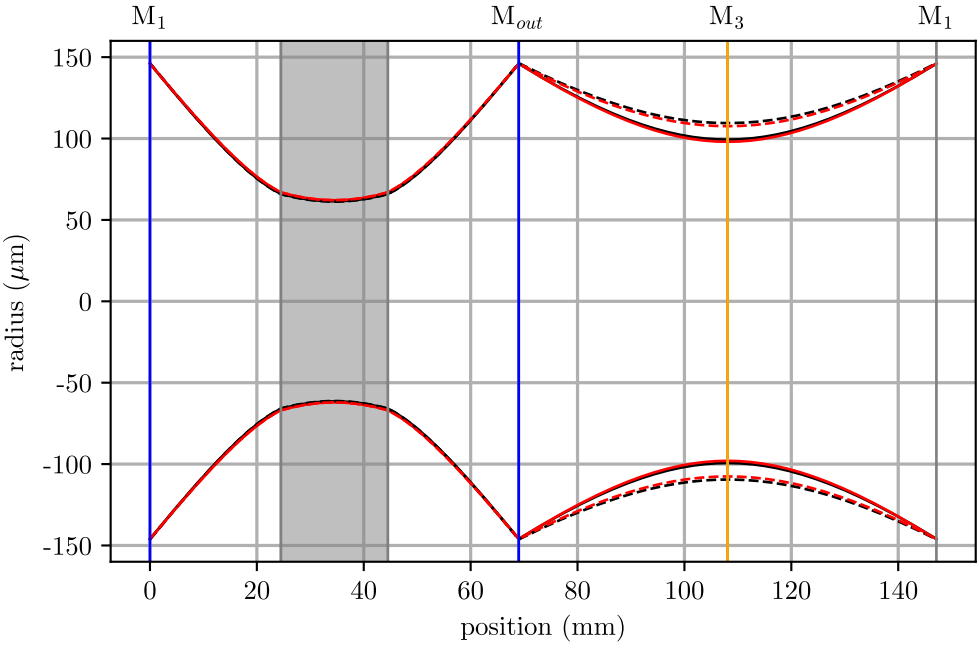

(a) Beam waist inside the resonator

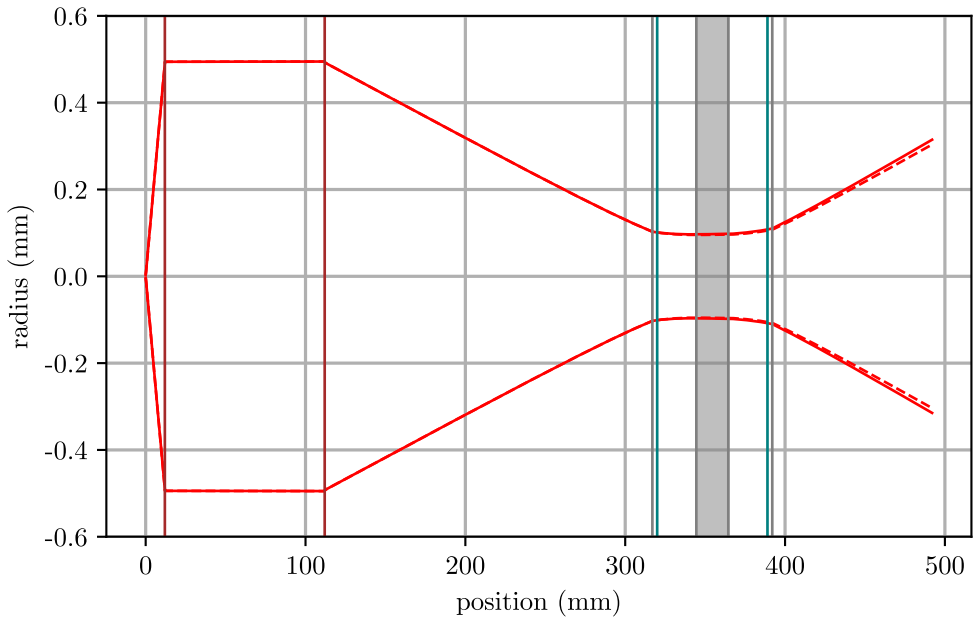

(b) Beam waist of the pump beam

Figure 3.4: Calculation of the beam waist inside the resonator for one round trip (a) and for the pump beam (b). The calculation is performed for the two orientations. For the resonator, we also include both polarisations. The red lines show the waist for horizontal polarisation and the black for vertical polarisation. Solid lines correspond to the sagittal plane and dashed lines to the tangential plane. The position of the crystal is marked with the grey shaded area. The blue vertical lines show the positions of the curved mirrors, the orange line the position of the flat mirror, the teal lines the refraction of the curved mirrors and the brown lines the position of lenses.

3.2.3 Stabilisations

We achieve long-term stability of the photon generation by using several stabilisations.

Crystal temperature We use a Peltier element mounted under the crystal holder to control the temperature of the crystal. The temperature is tuned between 15°C and 80°C with a stability of 0.1 K. Consequently, we can operate the source with both poling periods at maximum conversion efficiency. We choose the same poling period as in the previous version of the source [72] and detune the temperature to get a proper frequency spacing as explained in the following paragraphs.

Resonator length We use a piezo actuator attached to mirror M_3 to stabilise the resonator length. Similar to the previously explained transfer cavities, the SPDC resonator uses the PDH technique to produce the error signal. Therefore, we modulate the current of the 854 nm laser with an additional 20 MHz signal. Using the residual transmission of mirror M_1 as in S. Kucera's thesis [72] was not feasible. Mirror M_1 has a HR coating for the locking beam wavelength, thus only very little light enters the resonator, resulting in a very weak PDH signal. For unknown reasons, we observed jumps in the offset of the PDH signal. The amplitude of these jumps was bigger than the amplitude of the PDH signal itself, making locking over long times impossible. To overcome this problem, we switch to the reflection of the outcoupling mirror M_{out}. The lower reflectivity of this mirror leads to a signal with a much bigger amplitude. This has been shown to lead to a significant improvement in stability. The drawback of this method is that we need an additional optical element, a GP (reflectivity of 4 %), in the photon beam, leading to additional 4 % loss.

We use diagonally polarised light, split equally on the PBS. Due to the $\lambda/2$ waveplate in one source output, both directions have the same polarisation on the outcoupling mirror. Having lock lights from both directions enables the later-explained locking scheme for the interferometer.

Resonator frequency At least one polarisation mode of the resonator should be ion-resonant. We reach this by using an ion-resonant locking beam. Due to the birefringence of the crystal, the second polarisation mode is then shifted in frequency. The best conversion efficiency is reached when one half of the pump frequency is symmetric between the two

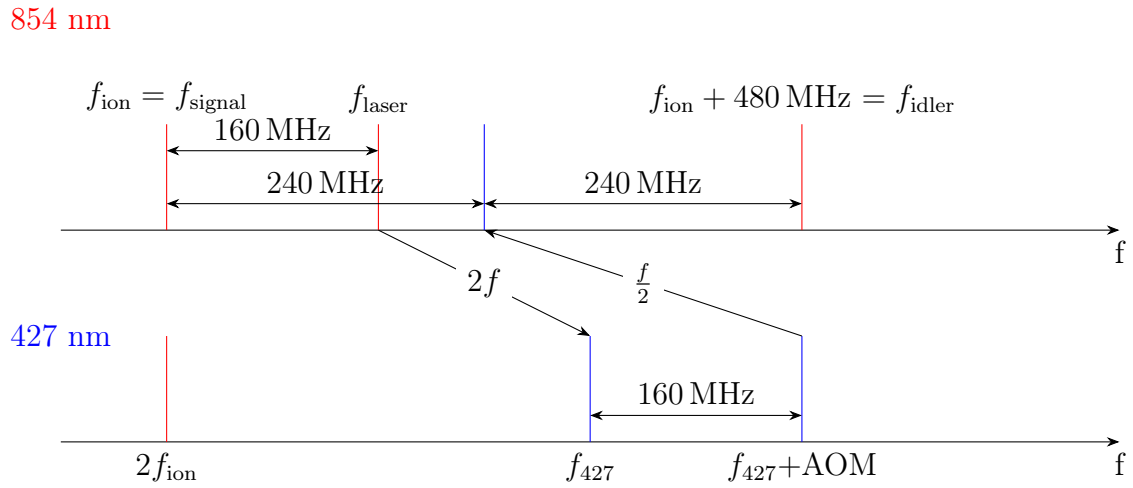

Figure 3.5: Frequencies and detunings of the laser beams used with the source. The upper frequency axis shows the range of the 854 nm laser. The lower axis is the range of the 427 nm laser. The fundamental laser runs at frequency f_{laser}. The frequency-doubling results in f_{427}. The ion resonance is at the frequency f_{ion}.

frequencies of the produced modes. As explained in chapter 2.2, the locking beam, as well as the pump beam are produced by the same laser using SHG, thus having a fixed frequency spacing. Therefore, we have to choose a proper frequency splitting between the polarisation modes, which is also well accessible by AOMs. We choose a splitting of 480 MHz between the polarisation modes. An overview of the used frequencies is shown in figure 3.5.

The fundamental laser runs at frequency f_{laser}, 160 MHz detuned to the ion resonance. As mentioned in chapter 2.2, the laser is frequency-doubled (f_{427}), and we use an additional AOM to detune the frequency by 160 MHz. Subsequent frequency halving in the SPDC process results in a detuning of 240 MHz from the ion resonance, which is precisely half the frequency difference of the two polarisation modes.

Interferometer stabilisation In the first version of the interferometric source, described in [72, 121, 73], we used residual reflections from high transmission (HT) optical elements (dichroic mirror, outcoupling mirror) to stabilise the Mach-Zehnder interferometer, formed between the first non-polarising beamsplitter (BS) and the PBS for the recombination of the photons. This technique has two main issues: i) The old locking scheme was based upon the assumption that the PBS for the photons acts more or less

as a BS for the pump beam. Together with different polarisation modes inside the pump interferometer, it turns out that the lock was not stable and reliable enough. ii) The stabilisation of the path length with piezo actuators attached to two separate mirrors leads to a beam displacement inside the interferometer, resulting in intensity fluctuations. Additionally, the stabilised beam path was not precisely the photon beam path, which resulted in undetectable path length changes.

In the version of the source used in this thesis, we used the SHG light produced by the locking beam to overcome these problems. As mentioned in the description of the stabilisation of the resonator length, we get lock light in both output directions of the resonator if we use diagonal light at the input of the PBS. The two locking beams produce a few hundred picowatts of 427 nm light superimposed on the input BS, forming a Mach-Zehnder interferometer. The stabilised interferometer is now identical to the one used in the SPDC process, so we have a much more stable operation.

As mentioned, the power of the SHG light is in the sub-nanowatt range, and there needs to be more than the sensitivity of conventional photodiodes for light detection in this power range. Therefore, we use a single-photon detector (APD) with a low-pass filter to convert the transistor-transistor logic (TTL) pulses to an analogue signal needed for the locking electronics. An additional advantage of this locking scheme, compared to the previously used one, is that the locking is now independent of the pump power. The following section will discuss the connection between the interferometer and the state phases.

3.2.4 Relationship between state and interferometer phase

The state phase φ depends on the interferometric phase φ_{inter}. A detailed calculation is shown in Appendix A. For the frequencies shown in figure 3.5, we have

$$\varphi \approx \varphi_{\text{inter}} \,. \tag{3.36}$$

Figure 3.6 shows the measured dependency between the interferometer phase and the photonic state phase. For the measurement, we stabilise the interferometer to a particular phase and perform a tomography measurement on the photonic state. Details about the tomography measurement are found in section 3.2.9. We then get the best state phase from the density matrix reconstruction. The measurement result shows a phase shift of

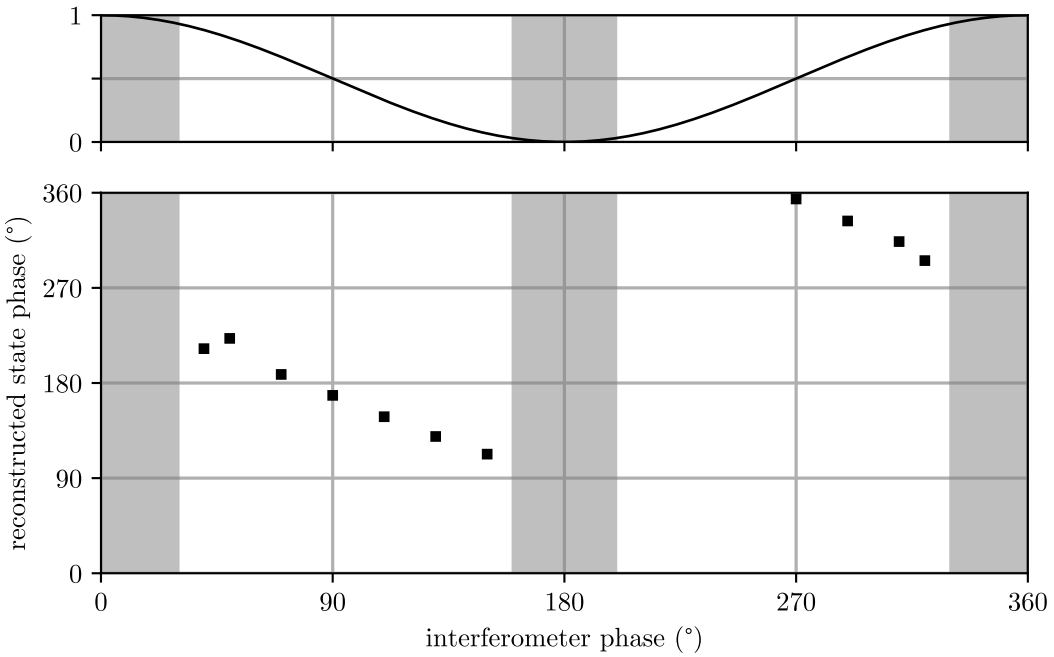

Figure 3.6: Dependency of the photonic state phase from the interferometer phase. Stabilisation is not possible in the grey-shaded areas because the slope of the fringe (upper plot) is too low.

$\pi/2$. We observed changes in this offset on the timescale of months, which still needs to be understood.

Because of the fringe signal, the slope of the locking signal change with the phase. Around the minima and maxima, therefore, no locking is possible (grey shaded areas in figure 3.6).

3.2.5 Output state of the source

The output state of the source is constructed out of the two amplitudes of the two pump directions. The output state of each pump direction is given as

$$|\psi\rangle = a^\dagger_{i,H} a^\dagger_{i,V} \, |0_{i,H}, 0_{i,V}\rangle \ , \tag{3.37}$$

where $i = 1, 2$ stands for the respective pump direction and $a^\dagger_{i,H,V}$ is the bosonic creation operator of a single photon in the corresponding polarisation mode. As described earlier, we superimpose both pump directions on a PBS. In general, the different pump directions

have different pump powers (due to imperfections of the BS, different losses, ...) and different conversion efficiencies. Therefore, we use a weight factor C_i for the different directions and write the input state at the PBS as

$$|\psi_{\text{in}}\rangle = \frac{1}{\sqrt{C_1^2 + C_2^2}} \left[C_1 a_{1,H}^\dagger a_{1,V}^\dagger + C_2 e^{\mathrm{i}\phi} a_{2,H}^\dagger a_{2,V}^\dagger \right] |0_{1,H}, 0_{1,V}, 0_{2,H}, 0_{2,V}\rangle$$

The PBS transforms now the input state according the following rules [122]

$$\begin{aligned} a_{1,H}^\dagger &= \sqrt{T_H} a_{A,H}^\dagger - \sqrt{R_H} a_{B,H}^\dagger \\ a_{2,H}^\dagger &= \sqrt{R_H} a_{A,H}^\dagger + \sqrt{T_H} a_{B,H}^\dagger \\ a_{1,V}^\dagger &= \sqrt{T_V} a_{A,V}^\dagger - \sqrt{R_V} a_{B,V}^\dagger \\ a_{2,V}^\dagger &= \sqrt{R_V} a_{A,V}^\dagger + \sqrt{T_V} a_{B,V}^\dagger \end{aligned} \tag{3.38}$$

with the transmission and reflection coefficents of the polarisation modes $T_{H,V}, R_{H,V}$. The complete output state after the PBS is then given by

$$\begin{aligned} |\psi_{\text{out}}\rangle = \frac{1}{\sqrt{C_1^2 + C_2^2}} \Bigg[& \left(C_1 \sqrt{T_H T_V} + C_2 e^{\mathrm{i}\phi} \sqrt{R_H R_V} \right) a_{A,H}^\dagger a_{A,V}^\dagger \\ & + \left(C_1 \sqrt{T_H R_V} - C_2 e^{\mathrm{i}\phi} \sqrt{R_H T_V} \right) a_{A,H}^\dagger a_{B,V}^\dagger \\ & + \left(C_1 \sqrt{R_H T_V} - C_2 e^{\mathrm{i}\phi} \sqrt{T_H R_V} \right) a_{A,V}^\dagger a_{B,H}^\dagger \\ & + \left(C_1 \sqrt{R_H R_V} + C_2 e^{\mathrm{i}\phi} \sqrt{T_H T_V} \right) a_{A,V}^\dagger a_{B,H}^\dagger \Bigg] |0_{A,H}, 0_{A,V}, 0_{B,H}, 0_{B,V}\rangle \quad . \end{aligned} \tag{3.39}$$

In the case of an ideal PBS ($T_H = R_V = 1$ and $T_V = R_H = 0$) this equation is simplified and we get

$$|\psi_{\text{out}}\rangle = \frac{1}{\sqrt{C_1^2 + C_2^2}} \left(C_1 a_{A,H}^\dagger a_{B,V}^\dagger - C_2 e^{\mathrm{i}\phi} a_{A,V}^\dagger a_{B,H}^\dagger \right) |0_{A,H}, 0_{A,V}, 0_{B,H}, 0_{B,V}\rangle \quad . \tag{3.40}$$

For equal weights and the correct phase, this is equivalent to the $|\Psi^+\rangle$ or $|\Psi^-\rangle$ Bell state.

Therefore, a critical step in the alignment of the source is to ensure that we have equal efficiencies for the photons and equal losses in the pump. Both parameters are independently measured by a signal-idler cross-correlation measurement as shown in 3.10. With the additional waveplate in one of the pump arms, we tune the coincidence rate of each arm to be equal. A proper alignment adjusts the efficiencies in the photon arm.

Table 3.1: Resonator properties for the two polarisation-axis H and V.

pol.	FSR	R_{out}	$\mathcal{F}$	$\delta\omega$	L_{int}	η_{esc}
H	$2\pi \cdot 1.8496\,\text{GHz}$	95.77 %	104(2)	$2\pi \cdot 17.6(3)\,\text{MHz}$	1.51 %	73.5 %
V	$2\pi \cdot 1.8293\,\text{GHz}$	96.68 %	152(3)	$2\pi \cdot 12.0(2)\,\text{MHz}$	0.65 %	83.5 %

Coming from equation (3.39) and setting $C_1 = C_2$ we calculate the maximal reachable fidelity with one of the two mentioned Bell states

$$F = \langle \Psi^{\pm} | \psi_{\text{out}} \rangle \langle \psi_{\text{out}} | \Psi^{\pm} \rangle = \frac{1}{4} \left| \left(e^{\mathrm{i}\phi} \mp 1 \right) \left(\sqrt{T_H R_V} \pm \sqrt{R_H T_V} \right) \right|^2 \tag{3.41}$$

Equation (3.41) shows that for a non-ideal beamsplitter, the fidelity of the $|\Psi^-\rangle$ state is always lower than the fidelity of the $|\Psi^-\rangle$ state. The PBS we use is specified with $T_H/T_V = 1000$, which means that the PBS does not limit our state fidelity.

3.2.6 Resonator linewidth and escape probability

The resonator linewidth can be measured using the two-photon correlation or a stabilised laser. In this section, we look at the second method. We scan the resonator length by applying a triangular voltage to the piezo at mirror M_3. The transmission through the resonator is measured by a photodiode, placed in the 0° output of mirror M_1. We send H-polarised or V-polarised light through the resonator by choosing the right photon path. The results for two subsequent measurements (H and V) are shown in figure 3.7. The two maxima correspond to the fundamental mode of the resonator. The small side peaks next to the central peak correspond to some higher modes. These cannot be avoided because we do not optimise the beam shape. Under the assumption of linear behaviour of the piezo actuator and the calculated FSR, we readout the linewidth $\delta\omega$ and the finesse $\mathcal{F}$ out of a fit to the scan. The reflectivity of the outcoupling mirror was already measured in [72]. With these variables, we calculate the expected internal loss L_{int} and the escape probability

$$\eta_{\text{esc}} = \frac{1 - R_{\text{out}}}{L_{\text{int}} + 1 - R_{\text{out}}}\,. \tag{3.42}$$

All values are summarised in table 3.1.

The measured linewidth is in good agreement with the linewidth of the produced SPDC photons in sec. 3.2.8. The errors in the measured variables result from taking the mean

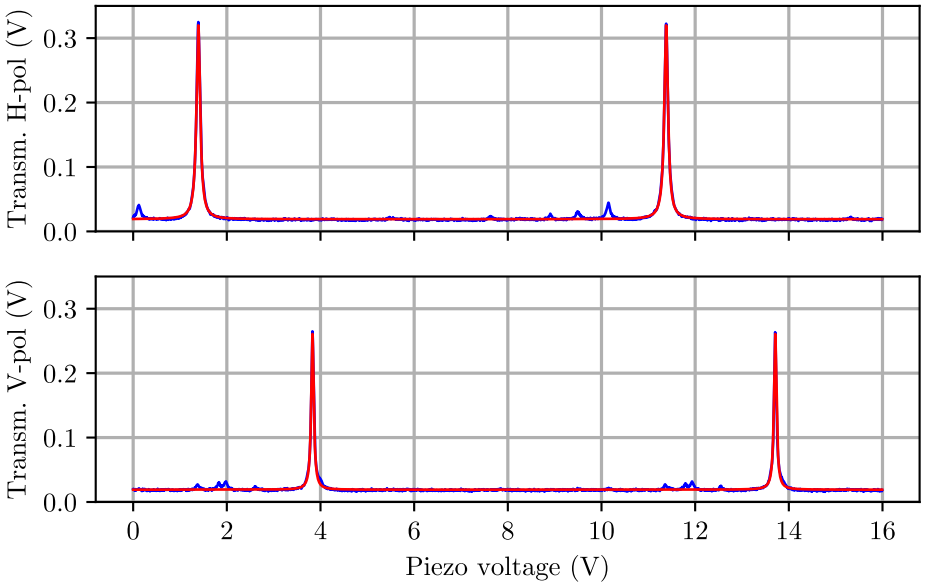

Figure 3.7: Scan of the SPDC resonator with different input polarisations. The upper plot shows the transmission for an H-polarised input and the lower one for a V-polarised input.

and standard deviation over the whole piezo range of 100 V (7 FSRs). The deviation is mainly explained by the non-linearity of the piezo actuator and the uncertainty in the real FSR. Unfortunately, removing the compensation crystal did not reduce the internal losses. We consider that the coating of M_3 is not as good as specified and leads to additional losses. Nevertheless, we narrowed the linewidth of the photons, which was one design goal.

3.2.7 Cluster structure

We first simulate the cluster structure for the estimated parameters of the source. The result is shown in figure 3.8.

Then, we measure the spectrally resolved cluster structure. Therefore we need a tunable narrow-band filter. This filter is a monolithic Fabry-Perot-Interferometer (FPI) constructed from a single plano-convex lens similar to [123, 124]. We use N-BK7 glass for the substrate. This material shows a suitable thermal expansion coefficient ($\alpha = 7.1 \times 10^{-6}\,\mathrm{K}^{-1}$), enabling us to tune the frequency over the whole FSR within a temperature range of $\sim 20\,^{\circ}\mathrm{C}$. The lens is coated on both sides with an HR coating

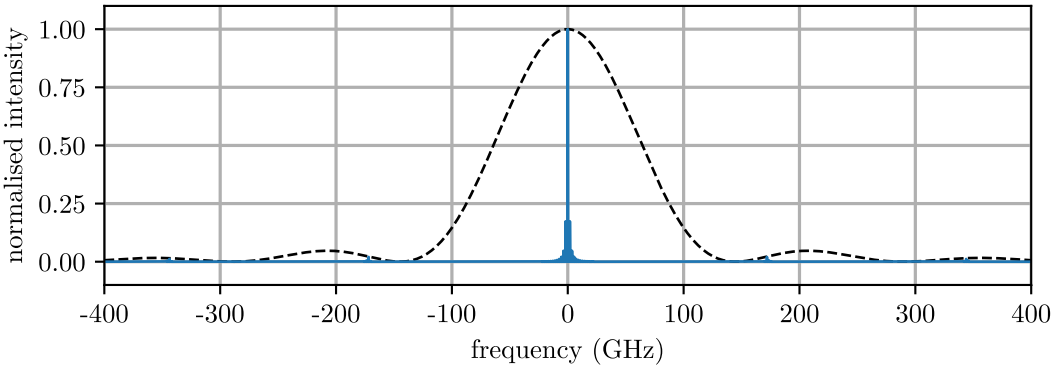

(a) Overview over the crystal bandwidth.

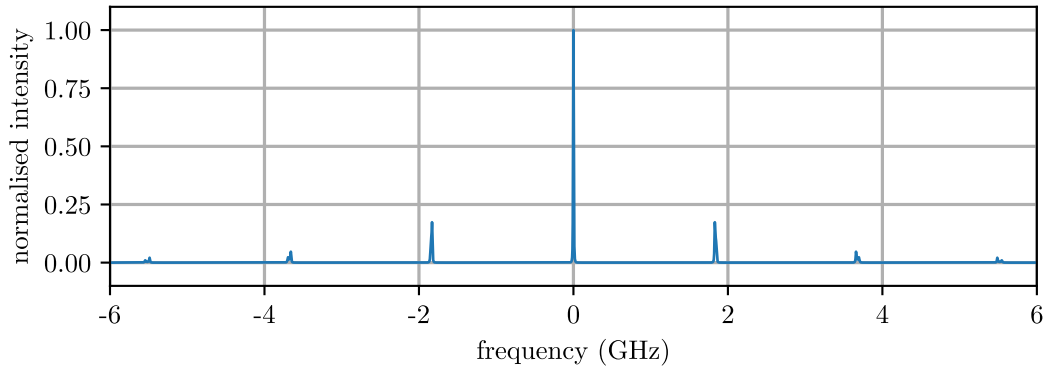

(b) Central cluster.

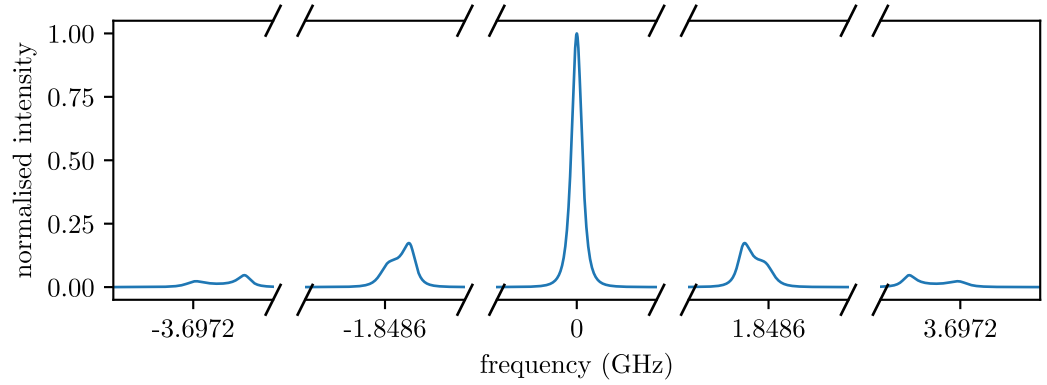

(c) Broken axis, to show width of single cluster modes.

Figure 3.8: Spectral envelope of generated photon pairs calculated from the measured resonator specifications. Part a) shows the bandwidth of the crystal, including the cluster structure. Part b) is zoomed in to show the details of the cluster. Part c) is even more zoomed to show the width of the cluster modes.

($R = 99.35\,\%$), resulting in a finesse of $\mathcal{F} = 481.7$. Our setup includes two of these filters with different lens thicknesses. The first lens has a linewidth of $\delta\omega_1 = 2\pi \cdot 111.7\,\mathrm{MHz}$ and

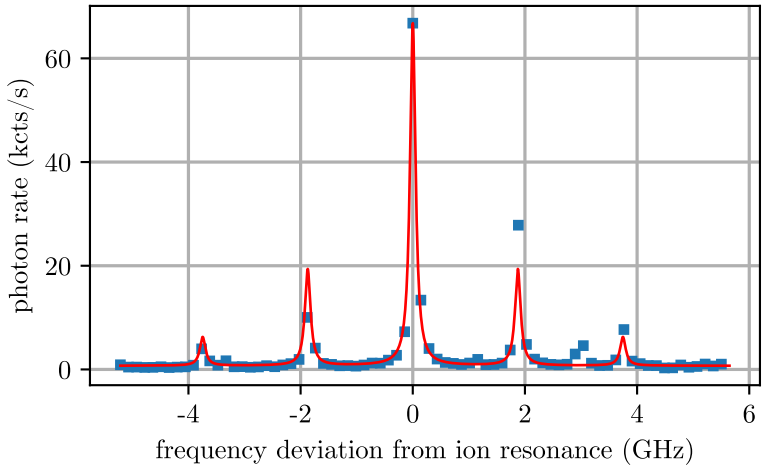

Figure 3.9: Photon count rate behind the FPI while scanning the temperature/frequency. The red line shows a fitted sum of Gaussian functions.

a FSR of $\omega_{F,1} = 2\pi \cdot 53.956\,\mathrm{GHz}$. The second one has a linewidth of $\delta\omega_2 = 2\pi \cdot 51.17\,\mathrm{MHz}$ and a FSR of $\omega_{F,2} = 2\pi \cdot 24.65\,\mathrm{GHz}$. We stabilise the FPI by stabilising the temperature of the lens to $< 1\,\mathrm{mK}$ ($\hat{=}3\,\mathrm{MHz}$).

To measure the cluster structure, we detune filter one by 0.05 K for each data point and record the transmitted counts for 2 s. After each measurement, we wait for 30 s until the temperature is stable again. Figure 3.9 shows the measurement result. The plotted signal (blue squares) is the convolution between the transmission of the spectral filter and the spectral envelope of the photons. The peak width is, therefore, mainly given by the filter linewidth. The red curve is a fit for the data. We use the sum of five Lorenzians as a fit function. From the fit, we extract the spacing of the peaks, which correspond to the FSR of the source resonator, matching the predictions and is 1.88 GHz. The linewidth is $\delta\omega = 2\pi \cdot 119\,\mathrm{MHz}$ and matches the filter linewidth. For the experiments, we use only the signal in the central peak that corresponds to $\sim 58\,\%$ of the whole signal (sum of all peaks).

3.2.8 Photonic time structure

The time structure of the photons is revealed by measuring the temporal signal-idler cross-correlation. The measurement is done separately for each pump direction. The total pump power was 20 mW, and we used no filter in the output. The results are shown

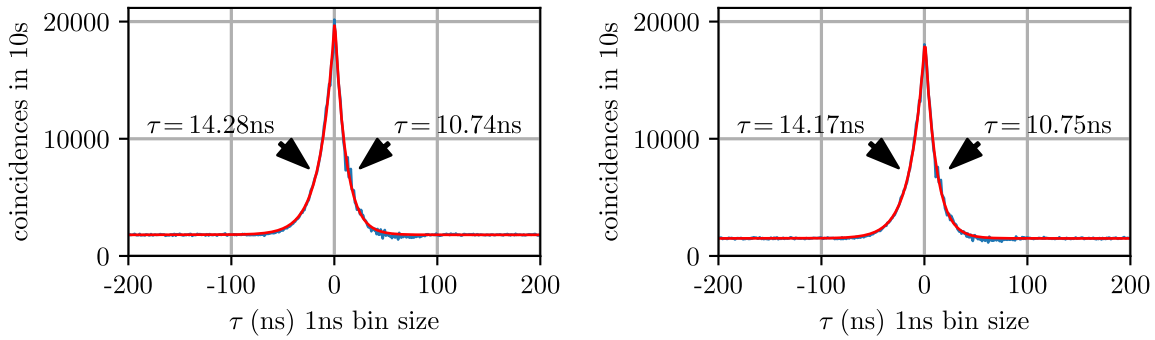

(a) Pump direction 1

(b) Pump direction 2

Figure 3.10: Multi mode $g^{(2)}$ correlation for the two pump directions. Independent from the pump direction, there is always the longer photon in one arm and the shorter photon in the other arm.

in figure 3.10. The resulting data is a double exponential function. The fit is drawn in red. From the fit, we get the decay times (or wave packet widths) of the two outputs, which differ slightly because of the different losses of the two polarisation modes. For the first pump direction (fig 3.10(a)) we see a decay time of 14.28 ns and 10.74 ns. For the second pump direction (fig 3.10(b)) we get 14.17 ns and 10.75 ns. Additionally to the decay times themselves, we see that each output is mapped to only one wave packet width. Therefore, the superposition erases the distinguishability between the photons in the frequency degree of freedom.

Out of the measurement data, we also extract the generated single-mode pair rate $R^{\mathrm{SM}}_{\mathrm{pair}}$, as well as the efficiencies for a photon detection η_1 and η_2, where these depend on the detector efficiency. We measure the rates R_1 and R_2 and calculate the coincidence rate C. The parameters we are looking for are then given by

$$R_1 = \eta_1 R^{\mathrm{SM}}_{\mathrm{pair}} \tag{3.43}$$

$$R_2 = \eta_2 R^{\mathrm{SM}}_{\mathrm{pair}} \tag{3.44}$$

$$C = \eta_1 \eta_2 R^{\mathrm{SM}}_{\mathrm{pair}} \tag{3.45}$$

$$R^{\mathrm{SM}}_{\mathrm{out}} = \eta_{\mathrm{esc,H}} \eta_{\mathrm{esc,V}} \eta_{\mathrm{chopper}} R^{\mathrm{SM}}_{\mathrm{pair}} \tag{3.46}$$

with the escape probability of the two polarisations $\eta_{\mathrm{esc,H/V}}$ and the chopper duty cycle η_{chopper}. For our source, we get a generated single-mode pair rate $R^{\mathrm{SM}}_{\mathrm{pair}} = 7.2 \times 10^4 \, \frac{\mathrm{pairs}}{\mathrm{s \cdot mW}}$ and efficiencies $\eta_1 \approx 9\,\%$ and $\eta_2 \approx 18\,\%$. The efficiencies include the detection efficiency of the Excelitas APDs. The available photon-pair rate outside the resonator, including the

Table 3.2: Comparison of different SPDC sources. $\delta\nu$: linewidth of the produced photons, LN: Lithiumniobat

Author(s) [Ref.]	$\delta\nu$ (MHz)	material	wavelengths (nm)	$R_{\text{pair}}^{\text{SM}}$ ($\frac{\text{pairs}}{\text{s·mW}}$)
Luo et. al. [100]	66	LN	532/890/1320	3×10^4
Tsai and Chen [101]	6.7	KTP	407/852/780	1.06×10^5
Niizeki et. al. [126]	2.4	LN	757/1514/1514	3.94×10^5
Moqanaki et. al. [127]	10.9	KTP	426/852/852	4.7×10^4

Table 3.3: Fidelity and purity for the two Bell-states, which the source can produce.

	with background correction		without background correction	
state	fidelity	purity	fidelity	purity
$\|\Psi^-\rangle$	98.68(3) %	98.46(6) %	91.95(6) %	85.8(1) %
$\|\Psi^+\rangle$	98.17(3) %	97.67(6) %	94.45(5) %	90.6(1) %

optical chopper, is $R_{\text{out}}^{\text{SM}} = 3.7 \times 10^4 \frac{\text{pairs}}{\text{s·mW}}$. With the maximum available pump power of 20 mW, $740 \times 10^3 \frac{\text{pairs}}{\text{s}}$ with a bandwidth of about 13 MHz are thus available. Compared to the previous version, we increase the photon-pair rate by a factor of 1.6. This is an excellent value compared to other SPDC sources, as seen from table 3.2. A more complete list and comparison is found in [125].

3.2.9 Polarisation entanglement

To verify the entanglement, we perform quantum state tomography. In the measurement, we place one FPI in each output arm of the source, followed by a set of a half-waveplate, a quarter-waveplate and a linear polariser, the projection setup. The detector, an APD, is placed in each arm behind the projection setup. For a full tomography, 16 different basis combinations have to be measured [128]. For each, we measure the two-photon correlations. The signal is the sum of all events in a time window of ±56 ns around the maximum. The background is calculated as described in section 3.2.11, far away from the maximum. Accidental coincidences from overlapping photons dominate the background. This background increases with the pump power. We subtract the background from the signal to specify the source performance and the maximal reachable state.

With the signal determined in this way, we reconstruct the density matrix via a maximum-

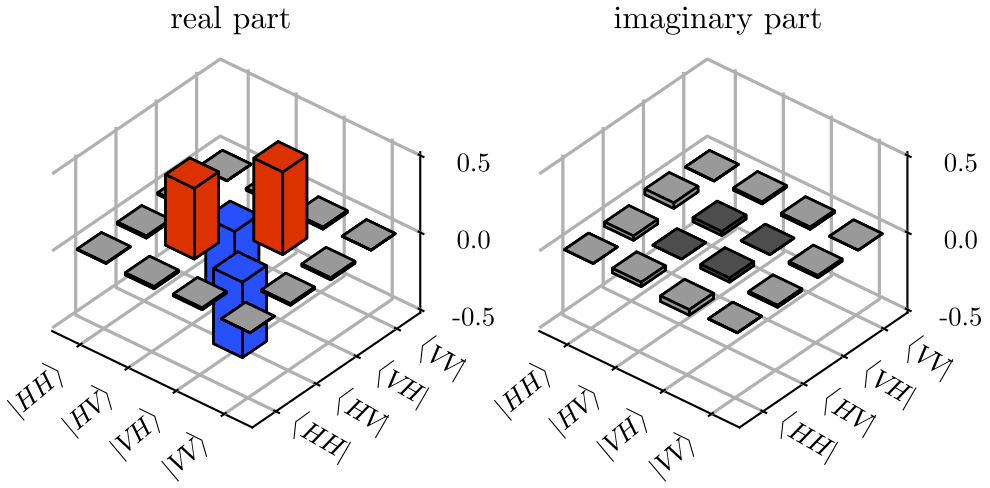

(a) $|\Psi^-\rangle$ Bell state

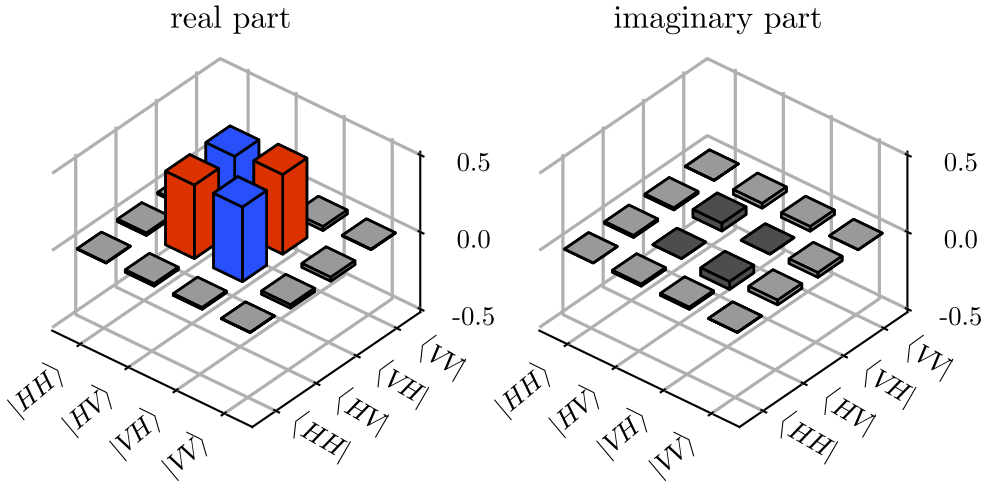

(b) $|\Psi^+\rangle$ Bell state

Figure 3.11: Reconstructed density matrix for to different phase settings. $\phi_{\text{inter}} = 90°$ results in a $|\Psi^-\rangle$ Bell-state, a phase of $\phi_{\text{inter}} = -90°$ results in a $|\Psi^+\rangle$ Bell-state.

likelihood algorithm [129]. Using a maximum-likelihood algorithm ensures that the final state is physical. Using a linear reconstruction, for example, could lead to unphysical results. We then calculate the fidelity to a given state and the purity from the density matrix.

The reconstructed density matrix for a $|\Psi^-\rangle$ and a $|\Psi^+\rangle$ state is shown in figure 3.11. For a state with phase $\phi = 270°$, the density matrix is later shown in figure 4.4a). Table 3.3 summarises the fidelity and the purity of both measurements. We generate both Bell-

states with equal fidelity. The slightly different fidelities and purities of the two states results from improper polarisation calibration and fluctuations in the state phase.

3.2.10 Signal-to-Background ratio

A critical number for all measurements including the source is the SBR because it influences the characterising variables of the experiments. Therefore, this section briefly summarises the results from [72]. We usually perform time-resolved correlation measurements between different photons in the experiments. The photons of the source show a thermal distribution, which means the generation is probabilistic. Additionally, the resonator gives rise to an exponential decay of the photon time structure. The result is an overlap of photons from different pairs. The amount of overlap compared to the observed photon is defined as the SBR.

The number of coincidences S in a correlation measurement, like the one of the previous section, for a given generated pair rate R_{pair} in a time bin Δt for a measurement time of T is given as

$$S = \eta_1 \eta_2 R_{\text{pair}} \left(1 - e^{-\Delta t/2\tau}\right) T\,, \tag{3.47}$$

where η_1 and η_2 are the detection efficiencies for the two photons. The exponential resonator decay which determines the $1/e$ temporal width of the photon wave packets is described by the $1/e$ time τ.

The total number of background events for a specific bin size Δt for the measurement time T is given by the product of the number of detected events in both channels corrected by the number of coincidences S. For low dark-count rates and large measurement times it is given by

$$B = \eta_1 \eta_2 R_{\text{pair}}^2 \Delta t T \tag{3.48}$$

Putting together the two equations (3.47) and (3.48) gives the SBR

$$\text{SBR} = \frac{S}{B} = \frac{1 - e^{-\Delta t/2\tau}}{R_{\text{pair}} \Delta t} \tag{3.49}$$

Figure 3.12) shows that it is possible to improve the SBR for a given pair rate by reducing the bin size Δt, but this goes at the cost of available coincidences. For the experiment, we record the photon counts of the two output arms of the source and calculate the

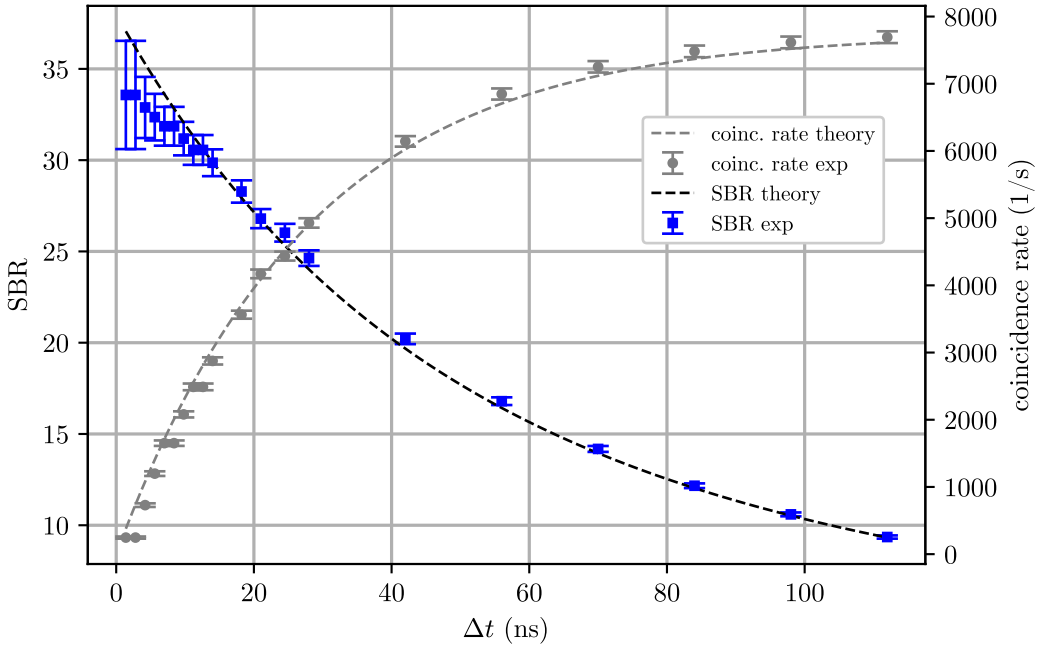

Figure 3.12: The SBR and the coincidence rate are plotted in dependence of the coincidence time window Δt. The data was recorded with a pump power of 20 mW. We take the Poissonian noise of the measured coincidences for the error bars. The theoretical calculations according to equation (3.49) for the SBR and equation (3.47) for the coincidence rate are shown as a dashed line. The photon pair rate R_{pair} is the only fit parameter.

signal-idler coincidence function for a variable coincidence time window Δt. When Δt is equals to the $1/e$ width of the photon wavepacket, we reach an SBR of about 30. For a coincidence window that covers 99.97 % of the photon, the SBR drops to value of about 10.

When designing a SPDC source, the maximal reachable SBR can be tuned by the exponential decay time τ. In the previous version of the source, there was an compensation crystal inside the resonator to compensate for the birefringence of the conversion crystal. By removing the crystal and shortening of the resonator, we reduce the time τ and therefore increase the SBR. The mean linewidth is reduced from $\tau = 17.8\,\text{ns}$ to $\tau = 12.53\,\text{ns}$. The SBR improvement is between a factor of 1.5 to 3, depending on the size of the coincidence time window.

3.2.11 Background correction for the photonic entanglement measurements

The background explained in the previous section, resulting from the temporal overlap of successive photons, together with the detector background is non-negligible. The measured quantum state properties will therefore deviate from the intrinsic values of the source. In order to specify the best possible fidelity of our produced states, we have to apply some background corrections. For applications, the non-background corrected values have to be used because the accidental coincidences, resulting form overlapping successive photons, can not be avoided and give rise to an intrinsic limitation of SPDC sources.

Figure 3.13 shows two typical correlation measurements for a polariser setting which results in maximal correlation and one with minimal correlation. The red area around zero in the time window Δt is the detected signal (C). The background (B) is taken as average over the same time window for values $\tau < -150\,\text{ns}$ and $\tau > 150\,\text{ns}$ (black area). Subtracting the background from the detected signal will result in negative, unphysical values. To avoid this, we use the background correction of [72]. We treat the background as Poisson-distributed P_B. We assume that signal and background are independent. The probability of detecting the signal C is then the sum over all combinations with $C = B+S$. With the assumption that all combinations have the same probability, we get the expected value for our signal S as

$$\langle S \rangle = \frac{\sum_{S=0}^{N} S \cdot P_B(C-S)}{\sum_{S=0}^{N} P_B(C-S)} \tag{3.50}$$

This procedure ensures that the signal S is always positive and physical.

3.3 Summary

This chapter presents the design and characterisation of our photon-pair source based on type-II conversion in a ppKTP crystal. The generated photons at 854 nm have orthogonal polarisation and are, in contrast to the previous version of the source, no longer degenerate. This is no limitation for the experiments presented in this thesis and future experiments. Through QFC, as presented in the next chapter, the wavelength can be shifted to any desired wavelength. The measured parameters of the source are a linewidth of $\delta\omega_H = 2\pi \cdot 17.6(3)\,\text{MHz}$ and $\delta\omega_V = 2\pi \cdot 12.0(2)\,\text{MHz}$, as well as a finesse of $\mathcal{F}_\mathcal{H} = 104(2)$ and $\mathcal{F}_\mathcal{V} = 152(3)$. The difference in the finesse, as well as in the FSR results in a cluster structure

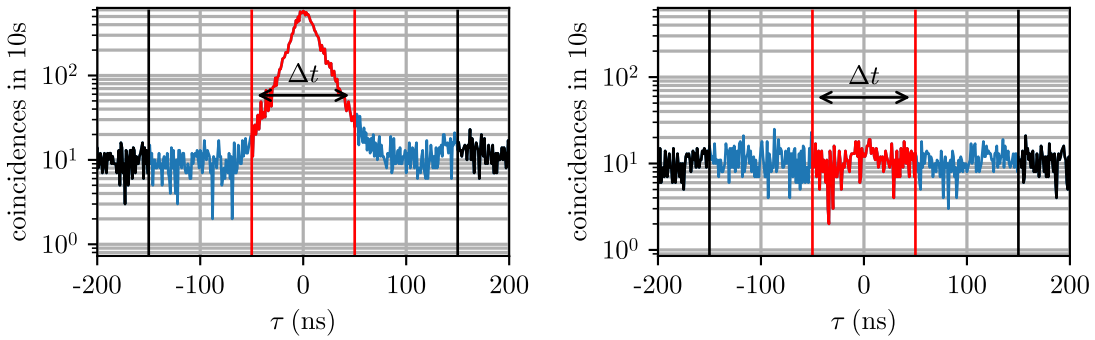

(a) Orthogonal projectors (b) Parallel projectors

Figure 3.13: Measured single mode $g^{(2)}$ correlation with a bin size of 1 ns. Coincidences are expected in the time window Δt around zero (red area). The black part of the curve is treated as the background.

with approximately three modes, whereby around 58 % of the photons are generated in the central mode. The usable single-mode photon-pair rate outside the resonator is $R_{\text{out}}^{\text{SM}} = 3.7 \times 10^4 \, \frac{\text{pairs}}{\text{s·mW}}$. With the maximum available pump power of 20 mW, we can produce $740 \times 10^3 \, \frac{\text{pairs}}{\text{s}}$ with a bandwidth of about 13 MHz. We characterise the entanglement in dependence of the interferometer phase and get a mean fidelity of 98 % with background correction (91 % without background correction) for both Bell states.

The presented and characterised source is then used in quantum network experiments with a quantum frequency converter and a single trapped $^{40}Ca^+$ ion, presented in the following chapters.

4 Quantum communication experiments without quantum node

The experiments of this chapter realise and characterise the distribution of entanglement over various distances. As a resource of entanglement, we use the photon-pair source described in chapter 3. The source and the calcium ion operate in the near-infrared regime at 854 nm. A wavelength in the near-infrared is a significant issue for long-haul entanglement distribution because fibre loss limits the entanglement rate. An unsuitable wavelength is a common problem for most quantum systems. Many other state-of-the-art quantum systems have also their interface transitions in the near IR or the visible regime [18, 130, 131]. It is advantageous to use telecom regime wavelengths (1260 nm - 1625 nm) to improve the transmission rate because the fibre absorption for these is minimal (see figure 4.1). One remedy for the described issue is the use of quantum frequency conversion (QFC) [52]. This technique preserves all properties of the photons except of the frequency, which is shifted. By choosing the pump frequency, the target frequency can be determined, which also enables the interconnection of different quantum systems, which without QFC would not be compatible due to different transition wavelengths.

The first section of this chapter will shortly describe the quantum frequency converter, built by M. Bock from the Becher lab and operated by T. Bauer. A full description and all specifications are found in the dissertation of M. Bock [70]. In section 4.2, we describe the four different measurement setups we investigated and the results of the measurements. The experiment of the last section (section 4.3) uses the converter to demonstrate entanglement distribution in a non-laboratory environment over a metropolitan fibre.

We published all results except the experiments with the metropolitan fibre in [75].

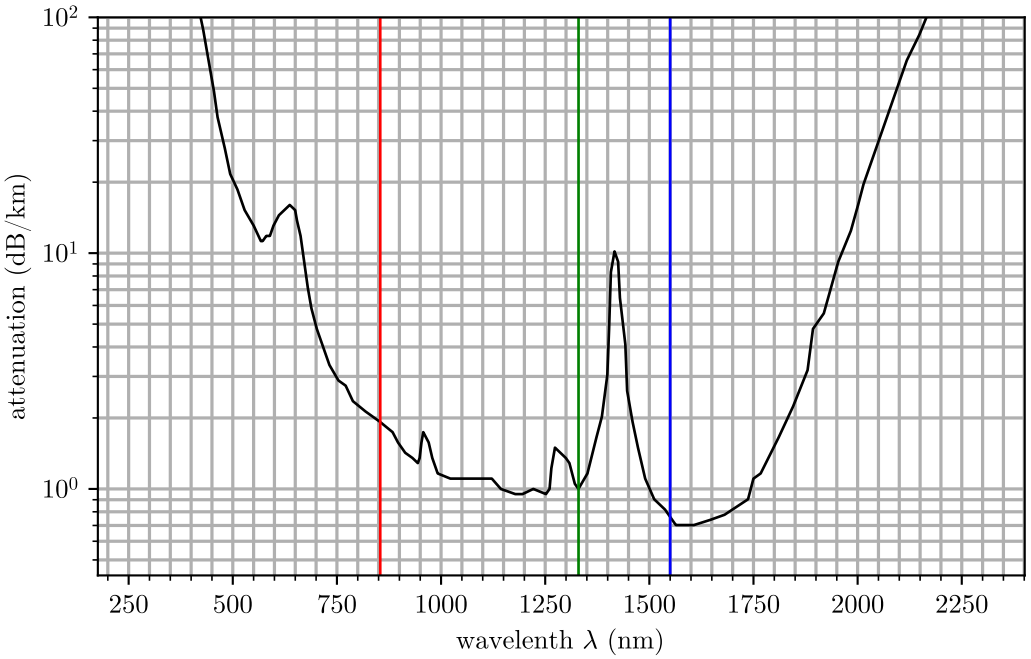

Figure 4.1: Attenuation of a standard glass-clad silica fibre with low OH-content from *Thorlabs GmbH*. Red line: $D_{5/2} \rightarrow P_{3/2}$ transition in Ca^+, green line: centre of the telecom O band, blue line: centre of the telecom C band.

4.1 The quantum frequency converter

In the following section, we will briefly describe the important parts of the converter. First, we summarise the key facts of the device, followed by a more detailed description of the photon path through the converter. The setup is based on Difference Frequency Conversion (DFG) in a PPLN waveguide [132]. To achieve DFG, the photons at 854 nm are overlapped with a strong pump at 1904 nm. The waveguide then stimulates the conversion to a photon at 1550 nm. This conversion process is strongly polarisation-dependent. A setup in a Sagnac-configuration [133, 134] (see figure 4.2) enables polarisation-independent conversion. An additional benefit of this configuration is that all fields have the same optical path; hence, no active stabilisation between the two polarisations is needed. Furthermore, the configuration allows for bi-directional conversion with the same efficiency.

After the photons generated in our lab arrive at the converter, they first pass a bandpass filter. Afterwards, they are overlapped with the pump light. Then, both fields are split into the orthogonal polarisation components H and V on a PBS. An achromatic HWP rotates the H-polarised component to V so that all beams have the same polarisation in the

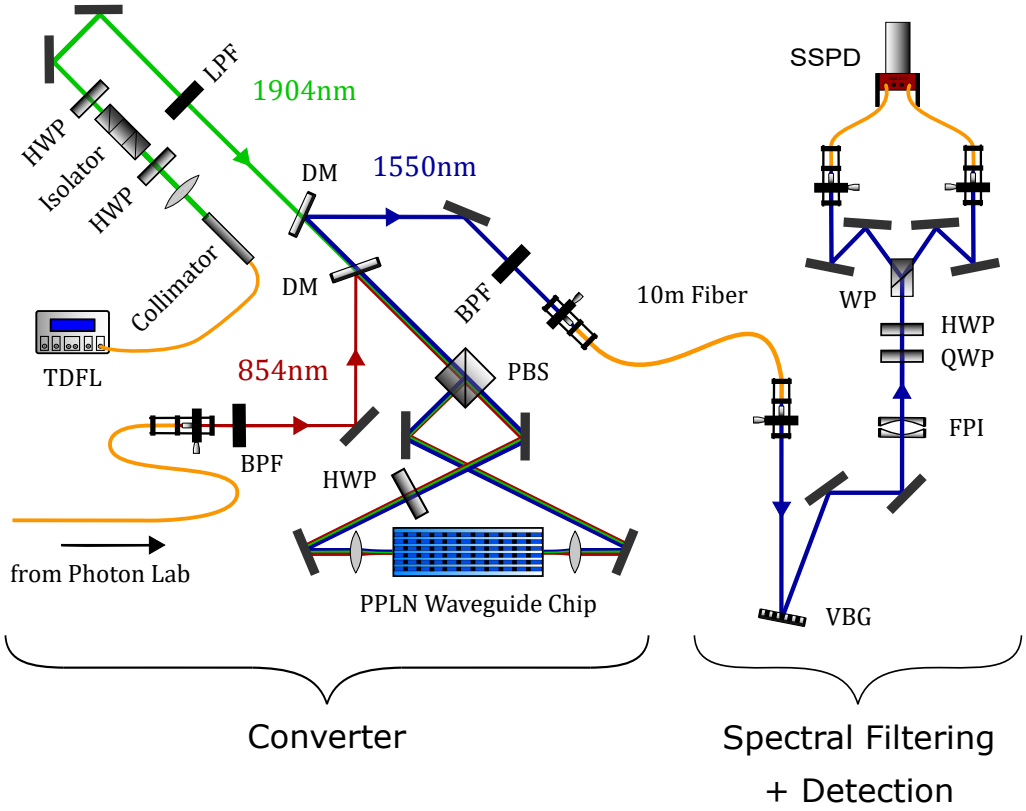

Figure 4.2: Schematic of the quantum frequency converter including the filtering and projection setup (adapted from [70]). The converter is set up in a Sagnac configuration. TDFL: Thulium-doped fibre laser, LPF: low-pass filter, BPF: bandpass filter, VBG: volume-Bragg grating, DM: dichroic mirror, HWP: half-wave plate, SNSPD: superconducting nanowire single photon detector, WP: Wollaston prism.

waveguide. The counterpropagating beams are coupled into the same waveguide, where the conversion occurs. The converted 1550 nm photons from the original V-component also pass the achromatic waveplate and are thereby rotated to H. Finally, all beams are overlapped again on the initial PBS, closing the Sagnac loop. The back- or unconverted light is filtered out by dichroic mirrors (DMs) and a bandpass filter. The pump beam gets separated by a second DM.

The broad, intrinsic conversion background, which results mainly from anti-Stokes Raman scattering[132, 135, 136], can significantly be reduced by a narrowband filtering stage. This filtering stage consists of a bandpass filter (filter bandwidth of 12 nm), a volume Bragg grating (filter bandwidth of 25 GHz) and a Fabry-Pérot etalon (FSR= 12.5 GHz, FWHM= 250 MHz). Spatial filtering happens by means of 10 m of optical fibre. Altogether, this leads to a background rate of $24\,s^{-1}$ in front of the detectors.

The external conversion efficiency, measured between the 854 nm coupler and the end of the 1550 nm fibre, is 57.2 %.

4.2 Entanglement distribution over large distances

In the following experiments, we show the preservation of photon-photon entanglement in four different settings. Except for the first, all setups include QFC to bridge large distances, and the last setup additionally includes back conversion to 854 nm, as depicted in figure 4.3. From the two photons, the non ion-resonant one (480 MHz shifted) is converted to the telecom range. We measured the entanglement for all configurations with four different source pump powers (5 mW, 10 mW, 15 mW and 20 mW) and a state phase of $\phi = 270°$; due to the alignment of the source, it was not possible to use a phase of $\phi = 0°$ or $\phi = 180°$ (see section 3.2.5).

4.2.1 Experimental setup

Setup a) The first experiment (figure 4.3a)) is for the characterisation of the source, and it is identical to the setup of the previous chapter (chapter 3). We filter each output of the source separately by a FPI. A projection setup after the FPI projects the photons.

Setup b) In the next setup (4.3b)) we send the detuned photons through 90 m of single-mode fibre to the labs of Prof. Becher, where we convert the photons to the telecom range. The state tomography is then performed between a 854 nm and a 1550 nm photon. We do not actively stabilise the polarisation of the fibre connecting the two labs because it turned out that the drifts are slow, so a recalibration after 2 h is sufficient.

Setup c) The third setup (figure 4.3c)) includes 20 km of single-mode fibre between the converter and the state detection stage. We wound the fibre onto a spool and put the spool inside a temperature-stabilised enclosure, slowing down polarisation drifts. This passive stabilisation and recalibration every hour was sufficient to maintain high polarisation fidelity ($> 99\,\%$). This configuration shows the supremacy of the telecom wavelength range. Sending light at 854 nm through this distance of fibre would result in an attenuation of -70 dB [137], which would make this experiment impossible. The converted light, in contrast, experiences only an attenuation of -3.4 dB [138].

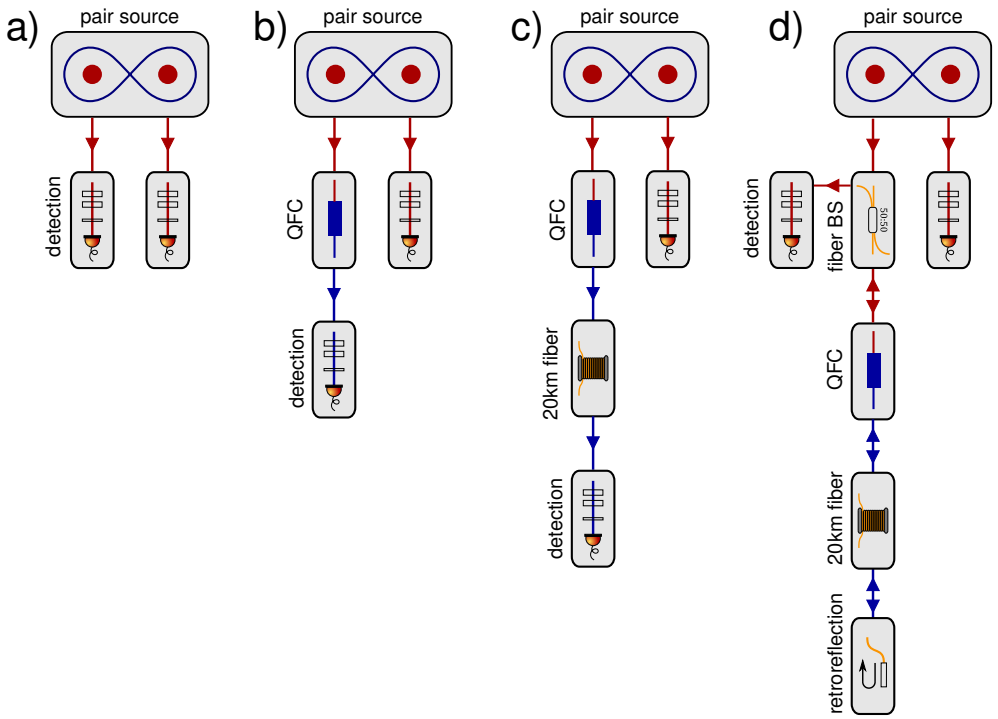

Figure 4.3: Schematic of the different measurement setups (adapted from [75]). a) The state is measured directly at the source. b) One photon is frequency-converted and measured directly after the conversion. c) After the conversion, we insert 20 km of fibre. d) A retroreflector terminates the 20 km fiber and so the photon is converted back to 854 nm.

Setup d) For the last experiment (figure 4.3d)) in this series, we use the fact that the converter is bi-directional, i.e., we terminate the 20 km fibre with a retroreflector pigtail. By this, the light travels the distance back, gets converted to 854 nm and is then split by a fibre beam splitter to guide the light to the detection setup in the photon lab. This setup shows that our interface can integrate a quantum memory with transitions in the near-infrared range like the Ca ion with communication through telecom fibres. Filtering is only performed for the 854 nm photons. This enables us to remove the converter's filter stage and gain efficiency. Using the fibre beam splitter reduces the intrinsic efficiency to 25 %. An optical circulator could improve the intrinsic efficiency by a factor of three.

For the 854 nm photon detection, we use the Excelitas APDs and the SSPDs in the lab of the AG Becher for the telecom photons, as described in section 2.6.

4.2.2 Polarisation control

For the measurement, we must first calibrate the polarisation rotations in both paths from source to projection. Depending on the setup, this includes the converter and the fibre link. We deterministically generate photons with linear (H) polarisation by blocking one pump direction of the interferometer. Additionally, we insert a quarter-wave plate in the outputs of the source, rotating the polarisation to R. We then perform single-qubit tomography with the detection setups with four different projection settings for each input polarisation. From this, we calculate the rotation matrix M, which is applied to the projection bases and transforms them accordingly.

4.2.3 Results

We perform quantum state tomography for all setups and pump powers and calculate the fidelity and purity of the reconstructed density matrix. A density matrix for each measurement setup, for a detection window of $\Delta t = 5\tau_{\text{mean}}$ and a pump power of 20 mW, is shown in figure 4.4. We use the recorded counts directly to calculate the SBR (see section 3.2.10). Thus, we summarise the coincidences for the HH, HV, VH and VV measurements and divide it by four times the mean background. Figure 4.5 show the summarised results.

The coloured dot-dashed lines in figure 4.5 show the background corrected results (see section 3.2.11). These fidelities represent the best possible value for each configuration. The deviations between the different measurement setups result from different polarisation calibrations and drifts of the polarisation during the measurements. We use these values to calculate the expected theoretical fidelity for a given pair rate according to [72]

$$F = \langle\Psi|\,\rho\,|\Psi\rangle = \frac{\frac{1}{4} + F_{\text{w/o BG}} \cdot \text{SBR}}{1 + \text{SBR}} \tag{4.1}$$

We show the result as a coloured dashed line. All measurements are near to their theoretical boundary. For a given pump power of the photon-pair source, we see only a slight deviation (within the error bars) between the different configurations. This result indicates the high process fidelity of the converter itself. Polarisation drifts of the included optical fibres and fluctuations of the photonic state phase explain the deviation of the measured fidelities between different configurations.

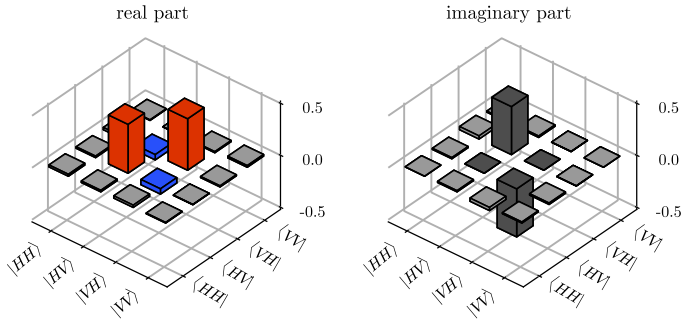

(a) SPDC source

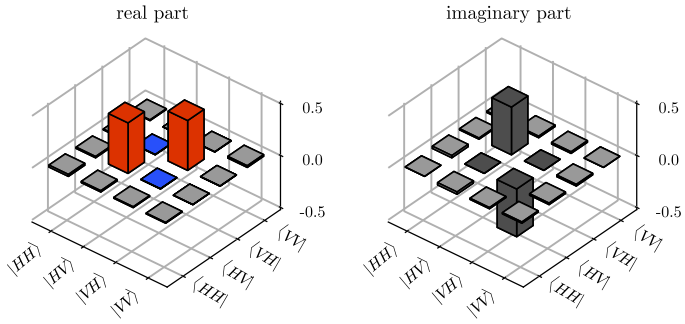

(b) SPDC source with conversion

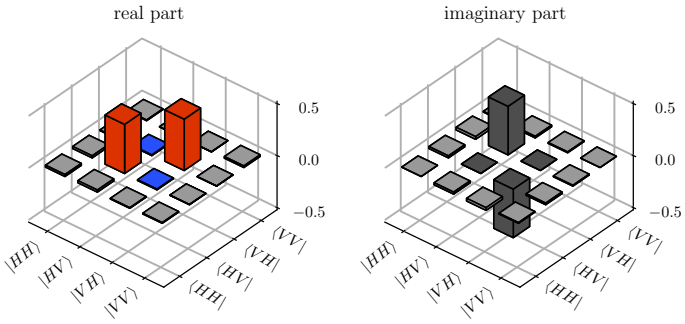

(c) SPDC source with conversion and 20 km of fiber.

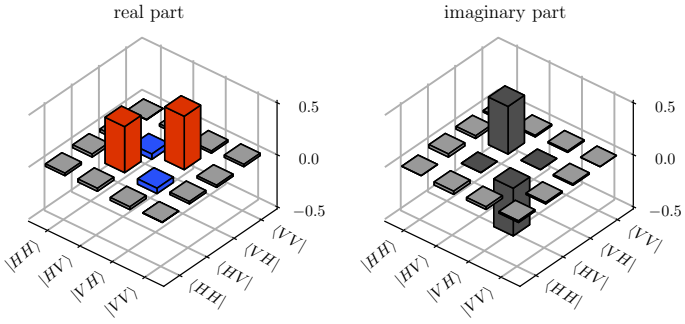

(d) SPDC source with back conversion including 40 km of fiber.

Figure 4.4: Each subplot shows a density matrix, which corresponds to one measurement setting. The evaluation is done for a detection window of $\Delta t = 5\tau_{\text{mean}}$ and a pump power of 20 mW

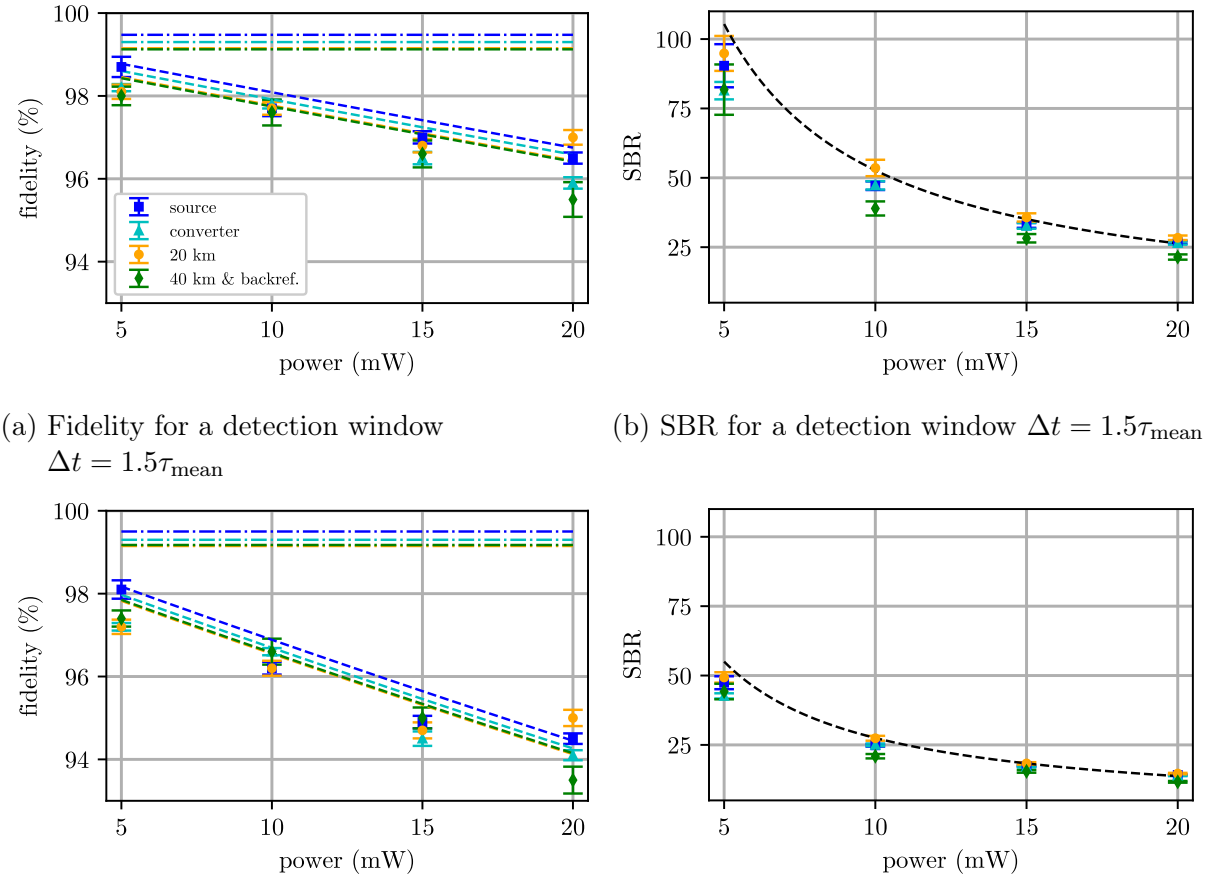

(a) Fidelity for a detection window $\Delta t = 1.5\tau_{\text{mean}}$

(b) SBR for a detection window $\Delta t = 1.5\tau_{\text{mean}}$

(c) Fidelity for a detection window $\Delta t = 5\tau_{\text{mean}}$

(d) SBR for a detection window $\Delta t = 5\tau_{\text{mean}}$

Figure 4.5: Measurement results for SBR and fidelity for two selected detection windows. The coloured dot-dashed lines in the fidelity plots represent the background-corrected fidelity for the four different settings, whereas the dashed line is the theoretically best possible fidelity calculated from the non-background corrected fidelity. The black dashed line in the SBR plots shows the theoretical expectation. The error bars for the fidelity are based on a Monte Carlo simulation, and the error bars for the SBR take Poissonian noise into account. The chosen time window for plots a) and b) is $1.5\tau_{\text{mean}}$. For the last two plots, the time window is $5\tau_{\text{mean}}$.

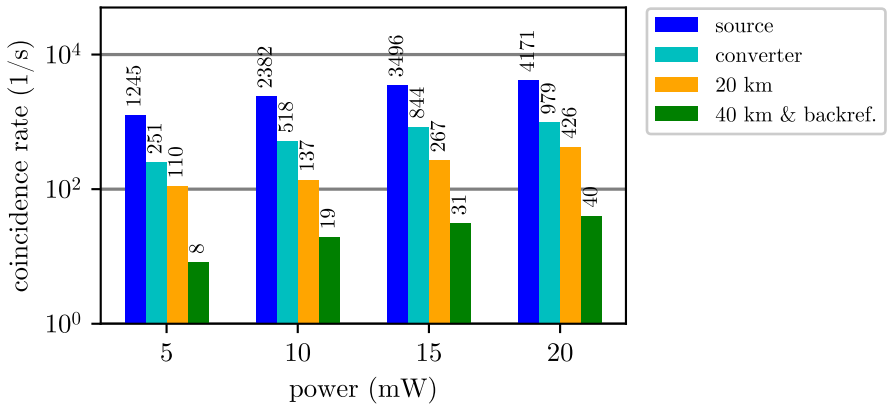

(a) Detected coincidence rate for $\Delta t = 1.5\tau_{\text{mean}}$

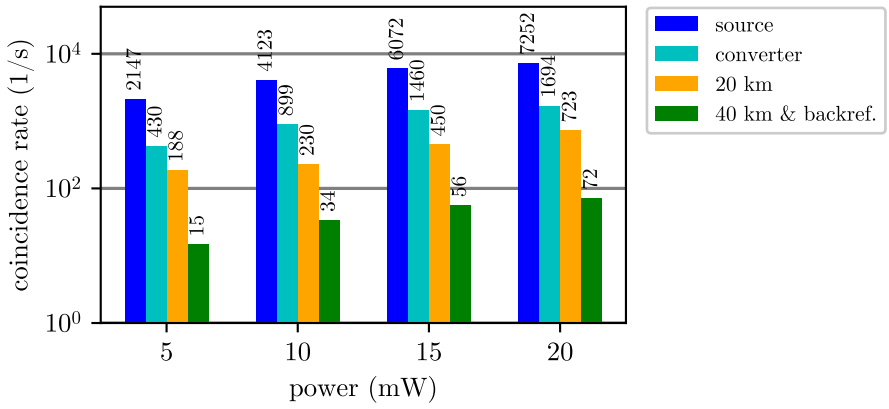

(b) Detected coincidence rate for $\Delta t = 5\tau_{\text{mean}}$

Figure 4.6: Detected coincidence rates for a detection window of $\Delta t = 1.5\tau_{\text{mean}}$ and $\Delta t = 5\tau_{\text{mean}}$ for the four different measurement settings.

Table 4.1: Efficiencies of the individual components of setup d).

part	efficiency	total efficiency
Fiber-fiber couplings	76 %	76 %
Fiber-BS (2x)	50 %	25 %
Transmission 854nm fiber (2x)	87 %	75.7 %
Conversion (2x)	57.2 %	32.7 %
Transmission 20km fiber (2x)	42 %	17.6 %
Retroreflector	87 %	87 %
Overall: source output to APD		0.7 %

We calculate the black dashed line for the SBR plot from equation (3.49) for the given pair rate. The error bars of the measured SBR is calculated by taking Poissonian noise into account. If we take more of the photonic wavepacket into account, the SBR decreases because more of the temporal shape of the photons overlap. Due to the lower SBR, we also see a slightly decreased fidelity. The measured coincidence rate for all pump powers and the different measurement settings are shown in figure 4.6. The numbers fit well with the measured efficiencies of the different setup components, summarised in table 4.1.

In summary, the measurements show the preservation of the entanglement with high fidelity through one or two conversion steps and distribution over up to 40 km of optical fibre. The QFC adds low noise to the generated photon pairs and thus enables the experiments in the next chapter, where we show a proof-of-principle demonstration of a quantum photonic interface connecting a quantum network node based on a $^{40}Ca^{+}$ single-ion memory.

4.3 Metropolitan fibre experiments

In the following section, we will show the preservation of photon-photon entanglement, this time between two remote stations, separated by 14 km of metropolitan fibre. We place the detection setup at the HTW. The route of the fibre through the city is shown in fig 4.7(a). The fibre runs under and over the ground and has several splices and patches, as seen from an Optical Time Domain Reflectometry (OTDR) measurement (see figure 4.7(b)). The overall damping is approximately 11.5 dB. Measurements have shown, that an active polarisation stabilisation is needed.

4.3.1 Polarisation stabilisation

For stabilising the polarisation over the metropolitan fibre, we use two reference lasers at 1550 nm with orthogonal polarisations (H and D). First, the beams from both lasers are combined into a single fibre. Then, they are coupled via the 1 % input of a 99:1 beam combiner into the metropolitan fibre. The 99 % input is used for the photons. At the end of the fibre, we install an in-fibre piezo-controller[1] to compensate for the polarisation drifts of the fibre. The polarisation controller is then again followed by an optical switch, which guides either the photons to a polarisation projection setup similar to the already presented ones and a set of SSPDs or the reference lasers to a polarimeter. A schematic of the setup is shown in figure 4.8.

Measurements without stabilisations have shown that the polarisation in the fibre is only stable for a few minutes due to environmental effects. Therefore, we decide to limit the measurement time to 30 s. After this time, we restart the stabilisation process. If the start value of a stabilisation process is too bad, we register it so we can discard the previous measurement. The stabilisation process works as follows: We activate both switches to route the lasers to the polarimeter. Then we switch on the first laser and run a gradient descent algorithm on the piezo controller to optimise the first polarisation. The algorithm stops if a certain threshold is reached or after 100 optimisation runs. Limiting the number of runs ensures that the other polarisation stays relatively high. After the optimisation of the first laser is finished, it is switched off, and we send the second polarisation, repeating the optimisation. We repeat the procedure until both polarisations are above a specific threshold, resulting in a compensated, stable polarisation rotation over the fibre.

[1] PolaRITE III PCD-M02-854

(a) Map of Saarbrücken with the route of the metropolitan fibre (red line). Bilder ©2023 AeroWest,CNES / Airbus,GeoBasis-DE/BKG,GeoContent,Maxar Technologies, Kartendaten ©2023 GeoBasis-DE/BKG (©2009), Google.

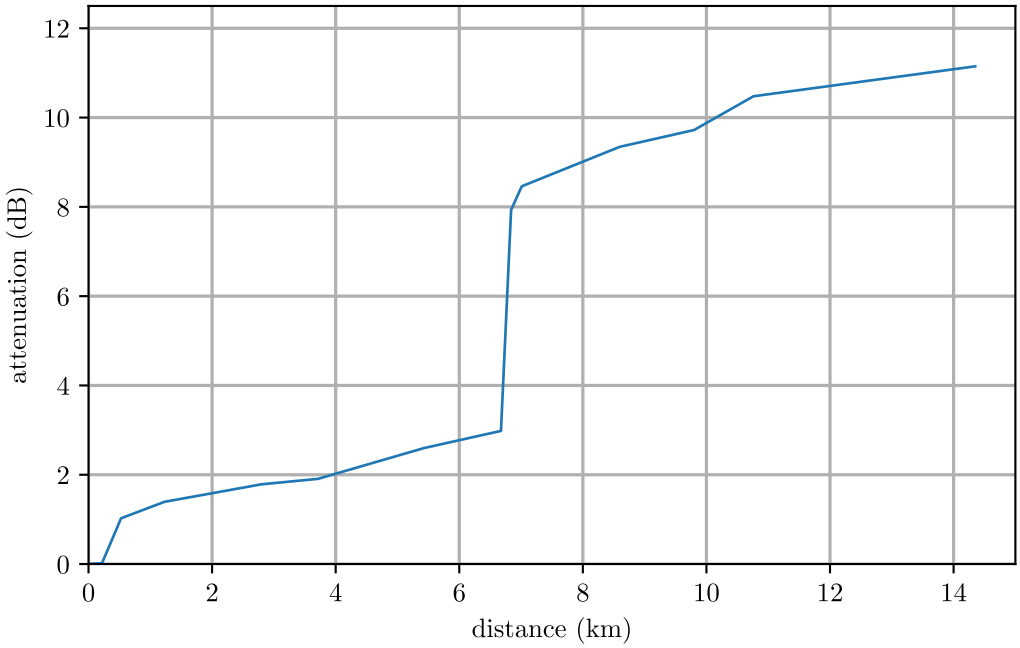

(b) OTDR measurement

Figure 4.7: Route and fibre attenuation of the metropolitan fibre. The attenuation, is plotted in dependence of the distance from the UdS. The jump in attenuation at around 7 km is probably a lossy fibre-fibre connection.

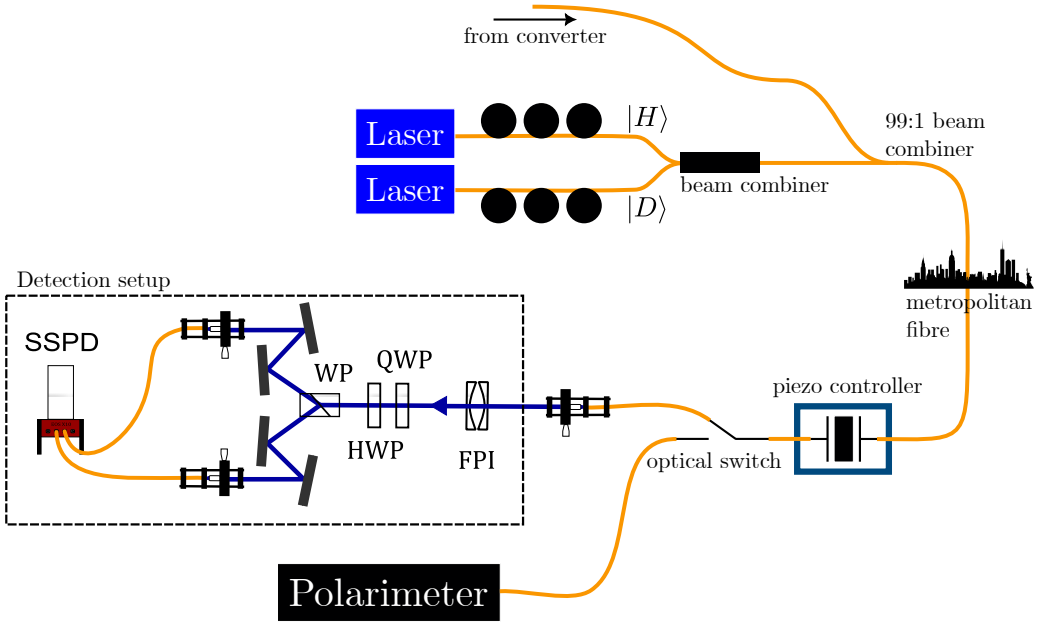

Figure 4.8: Schematic of the fibre stabilisation. Two lasers with polarisation H and D are send via the 1 % input of a 99:1 beam combiner through the metropolitan fibre. After the fibre, the polarisation can be adjusted via an in-fibre piezo-controller. Afterwards, another optical switch guides the light either to a detection setup or to a polarimeter.

After the polarisation over the metropolitan fibre is stable, we must calibrate the polarisation rotation on the whole path from the source to the detection setup at the HTW. We switch back to single photons from the source and perform single qubit tomography, as described earlier. Drift on all fibres except the metropolitan one show slow polarisation drifts. In order to still achieve stable polarisation over the entire distance, we run an optimisation of the polarisation of the metropolitan fibre between each basis combination of the tomography.

4.3.2 Results

We verify the entanglement by performing a quantum state tomography. We use a similar setup as in the measurement of the previous section. Instead of the 20 km fibre spool, we now connect the metropolitan fibre to the HTW. The filtering and projection setup is identical to the one we used in the previous experiments. Because of a different alignment of the source, we now use the $|\Psi^-\rangle$-Bell state. We measure 16 basis combinations but run

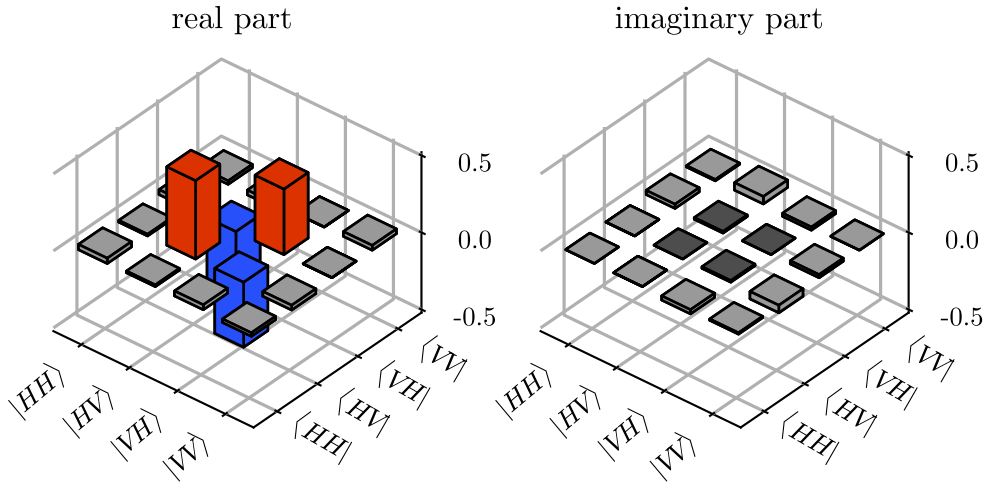

Figure 4.9: Not background corrected, reconstructed density matrix for the entanglement measurement over the metropolitan fibre and a detection window of $\Delta t = 5\tau_{\text{mean}}$. We use a pump power of 15 mW.

Table 4.2: Fidelity and purity over the metropolitan fibre for different detection windows.

		with background correction		without background correction	
state	Δt	fidelity	purity	fidelity	purity
$\|\Psi^-\rangle$	$1.5\tau_{\text{mean}}$	96.9(3) %	94.8(5) %	93.3(4) %	88.3(7) %
	$5\tau_{\text{mean}}$	96.6(2) %	94.1(4) %	90.9(3) %	84.3(5) %

a polarisation optimisation after each projection set. The setpoint for the polarisation stabilisation is a fidelity of 99 %.

A maximum-likelihood reconstruction reveals the density matrix shown in figure 4.9. From the density matrix, we calculate the fidelity and the purity. The results for different detection windows Δt are summarised in table 4.2

A background corrected fidelity of 97 % compared to 98 % without conversion and metropolitan fibre is a clear sign that the stabilisation is working as expected and the polarisation drifts of the fibre can be compensated. Compared to the measurements shown previously, the missing fidelity is explained by some inaccuracy in the rotation matrices or fluctuations of the polarisation between two stabilisation steps.

4.4 Summary

This chapter presents the distribution of entanglement in different settings with distances of up to 40 km, including a metropolitan fibre of 13 km. The entanglement is well preserved in all settings. Except for the metropolitan fibre, we reach the theoretical maximum possible fidelity. The causes of losses are well known, and solutions for improvements will be implemented where possible. For example, lossy fibre-fibre couplings are gradually replaced by splices.

The fluctuations of the polarisation over the metropolitan fibre are a considerable challenge for polarisation qubits. The presented approach already shows a good performance. Stabilising the polarisation every 30 s is sufficient to reach background corrected fidelities over 98 %. The additional time for a stabilisation step is only a few seconds, thus negligible. Nevertheless, we are testing different stabilisation methods; for example, it might be possible to use two different wavelengths, one above and one below 1550 nm. If there is no cross-talk between the wavelength channels and the wavelength dependency of the drifts can be predicted, then the stabilisation could run continuously.

The experience gained in the experiments in this chapter is used in the ion experiment to realise quantum state teleportation in three of the presented settings.

5 Quantum communication experiments with a single ion

In the previous chapters, we presented the characterisation of the photon-pair source, the preservation of entanglement in the QFC process, and the distribution of entanglement over large distances. In this chapter, we show the use of the photon pair source and the gained knowledge in different quantum communication experiments with a single ion as a quantum node. The goal is the entanglement transfer from photon-photon entanglement to ion-photon entanglement over the metropolitan fibre. To achieve this goal, we had to investigate two simpler experimental setups: the direct detection of the partner photon at 854 nm and detection in the labs of Christoph Becher, including QFC. The final setup includes QFC, the metropolitan fibre and the detection at the HTW.

In the first section of this chapter, we describe the protocol used for the entanglement transfer and the quantum state teleportation. The teleportation measurement, which is based on previous works of our group [16, 72, 82], will be presented in detail in chapter 6. In the following section (section 5.2), we show characterisation measurements used to determine the coherence time of the ion and the 393 nm detection efficiency. In the first experiment, which we describe in section 5.3, we use weak laser pulses instead of single photons to characterise the protocol and the newly implemented back-reflection stage. In the initial protocol, it was only possible to detect two out of four Bell states. The newly implemented back-reflection stage enables the detection of the missing two Bell states. In the following section (sec. 5.4), we present the entanglement transfer from photon-photon to ion-photon entanglement in three different settings.

We published the measurements for the entanglement transfer and the teleportation (see section 6.3) with detection at 854 nm in [76].

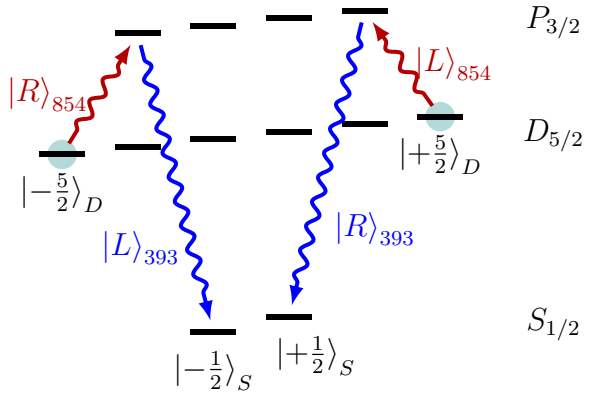

Figure 5.1: Relevant atomic energy levels and transitions for the used protocol. The teal circles at the $|\pm 5/2\rangle_D$ states indicate the initial superposition and the starting point of the protocol. An incoming 854 nm photon excites the ion to the short-lived $P_{3/2}$ state, from where the ion decays to the $S_{1/2}$ ground state in most cases. The corresponding polarisations for absorption of an 854 nm photon travelling along the magnetic field direction and for collecting a 393 nm photon travelling against the magnetic field direction are depicted next to the arrows.

5.1 Protocol for the quantum state teleportation

In this section, we will describe the protocol for quantum state teleportation, which is also used for the photon-photon to atom-photon entanglement transfer. The laser sequence and the used levels of the ion are identical for both measurements. The protocol is first verified by replacing the photon-pair source with a laser. In this case, we call it laser state transfer (LST). The relevant levels of the ion and the corresponding transitions are shown in 5.1.

The protocol starts with the preparation of a superposition of the outer $D_{5/2}$ Zeeman sublevels (see section 5.1.1)

$$|\Psi\rangle_D = \alpha\,|-5/2\rangle_D + \beta e^{\phi_0}\,|+5/2\rangle_D \qquad |\alpha|^2 + |\beta|^2 = 1 \tag{5.1}$$

The phase factor ϕ_0 consists of a constant offset due to the preparation and a time-dependent part $\omega_L t$, resulting from the Larmor precession with frequency ω_L. The Larmor precession results from the energy splitting of the Zeeman sublevels. In the case of the LST and the entanglement transfer we have $\alpha = \beta = 1/\sqrt{2}$. For the teleportation measurement, we want to teleport an arbitrary state out of the ion. Therefore, the coefficients vary. We validate the protocol with $\alpha = 0, \beta = 1$, as well as $\alpha = 1, \beta = 0$ and $\alpha = \beta = 1/\sqrt{2}$.

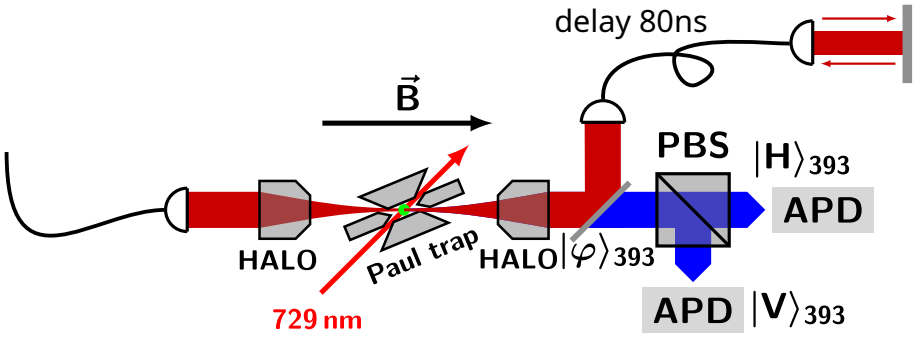

Figure 5.2: Setup of the ion. The 854 nm photons are focused onto the ion with the HALO. Non-absorbed photons are split from the 393 nm photons via a dichroic mirror, are collected with a single-mode (SM) fibre and are sent back with a total delay of 160 ns.

If the electron is in the $D_{5/2}$ state, the ion can absorb incoming photons at 854 nm; it is the so-called *receiver mode*. The state of the incoming photon expressed in the circular basis $|R\rangle, |L\rangle$ with amplitude factors γ and δ is[1]

$$|\Psi\rangle_{854} = \gamma\,|R\rangle_{854} + \delta\,|L\rangle_{854} \qquad |\gamma|^2 + |\delta|^2 = 1 \tag{5.2}$$

We focus the photons with the first HALO onto the ion along the magnetic field axis. We refer to a propagation direction along the magnetic field direction as *first* passage. The initial version of the protocol had only this *first* passage, and the new part is a *second* passage. If a photon is not absorbed, we collect it and send it back with a time delay of 160 ns. The delay allows us to distinguish between the two passages because the time of a coincidence between 854 nm and 393 nm photons is different. In the *second* passage, we use the second HALO to focus the photons again onto the ion. Figure 5.2 shows the setup of the ion part of the experiment. The difference between *first* and *second* passage is that now the photons counter-propagate to the magnetic field direction, which changes the transition-polarisation mapping. Normally, the atom is described in a stationary spherical system $(x^{(at)}, y^{(at)}, z^{(at)})$, whereas the photon is described in a moving Cartesian coordinate system $(x^{(ph)}, y^{(ph)}, z^{(ph)})$. The relationship between both coordinate systems is shown in figure 5.3. In the following, we will briefly describe how the polarisation of photons map to an atomic transition. The applied magnetic field defines the quantisation axis of the ion. Therefore, we fix the $z^{(at)}$-axis of the atomic coordinate system to be

[1] This is an abbreviated notation for a one-photon state in which we have also assumed post-selection of a successful event.

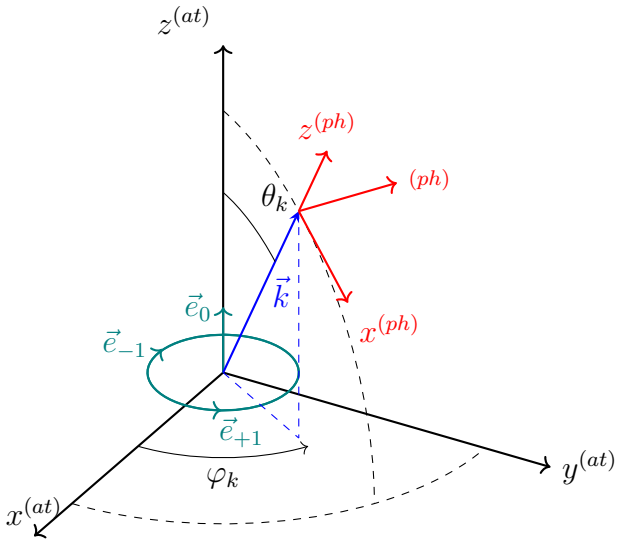

Figure 5.3: Relationship between the atomic $(x^{(at)}, y^{(at)}, z^{(at)})$ and photonic $(x^{(ph)}, y^{(ph)}, z^{(ph)}$, red) coordinate systems. The photonic system is rotated with respect to the atom system by the angels θ_k and φ_k. The $z^{(at)}$ axis points in direction of the wave vector $\vec{k}$ (blue) of the incoming photon. The $z^{(ph)}$ axis is defined by the quantization axis defined by an external magnetic field. The unity vectors of the helicity base are shown in teal.

parallel to the magnetic field axis $\mathbf{B} = (0, 0, B)$. We choose the $z^{(ph)}$-axis of the photonic system to be collinear with the wave vector $\mathbf{k}$ of the incoming light. Therefore, in general, the photonic and atomic systems are rotated by the angles θ_k and φ_k to each other (see figure 5.3).

We must transform one coordinate system into the other to describe the interaction. With the basis vectors of the helicity base

$$\mathbf{e}_{+1} = -\frac{1}{\sqrt{2}}\left(\mathbf{e}_x + \mathrm{i}\mathbf{e}_y\right) = -\frac{1}{\sqrt{2}}\begin{pmatrix}1\\ \mathrm{i}\\ 0\end{pmatrix} \tag{5.3}$$

$$\mathbf{e}_{-1} = \frac{1}{\sqrt{2}}\left(\mathbf{e}_x - \mathrm{i}\mathbf{e}_y\right) = \frac{1}{\sqrt{2}}\begin{pmatrix}1\\ -\mathrm{i}\\ 0\end{pmatrix} \tag{5.4}$$

$$\mathbf{e}_0 = \mathbf{e}_z = \begin{pmatrix}0\\ 0\\ 1\end{pmatrix} \tag{5.5}$$

we write the transformation between photon and atom base as [139]

$$\mathbf{e}_{+1}^{(ph)} = e^{\mathrm{i}\phi_k} \sin^2\left(\frac{\theta_k}{2}\right) \mathbf{e}_{-1}^{(at)} + \frac{\sin(\theta_k)}{\sqrt{2}} \mathbf{e}_0^{(at)} + e^{-\mathrm{i}\phi_k} \cos^2\left(\frac{\theta_k}{2}\right) \mathbf{e}_{+1}^{(at)} \tag{5.6}$$

$$\mathbf{e}_{-1}^{(ph)} = e^{\mathrm{i}\phi_k} \cos^2\left(\frac{\theta_k}{2}\right) \mathbf{e}_{-1}^{(at)} - \frac{\sin(\theta_k)}{\sqrt{2}} \mathbf{e}_0^{(at)} + e^{-\mathrm{i}\phi_k} \sin^2\left(\frac{\theta_k}{2}\right) \mathbf{e}_{+1}^{(at)} \tag{5.7}$$

or for the opposite transformation direction

$$\mathbf{e}_{+1}^{(at)} = e^{\mathrm{i}\phi_k} \left(\cos^2\left(\frac{\theta_k}{2}\right) \mathbf{e}_{+1}^{(ph)} - \sin^2\left(\frac{\theta_k}{2}\right) \mathbf{e}_{-1}^{(ph)} \right) \tag{5.8}$$

$$\mathbf{e}_{-1}^{(at)} = e^{-\mathrm{i}\phi_k} \left(\sin^2\left(\frac{\theta_k}{2}\right) \mathbf{e}_{+1}^{(ph)} + \cos^2\left(\frac{\theta_k}{2}\right) \mathbf{e}_{-1}^{(ph)} \right) . \tag{5.9}$$

For our setup, we always work in the table plane, which means the elevation angle ϕ_k always equals zero. The azimuth angle, defined between the direction of the magnetic field and the photon wave vector, changes depending on the passage.

For the *first* passage we have $\theta_k = 0$, which gives us

$$\mathbf{e}_{+1}^{ph} = \mathbf{e}_{+1}^{(at)} \tag{5.10}$$

$$\mathbf{e}_{-1}^{ph} = \mathbf{e}_{-1}^{(at)} \tag{5.11}$$

Therefore, for the *first* passage, we have the direct translation

$$|R\rangle_{854} \rightarrow \sigma_{854}^{+} \qquad\qquad |L\rangle_{854} \rightarrow \sigma_{854}^{-} \tag{5.12}$$

of the photon polarisation to the atomic transition.

For the *second* passage we have $\theta_k = \pi$, which gives us

$$\mathbf{e}_{+1}^{ph} = \mathbf{e}_{-1}^{(at)} \tag{5.13}$$

$$\mathbf{e}_{-1}^{ph} = \mathbf{e}_{+1}^{(at)} \tag{5.14}$$

which translated to

$$|R\rangle_{854} \rightarrow \sigma_{854}^{-} \qquad\qquad |L\rangle_{854} \rightarrow \sigma_{854}^{+} . \tag{5.15}$$

After the absorption, the ion is in the exited, short-lived $P_{3/2}$ state. There are three possible decay channels. With a probability of 93.47 % the ion decays to the $S_{1/2}$ ground

state, emitting a photon at 393 nm in the state $|\phi\rangle_{393}$. The detection of this photon heralds a successful absorption of the 854 nm photon. In the protocol, we only take heralded events into account. With a probability of 0.66 %, the ion decays to the $D_{3/2}$ state and with a probability of 5.87 % back to the $D_{5/2}$ state. In the first case, we get no herald, which lowers the efficiency of the protocol. In the second case, another photon can re-excite the ion. According to [72], this lowers the fidelity of the protocol because all following absorptions lead to an incoherent contribution to the final state. Depending on the absorption rate, the fidelity loss is between 0 % (low number of absorptions) and 3 % (large number of absorptions). With our photon pair source, we are in the range of 0.3 % fidelity loss, due to back decays.

The heralds are collected in the opposite direction of the magnetic field for both passages. Applying the above formalism, we see the mapping

$$|R\rangle_{393} \rightarrow \sigma^-_{393} \qquad\qquad |L\rangle_{393} \rightarrow \sigma^+_{393} \tag{5.16}$$

between transition and polarisation.

The described process is summarised in one Raman process operator for the *first* passage [99]

$$\hat{\mathrm{R}}^{1^{\mathrm{st}}}_{854,D} = |L\rangle_{393}\,|{-1/2}\rangle_S\,\langle R|_{854}\,\langle {-5/2}| + |R\rangle_{393}\,|{+1/2}\rangle_S\,\langle L|_{854}\,\langle {+5/2}| \tag{5.17}$$

and one for the *second* passage

$$\hat{\mathrm{R}}^{2^{\mathrm{nd}}}_{854,D} = |L\rangle_{393}\,|{-1/2}\rangle_S\,\langle L|_{854}\,\langle {-5/2}|_D + |R\rangle_{393}\,|{+1/2}\rangle_S\,\langle R|_{854}\,\langle {+5/2}|_D \tag{5.18}$$

Similar to the initial state (equation (5.1)), the final ground state superposition oscillates with the corresponding Larmor frequency. However, this time dependence does not affect the protocol, which can be explained in the following way. We stabilise the magnetic field so the Larmor frequency is constant. Therefore, the detection timestamp of the herald determines the phase of the Larmor precession at the moment of absorption. This phase is then taken into account in the data evaluation. In principle, it is also possible to correct the phase. To this end, the phase must be calculated in real-time, and the reference oscillator has to be shifted by this value. The experiment control we use does not allow this calculation, but the future version should have this feature.

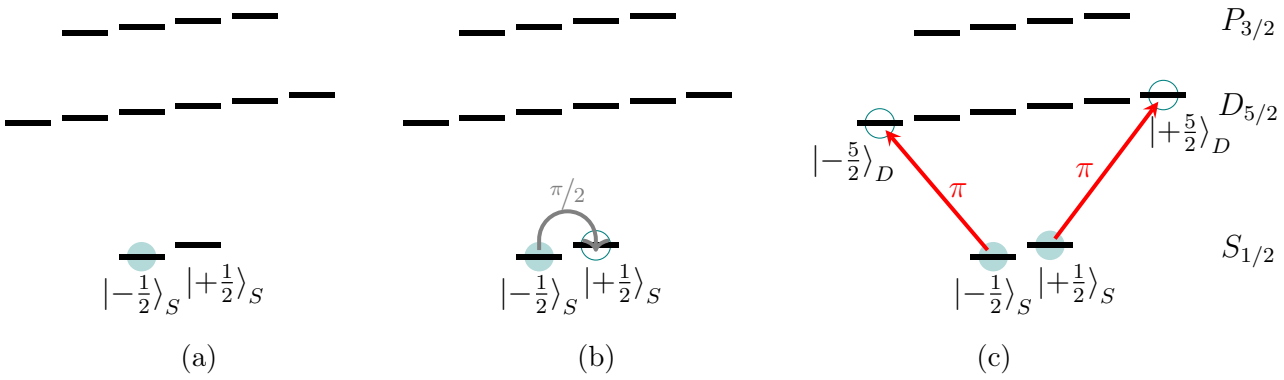

Figure 5.4: Pulse schema for the generation of a coherent superposition in the $D_{5/2}$ state. (a) The sequence start with the electron in the $|S_{1/2}, m = -1/2\rangle$ ground state. (b) The following RF $\pi/2$-pulse creates an equal superposition. (c) Two subsequent π-pulses at 729 nm creates the superposition in the outer $D_{5/2}$ states.

5.1.1 Pulse sequence

We must translate the previously described formalism into a sequence of laser pulses to run the experiment. In table 5.1, we summarise the pulses and their timings. The LST uses weak laser pulses instead of single photons within the exposure window. The strength of these pulses is adjusted so that, on average, there is less than one absorption per pulse, ensuring that we see the effect of the *second* passage.

The sequence starts with 200 µs Doppler cooling with the 397 nm laser. The 866 nm laser is used for repumping the population out of the $D_{3/2}$ state. Driving the $|S_{1/2}, m = +1/2\rangle$ to $|D_{5/2}, m = -\frac{3}{2}\rangle$ transition at 729 nm together with an additional 854 nm laser results in frequency-selective optical pumping to the $|S_{1/2}, m = -1/2\rangle$ state. Optical pumping is performed for 162 µs. In the case of the teleportation measurement, we then wait for an open window of the source-chopper to continue.

After the trigger from the source electronics, we generate a superposition of the ground state by applying an RF $\pi/2$-pulse, see also figure 5.4b). Two subsequent π-pulses at 729 nm create the intended superposition in the outer $D_{5/2}$ levels (figure 5.4c)).

After creating the superposition, we start the exposure to 854 nm photons and open the gates for all detectors. Additionally, we keep track of the time τ_D between the exposure start and the detection of a herald. In the case of the LST, the laser pulses start at a random delay within the window.

Table 5.1: Timings of the different pulses and detection windows in the teleportation sequence.

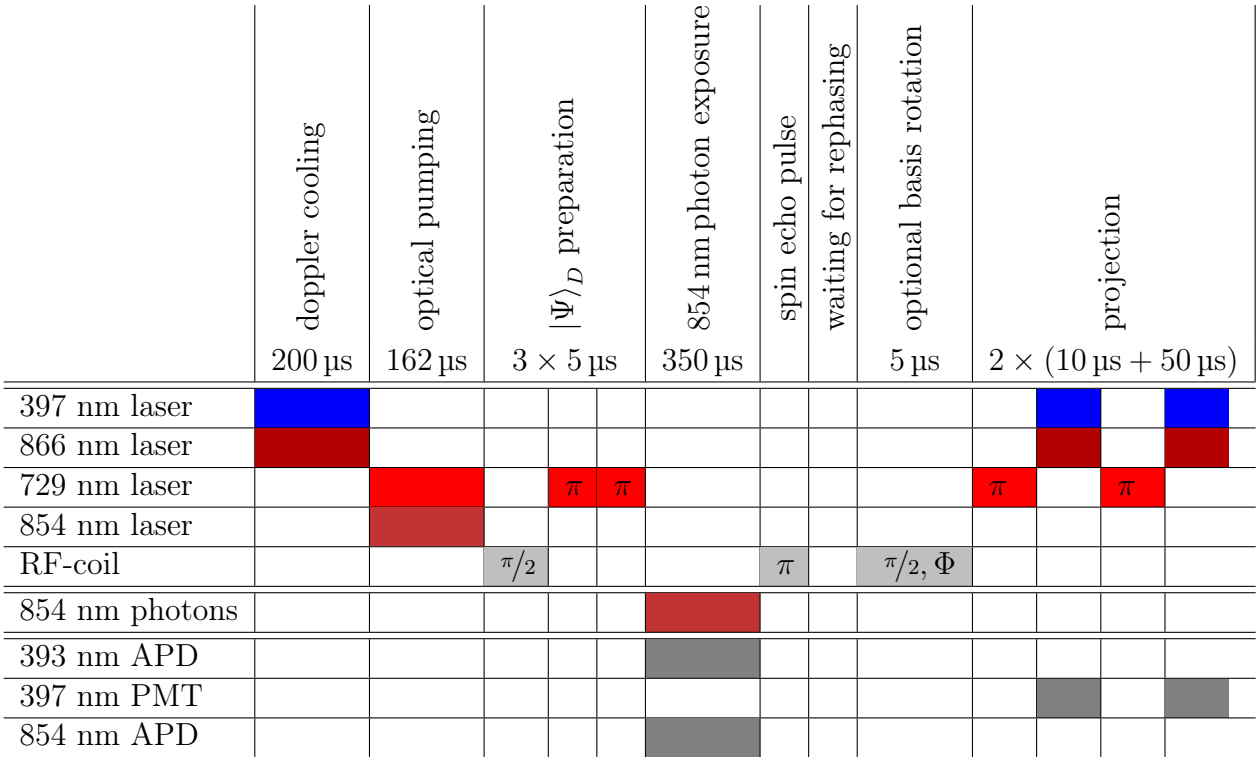

If we detect a 393 nm photon, we abort the waiting, stop the watch and apply an RF π spin-echo pulse. Then, we wait $\tau_S = 3 \times \tau_D$ in order to wait for re-phasing. The factor of three comes from the differences in the Larmor frequency between the $D_{5/2}$ and the $S_{1/2}$ state. After the spin-echo waiting time, we apply an optional RF $\pi/2$-pulse. This pulse closes the spin-echo sequence and rotates the state for a tomography measurement.

Finally, we perform the projection and state readout. For this purpose, we first shelve the population of the $|S_{1/2}, m = -1/2\rangle$ state to the $|D_{5/2}, m = -3/2\rangle$ state and perform fluorescence detection. Then we shelve the population back and perform another fluorescence detection.

Triggering the spin-echo pulses directly by detecting a 393 nm photon is impossible with our electronics. Therefore, we check every 500 ns whether absorption has occurred. The loop time is chosen as an integer multiple of the difference between the two Larmor frequencies. This way, we avoid fractional phase accumulations.

5.1.2 Expected efficiencies

In the following section, we will shortly discuss the different contributions to the efficiency of the protocol. The main limitations of the protocol are the absorption efficiency of the 854 nm photon and the collection and detection efficiency of the 393 nm photon. Other parts of the total efficiency are the internal efficiency of the scheme itself and losses of the different components together with couplings to optical fibres.

Absorption efficiency of the 854 nm photons: The emission pattern of the ion has a dipole form. The HALO in front of the ion only collects a fraction of this pattern. Taken into account the solid-angle of the HALO we obtain an overlap of $\eta_\sigma = 6\,\%$ for the σ-transitions [89]. We send the photons via optical fibres to the trap, whose beam profile is, to a good approximation, Gaussian. The ion only accepts light within its dipole pattern from which only a part is covered by the HALO. If the beam waist of the incoming beam fits the radius of aperture of the HALO, the overlap of the incoming light with the fraction of the dipole pattern is estimated as $\eta_{\mathrm{SM}} \approx 40\,\%$ [84]. The oscillator strength, given by the Einstein coefficients $A_{854}/\Gamma = 5.87\,\%$, is the third contribution to the absorption efficiency. Hence the maximal reachable absorption efficiency is

$$\eta_{\mathrm{abs},854} = \eta_{SM}\eta_\sigma \frac{A_{854}}{\Gamma} = 1.41 \times 10^{-3} \tag{5.19}$$

Collection and detection efficiency of the 393 nm photons: The heralds are collected via the second HALO and are projected via a Wollaston prism. Finally, we send them to a free-space APD with a quantum efficiency of $\eta_{APD,393} \approx 55\,\%$. Losses are much bigger in the blue wavelength range, and we expect them to be in the range of 10 %. So the detection efficiency for the blue photons is

$$\eta_{\mathrm{det},393} = \eta_\sigma \eta_{\mathrm{APD},393} \eta_{\mathrm{loss},393} = 2.97\,\% \tag{5.20}$$

Internal efficiency: As mentioned earlier the branching ratio of the $P_{3/2}$ state plays an essential role for the protocol. The first part of the internal efficiency is therefore $A_{393}/\Gamma = 93.47\,\%$.

Nevertheless, without the *second* passage, the main contribution comes from the fact that the ion only absorbs 50 % of the incoming polarisation. The second passage enables us to recover this 50 % for an ideal setup. To show this, we expand the Raman process operator

for the *first* passage (equation (5.17)) and *second* passage (equation (5.18)) by a term for the unabsorbed photons:

$$\hat{\mathrm{O}}^{1^{\mathrm{st}}}_{B,D} = \hat{\mathrm{R}}^{1^{\mathrm{st}}}_{B,D} + |R\rangle_B |{+5/2}\rangle_D \langle R|_B \langle {+5/2}|_D + |L\rangle_B |{-5/2}\rangle_D \langle L|_B \langle {-5/2}|_D \tag{5.21}$$

$$\hat{\mathrm{O}}^{2^{\mathrm{nd}}}_{B,D} = \hat{\mathrm{R}}^{2^{\mathrm{nd}}}_{B,D} + |R\rangle_B |{-5/2}\rangle_D \langle R|_B \langle {-5/2}|_D + |L\rangle_B |{+5/2}\rangle_D \langle L|_B \langle {+5/2}|_D \tag{5.22}$$

We start the derivation with the absorption of a photon in state $|\Psi\rangle$ (equation (5.2)) from the ion in state $|\phi\rangle$ (equation (5.1)). The joint state of the system is

$$\begin{aligned} |A\rangle = |\phi\rangle |\Psi\rangle = \alpha\gamma |R\rangle_B |{-5/2}\rangle_D + \beta e^{i\omega_D t}\gamma |R\rangle_B |{+5/2}\rangle_D \\ + \alpha\delta |L\rangle_B |{-5/2}\rangle_D + \beta e^{i\omega_D t}\delta |L\rangle_B |{+5/2}\rangle_D \end{aligned} \tag{5.23}$$

on which we apply the Raman operator for the *first* passage. The result is an absorbed and an unabsorbed part of the form

$$\begin{aligned} \hat{\mathrm{O}}^{1^{\mathrm{st}}}_{B,D} |A\rangle = \underbrace{\alpha\gamma |L\rangle_{393} |{-1/2}\rangle_S + \beta e^{i\omega_D t}\delta |R\rangle_{393} |{+1/2}\rangle_S}_{=|\Psi\rangle_{abs}} \\ + \underbrace{\beta e^{i\omega_D t}\gamma |R\rangle_B |{+5/2}\rangle_D + \alpha\delta |L\rangle_B |{-5/2}\rangle_D}_{=|\Psi\rangle_{nonabs}} \end{aligned} \tag{5.24}$$

We directly calculate the absorption probability from the absorbed part by projecting the herald and the ion. The teleportation measurement schema describes the details (section 6.2). We get the four combinations

$$\langle +| \langle H|\phi\rangle_{abs} = \frac{1}{2}\left(\alpha\gamma + \beta e^{i\omega_D t}\delta\right) \tag{5.25}$$

$$\langle +| \langle V|\phi\rangle_{abs} = \frac{1}{2i}\left(-\alpha\gamma + \beta e^{i\omega_D t}\delta\right) \tag{5.26}$$

$$\langle -| \langle H|\phi\rangle_{abs} = \frac{1}{2i}\left(\alpha\gamma - \beta e^{i\omega_D t}\delta\right) \tag{5.27}$$

$$\langle -| \langle V|\phi\rangle_{abs} = \frac{1}{2}\left(\alpha\gamma + \beta e^{i\omega_D t}\delta\right) \tag{5.28}$$

The absorption probability for the *first* passage is then given by

$$\begin{aligned} P^{1^{\mathrm{st}}}_{abs} &= \left|\langle +| \langle H|\phi\rangle_{abs}\right|^2 + \left|\langle +| \langle V|\phi\rangle_{abs}\right|^2 + \left|\langle -| \langle H|\phi\rangle_{abs}\right|^2 + \left|\langle -| \langle V|\phi\rangle_{abs}\right|^2 \\ &= \frac{1}{2}\left(\left|\alpha\gamma + \beta e^{i\omega_D t}\delta\right|^2 + \left|\alpha\gamma - \beta e^{i\omega_D t}\delta\right|^2\right) \end{aligned}$$

$$= \alpha^2\gamma^2 + \beta^2\delta^2 \tag{5.29}$$

The equation shows that we get a maximal achievable absorption probability of 50 % for the superposition with $\alpha = \beta = 1/\sqrt{2}$.

For the *second* passage, we apply the corresponding Raman operator and get the output state

$$\hat{\mathrm{O}}^{2^{\mathrm{nd}}}_{B,D} \left|\phi\right\rangle_{nonabs} = \alpha\delta \left|L\right\rangle_{393} \left|-1/2\right\rangle_S + \beta e^{i\omega_D t}\gamma \left|R\right\rangle_{393} \left|+1/2\right\rangle_S \tag{5.30}$$

The equation shows that the photon will be absorbed in the second passage, no matter the Larmor phase or time delay between the *first* and the *second* passage. Finally, we project the herald and the atom and get the four results

$$\left\langle +\right| \left\langle H|\phi\right\rangle_{abs} = \frac{1}{2}\left(\alpha\delta + \beta e^{i\omega_D t}\gamma\right) \tag{5.31}$$

$$\left\langle +\right| \left\langle V|\phi\right\rangle_{abs} = \frac{1}{2i}\left(-\alpha\delta + \beta e^{i\omega_D t}\gamma\right) \tag{5.32}$$

$$\left\langle -\right| \left\langle H|\phi\right\rangle_{abs} = \frac{1}{2i}\left(\alpha\delta - \beta e^{i\omega_D t}\gamma\right) \tag{5.33}$$

$$\left\langle -\right| \left\langle V|\phi\right\rangle_{abs} = \frac{1}{2}\left(\alpha\delta + \beta e^{i\omega_D t}\gamma\right) \tag{5.34}$$

The absorption probability for the *second* passage is then:

$$\begin{aligned} P^{2^{\mathrm{nd}}}_{abs} &= \left|\left\langle +\right| \left\langle H|\phi\right\rangle_{nonabs}\right|^2 + \left|\left\langle +\right| \left\langle V|\phi\right\rangle_{nonabs}\right|^2 + \left|\left\langle -\right| \left\langle H|\phi\right\rangle_{nonabs}\right|^2 + \left|\left\langle -\right| \left\langle V|\phi\right\rangle_{nonabs}\right|^2 \\ &= \frac{1}{2}\left(\left|\alpha\delta + \beta e^{i\omega_D t}\gamma\right|^2 + \left|\alpha\delta - \beta e^{i\omega_D t}\gamma\right|^2\right) \\ &= \alpha^2\delta^2 + \beta^2\gamma^2 \end{aligned} \tag{5.35}$$

We again get an absorption probability of 50 % for the equal superposition. In total, we get an absorption probability of

$$P = P^{1^{\mathrm{st}}}_{abs} + P^{2^{\mathrm{nd}}}_{abs} = 1 \tag{5.36}$$

and by that, double the intrinsic efficiency of our protocol.

For the actual experiment, the efficiency of the back-reflection part is limited by the collection efficiency of the fibre coupling. The second HALO is placed for the optimal collection of the heralds. However, we also use it to collect the transmitted 854 nm photons. This shifted position cuts the beam and leads to some aberrations, which reduce the fibre

coupling efficiency. The maximal reachable fibre coupling from the second HALO to the fibre is $\eta_{\mathrm{HALO/fiber}} = 40\,\%$ and enters twice into the efficiency. We use a partially transmitting mirror (R=98 %) as a retroreflector which is pressed to a physical contact (PC) fibre connector end. This gives an efficiency of $\eta_{\mathrm{BR}} = 90\,\%$. Together, we get a total efficiency of the back-reflection part of

$$\eta_{\mathrm{back}} = \eta^2_{\mathrm{HALO/fiber}}\eta_{\mathrm{BR}} = 14.4\,\%\,. \tag{5.37}$$

The total protocol efficiency is therefore expected to be

$$\eta_{\mathrm{total,1^{st}}} = \underbrace{\eta_{SM}\eta_\sigma\frac{A_{854}}{\Gamma}}_{854}\underbrace{0.5\frac{A_{393}}{\Gamma}}_{\text{internal}}\underbrace{\eta_\sigma\eta_{\mathrm{APD,393}}\eta_{\mathrm{loss,393}}}_{393} \approx 1.96\times10^{-5} \tag{5.38}$$

$$\eta_{\mathrm{total,2^{nd}}} = \underbrace{\eta_{SM}\eta_\sigma\frac{A_{854}}{\Gamma}}_{854}\underbrace{\eta_{\mathrm{back}}\frac{A_{393}}{\Gamma}}_{\text{internal}}\underbrace{\eta_\sigma\eta_{\mathrm{APD,393}}\eta_{\mathrm{loss,393}}}_{393} \approx 5.64\times10^{-6} \tag{5.39}$$

5.2 Characterisation measurements

Two characterisation measurements are performed before each experiment to check for the best performance.

Ramsey experiment: The first measurement quantifies the magnetic field fluctuation and, by this, the coherence time of the ion in the $D_{5/2}$ state. For reference, we also repeat this measurement without the 729 nm pulses. The sequence is the following:

1. We start with optical pumping to the $|S_{1/2}, m = -1/2\rangle$ state and apply an RF $\pi/2$-pulse afterwards. The pulses create an equal superposition in the ground state.
2. Two subsequent π-pulses at 729 nm transfer this superposition to the outer $D_{5/2}$ Zeeman sublevels.
3. After a certain waiting time, which is our scanning parameter, we transfer the population back to the $S_{1/2}$ state with two π-pulses at 729 nm.
4. Then we apply a spin-echo RF π pulse and wait three times the scanning parameter.
5. After the rephasing, we apply the second RF $\pi/2$-pulse with a variable phase offset which finishes the Ramsey sequence.

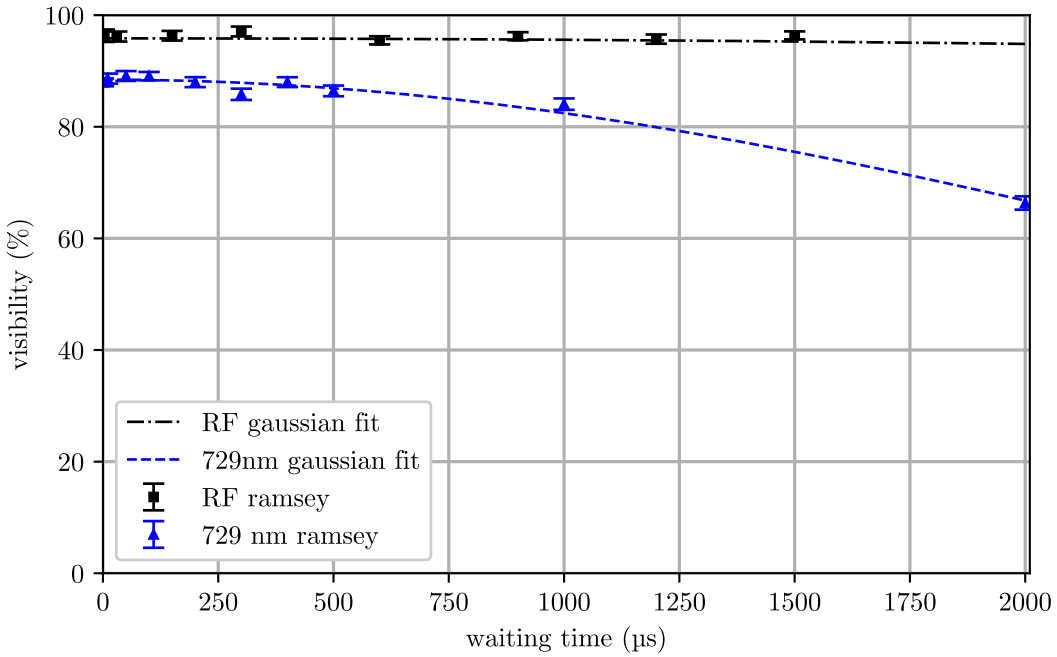

Figure 5.5: Visibility of the RF and 729 nm Ramsey measurement. The black dots are the measurement values, and the black dot-dashed line is a Gaussian fit to the data. The blue values correspond to the 729nm visibility, and the blue dashed line is a Gaussian fit. From the fit we extract the $1/e$ visibility to be 13.79 ms for the RF and 2.67 ms for the 729 nm measurement.

6. Finally, we perform state projection on the $S_{1/2}$ state using the previously described electron shelving technique with fluorescence detection.

We scan the phase between 0° and 360° for every waiting time in the excited state. From the resulting fringe, we extract the visibility. Figure 5.5 shows a typical result. From a Gaussian fit, we determine the coherence time [140]. The $1/e$ coherence time for the 729 nm Ramsey is 2.67 ms and for the RF Ramsey it is 13.79 ms. The plot shows that the curves do not start at 1. We identify imperfections of the π pulses at 729 nm, resulting from power fluctuations and sidebands in the laser spectrum, as the main reason for this. The pulse efficiency of the 729 nm pulses is typically in the range of 98 %.

The plot shows that the 729 nm visibility is almost constant in the range between 0 and 500 µs. The exposure time in the experiments is within this time range.

393 nm detection efficiency: The second measurement determines the detection efficiency of the 393 nm photons, which includes the detector efficiency, the collection

efficiency of the HALO and losses in the optical components. After the Doppler cooling we apply a 729 nm π-pulse on the $|S_{1/2}, m = -1/2\rangle$ to $|D_{5/2}, m = -5/2\rangle$ transition. After that, we switch on the 854 nm laser. The pulse is chosen long enough that we ensure the generation of a 393 nm photon. The 393 nm is projected and detected, as in the measurement protocol. To calculate the efficiency, we compare the number of detected 393 nm photons with the number of generated photons. The number of generated photons is given by the number of preparations and the photon generation efficiency. We get an efficiency of 1.61 %, which contains the collection efficiency, all coupling efficiencies, transmission losses and the quantum efficiency of the detector.

5.3 Laser state transfer

As proof of principle measurement of the newly implemented back-reflection part, we first perform a laser state transfer[18] with 854 nm laser pulses instead of single photons.

5.3.1 State reconstruction

We verify the photon-to-atom state mapping by sending light with fixed polarisation $\{\ |H\rangle,\ |V\rangle,\ |D\rangle,\ |A\rangle,\ |R\rangle,\ |L\rangle\ \}$ and performing quantum-state tomography of the atomic ground-state qubit for each of these input polarisations. Out of the data, we can reconstruct the atomic quantum state with the method described below.

We describe the atom in the basis $\{\ |-\rangle = |S_{1/2}, m = -1/2\rangle,\ |+\rangle = |S_{1/2}, m = +1/2\rangle\ \}$. The density matrix in this basis is then

$$\hat{\rho} = \alpha\,|-\rangle\langle-| + \beta\,|+\rangle\langle+| + \gamma\,|-\rangle\langle+| + \gamma*\,|+\rangle\langle-| = \begin{pmatrix} \alpha & \gamma \\ \gamma* & \beta \end{pmatrix} \tag{5.40}$$

and is reconstructed by two measurements. In the first measurement, we get the diagonal elements by projecting on the eigenstates $|+\rangle$ and $|-\rangle$. The second measurement projects the ion onto the superposition state

$$|\Psi(\Phi)\rangle = \frac{1}{\sqrt{2}}\left(|-\rangle + e^{\mathrm{i}\Phi}\,|+\rangle\right) \tag{5.41}$$

The superposition state is produced by the mentioned optional RF $\pi/2$ pulse after the spin-echo waiting time and before the projection. As explained earlier, phase Φ consists

of a constant and oscillating part. The oscillating part $\Delta\Phi$ is determined by the product between the effective Larmor frequency and the time difference between the preparation of the superposition in $D_{5/2}$ and the detection of the 393 nm photon. The effective Larmor frequency is measured independently, and we perform spectroscopies of all relevant transitions between different measurement runs. A phase histogram of all detected events for each polarisation reveals a sinusoidal curve, which gives the probabilities for each phase difference

Fitting the described phase histogram by a sinusoidal function

$$P(V, \Delta\Phi, \Phi_0) = \frac{1 + V \sin(\Delta\Phi - \Phi_0)}{2} \tag{5.42}$$

gives the visibility V and an offset phase Φ_0. The phase difference and superposition phase are related by $\Delta\Phi = \Phi + \pi/2$. We then rewrite (5.42) to

$$P(V, \Phi, \Phi_0) = \frac{1 + V \cos(\Phi - \Phi_0)}{2} \tag{5.43}$$

Putting together the probabilities at $\Phi = 0$ and $\Phi = \pi/2$ and the expectation values of the density matrix gives

$$\langle\Psi(0)|\,\hat{\rho}\,|\Psi(0)\rangle = \frac{\alpha + \beta}{2} + \Re(\gamma) \qquad \text{and} \qquad \langle\Psi(\pi/2)|\,\hat{\rho}\,|\Psi(\pi/2)\rangle = \frac{\alpha + \beta}{2} + \Im(\gamma) \tag{5.44}$$

Using the fact that the trace of a density matrix equals one gives us

$$\gamma = \Re(\gamma) + \mathrm{i}\Im(\gamma) = \frac{V}{2} \exp(\mathrm{i}\Phi_0) \tag{5.45}$$

Fitting a sinusoidal function to binned data leads to an intrinsic reduction in visibility. To take this into account, we use an adjusted fit function of the form

$$P(V, \Phi, \Phi_0) = \frac{V}{2} \frac{N}{\pi} \sin\left(\frac{\pi}{N}\right) \sin(\Delta\Phi - \Phi_0) + \frac{1}{2} \tag{5.46}$$

with the number of bins N, in the corrected data.

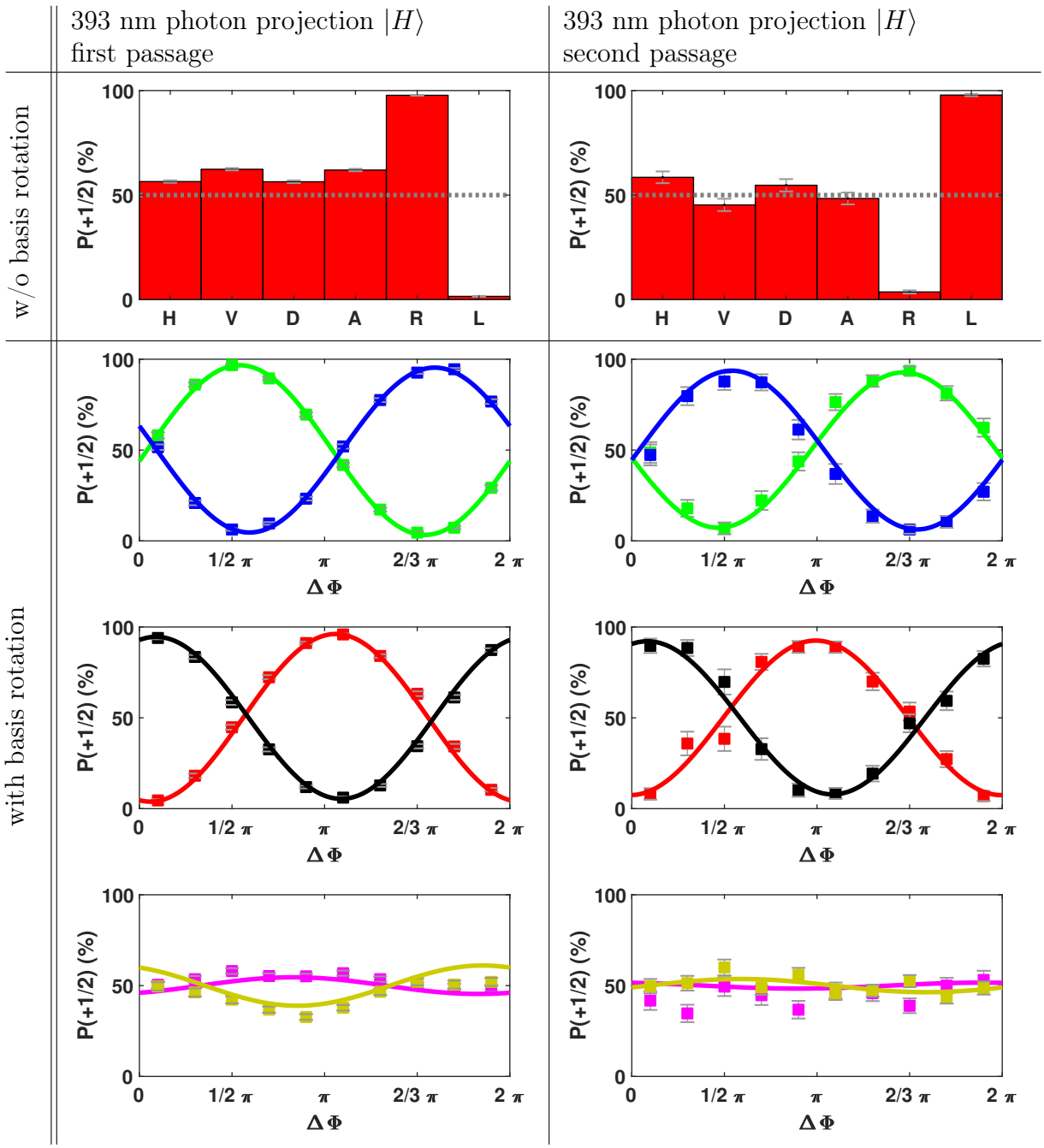

Figure 5.6: Measurement results for the LST for *first* and *second* passage. The first row is without RF $\pi/2$ pulse and thus the projection to the eigenstates. The other rows show the oscillations due to the Larmor precession. Second row: green $|H\rangle$ / blue $|V\rangle$, third row: red $|D\rangle$ / black $|A\rangle$, last row: magenta $|R\rangle$ / yellow $|L\rangle$.

5.3.2 Results

The results for the measurement are shown in table 5.6, where the probability to detect the ion in the $|S_{1/2}, m = +1/2\rangle$ state is plotted. The left column shows the data for the *first* passage, and the second column for the *second* passage. We set the phase offset for the $|H\rangle$ polarisation for the *first* passage, as well as for the $|V\rangle$ polarisation for the *second* passage, to zero. We then use these common offsets for the remaining evaluations.

The first row shows the projections on the eigenstate without the RF pulse. This measurement gives us the diagonal elements α and β of the density matrix in equation (5.40). For the linear input polarisations, the values are close to the ideal value of 50 % and for the circular polarisations near zero and one, respectively.

The other rows are for the different orthogonal pairs of input polarisation and show oscillations with the Larmor phase. We extract the off-diagonal element γ from these measurements in the superposition basis. The solid line shows a fit to the data and gives us the visibility V and the phase offset Φ_0, which are listed in table B.1 of the Appendix. Orthogonal polarisations show a phase shift of $\sim \pi$ where between the different sets of polarisation, we see a phase-shift of $\sim \pi/2$. We get a mean visibility for all linear polarisation fringes of 91.9 % for the *first* and 87 % for the *second* passage. The circular polarisations show a residual oscillation with 14.7 % for the *first* and 6.75 % for the *second* passage. We do not expect any oscillation for the circular bases in the ideal case. The existence of oscillations in these is explained by a slight rotation of the input polarisation to the atomic reference frame and the polarisation effects of the optical elements.

The plots for the orthogonal polarisation projection of the 393 nm photons are found in figure B.3 of the Appendix.

From the above-shown probabilities, we reconstruct the process χ-matrix [141] via a maximum-likelihood (ML) algorithm. Using a ML algorithm has the advantage that the resulting density matrix is physical, which is not necessarily the case if one uses a linear reconstruction on noisy data. The resulting matrices in the $\{1, \sigma_x, \sigma_y, \sigma_z\}$ for the different projection settings and both passages are shown in figure 5.7. We identify the process fidelity as the value of the maximum peak and summarise the values in table 5.2.

Some further investigation for explaining the reduced visibility of the fringes and the reduced process fidelity will be given in section 5.4.4.

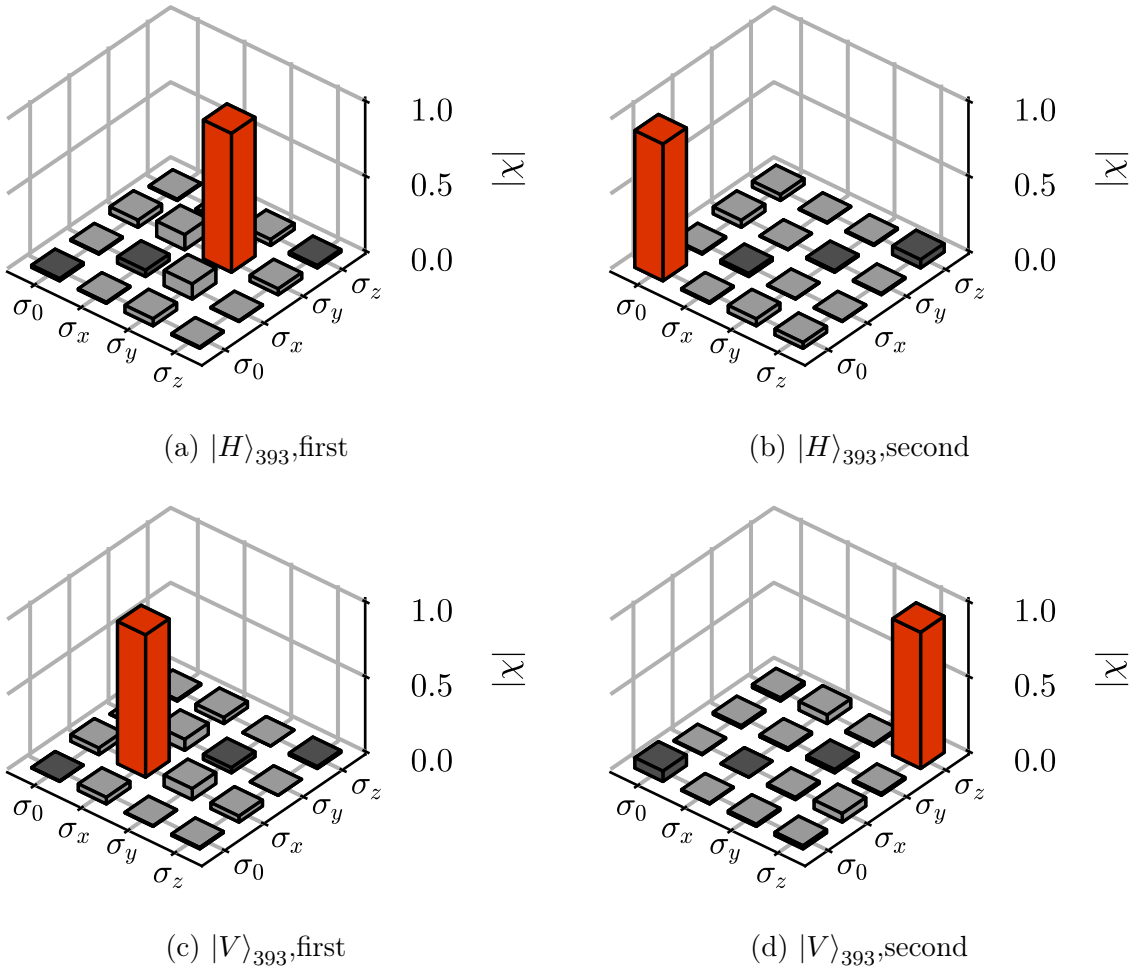

(a) $|H\rangle_{393}$,first

(b) $|H\rangle_{393}$,second

(c) $|V\rangle_{393}$,first

(d) $|V\rangle_{393}$,second

Figure 5.7: Reconstructed process matrix for the four different projection settings. (a) shows the projection of the 393 nm photon to H for the *first* passage and (b) for the *second* passage. Subfigure (c) is the projection of the 393 nm photon to V for the *first* passage and (d) for the *second* passage.

5.3.3 Summary

This experiment shows the functionality of the protocol. From the process matrices for the *second* passage, we see that the mapping of the polarisation ends in other states than in the *first* passage. This will later be used to get the complete four Bell state teleportation. The following section will use the same protocol with the photon pair source to realise a teleportation measurement.

Table 5.2: Summarised process fidelities for the LST measurement.

projection	fidelity
$\|H\rangle_{393}$,first	92.7 %
$\|V\rangle_{393}$,first	95.0 %
$\|H\rangle_{393}$,second	91.4 %
$\|V\rangle_{393}$,second	90.9 %

5.4 Entanglement transfer

The previously explained and tested protocol is now used with the photon pair source described in chapter 3 to transfer the entanglement between the two photons of a pair to atom-photon entanglement. The ion acts in receiver mode, and the protocol is an alternative to the direct atom-photon entanglement generation shown in [71].

In relation to the previous experiment, additional care must be taken regarding polarisation. The initial polarisation qubit is very sensitive to changes in the birefringence of the optical fibre guiding the photons from the source to the trap and the detectors. The data acquisition for the experiment runs for approximately two weeks, and the polarisation rotation has to be constant over the whole time. We use a reference laser and a reference path to check and compensate for the polarisation drifts. The polarisation is set with an in-fibre polarisation controller based on piezo actuators and a manual fibre paddle.

We measure three different settings. The first transfer creates entanglement between the ion and the partner photon directly, and the second setup converts the partner photon to the telecom wavelength range and thus creates entanglement between the ion and a telecom photon. The third setup also includes the QFC but sends the photons through a 13 km long metropolitan fibre. Therefore, photon detection happens in another part of the city. For the last setup, additional stabilisations of the polarisation have to be implemented.

The complete setup for the first set is shown in figure 5.8. One source output (B) is connected to a projection stage consisting of a half- and a quarter-waveplate and a Wollaston prism as a polariser. Both outputs of the prism are then detected by an APD. The other photon (A) of the pair is sent to the ion via a single-mode fibre. The mentioned controllers set the polarisation. Afterwards, the photons are focused on the ion via the HALO. After applying the protocol, we use the measurement results to characterise the joint atom-photon state between the photon and the ion.

The second setup is shown in figure 5.13. Photon B is now first sent to a QFC setup, where the wavelength is converted to 1550 nm. Afterwards, the photon is again projected by a projection stage consisting of a half- and a quarter-waveplate and a Wollaston prism as a polariser. Here both outputs are detected by SSPDs. Photon A is again sent to the ion. The setup is similar to the previously described one.

The third setup is shown in figure 5.16. Photon B is converted to the telecom wavelength range and sent to the HTW. The setup for photon A is identical to the previously described ones.

In the sections of this chapter, we will first describe how we reconstruct the ion-photon state and give details to the polarisation control. Details for stabilising the metropolitan fibre are found in chapter 4.3.1. Then we will show and discuss the results for the three different measurement setups.

5.4.1 State reconstruction

The evaluation steps needed for the reconstruction are very similar to the one for the LST. We need a topographically complete set of measurements, which are the 16 tensor products $\{\,\hat{\sigma}_i \otimes \hat{\sigma}_j \mid i,j = 0,\ldots,3\,\}$ of the Pauli spin operators [82, 129].

According to [82], we write the expectation value of the density matrix as

$$\langle \hat{\sigma}_i^{(\mathrm{ion})} \otimes \hat{\sigma}_j^{(\mathrm{ph})} \rangle_\rho = \mathrm{tr}\left(\hat{\sigma}_i^{(\mathrm{ion})} \otimes \hat{\sigma}_j^{(\mathrm{ph})} \rho\right) \tag{5.47}$$

$$= \lambda_{|0\rangle_j^{(\mathrm{ph})}} P(|0\rangle_j^{(\mathrm{ph})})\, \langle \hat{\sigma_i}^{(\mathrm{ion})} \rangle \Big|_{|0\rangle_j^{(\mathrm{ph})}} + \lambda_{|1\rangle_j^{(\mathrm{ph})}} P(|1\rangle_j^{(\mathrm{ph})})\, \langle \hat{\sigma_i}^{(\mathrm{ion})} \rangle \Big|_{|1\rangle_j^{(\mathrm{ph})}} \tag{5.48}$$

The eigenvalues $\lambda_{|0\rangle_j^{(\mathrm{ph})}}, \lambda_{|1\rangle_j^{(\mathrm{ph})}}$ correspond to the Pauli spin operators. The states $|0\rangle_j^{(\mathrm{ph})}$ and $|1\rangle_j^{(\mathrm{ph})}$ are the eigenstates, and $P(|0\rangle_j^{(\mathrm{ph})})$ and $P(|1\rangle_j^{(\mathrm{ph})})$ are the measured probabilities of detecting the qubit in the corresponding eigenstates. $\langle \hat{\sigma_i}^{(\mathrm{ion})} \rangle \Big|_{|0\rangle_j^{(\mathrm{ph})}}$ and $\langle \hat{\sigma_i}^{(\mathrm{ion})} \rangle \Big|_{|1\rangle_j^{(\mathrm{ph})}}$ are the conditioned mean values of the atomic spin operators under the condition that

the photonic qubit is measured in the $|0\rangle_j$ or $|1\rangle_j$ state. The so-defined expectation values are simplified, and we get

$$\langle \hat{\sigma_0}^{(\mathrm{ion})} \otimes \hat{\sigma_0}^{(\mathrm{ph})} \rangle = 1 \tag{5.49}$$

$$\langle \hat{\sigma_i}^{(\mathrm{ion})} \otimes \hat{\sigma_0}^{(\mathrm{ph})} \rangle = P(|0\rangle_j^{(\mathrm{ph})}) \langle \hat{\sigma_i} \rangle^{(\mathrm{ion})} \Big|_{|0\rangle_j^{(\mathrm{ph})}} + P(|1\rangle_j^{(\mathrm{ph})}) \langle \hat{\sigma_i} \rangle^{(\mathrm{ion})} \Big|_{|1\rangle_j^{(\mathrm{ph})}} \tag{5.50}$$

$$\langle \hat{\sigma_0}^{(\mathrm{ion})} \otimes \hat{\sigma_j}^{(\mathrm{ph})} \rangle = P(|0\rangle_j^{(\mathrm{ph})}) - P(|1\rangle_j^{(\mathrm{ph})}) \tag{5.51}$$

$$\langle \hat{\sigma_i}^{(\mathrm{ion})} \otimes \hat{\sigma_j}^{(\mathrm{ph})} \rangle = P(|0\rangle_j^{(\mathrm{ph})}) \langle \hat{\sigma_i} \rangle^{(\mathrm{ion})} \Big|_{|0\rangle_j^{(\mathrm{ph})}} - P(|1\rangle_j^{(\mathrm{ph})}) \langle \hat{\sigma_i} \rangle^{(\mathrm{ion})} \Big|_{|1\rangle_j^{(\mathrm{ph})}} \tag{5.52}$$

Using the method described in sec. 5.3.1 we reconstruct the atomic density matrix ρ_{at} under the condition of a photon detected in $|0\rangle_i$ or $|1\rangle_i$. Then we calculate the expectation value by $\langle \hat{\sigma_j} \rangle = \mathrm{tr}\left(\hat{\sigma_j} \rho_{at}\right)$.

The final atom-photon two-qubit density matrix is then given by

$$\rho = \frac{1}{4} \sum_{i,j=0}^{3} \langle \hat{\sigma}_i \otimes \hat{\sigma}_j \rangle_\rho \, \hat{\sigma}_i \otimes \hat{\sigma}_j \tag{5.53}$$

5.4.2 Polarisation control

We use two different techniques for polarisation control for the outputs of the source. We adjust the measurement basis for output B of the source (projection). The rotation matrix is measured with single photons via a single qubit tomography. For output A, we compensate the polarisation rotation induced by all components. The rotation is measured with the help of a reference laser and a polarimeter. More details are found in Appendix C.1.

5.4.3 Error correction

Our collected data is based on projective measurements in a defined basis. We estimate the probability p to detect the wanted state $|\phi\rangle$ and not the orthogonal state $|\phi_\perp\rangle$. To calculate this probability, we use a Bayesian approach [72, 82, 85]. We update the prior distribution with the finite number of measurements to get the posterior distribution of

p. Out of the distribution, we get the expectation value $\langle p \rangle$ and the standard deviation Δp. The advantage of the Bayesian approach is that

$$0 < \langle p \rangle < 1\,, \tag{5.54}$$

and the uncertainty is always larger than zero ($\Delta p > 0$). This approach can be used for several corrections of the measurement data, like background events, detection efficiencies or both together. A detailed description of the procedure is shown in [72]. For the entanglement transfer, we correct only for background events, similar to section 3.2.11, and in the case of the teleportation measurement, we additionally correct for the detection efficiency of the detectors.

This error correction method requires tremendous computational effort because several distributions must be evaluated. To face the problem of different amounts of data in the *first* and *second* passage, we rewrite the initial code of [72] in a more efficient programming language (C++) and use multi-threading where possible.

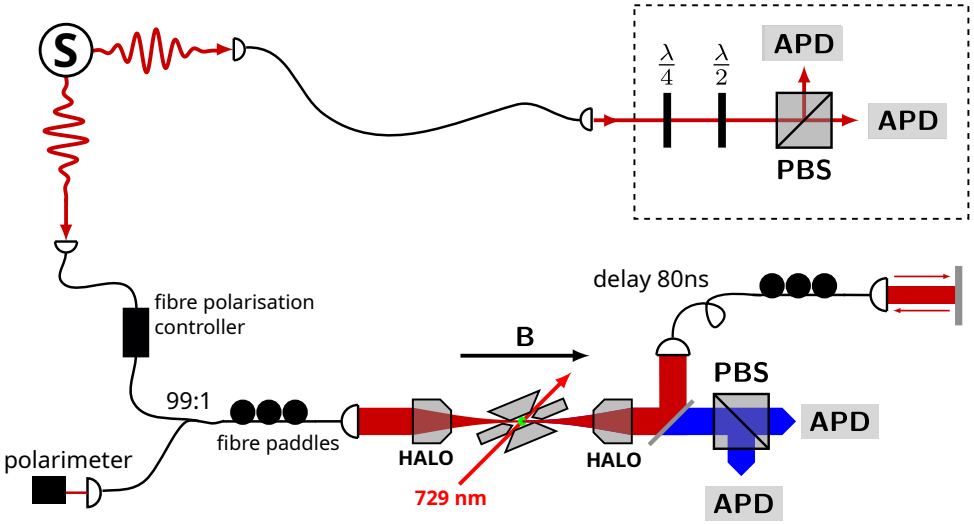

Figure 5.8: Experimental setup for the measurement. Photons from output port A of the source (S) are sent to the ion. Photons from port B are sent to a projection and detection setup. A fibre polarisation controller and a fibre paddle control the polarisation rotation on the path to the ion. A 99:1 beam splitter connects the reference polarimeter.

5.4.4 Entanglement transfer without conversion

For this experiment, we use a pump power of the source of 15 mW and an exposure window of 350 µs, which gives a good trade-off between measurement time, decoherence and expected final state fidelity. The average fidelity over the entire measurement time was $\langle\Psi^-|\,\hat{\rho}\,|\Psi^-\rangle = 91.64(2)\,\%$ and we expect no significant visibility reduction due to magnetic field fluctuation according to figure 5.5. The same measurement was also done with the $|\Psi^i\rangle = \frac{1}{\sqrt{2}}\left(|HV\rangle - i\,|VH\rangle\right)$ state as photonic input state. The results are presented in Appendix C.3. We perform a tomographic set of measurements on photon B and the ion to verify the entanglement. The projection setup is set to the six polarisations $\{\ |H\rangle_{854},\ |V\rangle_{854},\ |D\rangle_{854},\ |A\rangle_{854},\ |R\rangle_{854},\ |L\rangle_{854}\ \}$. As in the LST measurement, we perform the protocol with and without the optional RF pulse. We count clicks of the 393 nm and 854 nm APDs as coincidence if they lie in a window of ±84 ns, corresponding to 99 % of the two-photon wave-packet. Coincidences of the second passage are delayed by 160 ns and counted if they are within the same window size.

The results of the measurement are shown in figure 5.9, where the probability to detect the ion in $|S_{1/2}, m = +1/2\rangle$ is plotted. We combine the signal from both 393 nm detectors to increase the number of events. The data for each projection is shown in Appendix C.2.

Table 5.3: Phases and visibilities of the sinusoidal fits for the data shown in figure 5.9

projector	first passage				second passage			
	with correction		w/o correction		with correction		w/o correction	
	Phase (°)	Vis	Phase (°)	Vis	Phase (°)	Vis	Phase (°)	Vis
$\|H\rangle$	183(5)	0.75(5)	183(5)	0.68(5)	183(7)	0.80(8)	183(8)	0.41(5)
$\|V\rangle$	4(3)	0.76(4)	4(3)	0.68(3)	355(10)	0.8(1)	354(11)	0.38(7)
$\|D\rangle$	89(2)	0.59(2)	89(2)	0.55(2)	280(9)	0.41(6)	280(9)	0.26(4)
$\|A\rangle$	272(3)	0.67(3)	272(3)	0.62(3)	90(9)	0.46(7)	90(9)	0.29(4)
$\|R\rangle$	227(14)	0.10(2)	227(14)	0.09(2)	216(72)	0.2(2)	216(72)	0.1(1)
$\|L\rangle$	32(14)	0.16(4)	32(14)	0.15(4)	157(285)	0.1(3)	158(280)	0.0(1)

The left column shows the data for the *first* passage, and the right column for the *second* passage.

The red bars in the measurements of the eigenstates (first row) are with corrections, the grey ones without. Besides some deviations in the projection to $|H\rangle$, the result is near the ideal case discussed for the LST measurement. We also see that the error corrections make little to no difference for the *first* passage, as we have enough signal. For the *second* passage, we get much bigger error bars, and the error correction effect is much more significant. The number of signal events for the *second* passage is around 13 % of the ones from the *first* passage, which is in good agreement with the efficiency estimation.

The following rows in the figure correspond to the projection of a superposition state. The coloured points are the corrected data, whereas the grey ones are without corrections. The coloured solid lines are a sinusoidal fit to the corrected data, whereas the grey dashed line is the fit to the not corrected data. We get the visibility and the phase offset from the fit. The results are summarised in table 5.3. We observe the same phase shift between the different sets of polarisation as in the LST measurement.

We get a mean visibility for all linear polarisation fringes of 66.5 % with corrections (63.3 % without corrections) for the *first* and 60.8 % with correction (33.5 %) for the *second* passage. The circular polarisation show a residual oscillation with 12.5 % (12 % without corrections) for the *first* and 15 % (5 % without corrections) for the *second* passage.

We reconstruct the density matrices out of the results of the fit and the histograms, according to the described procedure in section 5.4.1. The reconstructed density matrix for the *first* and *second* passage are shown in figure 5.10. The fidelities and purities are summarised in table 5.4.

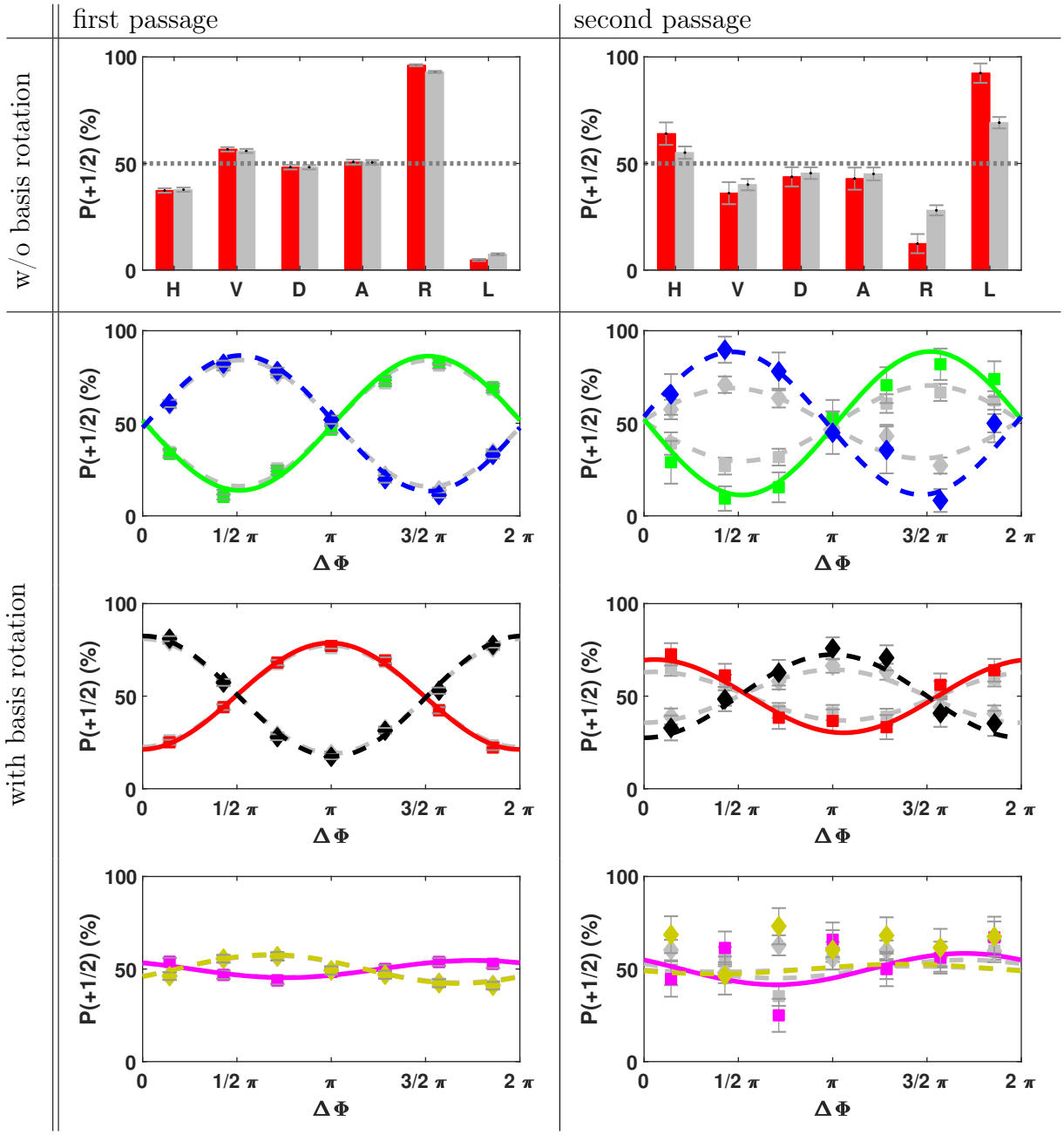

Figure 5.9: Measurement results for the photon-photon to atom-photon entanglement transfer evaluated for a waiting time of 350 µs for the *first* and *second* passage. The first row is without RF $\pi/2$-pulse. The other rows show oscillations due to the Larmor precession. Second row: green $|H\rangle$ / blue $|V\rangle$, third row: red $|D\rangle$ / black $|A\rangle$, last row: magenta $|R\rangle$ / yellow $|L\rangle$. Grey bars and lines show the data without corrections.

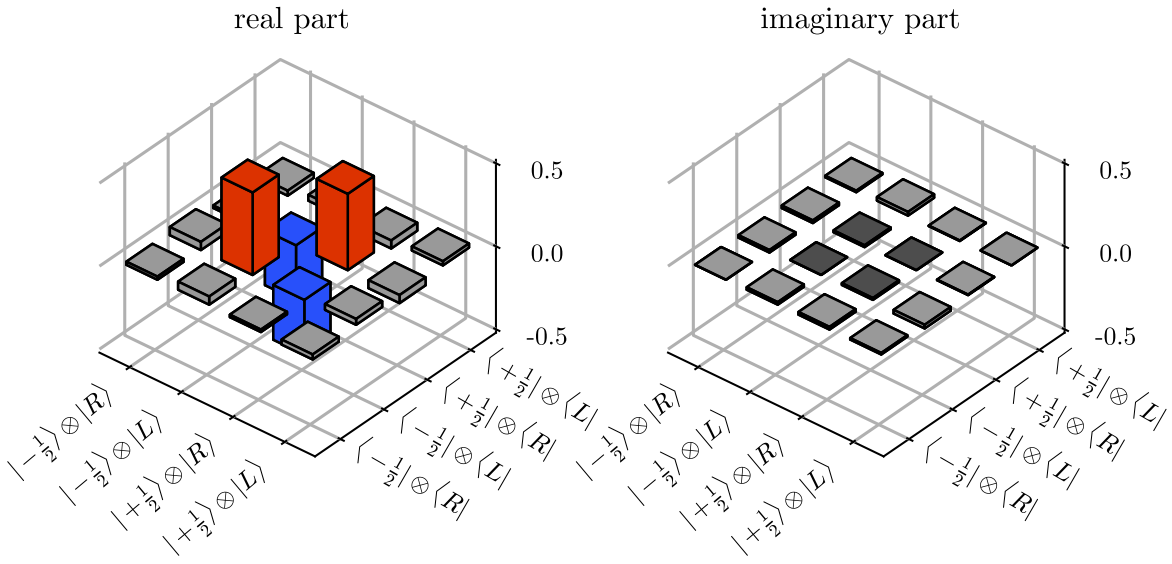

$$\begin{pmatrix} 0.019(3) & 0.049(4) & -0.016(9) & -0.03(1) \\ 0.049(4) & 0.497(3) & -0.35(1) & 0.036(9) \\ -0.016(9) & -0.35(1) & 0.460(3) & -0.048(4) \\ -0.03(1) & 0.036(9) & -0.048(4) & 0.025(3) \end{pmatrix} \qquad \begin{pmatrix} 0 & -0.015(2) & -0.017(4) & -0.010(5) \\ 0.015(2) & 0 & -0.011(5) & 0.022(4) \\ 0.017(4) & 0.011(5) & 0 & -0.003(2) \\ 0.010(5) & -0.022(4) & 0.003(2) & 0 \end{pmatrix}$$

(a) First passage

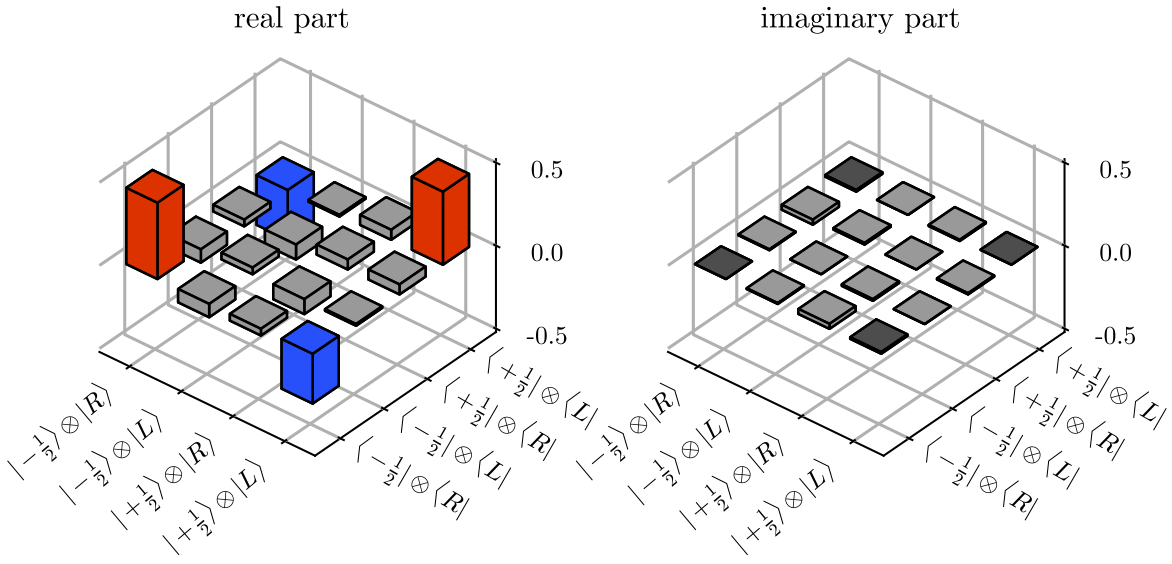

$$\begin{pmatrix} 0.46(2) & -0.08(2) & -0.04(7) & -0.31(2) \\ -0.08(2) & 0.04(2) & -0.09(2) & -0.01(7) \\ -0.04(7) & -0.09(2) & 0.06(2) & 0.06(2) \\ -0.31(2) & -0.01(7) & 0.06(2) & 0.44(2) \end{pmatrix} \qquad \begin{pmatrix} 0 & -0.005(7) & -0.03(3) & -0.01(1) \\ 0.005(7) & 0 & 0.01(1) & 0.01(3) \\ 0.03(3) & -0.01(1) & 0 & -0.007(7) \\ 0.01(1) & -0.01(3) & 0.007(7) & 0 \end{pmatrix}$$

(b) Second passage

Figure 5.10: Corrected reconstructed atom-photon density matrix for the *first* and *second* passage.

Table 5.4: Overview of the state fidelities and purities for a detection window size of 350 µs.

passage		with correction	w/o correction
first	fidelity	82.4(10)	78.0(9)
	purity	72(1)	65(1)
second	fidelity	76(2)	52(1)
	purity	64(5)	36(1)

Table 5.5: Overview of the state fidelities and purities for a detection window size of 50 µs.

passage		with correction	w/o correction
first	fidelity	89(2)	84(2)
	purity	83(3)	74(3)
second	fidelity	77(5)	
	purity	65(9)	

Discussion

In the following section, we will discuss some error sources which could explain the reduced fidelity and visibility.

First, we evaluate the entanglement transfer with events in the first 50 µs only. Figure 5.11 shows the results. We see a significant increase in visibility for the fringes of the *first* passage. The visibility of the fringes of the *second* passage and a projection to $|H\rangle$ / $|V\rangle$ slightly decrease, whereas the visibility for a projection to $|D\rangle$ / $|A\rangle$ increases. The insufficient signal counts explain this visibility reduction for the horizontal and vertical polarisations.

We get the fidelities and purities from a quantum state reconstruction summarised in table 5.5 . Due to the low signal, a not corrected reconstruction for the second passage was not possible. For the *first* passage, the fidelity increases by 6.7 % compared to the evaluation with a detection window of 350 µs. From the visibility of the Ramsey measurement, we infer the maximum process fidelity to 96 %. Together with the photon-state fidelity of 91.64(2) %, we expect a final state fidelity of 87 %. The reconstructed value for a waiting time of 50 µs agrees with this value.

To further investigate the problem, we vary the time offset from which measurement data is taken into account. The time window remains fixed at 50 µs. As mentioned above,

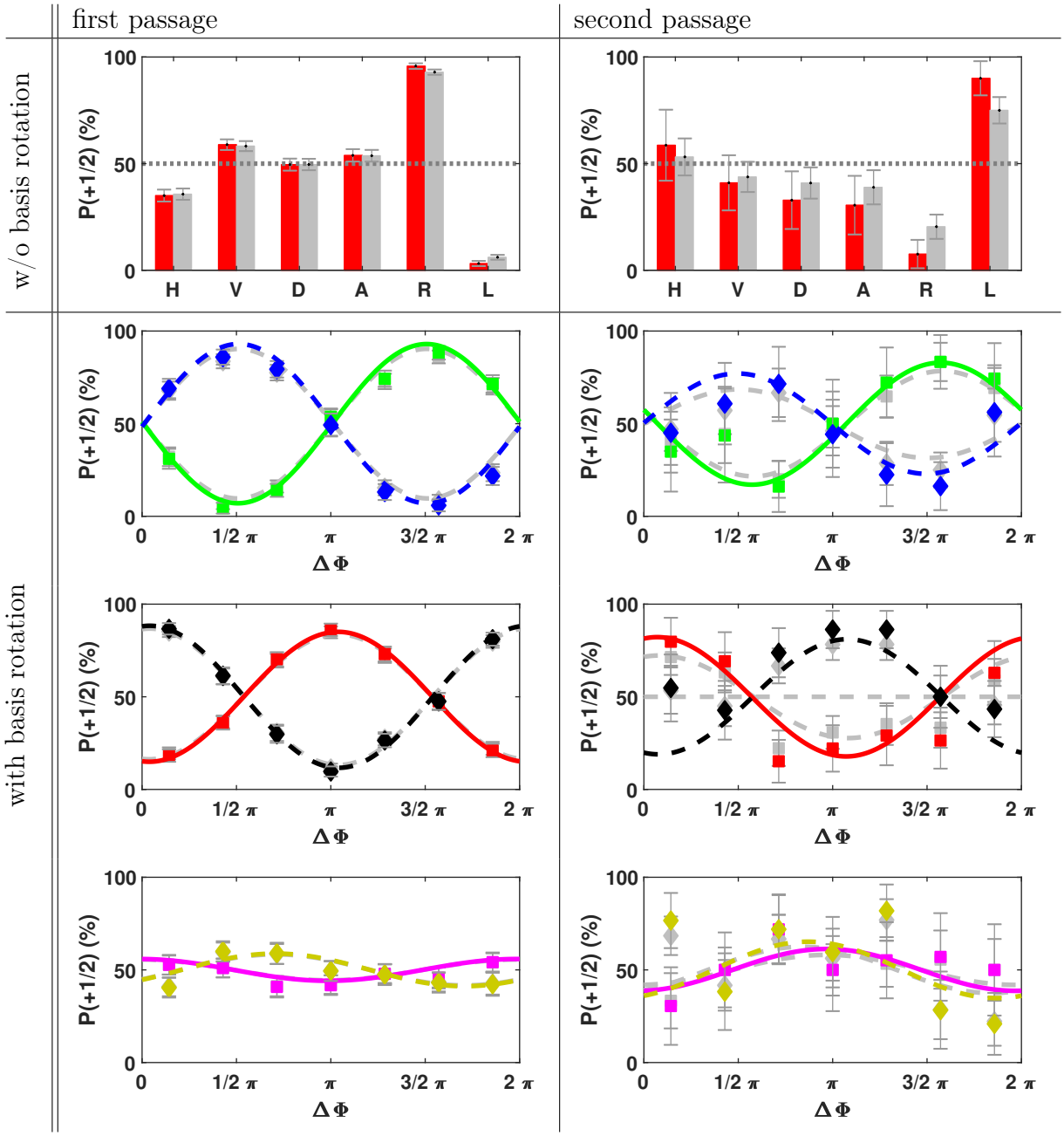

Figure 5.11: Measurement results for the photon-photon to atom-photon entanglement transfer evaluated for a waiting time of 50 µs for the *first* and *second* passage. The first row is without RF $\pi/2$-pulse. The other rows show oscillations due to the Larmor precession. Second row: green $|H\rangle$ / blue $|V\rangle$, third row: red $|D\rangle$ / black $|A\rangle$, last row: magenta $|R\rangle$ / yellow $|L\rangle$. Gray bars and lines show the data without corrections.

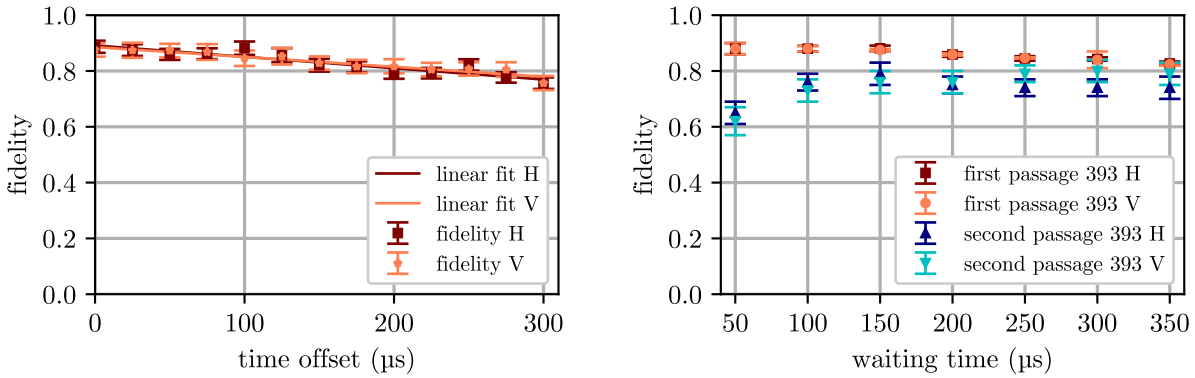

(a) Reconstructed fidelity depending on the time offset for a fixed waiting time of 50 µs

(b) Reconstructed fidelity depending on the waiting time.

Figure 5.12: Reconstructed fidelity for different waiting time and offset configurations. (a) shows the dependence on the time offset. The second passage is not plotted, because there is not enough data. In (b) we vary the waiting time.

we have insufficient signal events for the *second* passage. Therefore we exclude it in this analysis. The corresponding plot is shown in figure 5.12a. We observe a nearly linear decrease in fidelity with increasing time offset.

The same decrease in fidelity is observed if we vary the time window size instead of the time offset. The result is shown in figure 5.12b. For the *second* passage, we see an increase in fidelity first because the number of events increases. At a time window size of 150 µs we have the maximum fidelity for the *second* passage. After that, the fidelity decreases in the same way as in the *first* passage.

Therefore, we claim that the fidelity is mainly limited by decoherence due to magnetic field fluctuations, even though the effect is more substantial than expected from the Ramsey measurement.

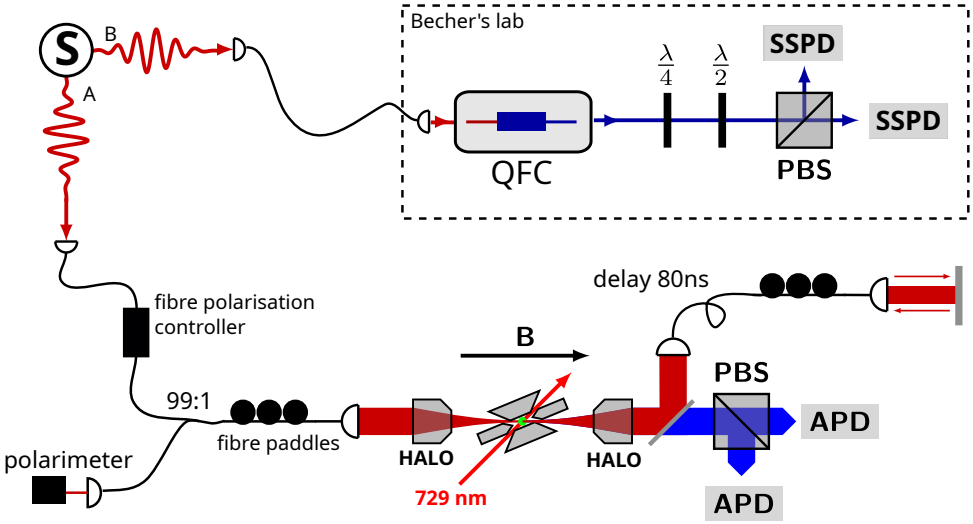

Figure 5.13: Experimental setup for the measurement with conversion. Photons from output port A of the source (S) are sent to the ion. Photons from port B are sent to a quantum frequency converter (QFC) and are then detected by a SSPD for each projection. A fibre polarisation controller and a fibre paddle control the polarisation rotation on the path to the ion. A 99:1 beam splitter connects the reference polarimeter.

5.4.5 Entanglement transfer with conversion to 1550 nm

For the reasons mentioned above, we use a source pump power of 15 mW, but we increase the exposure window to 400 µs. The average fidelity over the entire measurement time between the 854 nm photon and the 1550 nm photon was $\langle\Psi^-|\,\hat{\rho}\,|\Psi^-\rangle = 88.18(4)\,\%$, which is around 3 % lower than in the experiment without conversion. The deviation can be explained by a misalignment of a pump direction of the source. This was corrected during the measurement period. The projection setup is set to the six polarisations $\{\ |H\rangle_{1550},\ |V\rangle_{1550},\ |D\rangle_{1550},\ |A\rangle_{1550},\ |R\rangle_{1550},\ |L\rangle_{1550}\ \}$. We count clicks of the 393 nm APDs and the 1550 nm SSPDs as coincidence if they lie in a window of ±84 ns. The delay of the second passage does not change and is, therefore, still 160 ns.

The fibre connecting the source with the converter and the converter with the detectors is more unstable, than in the previous setup. Therefore, we measure a new rotation matrix approximately every 30 min in an automated way. Thereby the interferometer also relocks after this time and compensates for power drifts in the locking beam of the source.

Figure 5.14 shows the results for the measurement and the probability of detecting the ion

Table 5.6: Phases and visibilities of the sinusoidal fits for the data shown in figure 5.14.

projector	first passage				second passage			
	with correction		w/o correction		with correction		w/o correction	
	Phase (°)	Vis	Phase (°)	Vis	Phase (°)	Vis	Phase (°)	Vis
$\|H\rangle$	175(3)	0.78(4)	175(3)	0.68(3)	187(9)	0.87(10)	190(11)	0.37(7)
$\|V\rangle$	354(2)	0.76(2)	354(2)	0.66(2)	5(11)	0.8(1)	6(13)	0.33(7)
$\|D\rangle$	91(4)	0.69(4)	91(4)	0.61(4)	249(12)	0.8(1)	250(13)	0.31(7)
$\|A\rangle$	274(5)	0.73(5)	274(5)	0.65(4)	103(15)	0.5(1)	102(15)	0.23(6)
$\|R\rangle$	298(5)	0.21(2)	298(5)	0.19(2)	1(51)	0.2(1)	1(51)	0.08(7)
$\|L\rangle$	116(7)	0.20(3)	116(7)	0.18(2)	265(10)	0.35(6)	265(10)	0.19(4)

in the $|S_{1/2}, m = +1/2\rangle$ state. We combine the data for both 393 nm detectors to increase the signal. The data for each projection is shown in Appendix C.4.

The left column shows the data for the *first*, and the right column the data for the *second* passage. The first row shows the projection to the eigenstates, where the red bars are with corrections and the grey ones are without. For the first passage and a projection of the partner photon to $|H\rangle$- and $|A\rangle$ polarisation, we see some deviation from the ideal value of 50 %. Nearly the same deviation is seen in the orthogonal polarisation for the second passage, which is expected because we inverse the mapped polarisation inside the ion. A mismatch in the polarisation compensation and an imbalance of the source interferometer explain both deviations. The statistics for the second passage are much worse. Therefore, we see a more prominent effect of the error correction.

The other rows show the projection to the superposition state. The coloured points display the corrected data, and the grey ones the not corrected values. Fitting a sinusoidal function to the data gives the visibility V and the phase offset Φ_0. The summarised results for all fringes are shown in table 5.6. The observed phase shifts between the different sets of polarisations are the same as in the LST and the measurement without conversion. The phase of the fringes for a projected polarisation of $|D\rangle$ and $|A\rangle$ show some deviation caused by some polarisation mismatch of the back-reflection part.

For the *first* passage, we observe a mean corrected visibility for all linear polarisation fringes of 71.2 % (65 % without corrections). For the *second* passage, we get a mean corrected visibility of 71 % (31 % without corrections). The circular polarisations show a corrected residual visibility of 20.5 % (19.5 % without corrections) for the *first* and 27 % (13.5 % without corrections) for the *second* passage.

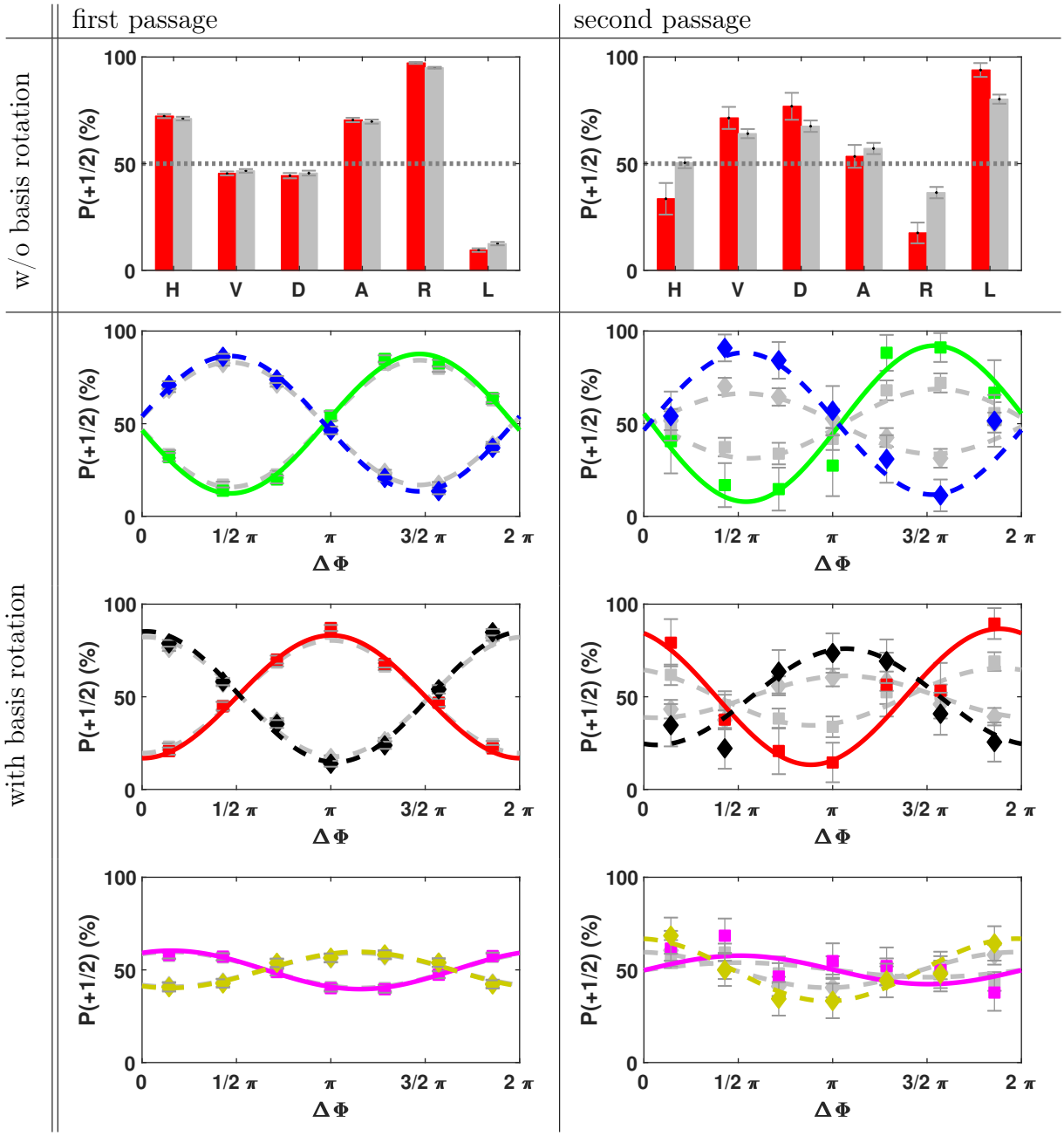

Figure 5.14: Measurement results for the photon-photon to atom-photon entanglement transfer with conversion evaluated for a waiting time of 400 µs for the *first* and *second* passage. The first row is without RF $\pi/2$-pulse. The other rows show oscillations due to the Larmor precession. Second row: green $|H\rangle$ / blue $|V\rangle$, third row: red $|D\rangle$ / black $|A\rangle$, last row: magenta $|R\rangle$ / yellow $|L\rangle$. Grey bars and lines show the data without corrections.

Table 5.7: Overview of the state fidelities and purities

passage		with correction	w/o correction
first	fidelity	84(1)	78.5(9)
	purity	81(2)	71(1)
second	fidelity	80(3)	51(2)
	purity	73(6)	36(1)

The results of the sinusoidal fits and the bar probabilities of the diagrams are then used to reconstruct the density matrix. The reconstructed density matrix for the *first* and *second* passage are shown in figure 5.15. Table 5.7 summarise the results for all the different settings. We get a corrected mean fidelity of 80.9 % (64.8 %). These values agree very well with the previous measurement, so we conclude that the conversion process induces no infidelity.

Discussion

The reconstructed density matrix in figure 5.15 reveals some imbalance between the two positive central peaks (red). This imbalance is explained as follow: (a) The two 854 nm detector channels showed a notable imbalance, which was corrected after the measurement for the entanglement transfer. (b) Over the measurement time for the entanglement transfer, one arm of the pump interferometer starts to misalign. The last mentioned point already leads to an imbalance between produced H and V photons in the photonic state, which is then transferred to the ion state. Nevertheless, the state fidelity with and without corrections is better than without conversion. The improvement in fidelity is explained by the improved polarisation stabilisation procedure and by periodic relocking of the pump interferometer of the source.

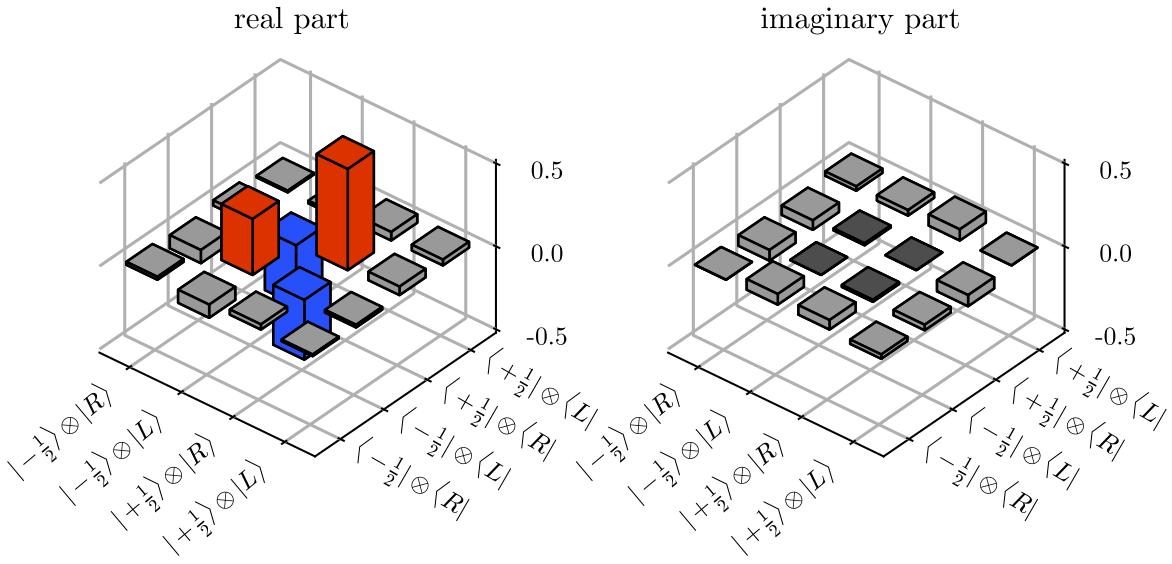

$$\begin{pmatrix} 0.018(4) & -0.079(4) & 0.032(6) & -0.01(1) \\ -0.079(4) & 0.338(4) & -0.37(1) & -0.017(6) \\ 0.032(6) & -0.37(1) & 0.610(4) & 0.051(4) \\ -0.01(1) & -0.017(6) & 0.051(4) & 0.035(4) \end{pmatrix} \qquad \begin{pmatrix} 0 & -0.064(2) & -0.059(2) & 0.027(6) \\ 0.064(2) & 0 & 0.012(6) & 0.034(2) \\ 0.059(2) & -0.012(6) & 0 & 0.067(2) \\ -0.027(6) & -0.034(2) & -0.067(2) & 0 \end{pmatrix}$$

(a) First passage

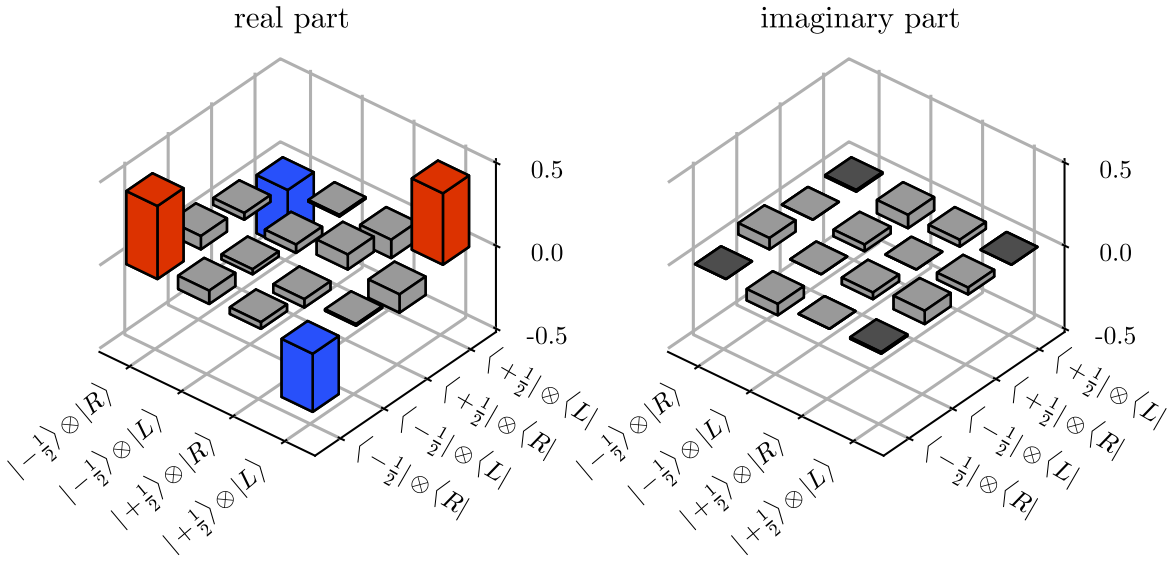

$$\begin{pmatrix} 0.44(2) & 0.08(2) & 0.04(3) & -0.36(4) \\ 0.08(2) & 0.03(2) & -0.05(4) & -0.01(3) \\ 0.04(3) & -0.05(4) & 0.09(2) & -0.11(2) \\ -0.36(4) & -0.01(3) & -0.11(2) & 0.43(2) \end{pmatrix} \qquad \begin{pmatrix} 0 & 0.068(9) & 0.00(1) & -0.01(2) \\ -0.068(9) & 0 & -0.04(2) & -0.08(1) \\ -0.00(1) & 0.04(2) & 0 & -0.041(9) \\ 0.01(2) & 0.08(1) & 0.041(9) & 0 \end{pmatrix}$$

(b) Second passage

Figure 5.15: Corrected reconstructed density matrix between ion and the 1550 nm photon for the *first* and *second* passage.

5.4.6 Entanglement transfer with conversion to 1550 nm and metropolitan fibre

In this experiment, we use a pump power of 15 mW and an exposure window of 400 µs. The initial photon-photon fidelity between one 854 nm photon and a 1550 nm photon detected at the HTW was $\langle\Psi^+|\,\hat{\rho}\,|\Psi^+\rangle = 83.6(3)\,\%$. The projection setup is set to the six polarisations $\{\ |H\rangle_{1550},\ |V\rangle_{1550},\ |D\rangle_{1550},\ |A\rangle_{1550},\ |R\rangle_{1550},\ |L\rangle_{1550}\}$. To classify two clicks as coincidence, we again use a window of ±84 ns. The delay for the second passage is again 160 ns.

As mentioned in chapter 4.3.1, the polarisation of the metropolitan fibre is only stable on a timescale of one minute. Therefore, we run a stabilisation process approximately every 40 s. To compensate for polarisation drifts over the whole path from source to the HTW, we measure a new rotation matrix every 30 minutes. In the stabilisation process, we also relock the interferometer of the source, compensating for power fluctuations of the locking beams.

The results of the measurement are shown in figure 5.17, as before we combine the data of both 393 nm detectors to increase the signal. The data for each detector is found in Appendix C.5. We depicted the probability to detect the ion in the $|S_{1/2}, m = +1/2\rangle$ state. We show only the data for the *first* passage. Due to a calibration error in the polarisation of the back-reflection, we do not see the expected behaviour for the *second* passage. The collected data for the *second* passage are nevertheless shown in the appendix (see figure C.16 and C.17). The projection to the eigenstates is shown in the first row. Red bars are with; grey bars are without corrections. The imbalance between the polarisations $|H\rangle$ and $|V\rangle$, as well as $|D\rangle$ and $|A\rangle$, is much smaller than in the measurement without the metropolitan fibre. The balance of the bars indicates that the polarisation calibration in this measurement run is more accurate than in the previously shown set.

The projections to the superpositions are shown in the following rows. Coloured points are corrected; grey ones are not corrected. As before, a sinusoidal fit reveals the visibility V and the phase offset Φ_0. We summarised the results for all fringes in table 5.8. The phase shift between the different sets of polarisations differs from the measurements before because we use the Ψ^+ state as input. In detail, this means the fringes for a projection of the partner photon to $|D\rangle$ and $|A\rangle$, as well as $|R\rangle$ and $|L\rangle$ are interchanged.

For all linear polarisation fringes, we observe a corrected mean visibility of 72.8 % (65.8 %

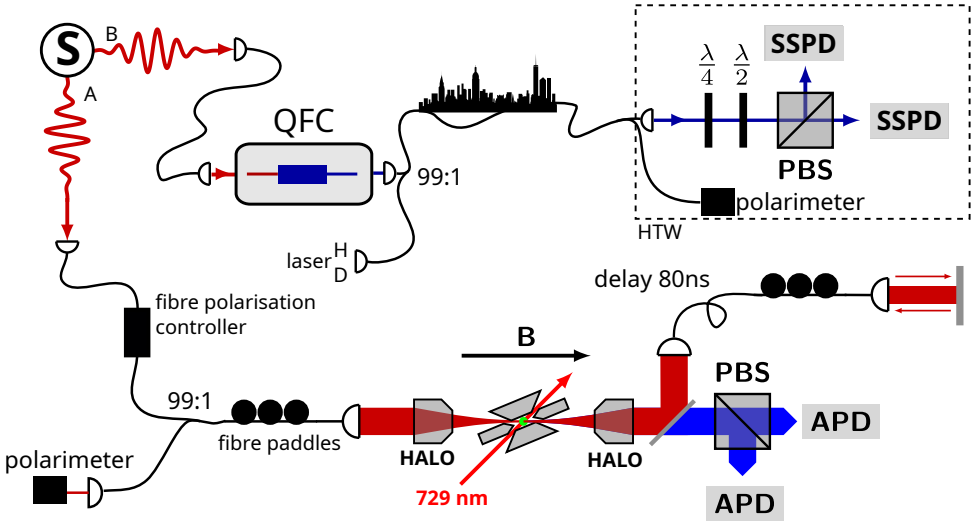

Figure 5.16: Experimental setup for the measurement with conversion and detection at the HTW. Photons from output port A of the source (S) are sent to the ion. A fibre polarisation controller and a fibre paddle control the polarisation on the path to the ion. A 99:1 beam splitter connects the reference polarimeter. Photons from port B are sent to a quantum frequency converter (QFC) and are then detected by a SSPD for each projection at the HTW after 14 km of metropolitan fibre. The fibre stabilisation lasers are inserted after the converter by a 99:1 beam splitter.

Table 5.8: Phases and visibilities of the sinusoidal fits for the data shown in figure 5.17.

projector	first passage			
	with correction		w/o correction	
	Phase (°)	Vis	Phase (°)	vis
$\|H\rangle$	169(5)	0.85(6)	169(5)	0.74(5)
$\|V\rangle$	345(8)	0.70(9)	345(8)	0.61(8)
$\|D\rangle$	247(5)	0.71(5)	247(5)	0.62(4)
$\|A\rangle$	73(8)	0.74(9)	73(8)	0.66(8)
$\|R\rangle$	32(48)	0.2(1)	32(48)	0.2(1)
$\|L\rangle$	284(50)	0.2(2)	284(50)	0.2(1)

without corrections). For the circular polarisations, we observe a corrected mean visibility of 20 % (20 % without corrections).

The results are shown in figure 5.17. We use this data to reconstruct the density matrix. The density matrix for the *first* passage is shown in figure 5.18. We summarise the results in table 5.9.

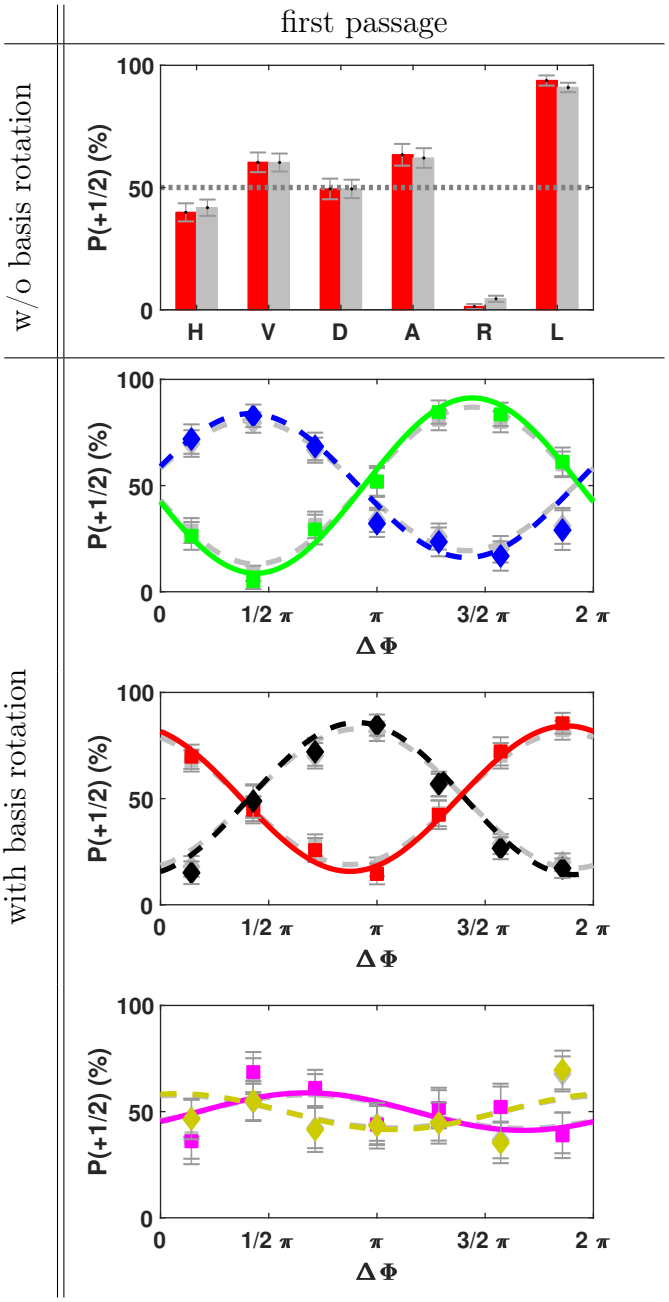

Figure 5.17: Measurement results for the photon-photon to atom-photon entanglement transfer to the HTW evaluated for a waiting time of 400 µs for the *first* passage only. The first row is without RF $\pi/2$-pulse. The other rows show oscillations due to the Larmor precession. Second row: green $|H\rangle$ / blue $|V\rangle$, third row: red $|D\rangle$ / black $|A\rangle$, last row: magenta $|R\rangle$ / yellow $|L\rangle$. Grey bars and lines show the data without corrections.

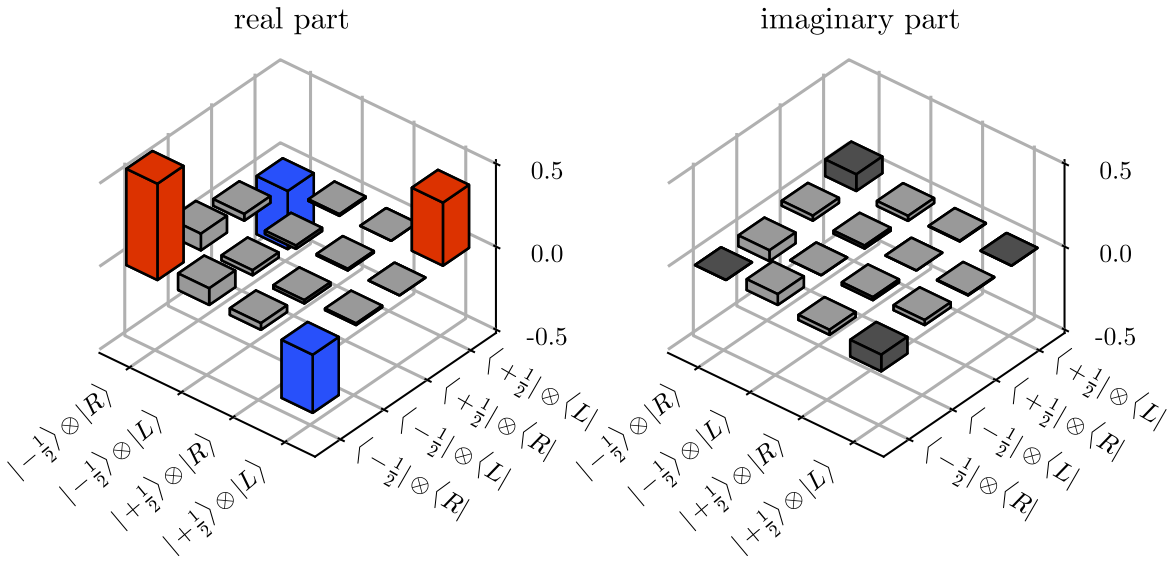

$$\begin{pmatrix} 0.58(1) & 0.10(2) & 0.04(4) & -0.35(2) \\ 0.10(2) & 0.03(1) & -0.02(2) & 0.01(4) \\ 0.04(4) & -0.02(2) & 0.01(1) & -0.00(2) \\ -0.35(2) & 0.01(4) & -0.00(2) & 0.38(1) \end{pmatrix} \quad \begin{pmatrix} 0 & -0.065(8) & 0.03(2) & 0.100(10) \\ 0.065(8) & 0 & -0.018(10) & -0.03(2) \\ -0.03(2) & 0.018(10) & 0 & -0.004(8) \\ -0.100(10) & 0.03(2) & 0.004(8) & 0 \end{pmatrix}$$

(a) First passage

Figure 5.18: Corrected reconstructed density matrix between ion and the 1550 nm photon detected at the HTW for the first passage.

Table 5.9: Overview of the state fidelities and purities

passage		with correction	w/o correction
first	fidelity	83(2)	79(2)
	purity	79(4)	71(3)

Discussion

The main limitation in this setup is the coincidence rate between detected 393 nm photons and 1550 nm photons. The photon rate at the HTW is in the range of $\sim 1500\,\mathrm{s}^{-1}$, which is approximately 1/30 of the rate of the previous measurement setup. The success probabilities and the number of coincidences are summarised in table 6.10. The mean polarisation fidelity of the metropolitan fibre was 99.4(8) %. Hence, we expect nearly no decreased fidelity due to the fibre drifts. The lower photon-photon fidelity is compensated by lower decoherence and better pulse efficiency of the 729 nm pulses, as seen by a Ramsey-

Table 5.10: Summary of the fidelities and purities of the entanglement transfer measurements for all three described settings.

passage		854 nm		1550 nm		1550 nm @ HTW	
		w corr.	w/o corr.	w corr.	w/o corr.	w corr.	w/o corr.
first	fidelity	82.4(10) %	78.0(9) %	84(1) %	78.5(9) %	83(2) %	79(2) %
	purity	72(1) %	65(1) %	81(2) %	71(1) %	79(4) %	71(3) %
second	fidelity	76(2) %	52(1) %	80(3) %	51(2) %		
	purity	64(5) %	36(1) %	73(6) %	36(1) %		

type experiment. Hence, the observed fidelity is nearly the same as in the measurement before.

5.5 Summary

In this chapter, we presented our protocol for transferring photon-photon entanglement to atom-photon entanglement. The protocol was performed in three different settings. In the first setting, we detected the partner photon in our labs. In the second setting, we included QFC to 1550 nm and detected the converted partner photon in the labs of the working group of Christoph Becher. In the last setup, we detected the converted partner photon after 14 km of metropolitan fibre at the HTW. The heralded absorption process thereby enables the protocol.

The resulting fidelities are all on the same level. We summarise the achieved fidelities and purities for the three settings in table 5.10. The high-efficiency quantum frequency converter thereby adds low background to the photon pair source. It thus enables the demonstrated quantum photonic interface in the low-loss, low-dispersion telecom wavelength range. It makes the connection of remote quantum network nodes based on $^{40}Ca^{+}$ single-ion memories possible. Furthermore, the fibre stabilisation enables the connection of remote quantum nodes over standard telecommunication fibres and adds nearly no infidelity to the transferred entanglement. The main limitation is the attenuation of the metropolitan fibre link, which only the provider can improve.

6 Quantum state teleportation

In this chapter, we show how to use the protocol presented in the previous chapter to realise quantum state teleportation [58]. The goal is the implementation of a full quantum state teleportation protocol, using all four Bell states, from a quantum bit at the UdS to one at the HTW. Similar to the previous chapter, we first carried out two simpler setups: the teleportation to a qubit at 854 nm in our labs and the teleportation to a qubit at 1550 nm in the labs of Christoph Becher, which includes QFC. The final setup includes QFC and the metropolitan fibre to teleport the qubit to the HTW.

In the first section of this chapter, we describe the general formalism of quantum state teleportation. In section 6.2, we map the general formalism to our system and show that the heralded absorption, together with a projection of the ion and the partner photon, constitutes a Bell-state measurement. In section 6.3, we show how our protocol is used to read out the atomic state by a teleportation measurement, employing the photon-pair source as a resource of entanglement. This technique is an alternative approach to the direct readout of the ion via the emission of a photon [15, 18]. The following measurement setup (section 6.4) is identical to the previous one, with the difference that the non-absorbed photon is now converted to the telecom range. This setup performs a direct readout to the telecom range and is the basis for quantum teleportation over long ranges. A real-world experiment is then reported in section 6.5. Here we use a metropolitan fibre that runs 14 km across Saarbrücken. The photon-pair source and the ion are placed at the UdS, whereas the detection happens at the HTW in Alt-Saarbrücken.

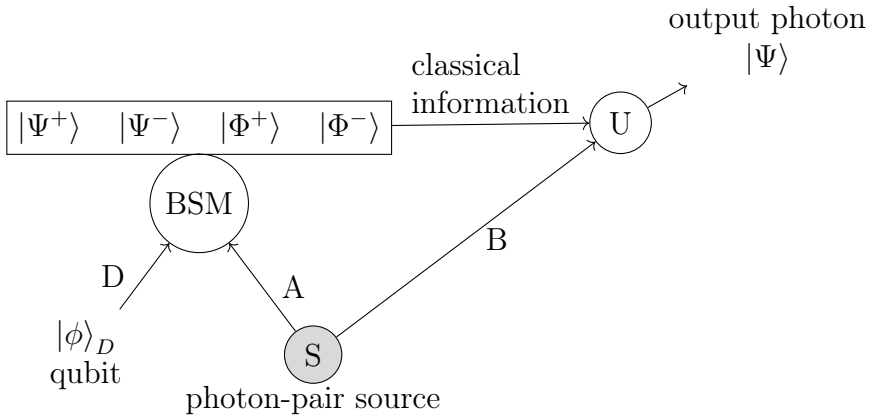

Figure 6.1: Schematic of quantum state teleportation. A photon-pair source (S) emits an entangled photon pair into the channels A and B. Photons in channel A are sent to a Bell state measurement (BSM) with a third qubit $|\phi\rangle_D$. The measurement outcome is the classical information needed to restore the initial qubit by a unitary operation (U) on the photon in channel B.

6.1 General quantum state teleportation

An overview of the teleportation protocol is depicted in figure 6.1. An essential part is a resource of entanglement, for example, an entangled photon pair source whose particles are in an entangled state

$$|\Psi^-\rangle_{A,B} = \frac{1}{\sqrt{2}}\left(|0\rangle_A \otimes |1\rangle_B + \mathrm{e}^{\mathrm{i}\phi}\,|1\rangle_A \otimes |0\rangle_B\right) \tag{6.1}$$

with a phase factor ϕ. One of these particles is sent to location A, which is commonly named Alice. The other one is sent to position B or Bob. Alice wants to transmit to Bob the qubit

$$|\phi\rangle_D = \alpha\,|0\rangle_D + \beta\,|1\rangle_D \qquad\qquad |\alpha|^2 + |\beta|^2 = 1\,, \tag{6.2}$$

which is stored on a third particle. For teleporting her qubit, she has to perform a Bell state measurement (BSM), i.e. the projection of photon A and her qubit D onto one of the following so-called Bell states:

$$|\Phi^\pm\rangle_{A,D} = \frac{1}{\sqrt{2}}\left(|0\rangle_A \otimes |0\rangle_D \pm |1\rangle_A \otimes |1\rangle_D\right) \tag{6.3}$$

$$|\Psi^\pm\rangle_{A,D} = \frac{1}{\sqrt{2}}\left(|0\rangle_A \otimes |1\rangle_D \pm |1\rangle_A \otimes |0\rangle_D\right) \tag{6.4}$$

Table 6.1: Unitary operations needed to restore the initial information of a teleportation schema in dependence of the measured Bell state.

Bell state	Unitary transformation	Unitary transformation $\phi = 180°$	Final state
$\left\|\Psi^+\right\rangle_{A,D}$	$\left\|0\right\rangle_B \left\langle 0\right\|_B + \mathrm{e}^{-\mathrm{i}\phi} \left\|1\right\rangle_B \left\langle 1\right\|_B$	σ_z	$\alpha \left\|0\right\rangle_B + \beta \left\|1\right\rangle_B$
$\left\|\Psi^-\right\rangle_{A,D}$	$\left\|0\right\rangle_B \left\langle 0\right\|_B - \mathrm{e}^{-\mathrm{i}\phi} \left\|1\right\rangle_B \left\langle 1\right\|_B$	$-\sigma_0$	$\alpha \left\|0\right\rangle_B + \beta \left\|1\right\rangle_B$
$\left\|\Phi^+\right\rangle_{A,D}$	$\left\|1\right\rangle_B \left\langle 0\right\|_B + \mathrm{e}^{-\mathrm{i}\phi} \left\|0\right\rangle_B \left\langle 1\right\|_B$	$-\mathrm{i}\sigma_y$	$\alpha \left\|0\right\rangle_B + \beta \left\|1\right\rangle_B$
$\left\|\Phi^-\right\rangle_{A,D}$	$\left\|1\right\rangle_B \left\langle 0\right\|_B - \mathrm{e}^{-\mathrm{i}\phi} \left\|0\right\rangle_B \left\langle 1\right\|_B$	$-\sigma_x$	$\alpha \left\|0\right\rangle_B + \beta \left\|1\right\rangle_B$

The joint initial state of all three particles is written as

$$\left|\Psi\right\rangle_{A,B} \otimes \left|\varphi\right\rangle_D = \frac{1}{\sqrt{2}} \left(\left|0\right\rangle_A \otimes \left|1\right\rangle_B + \mathrm{e}^{\mathrm{i}\phi} \left|1\right\rangle_A \otimes \left|0\right\rangle_B \right) \otimes \left(\alpha \left|0\right\rangle_D + \beta \left|1\right\rangle_D \right) . \tag{6.5}$$

We rewrite this equation using the definition of the four Bell states:

$$\begin{aligned} \left|\Psi\right\rangle_{A,B} \otimes \left|\varphi\right\rangle_D = \frac{1}{2} \Bigg(& \left(\alpha \left|0\right\rangle_B + \beta \mathrm{e}^{\mathrm{i}\phi} \left|1\right\rangle_B \right) \otimes \left|\Psi^+\right\rangle_{A,D} \\ & - \left(\alpha \left|0\right\rangle_B - \beta \mathrm{e}^{\mathrm{i}\phi} \left|1\right\rangle_B \right) \otimes \left|\Psi^-\right\rangle_{A,D} \\ & + \left(\beta \left|0\right\rangle_B + \alpha \mathrm{e}^{\mathrm{i}\phi} \left|1\right\rangle_B \right) \otimes \left|\Phi^+\right\rangle_{A,D} \\ & - \left(\beta \left|0\right\rangle_B - \alpha \mathrm{e}^{\mathrm{i}\phi} \left|1\right\rangle_B \right) \otimes \left|\Phi^-\right\rangle_{A,D} \Bigg) . \end{aligned} \tag{6.6}$$

This formula shows that the projection of photon A and qubit D onto one of the four Bell states transfers the information (amplitudes α and β) initially stored on qubit D to photon B. However, a unitary operation is needed to restore the initial information. The information about the needed operation is two-bit classical information, which needs to be transferred to Bob. This transmission of classical information limits the communication speed to the speed of light. The unitary operations with the corresponding Bell states are summarised in table 6.1.

6.2 Teleportation for the atom-photon system

We now map the general formalism to our atom-photon system. Our photon-pair source produces the general entangled state

$$\left|\Psi^{\varphi}\right\rangle_{A,B} = \frac{1}{\sqrt{2}} \left(\left|H\right\rangle_A \left|V\right\rangle_B + e^{\mathrm{i}\varphi} \left|V\right\rangle_A \left|H\right\rangle_B \right) \tag{6.7}$$

between the two output ports A and B. We rewrite this state in the $|R\rangle$ / $|L\rangle$ basis, as it is easier to describe the absorption by the ion in the circular basis. The state has the form

$$\begin{aligned}|\Psi^{\varphi}\rangle_{A,B} = \frac{\mathrm{i}}{2\sqrt{2}} \Big(&\left(1 + e^{\mathrm{i}\varphi}\right) \left(|R\rangle_A |R\rangle_B - |L\rangle_A |L\rangle_B\right) \\ &- \left(1 - e^{\mathrm{i}\varphi}\right) \left(|R\rangle_A |L\rangle_B - |L\rangle_A |R\rangle_B\right) \Big) \,. \end{aligned} \tag{6.8}$$

One photon, in our case photon A, is sent to the ion, the other one to a detection setup (see figure 5.8). The qubit state

$$|\varphi\rangle_D = \alpha\,|{-5/2}\rangle_D + \beta\,|{+5/2}\rangle_D \qquad\qquad |\alpha|^2 + |\beta|^2 = 1 \tag{6.9}$$

is the information we like to teleport onto photon B. The joint state of the whole system is

$$|\Phi\rangle_{\text{joint}} = |\Psi^{\varphi}\rangle_{A,B} \otimes |\varphi\rangle_D \tag{6.10}$$

$$\begin{aligned} &= \frac{\mathrm{i}}{2\sqrt{2}} \Big(\left(1 + e^{\mathrm{i}\varphi}\right) \left(|R\rangle_A |R\rangle_B - |L\rangle_A |L\rangle_B\right) \\ &- \left(1 - e^{\mathrm{i}\varphi}\right) \left(|R\rangle_A |L\rangle_B - |L\rangle_A |R\rangle_B\right) \Big) \otimes \left(\alpha\,|{-5/2}\rangle_D + \beta\,|{+5/2}\rangle_D\right) \end{aligned} \tag{6.11}$$

As for the general case, we rewrite the joint state with the definition of the four Bell states

$$|\Psi^{\pm}\rangle_{A,D} = \frac{1}{\sqrt{2}} \left(|R\rangle_A |{+5/2}\rangle_D \pm |L\rangle_A |{-5/2}\rangle_D\right) \tag{6.12}$$

$$|\Phi^{\pm}\rangle_{A,D} = \frac{1}{\sqrt{2}} \left(|R\rangle_A |{-5/2}\rangle_D \pm |L\rangle_A |{+5/2}\rangle_D\right) \,. \tag{6.13}$$

We conclude with the following joint state

$$\begin{aligned} &|\Psi\rangle_{A,B} \otimes |\varphi\rangle_D = \\ &\frac{\mathrm{i}}{2} \Bigg(\left(\left(1 + e^{\mathrm{i}\varphi}\right) \left(\alpha\,|R\rangle_B - \beta\,|L\rangle_B\right) + \left(1 - e^{\mathrm{i}\varphi}\right) \left(\beta\,|R\rangle_B - \alpha\,|L\rangle_B\right) \right) \otimes |\Phi^+\rangle_{A,D} \\ &+ \left(\left(1 + e^{\mathrm{i}\varphi}\right) \left(\alpha\,|R\rangle_B + \beta\,|L\rangle_B\right) - \left(1 - e^{\mathrm{i}\varphi}\right) \left(\beta\,|R\rangle_B + \alpha\,|L\rangle_B\right) \right) \otimes |\Phi^-\rangle_{A,D} \\ &+ \left(\left(1 + e^{\mathrm{i}\varphi}\right) \left(\beta\,|R\rangle_B - \alpha\,|L\rangle_B\right) + \left(1 - e^{\mathrm{i}\varphi}\right) \left(\alpha\,|R\rangle_B - \beta\,|L\rangle_B\right) \right) \otimes |\Psi^+\rangle_{A,D} \end{aligned}$$

$$+\left(\left(1+e^{\mathrm{i}\varphi}\right)\left(\beta\left|R\right\rangle_B+\alpha\left|L\right\rangle_B\right)-\left(1-e^{\mathrm{i}\varphi}\right)\left(\alpha\left|R\right\rangle_B+\beta\left|L\right\rangle_B\right)\right)\otimes\left|\Psi^-\right\rangle_{A,D}\Bigg) \tag{6.14}$$

This formula shows again that the projection of photon A and qubit D onto one of the four Bell states transfers the information initially stored on the ion to photon B. Table 6.2 shows the unitary operation needed to restore the initial information for a state phase of $\varphi = \pi$.

Table 6.2: Unitary operation to restore the initial information of a teleportation schema in dependence of the measured Bell state and the state phase of the initial photonic state.

Bell state	Transformation	Transformation for $\phi = \pi$
$\left\|\Psi^+\right\rangle$	$-\left(1-e^{\mathrm{i}\varphi}\right)\sigma_z-\mathrm{i}\left(1+e^{\mathrm{i}\varphi}\right)\sigma_y$	$-\sigma_z$
$\left\|\Psi^-\right\rangle$	$\left(1-e^{\mathrm{i}\varphi}\right)\sigma_0+\mathrm{i}\left(1+e^{\mathrm{i}\varphi}\right)\sigma_x$	σ_0
$\left\|\Phi^+\right\rangle$	$\left(1+e^{\mathrm{i}\varphi}\right)\sigma_z-\mathrm{i}\left(1-e^{\mathrm{i}\varphi}\right)\sigma_y$	$-i\sigma_y$
$\left\|\Phi^-\right\rangle$	$\left(1+e^{\mathrm{i}\varphi}\right)\sigma_0+\mathrm{i}\left(1-e^{\mathrm{i}\varphi}\right)\sigma_x$	$-\sigma_x$

The data shown in section 6.3 and 6.4 are also for this state phase. In this case, the joint state simplifies to

$$\begin{aligned}\left|\Psi\right\rangle_{A,B}\otimes\left|\varphi\right\rangle_D=\mathrm{i}\Big(&\left(\beta\left|R\right\rangle_B-\alpha\left|L\right\rangle_B\right)\otimes\left|\Phi^+\right\rangle_{A,D}\\&-\left(\beta\left|R\right\rangle_B+\alpha\left|L\right\rangle_B\right)\otimes\left|\Phi^-\right\rangle_{A,D}\\&+\left(\alpha\left|R\right\rangle_B-\beta\left|L\right\rangle_B\right)\otimes\left|\Psi^+\right\rangle_{A,D}\\&-\left(\alpha\left|R\right\rangle_B+\beta\left|L\right\rangle_B\right)\otimes\left|\Psi^-\right\rangle_{A,D}\Big)\end{aligned} \tag{6.15}$$

The BSM for the atom-photon system consists of three steps. The first step is the heralded absorption of photon A. The second step is the projection of the emitted 393 nm Raman photon onto a linear polarisation

$$\left|H\right\rangle_{393}=\frac{\left|R\right\rangle_{393}+\left|L\right\rangle_{393}}{\sqrt{2}}\qquad\left|V\right\rangle_{393}=\frac{\left|R\right\rangle_{393}-\left|L\right\rangle_{393}}{\mathrm{i}\sqrt{2}}\,. \tag{6.16}$$

In the last step, the ion needs to be projected onto a superposition of the $S_{1/2}$ Zeeman levels

$$\left|+\right\rangle_S=\frac{\left|-1/2\right\rangle_S+\left|+1/2\right\rangle_S}{\sqrt{2}}\qquad\left|-\right\rangle_S=\frac{\left|-1/2\right\rangle_S-\left|+1/2\right\rangle_S}{\mathrm{i}\sqrt{2}}\,. \tag{6.17}$$

Combining the Raman process operators (c.f. equation (5.17) and (5.18)), describing the heralded absorption in the *first* and *second* passage of the photon, and the projection operators from above gives

$$\begin{aligned} \langle H|_{393}\,\langle +|_S\,\hat{\mathrm{R}}^{1^{\mathrm{st}}}_{A,D} &= \frac{1}{\sqrt{2}}\,\langle \Phi^+|_{A,D} \\ \langle V|_{393}\,\langle -|_S\,\hat{\mathrm{R}}^{1^{\mathrm{st}}}_{A,D} &= \frac{1}{\sqrt{2}}\,\langle \Phi^+|_{A,D} \end{aligned} \tag{6.18}$$

$$\begin{aligned} \langle H|_{393}\,\langle -|_S\,\hat{\mathrm{R}}^{1^{\mathrm{st}}}_{A,D} &= \frac{\mathrm{i}}{\sqrt{2}}\,\langle \Phi^-|_{A,D} \\ \langle V|_{393}\,\langle +|_S\,\hat{\mathrm{R}}^{1^{\mathrm{st}}}_{A,D} &= \frac{1}{\mathrm{i}\sqrt{2}}\,\langle \Phi^-|_{A,D} \end{aligned} \tag{6.19}$$

$$\begin{aligned} \langle H|_{393}\,\langle +|_S\,\hat{\mathrm{R}}^{2^{\mathrm{nd}}}_{A,D} &= \frac{1}{\sqrt{2}}\,\langle \Psi^+|_{A,D} \\ \langle V|_{393}\,\langle -|_S\,\hat{\mathrm{R}}^{2^{\mathrm{nd}}}_{A,D} &= \frac{1}{\sqrt{2}}\,\langle \Psi^+|_{A,D} \end{aligned} \tag{6.20}$$

$$\begin{aligned} \langle H|_{393}\,\langle -|_S\,\hat{\mathrm{R}}^{2^{\mathrm{nd}}}_{A,D} &= \frac{\mathrm{i}}{\sqrt{2}}\,\langle \Psi^-|_{A,D} \\ \langle V|_{393}\,\langle +|_S\,\hat{\mathrm{R}}^{2^{\mathrm{nd}}}_{A,D} &= \frac{1}{\mathrm{i}\sqrt{2}}\,\langle \Psi^-|_{A,D}\ . \end{aligned} \tag{6.21}$$

We get eight combinations, of which always two project to the same Bell state. The *first* passage only projects on the $|\Phi^{\pm}\rangle$ states, thereby limiting the efficiency to 50 % if one only uses one passage. The *second* passage only projects on the $|\Psi^{\pm}\rangle$ states and therefore enables the projection onto all four Bell states.

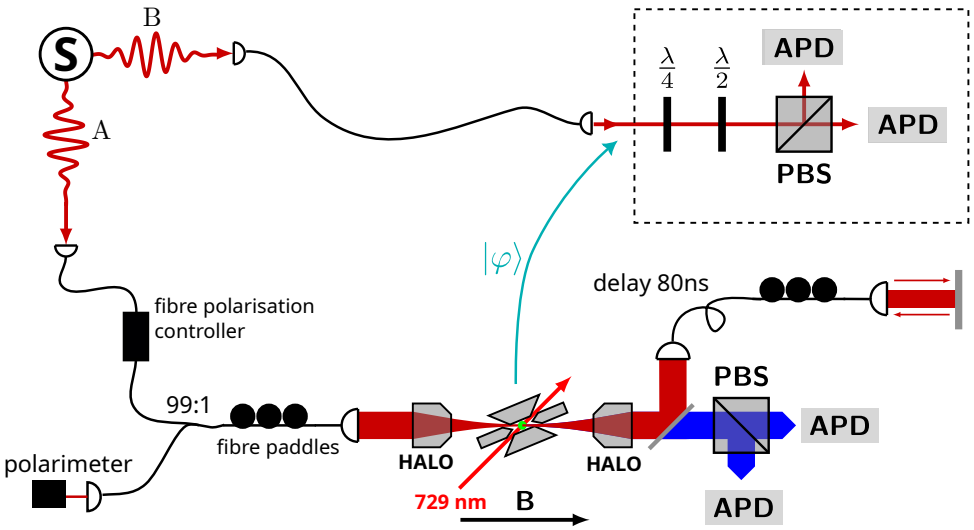

Figure 6.2: Experimental setup for the teleportation measurement. Photons from output port A of the source (S) are sent to the ion. Photons from port B are sent to a projection and detection setup. A fibre polarisation controller and fibre paddles control the polarisation rotation on the path to the ion. A 99:1 beam splitter connects the reference polarimeter. The teal arrow indicates the teleportation direction, beside of this the figure is similar to figure 5.8.

6.3 Results for the teleportation to 854 nm

The measurement setting is identical to the entanglement transfer of section 5.4.4. The scheme of the experimental setup is shown in figure 6.2. We prepare the atomic state

$$|\varphi\rangle_D = \alpha\,|-5/2\rangle_D + \beta\,|+5/2\rangle_D \tag{6.22}$$

with either $\alpha = \beta e^{-i\phi} = 1/\sqrt{2}$, $\alpha = 1, \beta = 0$ or $\alpha = 0, \beta = 1$. For the measurements shown in this section, we use the

$$|\Psi^-\rangle = \frac{1}{\sqrt{2}}\left(|HV\rangle - |VH\rangle\right) \tag{6.23}$$

state as photonic input state. The same measurement was also performed with the

$$|\Psi^i\rangle = \frac{1}{\sqrt{2}}\left(|HV\rangle - i\,|VH\rangle\right) \tag{6.24}$$

state. The results for that input state are presented in Appendix D.2.

As in the measurements shown in the previous chapter, the superposition phase is deter-

mined by the Larmor frequency and the detection time of the 393 nm photon. Hence, we probe the protocol with different but known phases in each run. The results are again histograms in dependence on the reconstructed phase for each of the photonic state projections. In contrast to the fringes and bar charts of the entanglement transfer, we plot the probability to detect the different projection states of photon B conditioned on the result of the BSM.

The coloured data points are again with corrections (in this case, we also correct for imbalances in the detection efficiencies of the APDs). The grey data points are without corrections. We fit the data with a sinusoidal function to extract the visibility V and the phase-offset Φ_0. Similar to the entanglement transfer, we get a high visibility in the $|H\rangle$ and $|D\rangle$ measurements and a small remaining oscillation for the $|R\rangle$ measurement. Furthermore, we observe a phase-shift of π between the $|\Phi^+\rangle$ and the $|\Phi^-\rangle$ state and the $|\Psi^+\rangle$ and the $|\Psi^-\rangle$ state. If we compare the $|\Psi\rangle$ with the $|\Phi\rangle$ results, we observe a phase shift of π only in the $|D\rangle$ measurement between $|\Phi^+\rangle$ and $|\Psi^+\rangle$ and $|\Phi^-\rangle$ and $|\Psi^-\rangle$. The phase shifts between the different states correspond to the expectation. Table 6.3 summarises the phases and visibilities of each measurement basis. The corresponding plots are shown in figure 6.3. The measurements in the energy eigenstates $|\pm 5/2\rangle$ show clearly a probability of 50 % for a projection to a linear polarisation. The *second* passage shows some deviation which results mainly from the low signal.

In the *first* passage, we transfer the information from the $|-5/2\rangle$ state to the right-circular component of the target photon and from the $|+5/2\rangle$ state to the left-circular component. In the *second* passage, the situation is interchanged.

The deviations from the ideal probabilities and the reduced visibility for the *second* passage is explained by some polarisation mismatch. We cannot precisely set the polarisation rotation of the back-reflection part to a unity rotation, which might come from polarising effects of the optical components and some cut-offs of the beam profile. Additionally, the polarisation is modified by some fibre paddles, which act only appropriately like an ideal quarter- or half-waveplate.

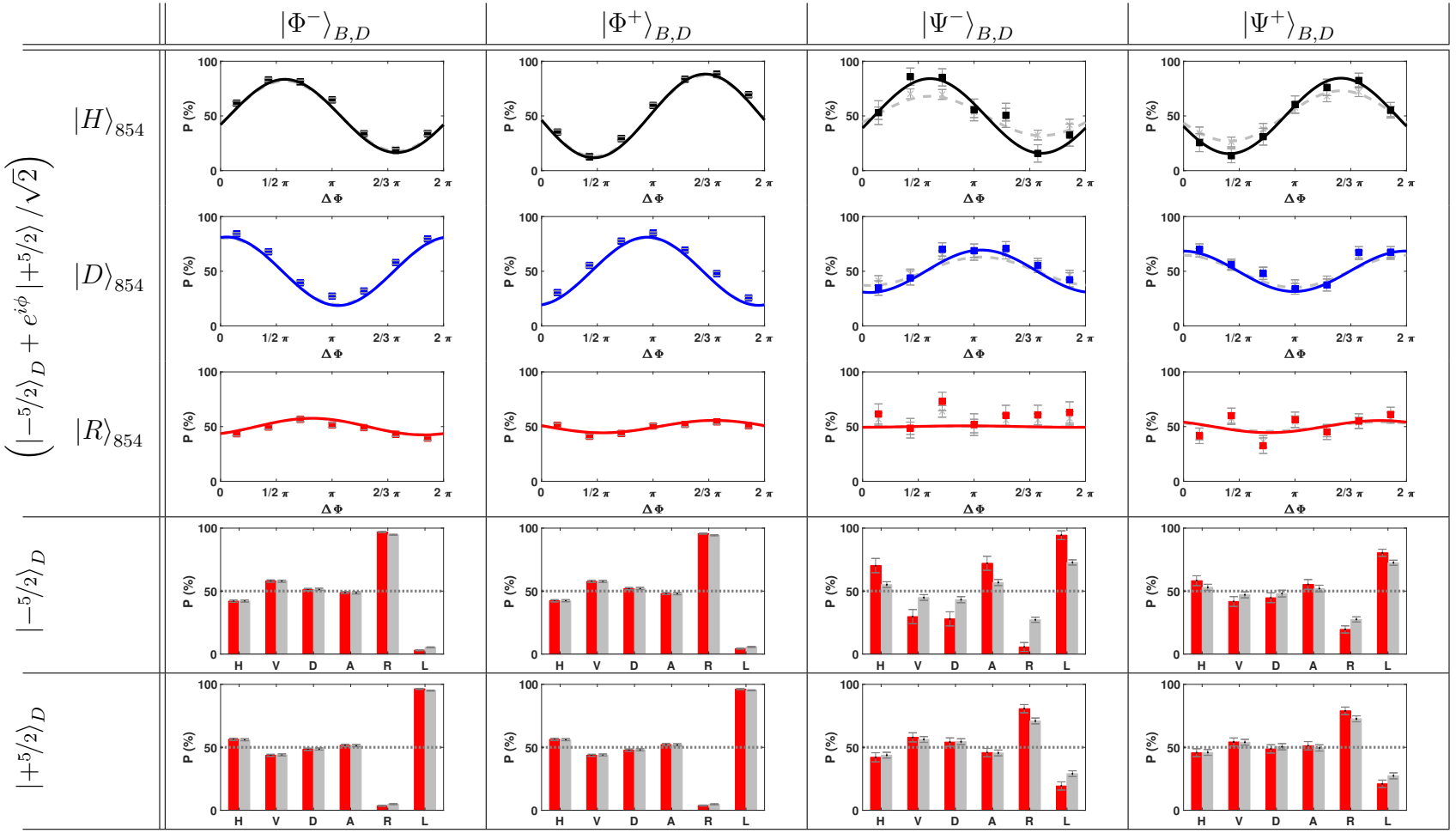

Figure 6.3: Histograms and fringes for the three input states and a projection to the four Bell states. The data is evaluated for a waiting time of 350 µs. Grey bars and lines show the data without corrections. The coloured ones with corrections.

Table 6.3: Phases and visibilities of the fringes for the teleportation measurement.

projector		with correction		w/o correction	
Bell	854	Phase (°)	Vis	Phase (°)	Vis
$\|\Phi^-\rangle$	$\|H\rangle$	14(6)	0.69(6)	14(6)	0.64(6)
	$\|D\rangle$	280(9)	0.65(9)	280(9)	0.61(8)
	$\|R\rangle$	58(17)	0.16(5)	58(18)	0.15(4)
$\|\Phi^+\rangle$	$\|H\rangle$	174(6)	0.79(6)	174(6)	0.74(6)
	$\|D\rangle$	80(9)	0.64(9)	80(9)	0.61(9)
	$\|R\rangle$	189(19)	0.12(4)	189(19)	0.11(4)
$\|\Psi^+\rangle$	$\|H\rangle$	164(4)	0.71(4)	164(3)	0.46(3)
	$\|D\rangle$	268(16)	0.4(1)	268(19)	0.29(9)
	$\|R\rangle$	228(76)	0.1(2)	228(76)	0.1(1)
$\|\Psi^-\rangle$	$\|H\rangle$	19(11)	0.7(1)	19(13)	0.36(7)
	$\|D\rangle$	102(15)	0.4(1)	102(20)	0.26(9)
	$\|R\rangle$	77(866)	0.0(2)	81(859)	0.0(1)

Finally, we reconstruct the quantum process matrices. We use a ML algorithm. As shown in the calculations of section 6.2, two measurements each result in the same Bell state. We combine these measurements for the reconstruction to increase the signal. The corresponding individual evaluations for the eight different cases are shown in the appendix (see figure D.19 and figure D.20). The corresponding process matrices for the combined evaluation are shown in figure 6.4. For the Bell states corresponding to the *first* passage, we see that either a σ_x or a σ_y rotation needs to be applied to restore the initial state. For the Bell state corresponding to the *second* passage, we either get the correct state directly or need a σ_z rotation. We identify the height of the corresponding entry as the process fidelity and summarise the results in table 6.4. As discussed in section 5.4.4, magnetic field fluctuations are the main sources of the loss of fidelity and the reduced fringe visibility. For the *second* passage, we are mainly limited by the losses of the back-reflection part and the accuracy of the polarisation setting.

Table 6.4: Summarised process fidelities for the four different Bell states.

state	fidelity w corrections	fidelity w/o corrections
$\|\Phi^-\rangle$	84(8) %	83(7) %
$\|\Phi^+\rangle$	86(7) %	85(6) %
$\|\Psi^-\rangle$	77(12) %	66(6) %
$\|\Psi^+\rangle$	76(8) %	69(5) %

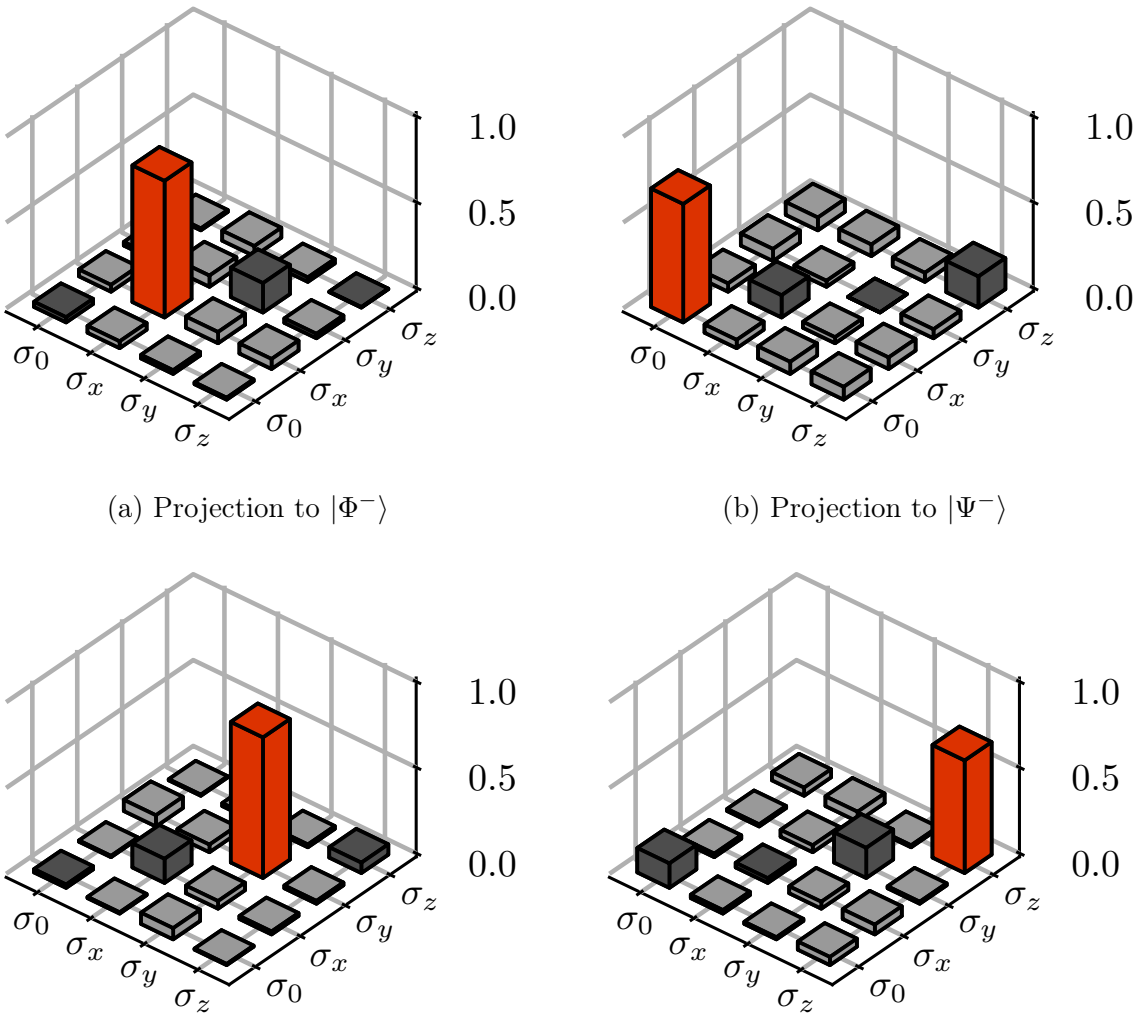

(a) Projection to $|\Phi^-\rangle$

(b) Projection to $|\Psi^-\rangle$

(c) Projection to $|\Phi^+\rangle$

(d) Projection to $|\Psi^+\rangle$

Figure 6.4: Reconstructed process matrices of the quantum state teleportation. (a) and (b) show the result for a projection to the $|\Phi^-\rangle$ and $|\Phi^+\rangle$ Bell state, (c) and (d) for a projection to the $|\Psi^-\rangle$ and $|\Psi^+\rangle$ Bell-state.

6.3.1 Protocol efficiencies and success probabilities

We calculate the protocol efficiency from the recorded events and the number of trials. In total, we perform

$$N_{\text{run}} = 511\,670\,886 \tag{6.25}$$

runs, where one run is equal to one exposure window. In these runs, we detect

$$N_{\text{coinc,first}} = 89\,838 \tag{6.26}$$

coincidences between the 393 nm photons and the 854 nm photon for the *first* passage and

$$N_{\text{coinc,second}} = 11\,322 \tag{6.27}$$

coincidences for the *second* passage.

The success probability per exposure window and passage is calculated as

$$\eta_{\text{succ,run,first}} = \frac{N_{\text{coinc,first}}}{N_{\text{run}}} = 1.76 \times 10^{-4} \tag{6.28}$$

$$\eta_{\text{succ,run,second}} = \frac{N_{\text{coinc,second}}}{N_{\text{run}}} = 2.21 \times 10^{-5}\,. \tag{6.29}$$

We further calculate the total exposure time by multiplying the number of runs and the photon exposure time $T_{\text{exp,photon}} = 350\,\text{ns}$ to get

$$T_{\text{tot,exp}} = N_{\text{run}} T_{\text{exp,photon}} = 1.79 \times 10^{5}\,\text{s} = 49.75\,\text{h}\,. \tag{6.30}$$

In order to calculate the success probability per photon pair, we first need the number of generated photons. Out of the brightness of the source of $5.17 \times 10^4\,\frac{1}{\text{mWs}}$ and the used pump power of 15 mW. We generated

$$N_{\text{pair}} = 1.388\,803 \times 10^{11} \tag{6.31}$$

photon pairs in the total exposure time. Then, we calculate the success probability per photon to be

$$\eta_{\text{succ,pair,first}} = \frac{N_{\text{coinc,first}}}{N_{\text{pair}}} = 6.47 \times 10^{-7} \tag{6.32}$$

$$\eta_{\text{succ,pair,second}} = \frac{N_{\text{coinc,second}}}{N_{\text{pair}}} = 8.15 \times 10^{-8}\,. \tag{6.33}$$

Finally, we calculate the absorption probability η_{abs} of the 854 nm photons. The probability of detecting the partner photon, including the detection efficiency of the APDs, spectral filtering and all optical components, is $\eta_{854,\text{B}} = 12.60\,\%$. This number is calculated out of the photon-photon correlation. For the 854 nm photons sent to the ion, we have to consider the coupling efficiency to the trap $\eta_{854,\text{A}} = 30.00\,\%$. The efficiency to detect a 393 nm heralding photon is measured independently. Coincidences between absorption herald and arm B photon within a gate of ± 84 ns are taken into account, corresponding to $\eta_{gate} = 99.9\,\%$ of the 854 nm photon wave packet.We get an efficiency of $\eta_{393} = 1.64\,\%$. The absorption efficiency is then given by

$$\eta_{\text{abs,first}} = \frac{\eta_{\text{succ,pair,first}}}{\eta_{854,\text{A}}\eta_{854,\text{B}}\eta_{393}\eta_{gate}} = 1.04 \times 10^{-3} \tag{6.34}$$

$$\eta_{\text{abs,second}} = \frac{\eta_{\text{succ,pair,second}}}{\eta_{854,\text{A}}\eta_{854,\text{B}}\eta_{393}\eta_{gate}} = 1.32 \times 10^{-4}\,. \tag{6.35}$$

These numbers agree with the previous measurement of our ion trap setup [142, 102, 72].

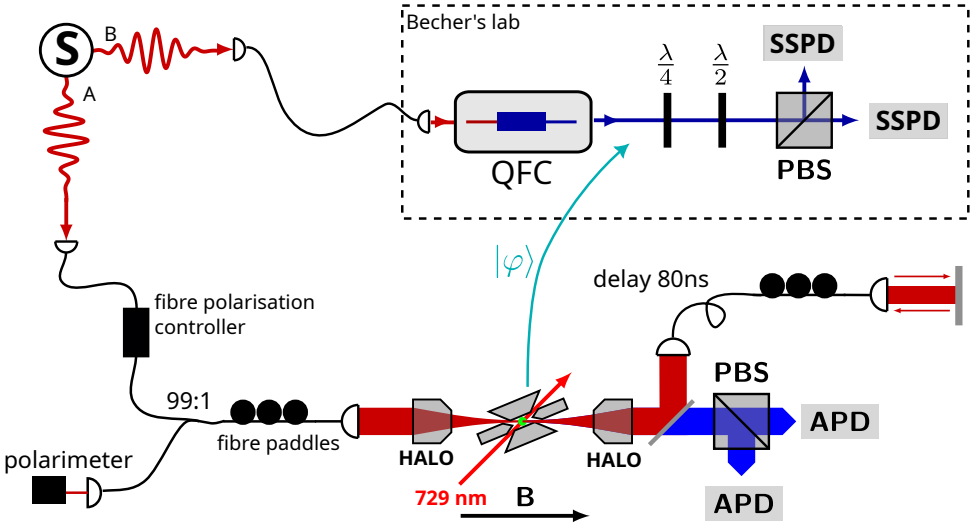

Figure 6.5: Experimental setup for the measurement with conversion. Photons from output port A of the source (S) are sent to the ion. Photons from port B are sent to a quantum frequency converter (QFC) and are then detected by a SSPD for each projection. A fibre polarisation controller and a fibre paddle control the polarisation rotation on the path to the ion. A 99:1 beam splitter connects the reference polarimeter. The teal arrow indicates the teleportation direction, beside of this the figure is similar to figure 5.13.

6.4 Results for the teleportation to 1550 nm

The measurement setting for the teleportation including QFC is identical to the entanglement transfer with conversion (section 5.4.5). The input state for the teleportation is thereby identical as in the measurement presented before. A scheme of the measurement setup is shown in figure 6.5.

In figure 6.4, we show the histograms and fringes. In table 6.5, we summarise the phases and visibilities from a sinusoidal fit to the data. The fringes for detecting the superposition state are similar to the measurement without conversion. The eigenstates show much more deviation from the ideal values, especially the histograms for the *second* passage. Some misalignment in the detection setup behind the converter, which was corrected after measuring the $|-5/2\rangle_D$ $|H\rangle$ / $|V\rangle$ basis, explain this.

From the fringes, we reconstruct the quantum process matrices. We combine the measurement data for a projection to the same Bell state to increase the signal. The eight individual results are shown in Appendix D.3. The process matrices are depicted in figure

Table 6.5: Phases and visibilities of the fringes for the teleportation measurement with conversion.

projector		with correction		w/o correction	
Bell	854	Phase (°)	Vis	Phase (°)	Vis
	$\|H\rangle$	345(12)	0.8(1)	345(13)	0.7(1)
$\|\Phi^-\rangle$	$\|D\rangle$	264(10)	0.7(1)	264(10)	0.7(1)
	$\|R\rangle$	112(33)	0.2(1)	112(32)	0.2(1)
	$\|H\rangle$	182(11)	0.8(1)	182(11)	0.7(1)
$\|\Phi^+\rangle$	$\|D\rangle$	102(7)	0.68(7)	102(7)	0.63(7)
	$\|R\rangle$	301(28)	0.2(1)	301(27)	0.21(10)
	$\|H\rangle$	200(15)	0.9(2)	199(28)	0.4(2)
$\|\Psi^+\rangle$	$\|D\rangle$	270(19)	0.6(2)	271(34)	0.3(2)
	$\|R\rangle$	58(64)	0.1(1)	60(54)	0.06(6)
	$\|H\rangle$	358(15)	0.7(2)	358(27)	0.4(2)
$\|\Psi^-\rangle$	$\|D\rangle$	76(30)	0.5(2)	77(43)	0.3(2)
	$\|R\rangle$	242(20)	0.21(7)	242(25)	0.14(6)

Table 6.6: Summarised process fidelities for the four different Bell states depicted in figure 6.6.

state	fidelity w corrections	fidelity w/o corrections
$\|\Phi^-\rangle$	86(8) %	86(6) %
$\|\Phi^+\rangle$	86(7) %	85(6) %
$\|\Psi^-\rangle$	78(12) %	67(8) %
$\|\Psi^+\rangle$	82(12) %	67(8) %

6.6. As expected, the required unitary operations to restore the initial state are identical to the previous measurement. For the Bell states corresponding to the *first* passage, either a σ_x or a σ_y rotation needs to be applied, and for the Bell states corresponding to the *second* passage, we either get the correct state directly or need a σ_z rotation.

The process fidelities are summarised in table 6.6. The results for the *first* passage are on the same level as in the case without projection. The *second* passage is slightly better than before.

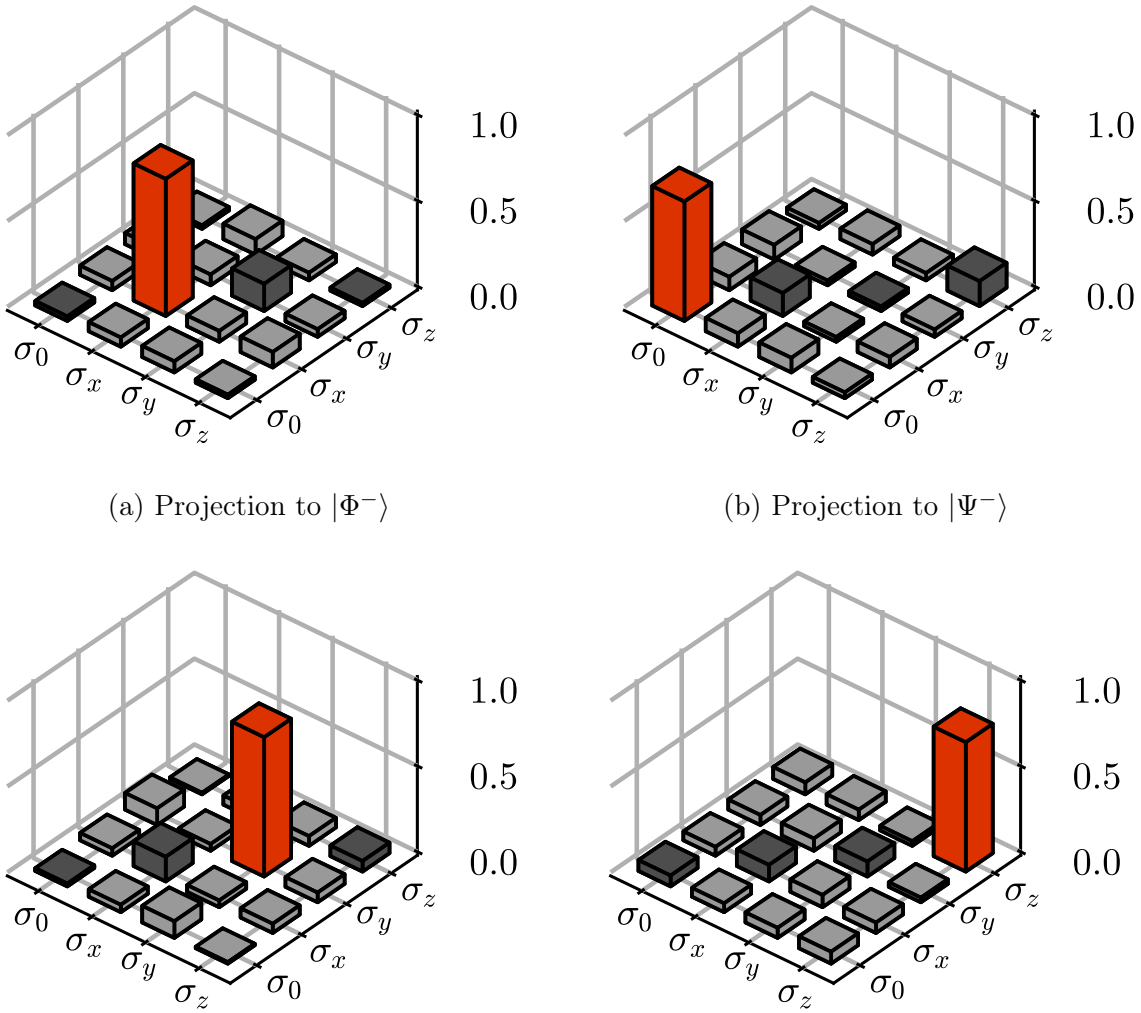

(a) Projection to $|\Phi^-\rangle$

(b) Projection to $|\Psi^-\rangle$

(c) Projection to $|\Phi^+\rangle$

(d) Projection to $|\Psi^+\rangle$

Figure 6.6: Reconstructed process matrices of the quantum state teleportation with conversion. (a) and (b) show the result for a projection to the $|\Phi^-\rangle$ and $|\Phi^+\rangle$ Bell state, (c) and (d) for a projection to the $|\Psi^-\rangle$ and $|\Psi^+\rangle$ Bell-state.

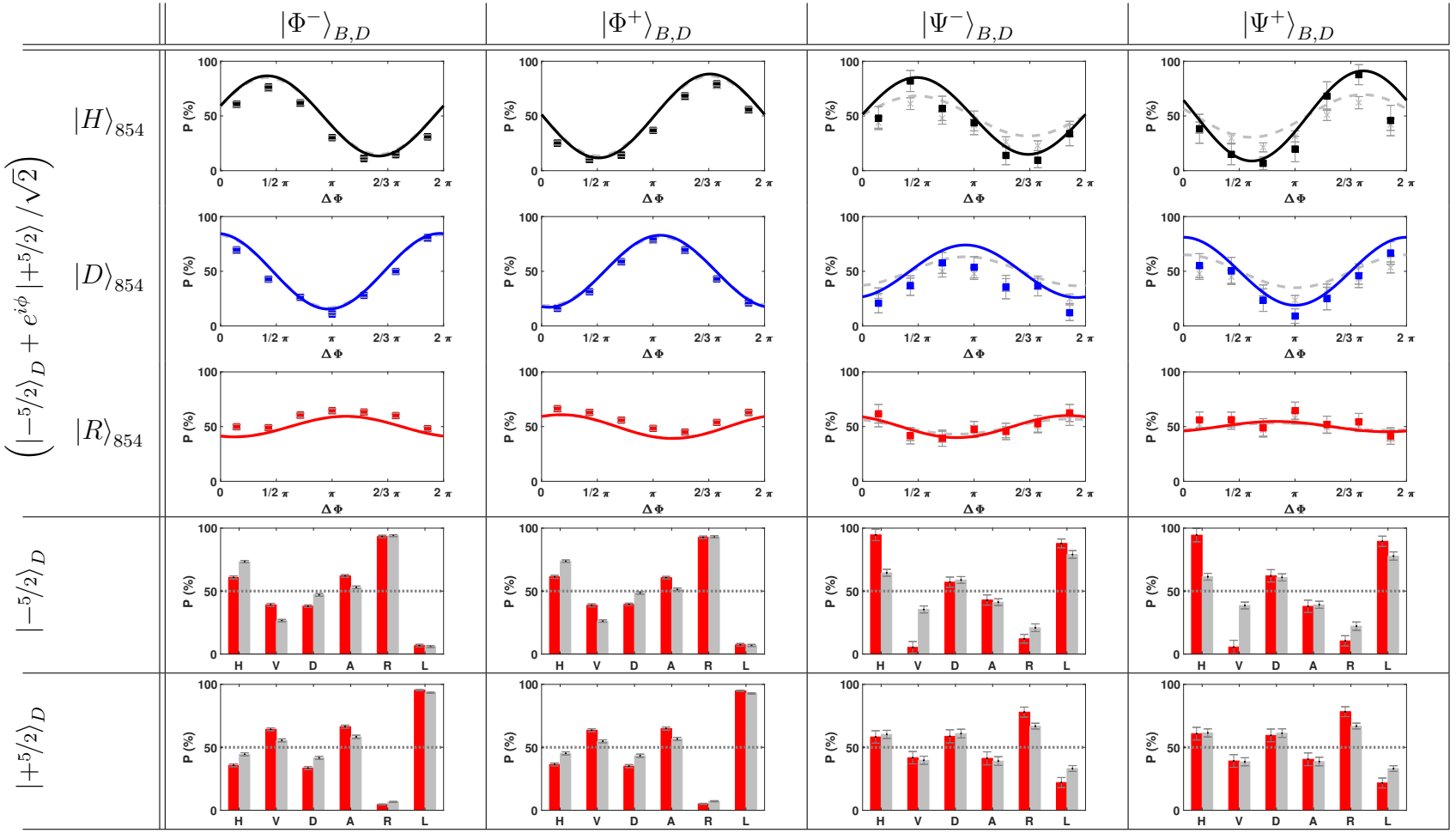

Figure 6.7: Histograms and fringes for the three input states and a projection to the four Bell states. The data is evaluated for a waiting time of 400 µs. Grey bars and lines show the data without corrections. The coloured ones with corrections.

6.4.1 Protocol efficiencies and success probabilities

The calculation of the protocol efficiency and success probabilities is carried out identically to the previous section. We summarise the corresponding values in table 6.7.

Table 6.7: Protocol efficiency and success probabilities for the teleportation with conversion.

number of runs N_{run}	404 915 226
coincidences, *first* passage $N_{\text{coinc,first}}$	65 762
coincidences, *second* passage $N_{\text{coinc,second}}$	9133
total exposure time $T_{\text{tot,exp}}$	44.99 h
number of generated photons N_{pair}	$1.256\,047 \times 10^{11}$
$\eta_{854,\text{A}}$	30.00 %
$\eta_{854,\text{B}}$	9.40 %
η_{393}	1.64 %
success probability per exposure window, *first* passage $\eta_{\text{succ,run,first}}$	1.62×10^{-4}
success probability per exposure window, *second* passage $\eta_{\text{succ,run,second}}$	2.26×10^{-5}
success probability per photon, *first* passage $\eta_{\text{succ,pair,first}}$	5.24×10^{-7}
success probability per photon, *second* passage $\eta_{\text{succ,pair,second}}$	7.27×10^{-8}
absorption efficiency, *first* passage	1.13×10^{-3}
absorption efficiency, *second* passage	1.57×10^{-4}

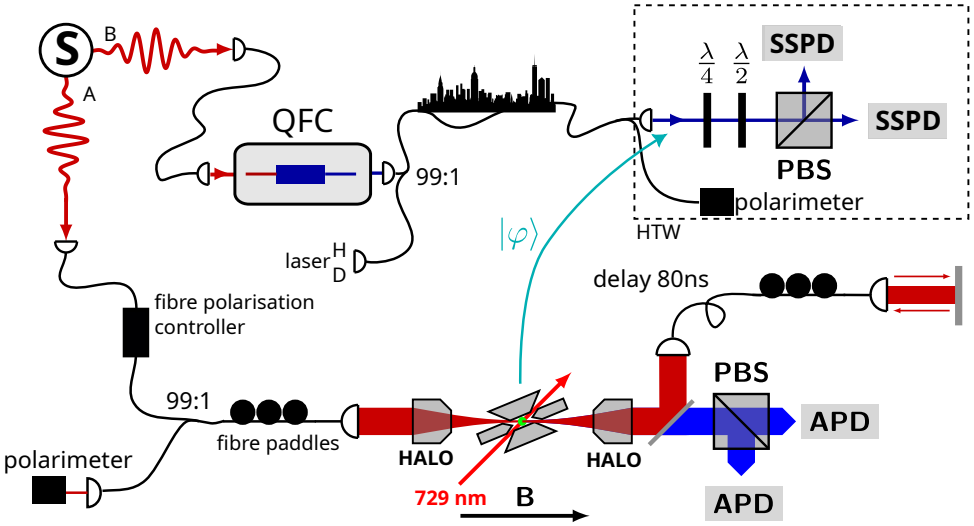

Figure 6.8: Experimental setup for the measurement with conversion and detection at the HTW. Photons from output port A of the source (S) are sent to the ion. A fibre polarisation controller and a fibre paddle control the polarisation on the path to the ion. A 99:1 beam splitter connects the reference polarimeter. Photons from port B are sent to a quantum frequency converter (QFC) and are then detected by a SSPD for each projection at the HTW after 14 km of metropolitan fibre. The fibre stabilisation lasers are inserted after the converter by a 99:1 beam splitter. The teal arrow indicates the teleportation direction, beside of this the figure is similar to figure 5.16.

6.5 Results for the teleportation to the HTW

The setting for the presented measurement is similar to the entanglement transfer to the HTW. A scheme of the measurement setup is shown in figure 6.8. In contrast to the previous teleportation measurements, the photons are now in the

$$|\Psi^+\rangle = \frac{1}{\sqrt{2}}\left(|HV\rangle + |VH\rangle\right) \tag{6.36}$$

Bell state because the locking point of the source interferometer was much more stable. The teleported states are identical to the previously shown teleportation measurements. We repeat the evaluation steps for the data as described earlier. The histograms and fringes are shown in figure 6.9. The visibilities and phases for a sinusoidal fit to the data are summarised in table 6.8.

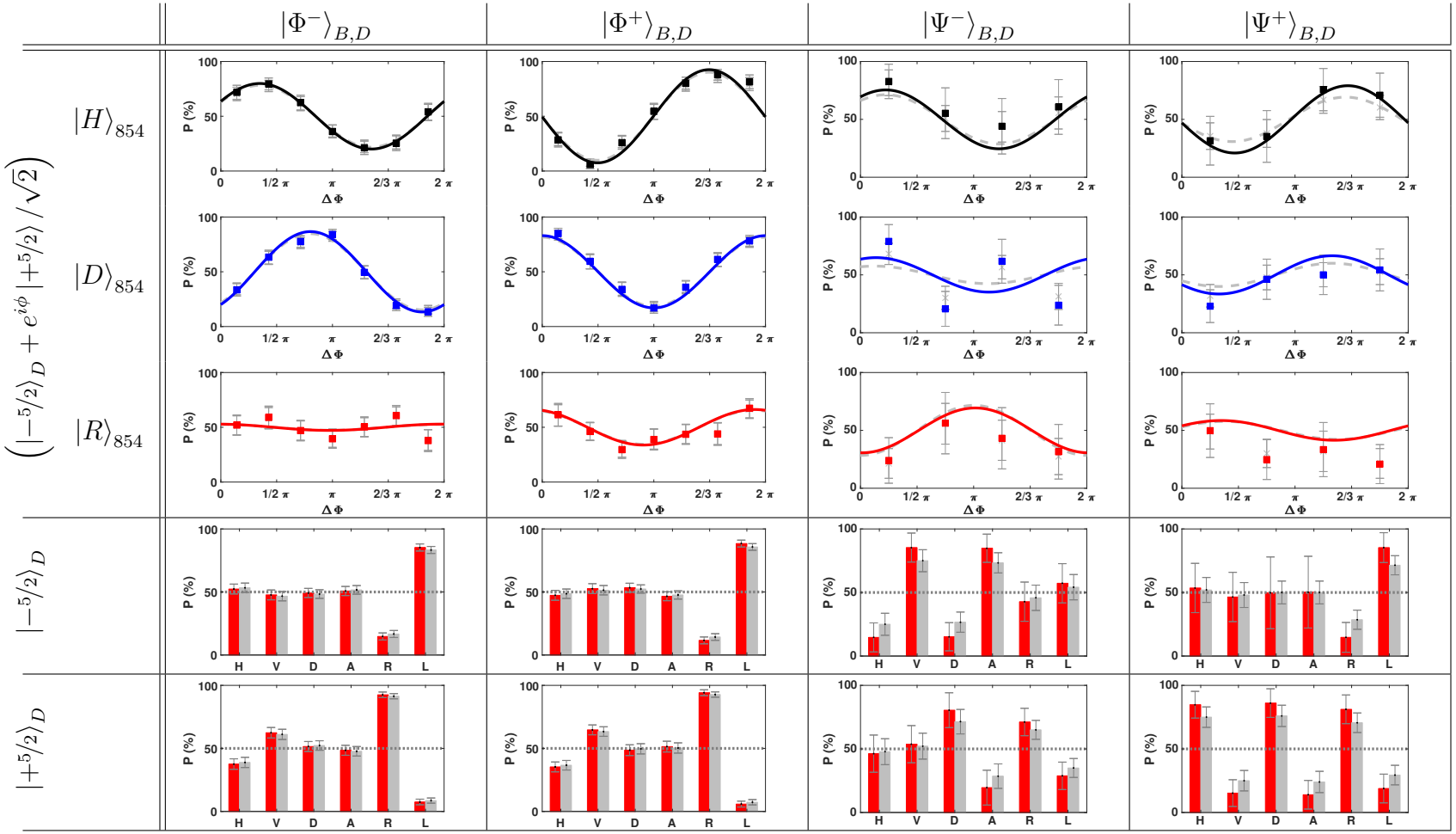

Figure 6.9: Histograms and fringes for the three input states and the four Bell states. The data is evaluated for a waiting time of 400 µs. Grey bars and lines show the data without corrections. The coloured ones with corrections.

Table 6.8: Phases and visibilities of the fringes for the teleportation measurement with conversion and detection at the HTW.

projector		with correction		w/o correction	
Bell	854	Phase (°)	Vis	Phase (°)	Vis
	$\|H\rangle$	333(2)	0.62(2)	333(2)	0.57(2)
$\|\Phi^-\rangle$	$\|D\rangle$	55(5)	0.76(6)	55(5)	0.70(5)
	$\|R\rangle$	265(129)	0.1(1)	265(129)	0.1(1)
	$\|H\rangle$	179(8)	0.88(9)	179(8)	0.80(8)
$\|\Phi^+\rangle$	$\|D\rangle$	270(6)	0.68(6)	270(6)	0.63(6)
	$\|R\rangle$	253(17)	0.34(10)	253(17)	0.31(9)
	$\|H\rangle$	183(17)	0.4(1)	179(19)	0.3(1)
$\|\Psi^+\rangle$	$\|D\rangle$	151(38)	0.4(3)	152(46)	0.3(2)
	$\|R\rangle$	319(105)	0.2(3)	319(83)	0.2(4)
	$\|H\rangle$	291(36)	0.3(2)	294(40)	0.3(2)
$\|\Psi^-\rangle$	$\|D\rangle$	354(26)	0.4(2)	356(28)	0.3(1)
	$\|R\rangle$	113(32)	0.3(1)	117(38)	0.3(2)

Table 6.9: Summarised process fidelities for the two different Bell states.

state	fidelity w corrections	fidelity w/o corrections
$\|\Phi^-\rangle$	80(6) %	78(6) %
$\|\Phi^+\rangle$	87(5) %	86(5) %

Finally, we reconstruct the quantum process matrices out of the fitted fringes. Measurement data corresponding to a projection to the same Bell state are combined. Figure 6.10 shows the resulting process matrices. Due to the different Bell state of the photons, we get a different mapping between the result of the Bell measurement and the applied unitary operation. In the case of the $|\Phi^-\rangle$-state, we have to apply no rotation, and in the case of the $|\Phi^+\rangle$-state, we have to apply a σ_z rotation.

The extracted process fidelity is summarised in table 6.9. The results for a projection to the $|\Phi^+\rangle$-state is on the same level as in the measurements before, and the fidelity for the other state is slightly worse.

Due to a calibration error in the polarisation of the back-reflection, we do not see the expected behaviour for the *second* passage. Hence, the data is not shown, because no process matrix could be reconstructed.

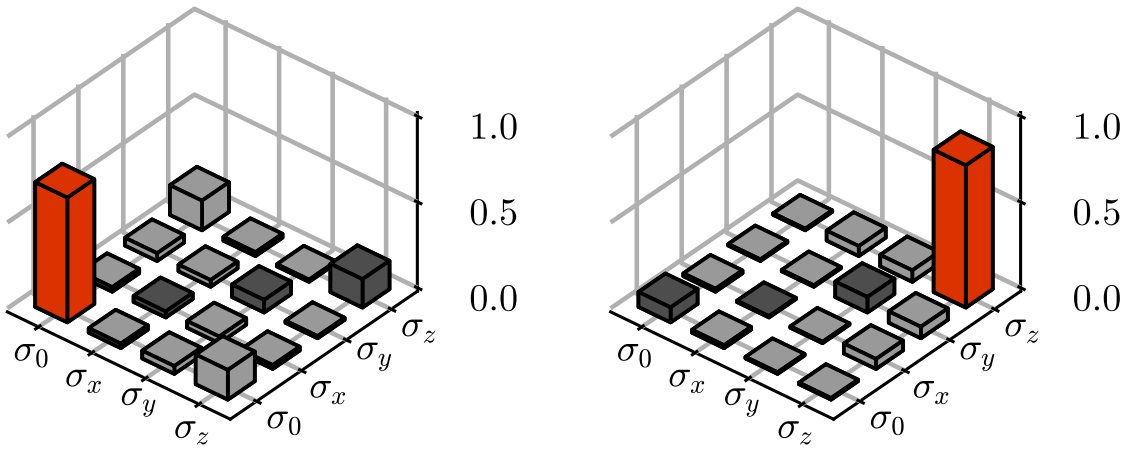

(a) Projection to $|\Phi^-\rangle$ (b) Projection to $|\Phi^+\rangle$

Figure 6.10: Reconstructed process matrices of the quantum state teleportation with conversion. (a) and (b) show the result for a projection to the $|\Phi^-\rangle$ and $|\Phi^+\rangle$ Bell state.

6.5.1 Protocol efficiencies and success probabilities

The calculation of the protocol efficiency and success probabilities is carried out identically to section 6.3. We summarise the corresponding values in table 6.10.

Table 6.10: Protocol efficiency and success probabilities for the teleportation with conversion and detection at the HTW.

number of runs N_{run}	710 093 240
coincidences, *first* passage $N_{\text{coinc,first}}$	5489
coincidences, *second* passage $N_{\text{coinc,second}}$	793
total exposure time $T_{\text{tot,exp}}$	78.90 h
number of generated photons N_{pair}	$3.054\,821 \times 10^{11}$
$\eta_{854,\text{A}}$	33.00 %
$\eta_{854,\text{B}}$	0.11 %
η_{393}	1.80 %
success probability per exposure window, *first* passage $\eta_{\text{succ,run,first}}$	7.73×10^{-6}
success probability per exposure window, *second* passage $\eta_{\text{succ,run,second}}$	1.12×10^{-6}
success probability per photon, *first* passage $\eta_{\text{succ,pair,first}}$	1.80×10^{-8}
success probability per photon, *second* passage $\eta_{\text{succ,pair,second}}$	2.60×10^{-9}
absorption efficiency, *first* passage	2.75×10^{-3}
absorption efficiency, *second* passage	3.97×10^{-4}

Table 6.11: Summary of the process fidelities of the teleportation measurement for all three described settings.

	854 nm		1550 nm		1550 nm @ HTW	
state	w corr.	w/o corr.	w corr.	w/o corr.	w corr.	w/o corr.
$\|\Phi^-\rangle$	84(8) %	83(7) %	86(8) %	86(6) %	80(6) %	78(6) %
$\|\Phi^+\rangle$	86(7) %	85(6) %	86(7) %	85(6) %	87(5) %	86(5) %
$\|\Psi^-\rangle$	77(12) %	66(6) %	78(12) %	67(8) %		
$\|\Psi^+\rangle$	76(8) %	69(5) %	82(12) %	67(8) %		

6.6 Summary

In this chapter, we presented the results for full quantum state teleportation protocol, using all four Bell states, based on the heralded absorption of one photon of a SPDC pair. We performed the protocol in three different settings. In the first setup, we teleported the qubit stored in the ion to a photon at 854 nm, which we detected in our lab. In the second setup, we included QFC and teleported the qubit to a photon at 1550 nm. The detection happened in the labs of Christoph Becher. We included the metropolitan fibre in the last setup and teleported the qubit to the HTW.

The resulting process fidelities for the teleportation measurements are summarised in table 6.11. The quantum frequency converter adds low background to the photon pair source. It thus enables the demonstrated quantum photonic interface in the low-loss, low-dispersion telecom wavelength range. It makes the connection of remote quantum network nodes based on $^{40}Ca^+$ single-ion memories possible. Furthermore, the fibre stabilisation enables the connection of remote quantum nodes over standard telecommunication fibres and adds nearly no infidelity to the transferred entanglement or the teleported state. The main limitation is the attenuation of the metropolitan fibre link.

The described protocol and the measurements illustrate how SPDC photon pair sources, as a resource of entanglement, and single atoms as quantum memories can be integrated into a quantum network. It will enable us to establish remote entanglement for quantum repeater operations over the metropolitan fibre link. Furthermore, the protocol shows the power of heralded operations to reach high fidelities despite a low success probability.

7 Summary and outlook

Quantum communication is a rapidly evolving field that has the potential to revolutionise the way we exchange information and secure data. In the future, it is expected that quantum networks will connect multiple quantum devices over long distances, enabling the creation of large-scale quantum communication networks or a quantum internet. One essential building block for such a network is a quantum repeater, which makes it possible to overcome the limitation of fibre attenuation. Especially single ion platforms show impressive progress in network operations, including a first repeater implementation, [143, 51, 144] and in quantum processors [145, 146]. Once a connection between two stationary nodes is established, data can be transmitted. For quantum data transmission, quantum state teleportation is a suitable protocol. The channel can also be used to exchange encryption keys via QKD. The protocols and interfaces developed in this thesis target the ion platform.

In this context, the main goal of this thesis was to demonstrate full quantum state teleportation over a metropolitan fibre, using all four Bell states, based on the heralded absorption of one photon of a SPDC pair. We applied several improvements to the photon pair source to reach this goal and proved the preservation of entanglement, including quantum frequency conversion and over long distances.

In the following sections, we review and discuss the most important experimental results as well as possible directions and challenges for future works.

7.1 Summary

The central element of all experiments of this thesis is the photon-pair source, described and characterised in-depth in chapter 3. The source produces photons at 854 nm and reaches a single-mode pair rate of $7.2 \times 10^4 \, \frac{\text{pairs}}{\text{s mW}}$, for a pump power of up to 20 mW. This is an improvement in the brightness of 1.6 compared to the previous version of the

source [72]. One photon of the pair is resonant to the $P_{3/2}$ to $D_{5/2}$ transition in $^{40}Ca^{+}$. Additionally, the signal-to-background ratio (SBR) is improved, and the stabilisation is much more reliable. The source reaches fidelities with a maximally entangled state of up to 99 %, and we can choose between the $|\Psi^{+}\rangle$ and $|\Psi^{-}\rangle$ Bell state or any phase in-between.

To use our source, for example, in quantum networks, the entangled photon pairs must be transmitted over long distances. The fibre attenuation at the photon wavelength is here the main limitation. Our solution to this problem is QFC, where one photon is converted to the low loss, low-dispersion wavelength range at 1550 nm. In chapter 4, we showed the preservation of the entanglement between the photons of a pair in four different settings with distances up to 40 km. We also demonstrated the back conversion to 854 nm with the same converter. The results revealed that the conversion process and the long distances do not influence the fidelity of the state and that we reached the maximum possible fidelity in all settings only limited by the SBR of the source itself. By employing this interface, we could extend our quantum network infrastructure towards further fundamental operations, like the shown teleportation measurement described in chapter 5. In chapter 5, we presented our protocol for an atom-photon entanglement transfer and a full quantum state teleportation measurement, using all four Bell states. Both measurements are based on the heralded absorption of one photon of a pair. In our protocol, we operate the ion in the receiver mode of the programmable atom-photon quantum interface introduced in [18]. Additionally, we demonstrated the atom-photon entanglement transfer in three different settings, including QFC and a metropolitan fibre. In chapter 6, we used the protocol to measure teleportation from a qubit stored on the ion to a single photon. The measurement was also performed in three different settings, including QFC and a metropolitan fibre. In both cases, QFC extends our protocol to the telecom wavelength range and enables us to bridge large distances. The conversion, as well as the metropolitan fibre, influence the state fidelities of the transfer and the process fidelity of the teleportation only slightly.

7.2 Discussion & Outlook

The long-term goal for quantum communication is to realise a worldwide quantum internet. One crucial step towards this goal is the realisation of a quantum repeater, for which efficient light-matter interfaces are essential. Our photon pair source and the presented teleportation protocol aim precisely in this direction. Furthermore, a full quantum

teleportation, which uses all four Bell states, is an important communication protocol once a connection between two parties is established. The qubit rate and fidelity have to be maximised for all network operations. In the case of our source, both parameters are connected: If we increase the qubit rate by increasing the pump power, the fidelity decreases, which has implications for further improvements. Increasing the qubit rate by increasing the pump power will lower the state fidelity. Therefore, in order to increase the efficiency and maintain high fidelity, it is only possible to reduce losses in the photon paths, for example, by optimising the spacial beam shape of the output of the source or by repairing two lossy splices, which decrease the coupling to the ion to 85 %. Another possibility to improve the source is the replacement of the non-optimal flat mirror, which will decrease losses inside the resonator and increase the photon-pair escape probability.

Further improvements can be reached by modifying the length of the photon wave packet by redesigning the resonator, where the optimal parameters depend on the application and the technical limitations of the resonator. For example, shorter photonic wave packets would improve the SBR because of less temporal overlap between two subsequent photons and hence less accidental coincidences. At the same time, this shortening would reduce the spectral overlap with the ion and would thereby lower the absorption probability. Conversely, longer photonic wave packets would optimise the absorption signal but increase the background of accidental coincidences.

Apart from the source, there is great potential for improvement, especially in the ion experiment. Here we have high fidelities but very low absorption rates. Even the best-achieved detection efficiency at 854 nm with in-vacuum lenses is only 0.024 [19]. An optical resonator around the ion would exploit the vacuum-modification effects to enhance the emission into and the absorption from a specific optical mode. Schupp et al. [131] have shown a setup with a 20 mm long cavity resonant to the $P_{3/2}$ - $D_{5/2}$ transition. They could demonstrate strongly increased coupling efficiency, but their operations are still slow because of the large cavity size. We are working on a new trap with a ~ 100 times shorter fibre cavity resonant with the mentioned transition. In the teleportation protocol, this cavity would drastically increase the absorption of incoming photons. Another improvement would be to increase the collection efficiency of the heralding 393 nm photons. This improvement is possible with a second cavity, resonant to the $P_{3/2}$ - $S_{1/2}$ transition. Placing one fibre cavity around the ion is already challenging due to the dielectric surface, which disturbs the electric field of the trap. A second resonator for the heralds would be even more challenging because UV optics are generally harder to handle.

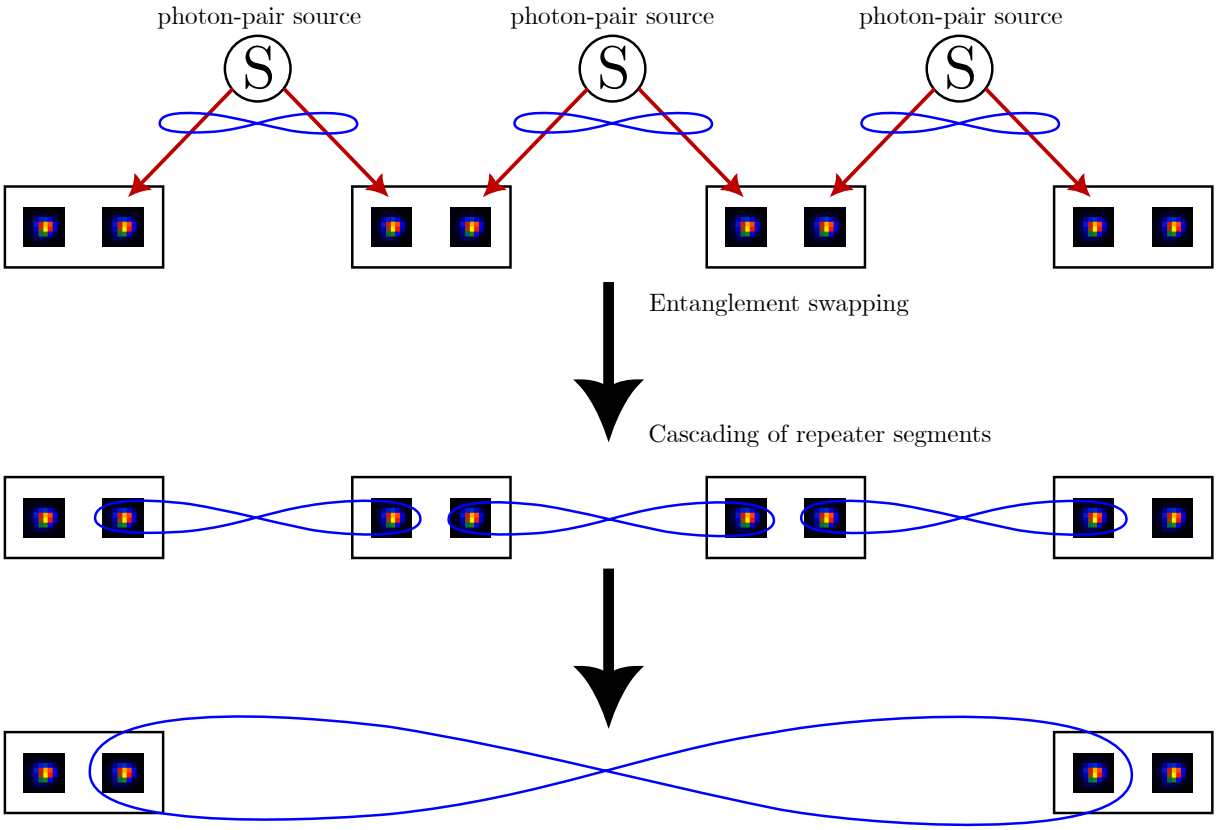

Figure 7.1: Quantum repeater scheme with SPDC sources. The scheme starts with an entangled photon-pair source in between two stationary nodes. Each node consists of an ion trap with two ions. First, entanglement between the inner ions are generated through heralded absorption. In the next step, several repeater nodes are cascaded, and entanglement between the outer nodes is established via further swapping operations by local gates between two ions.

The increased absorption probability through the implementation of a fibre cavity resonant to the $P_{3/2}$ - $D_{5/2}$ transition would also enable repeater operations as presented in figure 7.1. If the second photon is converted back to the ion wavelength after, for example, the metropolitan fibre, it can be absorbed by a second ion, establishing ion-ion entanglement. This entanglement swapping is the basic function of a quantum repeater. Trapping a second ion and performing entanglement swapping is straightforward and was already shown [147]. For the realisation of a repeater, the source would be placed between two ion traps, with two ions each. Then, we would apply the described protocol for entangling the two inner ions. Once the other ion is entangled similarly, the entanglement can be swapped over the whole distance. The heralding enables thereby asynchronous operation.

The main limitation of the mentioned scheme is the detection probability of the herald. Therefore, a scheme which only uses the emission from the ion has some benefits. In this protocol, one would use the direct emission of a photon from the ion [71, 84]. In figure 7.1, the direction of the red arrows is reversed, and the source is replaced by a BSM. The BSM swaps the entanglement from ion-photon to ion-ion entanglement. One drawback of this scheme is that, so far, only a partial Bell state analysis could be performed for photonic qubits[148, 39]. In these experiments, two of the four Bell states or, probabilistically, three Bell states [149] could be detected. The efficiency of these methods is 50 %, the optimum when using only linear optics [150]. To detect all four Bell states, hyperentanglement is needed [151].

Another use case of the source would be to create hybrid entanglement by entangling a trapped ion with a colour centre in diamond, for example, a negatively-charged tin-vacancy centre (SnV^-) [152, 153]. We could use our protocol and the conversion process as described on the ion side. For the SnV^-, another converter is needed to transfer the emitted photons to the same wavelength in the telecom range. A BSM between both telecom photons will then entangle the ion with the colour centre. Special care has to be taken on the spectral properties of the photons, mainly their linewidth and temporal profile. The natural linewidth of the SnV^- is 20 MHz and thus similar to the linewidth of the source. Therefore, a HOM measurement should show a sufficient interference contrast.

7.3 Conclusion

In the detailed investigations of this work, we improved the brightness, the SBR and the stability of the source. We could show the feasibility of the entanglement distribution over long distances, including controlling the polarisation of a metropolitan fibre. Furthermore, we demonstrated, for our knowledge for the first time, full quantum state teleportation, using all four Bell states, from a single trapped $^{40}Ca^+$ to a polarisation qubit of a SPDC photon. Several future improvements are readily identified. As the next step, we will investigate protocols in absorption and emission at 854 nm and one fibre resonator around the ion, as described above. The knowledge gained can also be transferred and used there. In summary, the $^{40}Ca^+$ platform has enormous potential as a network node or a quantum repeater and for the mentioned protocols.

Bibliography

[1] Kimble, H. J. The quantum internet. *Nature* **453**, 1023–1030 (2008). URL https://doi.org/10.1038/nature07127.

[2] Wehner, S., Elkouss, D. & Hanson, R. Quantum internet: A vision for the road ahead. *Science* **362**, eaam9288 (2018). URL https://www.science.org/doi/abs/10.1126/science.aam9288.

[3] Jiang, L., Taylor, J. M., Sørensen, A. S. & Lukin, M. D. Distributed quantum computation based on small quantum registers. *Phys. Rev. A* **76**, 062323 (2007). URL https://link.aps.org/doi/10.1103/PhysRevA.76.062323.

[4] Monroe, C. *et al.* Large-scale modular quantum-computer architecture with atomic memory and photonic interconnects. *Phys. Rev. A* **89**, 022317 (2014). URL https://link.aps.org/doi/10.1103/PhysRevA.89.022317.

[5] Briegel, H.-J., Dür, W., Cirac, J. I. & Zoller, P. Quantum repeaters: The role of imperfect local operations in quantum communication. *Phys. Rev. Lett.* **81**, 5932–5935 (1998). URL https://link.aps.org/doi/10.1103/PhysRevLett.81.5932.

[6] Ekert, A. K. Quantum cryptography based on bell's theorem. *Phys. Rev. Lett.* **67**, 661–663 (1991). URL https://link.aps.org/doi/10.1103/PhysRevLett.67.661.

[7] Proctor, T. J., Knott, P. A. & Dunningham, J. A. Multiparameter estimation in networked quantum sensors. *Phys. Rev. Lett.* **120**, 080501 (2018). URL https://link.aps.org/doi/10.1103/PhysRevLett.120.080501.

[8] Komar, P. *et al.* A quantum network of clocks. *Nature Physics* **10**, 582–587 (2014). URL https://doi.org/10.1038/nphys3000.

[9] Berera, A. & Calderón-Figueroa, J. Viability of quantum communication across interstellar distances. *Phys. Rev. D* **105**, 123033 (2022). URL https://link.aps.org/doi/10.1103/PhysRevD.105.123033.

[10] DiVincenzo, D. P. The physical implementation of quantum computation. *Fortschritte der Physik* **48**, 771–783 (2000). URL https://doi.org/10.1002/1521-3978(200009)48:9/11<771::AID-PROP771>3.0.CO;2-E.

[11] Stute, A. *et al.* Tunable ion–photon entanglement in an optical cavity. *Nature* **485**, 482–485 (2012). URL https://doi.org/10.1038/nature11120.

[12] Krutyanskiy, V. *et al.* Light-matter entanglement over 50 km of optical fibre. *npj Quantum Information* **5**, 1–5 (2019). URL https://doi.org/10.1038/s41534-019-0186-3.

[13] Begley, S., Vogt, M., Gulati, G. K., Takahashi, H. & Keller, M. Optimized multi-ion cavity coupling. *Phys. Rev. Lett.* **116**, 223001 (2016). URL https://link.aps.org/doi/10.1103/PhysRevLett.116.223001.

[14] Blinov, B. B., Moehring, D. L., Duan, L.-M. & Monroe, C. Observation of entanglement between a single trapped atom and a single photon. *Nature* **428**, 153–157 (2004). URL https://doi.org/10.1038/nature02377.

[15] Stute, A. *et al.* Quantum-state transfer from an ion to a photon. *Nature photonics* **7**, 219–222 (2013). URL https://doi.org/10.1038/nphoton.2012.358.

[16] Kurz, C. *et al.* Experimental protocol for high-fidelity heralded photon-to-atom quantum state transfer. *Nature communications* **5**, 1–5 (2014). URL https://doi.org/10.1038/ncomms6527.

[17] Kalb, N., Reiserer, A., Ritter, S. & Rempe, G. Heralded storage of a photonic quantum bit in a single atom. *Phys. Rev. Lett.* **114**, 220501 (2015). URL https://link.aps.org/doi/10.1103/PhysRevLett.114.220501.

[18] Kurz, C., Eich, P., Schug, M., Müller, P. & Eschner, J. Programmable atom-photon quantum interface. *Physical Review A* **93** (2016). URL https://link.aps.org/doi/10.1103/PhysRevA.93.062348.

[19] Stephenson, L. J. *et al.* High-rate, high-fidelity entanglement of qubits across an elementary quantum network. *Phys. Rev. Lett.* **124**, 110501 (2020). URL https://link.aps.org/doi/10.1103/PhysRevLett.124.110501.

[20] Wang, Y. *et al.* Single-qubit quantum memory exceeding ten-minute coherence time. *Nature Photonics* **11**, 646–650 (2017). URL https://doi.org/10.1038/s41566-017-0007-1.

[21] Langer, C. *et al.* Long-lived qubit memory using atomic ions. *Phys. Rev. Lett.* **95**, 060502 (2005). URL https://link.aps.org/doi/10.1103/PhysRevLett.95.060502.

[22] Ruster, T. *et al.* A long-lived zeeman trapped-ion qubit. *Applied Physics B* **122**, 1–7 (2016). URL https://doi.org/10.1007/s00340-016-6527-4.

[23] Wang, P. *et al.* Single ion qubit with estimated coherence time exceeding one hour. *Nature communications* **12**, 1–8 (2021). URL https://doi.org/10.1038/s41467-020-20330-w.

[24] Bruzewicz, C. D., Chiaverini, J., McConnell, R. & Sage, J. M. Trapped-ion quantum computing: Progress and challenges. *Applied Physics Reviews* **6**, 021314 (2019). URL https://doi.org/10.1063/1.5088164.

[25] Friis, N. *et al.* Observation of entangled states of a fully controlled 20-qubit system. *Phys. Rev. X* **8**, 021012 (2018). URL https://link.aps.org/doi/10.1103/PhysRevX.8.021012.

[26] Brewer, S. M. *et al.* $^{27}\mathrm{al}^{+}$ quantum-logic clock with a systematic uncertainty below 10^{-18}. *Phys. Rev. Lett.* **123**, 033201 (2019). URL https://link.aps.org/doi/10.1103/PhysRevLett.123.033201.

[27] Gilmore, K. A. *et al.* Quantum-enhanced sensing of displacements and electric fields with two-dimensional trapped-ion crystals. *Science* **373**, 673–678 (2021). URL https://www.science.org/doi/abs/10.1126/science.abi5226.

[28] Marciniak, C. D. *et al.* Optimal metrology with programmable quantum sensors. *Nature* **603**, 604–609 (2022). URL https://doi.org/10.1038/s41586-022-04435-4.

[29] Tittel, W. & Weihs, G. Photonic entanglement for fundamental tests and quantum communication (2001). URL https://arxiv.org/abs/quant-ph/0107156.

[30] Lukens, J. M. & Lougovski, P. Frequency-encoded photonic qubits for scalable quantum information processing. *Optica* **4**, 8–16 (2017). URL https://opg.optica.org/optica/abstract.cfm?URI=optica-4-1-8.

[31] Brendel, J., Gisin, N., Tittel, W. & Zbinden, H. Pulsed energy-time entangled twin-photon source for quantum communication. *Phys. Rev. Lett.* **82**, 2594–2597 (1999). URL https://link.aps.org/doi/10.1103/PhysRevLett.82.2594.

[32] Mair, A., Vaziri, A., Weihs, G. & Zeilinger, A. Entanglement of the orbital angular momentum states of photons. *Nature* **412**, 313–316 (2001). URL https://doi.org/10.1038/35085529.

[33] Yin, J. *et al.* Quantum teleportation and entanglement distribution over 100-kilometre free-space channels. *Nature* **488**, 185–188 (2012). URL https://doi.org/10.1038/nature11332.

[34] Ma, X.-S. *et al.* Quantum teleportation over 143 kilometres using active feed-forward. *Nature* **489**, 269–273 (2012). URL https://doi.org/10.1038/nature11472.

[35] Ren, J.-G. *et al.* Ground-to-satellite quantum teleportation. *Nature* **549**, 70–73 (2017). URL https://doi.org/10.1038/nature23675.

[36] Tamura, Y. *et al.* Lowest-ever 0.1419-db/km loss optical fiber. In *Optical Fiber Communication Conference Postdeadline Papers*, Th5D.1 (Optica Publishing Group, 2017). URL https://opg.optica.org/abstract.cfm?URI=OFC-2017-Th5D.1.

[37] Li, M.-J. & Hayashi, T. Chapter 1 - advances in low-loss, large-area, and multicore fibers. In Willner, A. E. (ed.) *Optical Fiber Telecommunications VII*, 3–50 (Academic Press, 2020). URL https://www.sciencedirect.com/science/article/pii/B9780128165027000014.

[38] Wootters, W. K. & Zurek, W. H. A single quantum cannot be cloned. *Nature* **299**, 802–803 (1982). URL https://doi.org/10.1038/299802a0.

[39] Bouwmeester, D. *et al.* Experimental quantum teleportation. *Nature* **390**, 575–579 (1997). URL https://doi.org/10.1038/37539.

[40] Żukowski, M., Zeilinger, A., Horne, M. A. & Ekert, A. K. "event-ready-detectors" bell experiment via entanglement swapping. *Phys. Rev. Lett.* **71**, 4287–4290 (1993). URL https://link.aps.org/doi/10.1103/PhysRevLett.71.4287.

[41] Pan, J.-W., Bouwmeester, D., Weinfurter, H. & Zeilinger, A. Experimental entanglement swapping: Entangling photons that never interacted. *Phys. Rev. Lett.* **80**,

3891–3894 (1998). URL https://link.aps.org/doi/10.1103/PhysRevLett.80.3891.

[42] Sangouard, N., Simon, C., de Riedmatten, H. & Gisin, N. Quantum repeaters based on atomic ensembles and linear optics. *Rev. Mod. Phys.* **83**, 33–80 (2011). URL https://link.aps.org/doi/10.1103/RevModPhys.83.33.

[43] Jacobs, B. C., Pittman, T. B. & Franson, J. D. Quantum relays and noise suppression using linear optics. *Phys. Rev. A* **66**, 052307 (2002). URL https://link.aps.org/doi/10.1103/PhysRevA.66.052307.

[44] Collins, D., Gisin, N. & de Riedmatten, H. Quantum relays for long distance quantum cryptography. *Journal of Modern Optics* **52**, 735–753 (2005). URL https://doi.org/10.1080/09500340412331283633.

[45] Munro, W. J., Azuma, K., Tamaki, K. & Nemoto, K. Inside quantum repeaters. *IEEE Journal of Selected Topics in Quantum Electronics* **21**, 78–90 (2015). URL https://doi.org/10.1109/JSTQE.2015.2392076.

[46] Muralidharan, S. *et al.* Optimal architectures for long distance quantum communication. *Scientific Reports* **6**, 20463 (2016). URL https://doi.org/10.1038/srep20463.

[47] Duan, L.-M. & Monroe, C. Colloquium: Quantum networks with trapped ions. *Rev. Mod. Phys.* **82**, 1209–1224 (2010). URL https://link.aps.org/doi/10.1103/RevModPhys.82.1209.

[48] Uphoff, M., Brekenfeld, M., Rempe, G. & Ritter, S. An integrated quantum repeater at telecom wavelength with single atoms in optical fiber cavities. *Applied Physics B* **122**, 46 (2016). URL https://doi.org/10.1007/s00340-015-6299-2.

[49] Sangouard, N., Dubessy, R. & Simon, C. Quantum repeaters based on single trapped ions. *Phys. Rev. A* **79**, 042340 (2009). URL https://link.aps.org/doi/10.1103/PhysRevA.79.042340.

[50] Avis, G. *et al.* Requirements for a processing-node quantum repeater on a real-world fiber grid (2022). URL https://arxiv.org/abs/2207.10579.

[51] Krutyanskiy, V. *et al.* A telecom-wavelength quantum repeater node based on a trapped-ion processor (2022). URL https://arxiv.org/abs/2210.05418.

[52] Kumar, P. Quantum frequency conversion. *Opt. Lett.* **15**, 1476–1478 (1990). URL https://opg.optica.org/ol/abstract.cfm?URI=ol-15-24-1476.

[53] Huang, J. & Kumar, P. Observation of quantum frequency conversion. *Phys. Rev. Lett.* **68**, 2153–2156 (1992). URL https://link.aps.org/doi/10.1103/PhysRevLett.68.2153.

[54] Yu, Y. *et al.* Entanglement of two quantum memories via fibres over dozens of kilometres. *Nature* **578**, 240–245 (2020). URL https://doi.org/10.1038/s41586-020-1976-7.

[55] Weber, J. H. *et al.* Two-photon interference in the telecom c-band after frequency conversion of photons from remote quantum emitters. *Nature nanotechnology* **14**, 23–26 (2019). URL https://doi.org/10.1038/s41565-018-0279-8.

[56] Craddock, A. N. *et al.* Quantum interference between photons from an atomic ensemble and a remote atomic ion. *Phys. Rev. Lett.* **123**, 213601 (2019). URL https://link.aps.org/doi/10.1103/PhysRevLett.123.213601.

[57] Shannon, C. E. Communication theory of secrecy systems. *The Bell System Technical Journal* **28**, 656–715 (1949). URL https://doi.org/10.1002/j.1538-7305.1949.tb00928.x.

[58] Bennett, C. H. *et al.* Teleporting an unknown quantum state via dual classical and einstein-podolsky-rosen channels. *Phys. Rev. Lett.* **70**, 1895–1899 (1993). URL https://link.aps.org/doi/10.1103/PhysRevLett.70.1895.

[59] Sherson, J. F. *et al.* Quantum teleportation between light and matter. *Nature* **443**, 557–560 (2006). URL https://doi.org/10.1038/nphoton.2016.180.

[60] Chen, Y.-A. *et al.* Memory-built-in quantum teleportation with photonic and atomic qubits. *Nature Physics* **4**, 103–107 (2008). URL https://doi.org/10.1038/nphys832.

[61] Bussières, F. *et al.* Quantum teleportation from a telecom-wavelength photon to a solid-state quantum memory. *Nature Photonics* **8**, 775–778 (2014). URL https://doi.org/10.1038/nphoton.2014.215.

[62] Nölleke, C. *et al.* Efficient teleportation between remote single-atom quantum memories. *Phys. Rev. Lett.* **110**, 140403 (2013). URL https://link.aps.org/doi/10.1103/PhysRevLett.110.140403.

[63] Langenfeld, S. *et al.* Quantum teleportation between remote qubit memories with only a single photon as a resource. *Phys. Rev. Lett.* **126**, 130502 (2021). URL https://link.aps.org/doi/10.1103/PhysRevLett.126.130502.

[64] Bao, X.-H. *et al.* Quantum teleportation between remote atomic-ensemble quantum memories. *Proceedings of the National Academy of Sciences* **109**, 20347–20351 (2012). URL https://www.pnas.org/doi/abs/10.1073/pnas.1207329109.

[65] Pfaff, W. *et al.* Unconditional quantum teleportation between distant solid-state quantum bits. *Science* **345**, 532–535 (2014). URL https://www.science.org/doi/abs/10.1126/science.1253512.

[66] Hermans, S. L. N. *et al.* Qubit teleportation between non-neighbouring nodes in a quantum network. *Nature* **605**, 663–668 (2022). URL https://doi.org/10.1038/s41586-022-04697-y.

[67] Dynes, J. F. *et al.* Cambridge quantum network. *npj Quantum Information* **5**, 1–8 (2019). URL https://doi.org/10.1038/s41534-019-0221-4.

[68] Chen, J.-P. *et al.* Twin-field quantum key distribution over a 511 km optical fibre linking two distant metropolitan areas. *Nature Photonics* **15**, 570–575 (2021). URL https://doi.org/10.1038/s41566-021-00828-5.

[69] Valivarthi, R. *et al.* Quantum teleportation across a metropolitan fibre network. *Nature Photonics* **10**, 676–680 (2016). URL https://doi.org/10.1038/nphoton.2016.180.

[70] Bock, M. *Polarization-Preserving Quantum Frequency Conversion for Trapped-Atom based Quantum Networks.* Ph.D. thesis, Saarland University (2020). URL http://dx.doi.org/10.22028/D291-35322.

[71] Bock, M. *et al.* High-fidelity entanglement between a trapped ion and a telecom photon via quantum frequency conversion. *Nature communications* **9**, 1–7 (2018). URL https://doi.org/10.1038/s41467-018-04341-2.

[72] Kucera, S. *Experimental distribution of entanglement in ion-photon quantum networks : photon-pairs as resource.* Ph.D. thesis, Saarland University (2019). URL https://dx.doi.org/10.22028/D291-28393.

[73] Arensk̈otter, E., Kucera, S. & Eschner, J. Polarization-entangled photon pairs from a cavity-enhanced down-conversion source in sagnac configuration. In *2017*

Conference on Lasers and Electro-Optics Europe & European Quantum Electronics Conference (CLEO/Europe-EQEC), 1–1 (2017). URL https://doi.org/10.1109/CLEOE-EQEC.2017.8087429.

[74] Arenskötter, E. *et al.* Quantum state teleportation from a single ion to a single photon by heralded absorption. In *Conference on Lasers and Electro-Optics*, FM2H.6 (Optica Publishing Group, 2018). URL https://opg.optica.org/abstract.cfm?URI=CLEO_QELS-2018-FM2H.6.

[75] Arenskötter, E. *et al.* Telecom quantum photonic interface for a $^{40}Ca^{+}$ single-ion quantum memory. *npj Quantum Information* **9**, 34 (2023). URL https://doi.org/10.1038/s41534-023-00701-z.

[76] Arenskötter, E. *et al.* Quantum teleportation with full bell-basis detection between a $^{40}Ca^{+}$ ion and a single photon (2023). URL https://arxiv.org/abs/2301.06091.

[77] Leibfried, D., Blatt, R., Monroe, C. & Wineland, D. Quantum dynamics of single trapped ions. *Rev. Mod. Phys.* **75**, 281–324 (2003). URL https://link.aps.org/doi/10.1103/RevModPhys.75.281.

[78] HighFinesse. *WS7-60 Series* (2021). URL https://www.highfinesse.com/en/wavelengthmeter/wavelengthmeter-further-information/technical-information-wavelengthmeter-ws7-60-series.pdf.

[79] Jin, J. & Church, D. A. Precision lifetimes for the ca^{+} 4p ^{2}p levels: Experiment challenges theory at the 1% level. *Phys. Rev. Lett.* **70**, 3213–3216 (1993). URL https://link.aps.org/doi/10.1103/PhysRevLett.70.3213.

[80] Kreuter, A. *et al.* Experimental and theoretical study of the $3d\,^{2}d$–level lifetimes of $^{40}Ca^{+}$. *Phys. Rev. A* **71**, 032504 (2005). URL https://link.aps.org/doi/10.1103/PhysRevA.71.032504.

[81] Huwer, J. Experimental tools for quantum networking operations with single photons and single ions (2013). URL http://dx.doi.org/10.22028/D291-22940.

[82] Kurz, C. *Quantum networking with single ions and single photons interfaced in free space*. Ph.D. thesis, Saarland University (2015). URL https://dx.doi.org/10.22028/D291-23091.

[83] Kreis, M. *Spectral properties of single Raman-scattered photons*. Ph.D. thesis, Saarland University (2022). URL http://dx.doi.org/10.22028/D291-37772.

[84] Eich, P. *Single-ion based quantum interfaces for quantum-network applications*. Ph.D. thesis, Saarland University (2019). URL http://dx.doi.org/10.22028/D291-28381.

[85] Müller, P. *Raman scattering of single photons and its use for quantum networks and high-precision measurements*. Ph.D. thesis, Saarland University (2021). URL http://dx.doi.org/10.22028/D291-35347.

[86] Lam, H. *Suppression of magnetic-noise-induced decoherence in Zeeman trapped ion qubits.* Master's thesis, Saarland University (2021).

[87] Elshehy, O. *Permanent-magnet-based Zeeman field generation in an ion trap*. Master's thesis, Saarland University (2018).

[88] Earnshaw, S. On the nature of the molecular forces which regulate the constitution of the luminiferous ether. *Transactions of the Cambridge Philosophical Society* **7**, 97 (1848). URL https://ui.adsabs.harvard.edu/abs/1848TCaPS...7...97E.

[89] Schug, M. *Single photons from single ions: quantum interference and distant ion interaction*. Ph.D. thesis, Saarland University (2015). URL http://dx.doi.org/10.22028/D291-23094.

[90] Schuck, C. *Interfacing single ions and single photons for quantum networks*. Ph.D. thesis, ICFO - The Institute of Photonic Sciences (2009). URL https://dialnet.unirioja.es/servlet/tesis?codigo=258830.

[91] Zimmermann, K., Okhapkin, M. V., Herrera-Sancho, O. A. & Peik, E. Laser ablation loading of a radiofrequency ion trap. *Applied Physics B* **107**, 883–889 (2012). URL https://doi.org/10.1007/s00340-012-4884-1.

[92] Rohde, F. *Remote ion traps for quantum networking: Two-photon interference and correlations*. Ph.D. thesis, ICFO - The Institute of Photonic Sciences (2009). URL https://dialnet.unirioja.es/servlet/tesis?codigo=258849.

[93] Drever, R. W. P. *et al.* Laser phase and frequency stabilization using an optical resonator. *Applied Physics B* **31**, 97–105 (1983). URL https://doi.org/10.1007/BF00702605.

[94] Rohde, F. *et al.* A diode laser stabilization scheme for 40Ca+ single-ion spectroscopy. *Journal of Physics B: Atomic, Molecular and Optical Physics* **43**, 115401 (2010). URL https://dx.doi.org/10.1088/0953-4075/43/11/115401.

[95] Kreis, M. *Magnetfeldstabilisierung für Hochpräzise Einzelatom Spektroskopie*. Master's thesis, Saarland University (2014).

[96] Almendros, M. *Towards long-distance quantum communication*. Ph.D. thesis, Universitat Politècnica de Catalunya (UPC) (2010). URL https://dialnet.unirioja.es/servlet/tesis?codigo=237466.

[97] Kucera, S. *Digitale Laser-Leistungsstabilisierung für Einzelatomspektroskopie*. Diploma thesis, Saarland University (2013).

[98] Haase, A., Piro, N., Eschner, J. & Mitchell, M. W. Tunable narrowband entangled photon pair source for resonant single-photon single-atom interaction. *Opt. Lett.* **34**, 55–57 (2009). URL http://opg.optica.org/ol/abstract.cfm?URI=ol-34-1-55.

[99] Müller, P. & Eschner, J. Single calcium-40 ion as quantum memory for photon polarization: A case study. *Applied Physics B: Lasers and Optics* **114**, 303–306 (2014). URL https://doi.org/10.1007/s00340-013-5681-1.

[100] Luo, K.-H. *et al.* Direct generation of genuine single-longitudinal-mode narrowband photon pairs. *New Journal of Physics* **17**, 073039 (2015). URL https://dx.doi.org/10.1088/1367-2630/17/7/073039.

[101] Tsai, P.-J. & Chen, Y.-C. Ultrabright, narrow-band photon-pair source for atomic quantum memories. *Quantum Science and Technology* **3**, 034005 (2018). URL https://dx.doi.org/10.1088/2058-9565/aa86e7.

[102] Lenhard, A. *et al.* Telecom-heralded single-photon absorption by a single atom. *Physical Review A - Atomic, Molecular, and Optical Physics* **92**, 1–8 (2015). URL https://link.aps.org/doi/10.1103/PhysRevA.92.063827.

[103] Kwiat, P. G., Eberhard, P. H., Steinberg, A. M. & Chiao, R. Y. Proposal for a loophole-free bell inequality experiment. *Phys. Rev. A* **49**, 3209–3220 (1994). URL https://link.aps.org/doi/10.1103/PhysRevA.49.3209.

[104] Fiorentino, M., Messin, G., Kuklewicz, C. E., Wong, F. N. C. & Shapiro, J. H. Generation of ultrabright tunable polarization entanglement without spatial, spectral, or temporal constraints. *Phys. Rev. A* **69**, 041801 (2004). URL https://link.aps.org/doi/10.1103/PhysRevA.69.041801.

[105] Fedrizzi, A., Herbst, T., Poppe, A., Jennewein, T. & Zeilinger, A. A wavelength-tunable fiber-coupled source of narrowband entangled photons. *Opt. Express*

15, 15377–15386 (2007). URL http://opg.optica.org/oe/abstract.cfm?URI=oe-15-23-15377.

[106] New, G. *Introduction to nonlinear optics* (Cambridge University Press, 2011).

[107] Kleinman, D. A. Nonlinear dielectric polarization in optical media. *Phys. Rev.* **126**, 1977–1979 (1962). URL https://link.aps.org/doi/10.1103/PhysRev.126.1977.

[108] Boulanger, B. *et al.* Relative sign and absolute magnitude of d(2) nonlinear coefficients of ktp from second-harmonic-generation measurements. *J. Opt. Soc. Am. B* **11**, 750–757 (1994). URL https://opg.optica.org/josab/abstract.cfm?URI=josab-11-5-750.

[109] Boyd, R. W. *Nonlinear optics* (Academic press, 2020).

[110] Ou, Z.-Y. J. *Multi-photon quantum interference*, vol. 43 (Springer, 2007).

[111] Shen, Y.-R. Principles of nonlinear optics (1984).

[112] Christ, A., Brecht, B., Mauerer, W. & Silberhorn, C. Theory of quantum frequency conversion and type-ii parametric down-conversion in the high-gain regime. *New Journal of Physics* **15**, 053038 (2013). URL https://dx.doi.org/10.1088/1367-2630/15/5/053038.

[113] Meschede, D. *Optik, Licht und Laser* (Springer-Verlag, 2009).

[114] Eckardt, R. C., Nabors, C. D., Kozlovsky, W. J. & Byer, R. L. Optical parametric oscillator frequency tuning and control. *J. Opt. Soc. Am. B* **8**, 646–667 (1991). URL https://opg.optica.org/josab/abstract.cfm?URI=josab-8-3-646.

[115] Pomarico, E., Sanguinetti, B., Osorio, C. I., Herrmann, H. & Thew, R. T. Engineering integrated pure narrow-band photon sources. *New Journal of Physics* **14**, 033008 (2012). URL https://dx.doi.org/10.1088/1367-2630/14/3/033008.

[116] Kuzucu, O. & Wong, F. N. C. Pulsed sagnac source of narrow-band polarization-entangled photons. *Phys. Rev. A* **77**, 032314 (2008). URL https://link.aps.org/doi/10.1103/PhysRevA.77.032314.

[117] Saleh, B. E. A. & Teich, M. C. *Optik und Photonik* (John Wiley & Sons, 2020).

[118] Wolfgramm, F. *Atomic quantum metrology with narrowband entangled and squeezed states of light*. Ph.D. thesis (2011). URL http://hdl.handle.net/2117/94721.

[119] Predojević, A., Zhai, Z., Caballero, J. M. & Mitchell, M. W. Rubidium resonant squeezed light from a diode-pumped optical-parametric oscillator. *Phys. Rev. A* **78**, 063820 (2008). URL https://link.aps.org/doi/10.1103/PhysRevA.78.063820.

[120] Le Targat, R., Zondy, J.-J. & Lemonde, P. 75%-efficiency blue generation from an intracavity ppktp frequency doubler. *Optics Communications* **247**, 471–481 (2005). URL https://www.sciencedirect.com/science/article/pii/S0030401804012374.

[121] Arensk̈otter, E. *Photonenpaarquelle für Einzelatom-Einzelphoton Wechselwirkung*. Master's thesis, Saarland University (2016).

[122] Sansoni, L. *et al.* A two-channel, spectrally degenerate polarization entangled source on chip. *npj Quantum Information* **3**, 1–5 (2017). URL https://doi.org/10.1038/s41534-016-0005-z.

[123] Palittapongarnpim, P., MacRae, A. & Lvovsky, A. I. Note: A monolithic filter cavity for experiments in quantum optics. *Review of Scientific Instruments* **83**, 066101 (2012). URL https://doi.org/10.1063/1.4726458.

[124] Ahlrichs, A., Berkemeier, C., Sprenger, B. & Benson, O. A monolithic polarization-independent frequency-filter system for filtering of photon pairs. *Applied Physics Letters* **103**, 241110 (2013). URL https://doi.org/10.1063/1.4846316.

[125] Slattery, O., Ma, L., Zong, K. & Tang, X. Background and review of cavity-enhanced spontaneous parametric down-conversion. *Journal of Research of the National Institute of Standards and Technology* **124**, 1 (2019).

[126] Niizeki, K. *et al.* Ultrabright narrow-band telecom two-photon source for long-distance quantum communication. *Applied Physics Express* **11**, 042801 (2018). URL https://dx.doi.org/10.7567/APEX.11.042801.

[127] Moqanaki, A., Massa, F. & Walther, P. Novel single-mode narrow-band photon source of high brightness tuned to cesium d2 line. *APL Photonics* **4**, 090804 (2019). URL https://doi.org/10.1063/1.5095616.

[128] Hradil, Z. Quantum-state estimation. *Phys. Rev. A* **55**, R1561–R1564 (1997). URL https://link.aps.org/doi/10.1103/PhysRevA.55.R1561.

[129] James, D. F. V., Kwiat, P. G., Munro, W. J. & White, A. G. Measurement of qubits. *Phys. Rev. A* **64**, 052312 (2001). URL https://link.aps.org/doi/10.1103/PhysRevA.64.052312.

[130] Meyer, H. M. *et al.* Direct photonic coupling of a semiconductor quantum dot and a trapped ion. *Phys. Rev. Lett.* **114**, 123001 (2015). URL https://link.aps.org/doi/10.1103/PhysRevLett.114.123001.

[131] Schupp, J. *et al.* Interface between trapped-ion qubits and traveling photons with close-to-optimal efficiency. *PRX Quantum* **2**, 020331 (2021). URL https://link.aps.org/doi/10.1103/PRXQuantum.2.020331.

[132] Krutyanskiy, V., Meraner, M., Schupp, J. & Lanyon, B. P. Polarisation-preserving photon frequency conversion from a trapped-ion-compatible wavelength to the telecom c-band. *Applied Physics B* **123**, 1–9 (2017). URL https://doi.org/10.1007/s00340-017-6806-8.

[133] Ikuta, R. *et al.* Polarization insensitive frequency conversion for an atom-photon entanglement distribution via a telecom network. *Nature communications* **9**, 1–8 (2018). URL https://doi.org/10.1038/s41467-018-04338-x.

[134] van Leent, T. *et al.* Long-distance distribution of atom-photon entanglement at telecom wavelength. *Phys. Rev. Lett.* **124**, 010510 (2020). URL https://link.aps.org/doi/10.1103/PhysRevLett.124.010510.

[135] Zaske, S., Lenhard, A. & Becher, C. Efficient frequency downconversion at the single photon level from the red spectral range to the telecommunications c-band. *Opt. Express* **19**, 12825–12836 (2011). URL https://opg.optica.org/oe/abstract.cfm?URI=oe-19-13-12825.

[136] Kuo, P. S., Pelc, J. S., Langrock, C. & Fejer, M. M. Using temperature to reduce noise in quantum frequency conversion. *Opt. Lett.* **43**, 2034–2037 (2018). URL https://opg.optica.org/ol/abstract.cfm?URI=ol-43-9-2034.

[137] Nufern. *Nufern 780 nm Select Cut-OffSingle-Mode Fiber* (2006). URL http://princetel.com/datasheets/nufern_780hp.pdf.

[138] Corning. *Corning® SMF-28® ULL Optical Fiber* (2014). URL https://www.corning.com/media/worldwide/coc/documents/Fiber/SMF-28%20ULL.pdf.

[139] Hertel, I. V. & Schulz, C.-P. *Atome, Moleküle und optische Physik 1: Atome und Grundlagen ihrer Spektroskopie* (Springer-Verlag, 2017).

[140] Toyoda, K., Shiibara, H., Haze, S., Yamazaki, R. & Urabe, S. Experimental study of the coherence of a terahertz-separated metastable-state qubit in $^{40}Ca^{+}$. *Phys. Rev. A* **79**, 023419 (2009). URL https://link.aps.org/doi/10.1103/PhysRevA.79.023419.

[141] Chuang, I. L. & Nielsen, M. A. *Quantum Computation and Quantum Information* (Cambridge University Press, 2010).

[142] Brito, J., Kucera, S., Eich, P., Müller, P. & Eschner, J. Doubly heralded single-photon absorption by a single atom. *Applied Physics B: Lasers and Optics* **122**, 1–5 (2016). URL https://doi.org/10.1007/s00340-015-6276-9.

[143] Krutyanskiy, V. *et al.* Entanglement of trapped-ion qubits separated by 230 meters. *Phys. Rev. Lett.* **130**, 050803 (2023). URL https://link.aps.org/doi/10.1103/PhysRevLett.130.050803.

[144] Drmota, P. *et al.* Robust quantum memory in a trapped-ion quantum network node. *Phys. Rev. Lett.* **130**, 090803 (2023). URL https://link.aps.org/doi/10.1103/PhysRevLett.130.090803.

[145] Pogorelov, I. *et al.* Compact ion-trap quantum computing demonstrator. *PRX Quantum* **2**, 020343 (2021). URL https://link.aps.org/doi/10.1103/PRXQuantum.2.020343.

[146] Noel, C. *et al.* Measurement-induced quantum phases realized in a trapped-ion quantum computer. *Nature Physics* **18**, 760–764 (2022). URL https://doi.org/10.1038/s41567-022-01619-7.

[147] Riebe, M. *et al.* Deterministic entanglement swapping with an ion-trap quantum computer. *Nature Physics* **4**, 839–842 (2008). URL https://doi.org/10.1038/nphys1107.

[148] Mattle, K., Weinfurter, H., Kwiat, P. G. & Zeilinger, A. Dense coding in experimental quantum communication. *Phys. Rev. Lett.* **76**, 4656–4659 (1996). URL https://link.aps.org/doi/10.1103/PhysRevLett.76.4656.

[149] van Houwelingen, J. A. W., Brunner, N., Beveratos, A., Zbinden, H. & Gisin, N. Quantum teleportation with a three-bell-state analyzer. *Phys. Rev. Lett.* **96**, 130502 (2006). URL https://link.aps.org/doi/10.1103/PhysRevLett.96.130502.

[150] Lütkenhaus, N., Calsamiglia, J. & Suominen, K.-A. Bell measurements for teleportation. *Phys. Rev. A* **59**, 3295–3300 (1999). URL https://link.aps.org/doi/10.1103/PhysRevA.59.3295.

[151] Schuck, C., Huber, G., Kurtsiefer, C. & Weinfurter, H. Complete deterministic linear optics bell state analysis. *Phys. Rev. Lett.* **96**, 190501 (2006). URL https://link.aps.org/doi/10.1103/PhysRevLett.96.190501.

[152] Görlitz, J. *et al.* Spectroscopic investigations of negatively charged tin-vacancy centres in diamond. *New Journal of Physics* **22**, 013048 (2020). URL https://dx.doi.org/10.1088/1367-2630/ab6631.

[153] Trusheim, M. E. *et al.* Transform-limited photons from a coherent tin-vacancy spin in diamond. *Phys. Rev. Lett.* **124**, 023602 (2020). URL https://link.aps.org/doi/10.1103/PhysRevLett.124.023602.

Appendix

A Relationship between state and interferometer phase: Calculation

In order to see the dependence of the state phase on the interferometric phase and get an expression for it, we consider the setup shown in figure A.2. We first calculate an expression for the state phase and for the interferometer phase separately. Finally, we use the two expressions to express the state phase using the interferometer phase.

State phase

The total phase of the photonic state φ is the sum of the phase of the pump φ_p and the phase of the signal and idler photons $\varphi_{i,p}$:

$$\varphi = \varphi_p + \varphi_s + \varphi_i \tag{A.1}$$

The phase of the pump results directly from the optical path difference between the first BS and the conversion crystal plus an additional phase due to the HWP (thickness d_1, reflective index n_p)

$$\varphi_p = k_p \left(L_B - L_A\right) + \frac{d_1}{c} n_p \omega_p \,. \tag{A.2}$$

The path differences between conversion crystal and second BS determine the phase of the signal and the idler photons. The HWP (thickness d_2, refractive index $n_{s,i}$) gives rises to another phase-shift:

$$\varphi_{s,i} = k_{s,i} \left(L'_B - L'_A\right) + \frac{d_2}{c} n_{s,i} \omega_{s,i} \,. \tag{A.3}$$

Substituting the expressions for the phases in equation (A.1) yields

$$\varphi = k_p \left(L_B - L_A\right) + k_s \left(L'_B - L'_A\right) + k_i \left(L'_B - L'_A\right) + \frac{d_1}{c} n_p \omega_p + \frac{d_2}{c} \left(n_s \omega_s + n_i \omega_i\right) \,. \tag{A.4}$$

We then use the phase-matching condition for the SPDC process (3.7) and rewrite (A.4) to get

$$\varphi = \frac{\omega_p}{c} \left(\left(L_B + L'_B\right) - \left(L_A + L'_A\right) \right) + \frac{d_1}{c} n_p \omega_p + \frac{d_2}{c} \left(n_s \omega_s + n_i \omega_i\right) \,. \tag{A.5}$$

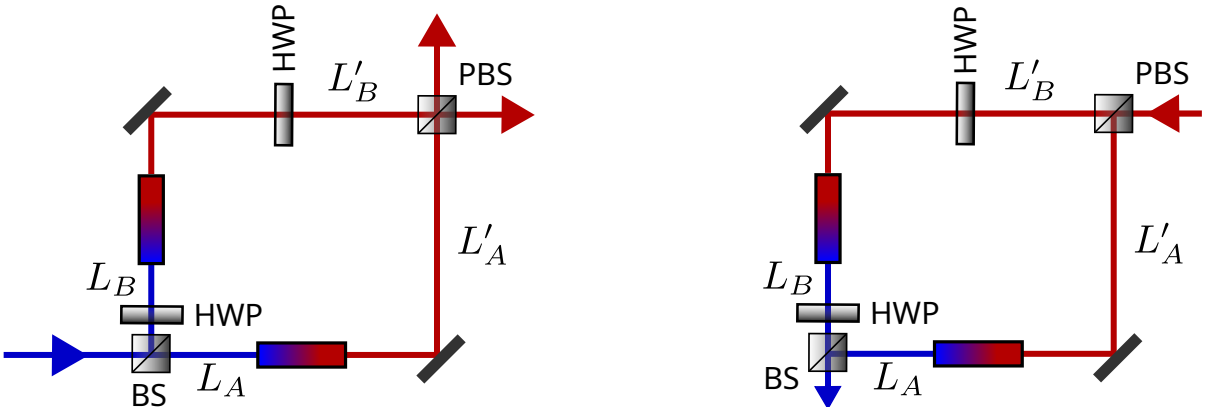

(a) photon path (b) SHG path

Figure A.2: Simplified schematic of the light path for calculating the phase factor of the photonic state. Adapted from [104].

Interferometer phase

To calculate an expression for the interferometer phase, we now repeat the previously made considerations with the expressions for the SHG instead of the SPDC. Both directions of the locking beam have vertical polarisation at the cavity mirror, and the crystal fulfils a quasi-phase-matching for a type-II SPDC process. We measured the polarisation of the produced SHG light and identified it as vertically polarised. Therefore, we have type-0 phase-matching for the SHG process.

The phase factor of the lock light is given as

$$\varphi_l = k_l \left(L'_B - L'_A\right) + \frac{d_2}{c} n_l \omega_l \tag{A.6}$$

The phase of the produced SHG light is given as

$$\varphi_{\mathrm{SHG}} = k_{\mathrm{SHG}} \left(L_B - L_A\right) + \frac{d_1}{c} n_{\mathrm{SHG}} \omega_{\mathrm{SHG}} \tag{A.7}$$

Since two red photons are needed to create one SHG photon, we get a factor of two in the phase of the lock light. The total phase is then given as

$$\varphi_{\mathrm{inter}} = \varphi_{\mathrm{SHG}} + 2\varphi_l \tag{A.8}$$

$$= k_{\mathrm{SHG}} \left(L_B - L_A\right) + 2k_l \left(L'_B - L'_A\right) + 2\frac{d_2}{c} n_l \omega_l + \frac{d_1}{c} n_{\mathrm{SHG}} \omega_{\mathrm{SHG}} \,. \tag{A.9}$$

Appendix A: Relationship between state and interferometer phase: Calculation

Using the phase matching condition for the SHG light

$$k_{\mathrm{SHG}} = 2k_l \,, \tag{A.10}$$

we rewrite (A.9) and get

$$\varphi_{\mathrm{inter}} = \frac{\omega_{\mathrm{SHG}}}{c}\left(\left(L_B + L'_B\right) - \left(L_A + L'_A\right)\right) + 2\frac{d_2}{c} n_l \omega_l + \frac{d_1}{c} n_{\mathrm{SHG}} \omega_{\mathrm{SHG}} \,. \tag{A.11}$$

The frequencies and detunings for our setup are described in section 3.2.3. We express the frequencies in (A.11) and (A.5) in the following way

$$\begin{aligned} \omega_l &= \omega_{\mathrm{ion}} \\ \omega_i &= \omega_{\mathrm{ion}} + \delta\omega_r \\ \omega_p &= \omega_{427} + 2\pi \cdot 160\,\mathrm{MHz} \\ \omega_{\mathrm{SHG}} &= \omega_p + \delta\omega_b \end{aligned}$$

Finally, we express the photonic state phase in dependence on the SHG phase

$$\varphi = \varphi_{\mathrm{inter}} + \varphi_{\mathrm{off}} \tag{A.12}$$

with

$$\begin{aligned} \varphi_{\mathrm{off}} = &- \frac{\delta\omega_b}{c}\left(\left(L_B + L'_B\right) - \left(L_A + L'_A\right)\right) \\ &+ \frac{d_2}{c}\omega_{\mathrm{ion}}\left(n_i - n_s\right) + \frac{d_2}{c} n_i \delta\omega_r \\ &+ \frac{d_1}{c}\omega_p\left(n_p - n_{\mathrm{SHG}}\right) - \frac{d_1}{c} n_{\mathrm{SHG}} \delta\omega_b \end{aligned} \tag{A.13}$$

For the given frequency shifts $\delta\omega_b = 480\,\mathrm{MHz}$ and $\delta\omega_r = 480\,\mathrm{MHz}$, the offset is in the order of a few degrees. Additionally, the differences in the refractive index are neglectable. In good approximation, we therefore conclude with

$$\varphi \approx \varphi_{\mathrm{inter}} \,. \tag{A.14}$$

B Laser state transfer

This section depicts further results and plots for the LST measurement and the values for the phases and visibilities.

Table B.1: Phase and visibility of the fringes for the $|S_{1/2}, m = +1/2\rangle$ state

projector		first passage w/o correction		second passage w/o correction	
		Phase (°)	Vis	Phase (°)	Vis
$\|H\rangle$	$\|H\rangle$	8(1)	0.93(1)	174(4)	0.86(5)
$\|H\rangle$	$\|V\rangle$	197(1)	0.91(1)	7(4)	0.87(4)
$\|H\rangle$	$\|D\rangle$	101(2)	0.92(2)	89(4)	0.85(4)
$\|H\rangle$	$\|A\rangle$	286(2)	0.89(2)	285(4)	0.84(4)
$\|H\rangle$	$\|R\rangle$	59(24)	0.09(4)	251(160)	0.03(10)
$\|H\rangle$	$\|L\rangle$	244(17)	0.22(6)	16(34)	0.07(4)
$\|V\rangle$	$\|H\rangle$	184(1)	0.933(9)	345(4)	0.95(4)
$\|V\rangle$	$\|V\rangle$	14(1)	0.91(1)	187(3)	0.88(3)
$\|V\rangle$	$\|D\rangle$	278(2)	0.94(2)	256(2)	0.90(2)
$\|V\rangle$	$\|A\rangle$	101(2)	0.92(2)	101(4)	0.81(5)
$\|V\rangle$	$\|R\rangle$	194(18)	0.13(4)	52(38)	0.10(7)
$\|V\rangle$	$\|L\rangle$	52(20)	0.15(5)	207(38)	0.07(4)

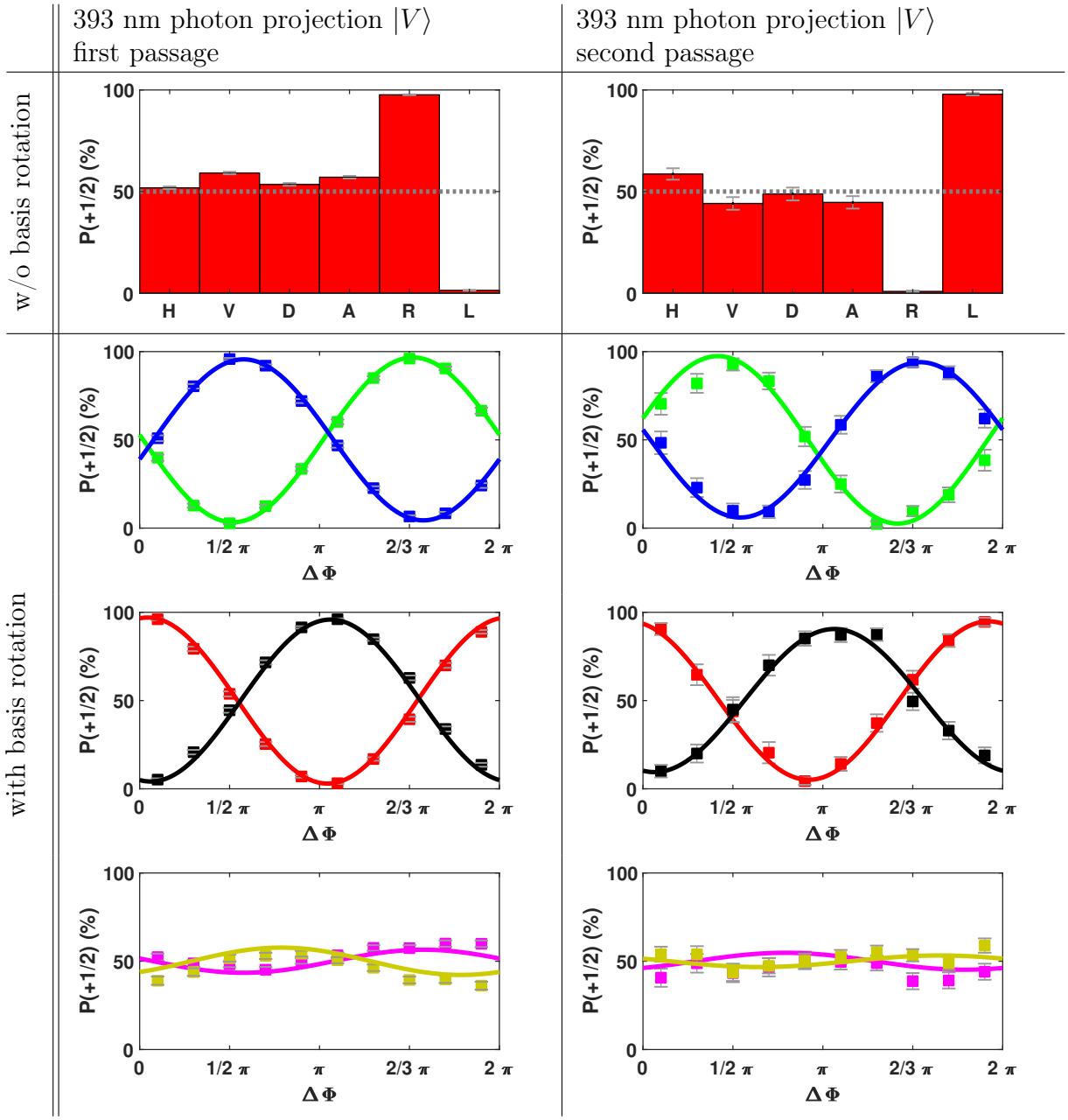

Figure B.3: Measurement results for the LST for *first* and *second passage*. The first row is without RF $\pi/2$ pulse and thus the projection to the eigenstates. The other rows show the oscillations due to the Larmor precession. Second row: green $|H\rangle$ / blue $|V\rangle$, third row: red $|D\rangle$ / black $|A\rangle$, last row: magenta $|R\rangle$ / yellow $|L\rangle$.

C Photon-photon to atom-photon entanglement

In the following section, we show additional plots and evaluations for the entanglement transfer settings of the main text. Additionally, we give more details about the polarisation control.

C.1 Polarisation control

We use two different techniques for polarisation control for the outputs of the source. We adjust the measurement basis for output B of the source (projection). In order to measure the polarisation rotation matrix of the whole path from the source to the 854 nm APDs, we perform a single-qubit tomography with the detection setup. We deterministically generate photons with horizontal polarisation if we block one pump direction of the source. Furthermore, an additional quarter-wave plate directly after the source enables us to generate photons with right-circular polarisation. The two input polarisation with four projections each enables us to calculate the rotation matrix M and to adjust the measurement basis accordingly. As we use only a short fibre for this connection, the polarisation is very stable, and we only need to measure a new rotation matrix after a few days.

For output A, we compensate the polarisation rotation induced by all components. As mentioned, we use a reference laser for this. We sent the laser out of the back-reflection direction. The polarisation is set by minimising the absorption of the ion if it is prepared in one of the outer $D_{5/2}$ states. Thus the polarisation at the position of the ion is right-circular. An optional quarter-waveplate, calibrated with a polarimeter, rotates this polarisation horizontally. The reference laser is sent to a reference polarimeter placed on the trap table connected by the 1 % output of a 99:1 fibre beam-splitter. The 99 % output is connected to the fibre to the source. With the two input polarisations, we first compensate the polarisation to the reference polarimeter and then to another polarimeter in front of the source. By this, both polarimeters show the input polarisation. The last step is to send another laser in the photon direction. The polarisation of this laser is set by a setup similar to the projection setup. By this, we are able to produce an arbitrary input polarisation. The light is reflected from the retroreflector and then detected at the reference polarimeter. Additional fibre paddles in the delay fibre of the back-reflection parts enable us to compensate for the polarisation of the back-reflection part. Because we previously set the polarisation of the path from source to trap and from trap to reference

point to unity, we only see the polarisation rotation of the back-reflection part. The fibre connecting the source and the trap has a length of $\sim 15\,\mathrm{m}$. If the temperature in the laboratory is stable, it is sufficient to readjust the polarisation once a day to compensate for slow drifts in polarisation.

C.2 Without conversion $|\Psi^-\rangle$

In the following section, we will show the plots for each of the 393 nm detectors separately and the corresponding density matrix reconstruction.

Table C.2: Phases and visibilities of the fringes for the data shown in figure C.4 and C.5.

projector		first passage				second passage			
		with correction		w/o correction		with correction		w/o correction	
		Phase (°)	Vis	Phase (°)	Vis	Phase (°)	Vis	Phase (°)	Vis
$\|H\rangle$	$\|H\rangle$	176(3)	0.75(4)	176(3)	0.70(3)	165(10)	0.9(1)	162(11)	0.45(8)
$\|H\rangle$	$\|V\rangle$	359(3)	0.78(4)	359(3)	0.72(4)	1(10)	0.82(8)	2(13)	0.43(8)
$\|H\rangle$	$\|D\rangle$	82(1)	0.591(10)	82(1)	0.56(1)	277(22)	0.4(1)	278(23)	0.21(8)
$\|H\rangle$	$\|A\rangle$	266(3)	0.69(3)	266(3)	0.65(3)	81(15)	0.6(2)	81(14)	0.31(8)
$\|H\rangle$	$\|R\rangle$	239(31)	0.10(5)	239(31)	0.09(5)	138(133)	0.1(3)	147(150)	0.1(2)
$\|H\rangle$	$\|L\rangle$	32(21)	0.16(6)	32(21)	0.15(5)	189(95)	0.1(2)	188(101)	0.1(1)
$\|V\rangle$	$\|H\rangle$	353(2)	0.77(3)	353(2)	0.71(2)	9(9)	0.88(9)	6(11)	0.56(10)
$\|V\rangle$	$\|V\rangle$	170(4)	0.74(5)	170(4)	0.68(4)	135(19)	0.7(2)	139(21)	0.3(1)
$\|V\rangle$	$\|D\rangle$	257(4)	0.63(4)	257(4)	0.60(4)	84(22)	0.6(2)	83(23)	0.3(1)
$\|V\rangle$	$\|A\rangle$	80(2)	0.66(2)	80(2)	0.62(2)	260(21)	0.6(2)	259(22)	0.3(1)
$\|V\rangle$	$\|R\rangle$	4(25)	0.11(5)	4(26)	0.11(5)	55(51)	0.3(3)	54(49)	0.2(1)
$\|V\rangle$	$\|L\rangle$	186(13)	0.19(4)	186(13)	0.18(4)	184(124)	0.2(4)	171(196)	0.0(2)

Table C.3: Overview of the state fidelities and purities

passage		393 nm projection	with correction	w/o correction
first	fidelity	$\|H\rangle$	82.7(7)	79.0(7)
	purity		72(1)	66(1)
	fidelity	$\|V\rangle$	82.4(5)	78.6(5)
	purity		72(2)	66(1)
second	fidelity	$\|H\rangle$	74(4)	51(2)
	purity		61(7)	35(2)
	fidelity	$\|V\rangle$	79(4)	56(2)
	purity		71(7)	40(2)

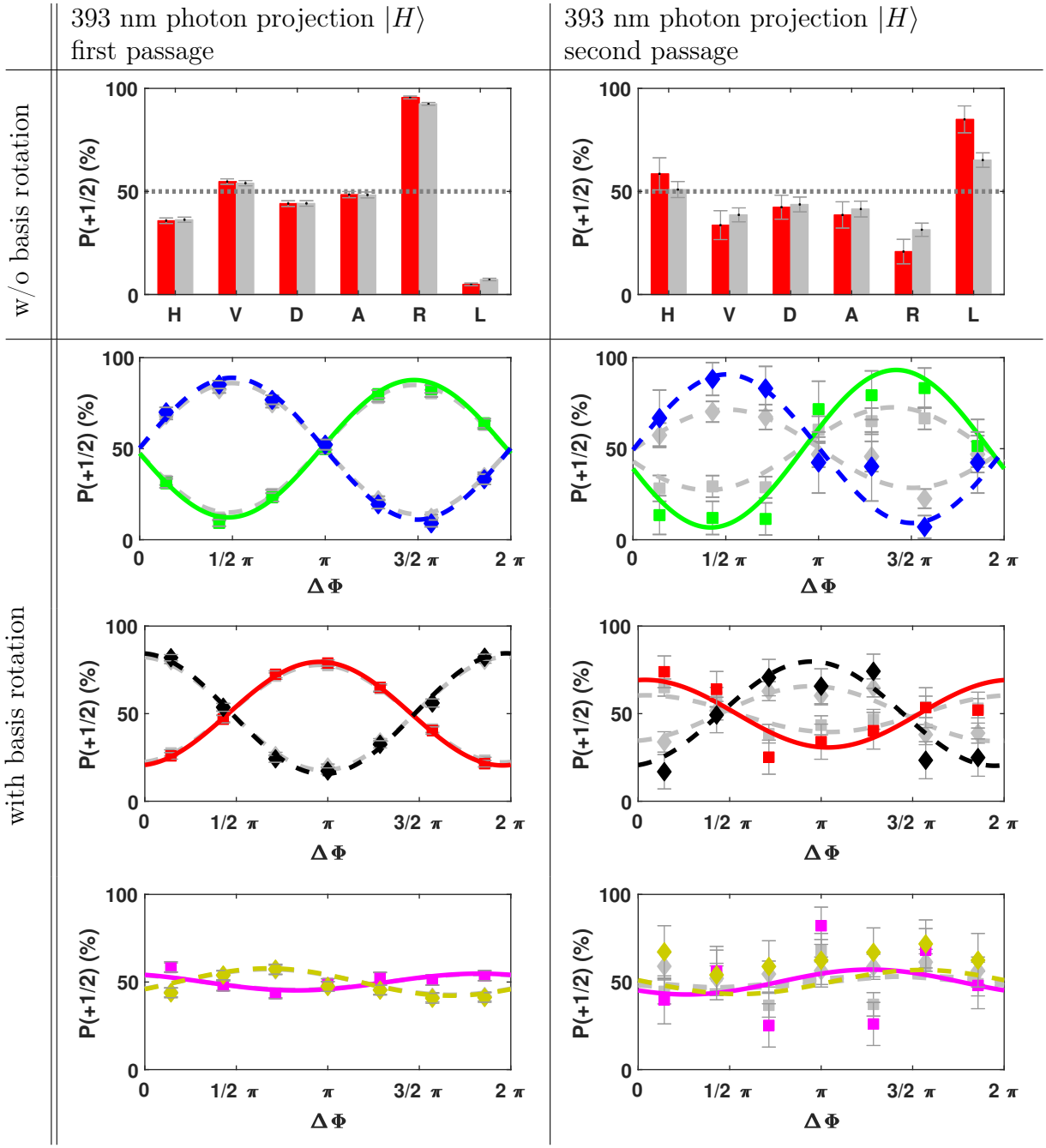

Figure C.4: Measurement results for the photon-photon to atom-photon entanglement transfer evaluated for a waiting time of 350 µs for the *first* and *second* passage. The 393 nm photon is projected to $|H\rangle$. The first row is without RF $\pi/2$-pulse. The other rows show oscillations due to the Larmor precession. Second row: green $|H\rangle$ / blue $|V\rangle$, third row: red $|D\rangle$ / black $|A\rangle$, last row: magenta $|R\rangle$ / yellow $|L\rangle$. Grey bars and lines show the data without background correction.

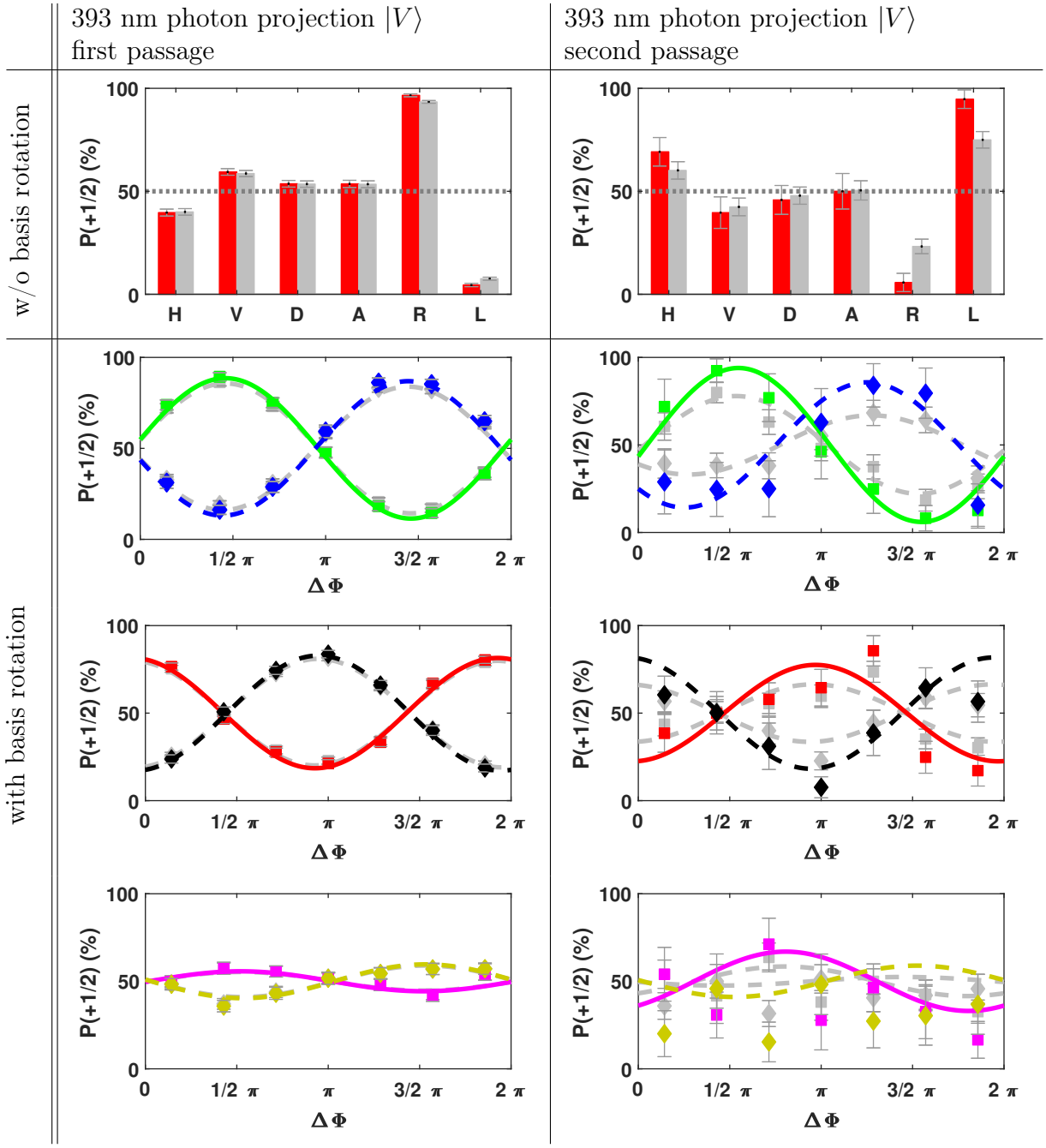

Figure C.5: Measurement results for the photon-photon to atom-photon entanglement transfer evaluated for a waiting time of 350 µs for the *first* and *second* passage. The 393 nm photon is projected to $|V\rangle$. The first row is without RF $\pi/2$-pulse. The other rows show oscillations due to the Larmor precession. Second row: green $|H\rangle$ / blue $|V\rangle$, third row: red $|D\rangle$ / black $|A\rangle$, last row: magenta $|R\rangle$ / yellow $|L\rangle$. Grey bars and lines show the data without background correction.

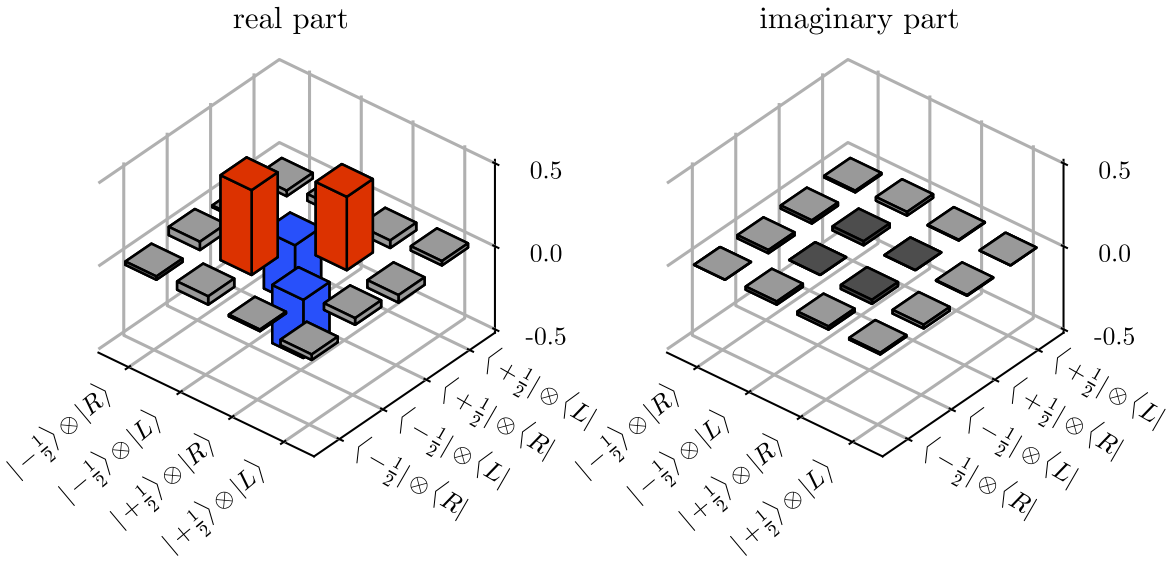

$$\begin{pmatrix} 0.020(5) & 0.050(6) & -0.01(2) & -0.033(9) \\ 0.050(6) & 0.511(5) & -0.350(9) & 0.04(2) \\ -0.01(2) & -0.350(9) & 0.442(5) & -0.045(6) \\ -0.033(9) & 0.04(2) & -0.045(6) & 0.026(5) \end{pmatrix} \quad \begin{pmatrix} 0 & -0.019(3) & -0.019(6) & -0.010(5) \\ 0.019(3) & 0 & 0.024(5) & 0.022(6) \\ 0.019(6) & -0.024(5) & 0 & 0.004(3) \\ 0.010(5) & -0.022(6) & -0.004(3) & 0 \end{pmatrix}$$

(a) First passage

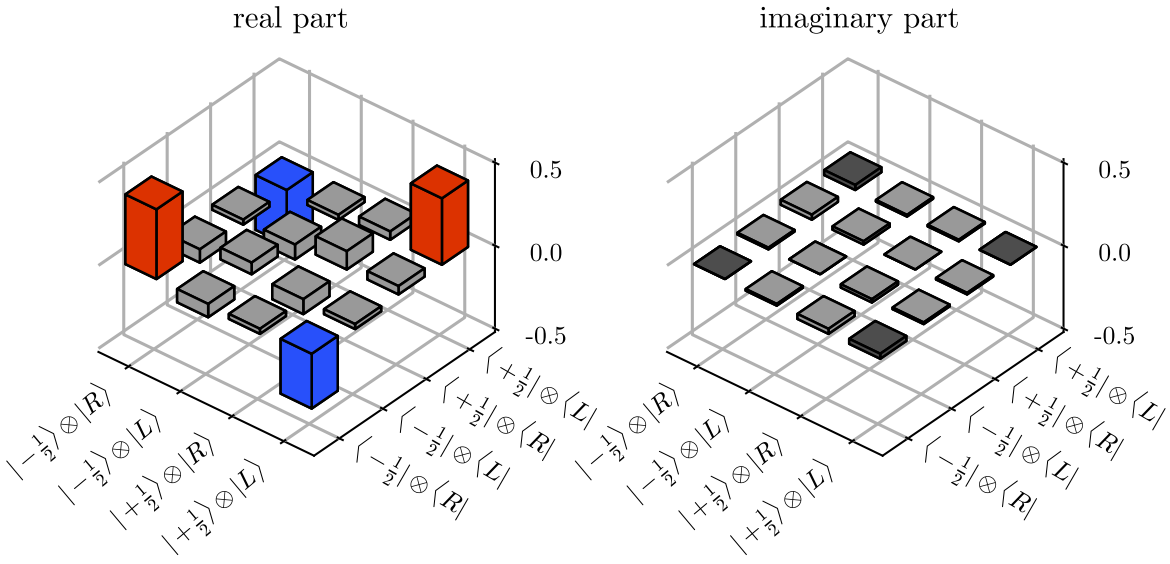

$$\begin{pmatrix} 0.42(3) & -0.08(3) & -0.03(8) & -0.33(4) \\ -0.08(3) & 0.07(3) & -0.09(4) & -0.03(8) \\ -0.03(8) & -0.09(4) & 0.11(3) & 0.05(3) \\ -0.33(4) & -0.03(8) & 0.05(3) & 0.40(3) \end{pmatrix} \quad \begin{pmatrix} 0 & 0.010(9) & 0.03(3) & 0.03(2) \\ -0.010(9) & 0 & 0.02(2) & -0.01(3) \\ -0.03(3) & -0.02(2) & 0 & -0.009(9) \\ -0.03(2) & 0.01(3) & 0.009(9) & 0 \end{pmatrix}$$

(b) Second passage

Figure C.6: Background corrected reconstructed atom-photon density matrix for the first and second passage, and the 393 nm projected onto $|H\rangle$.

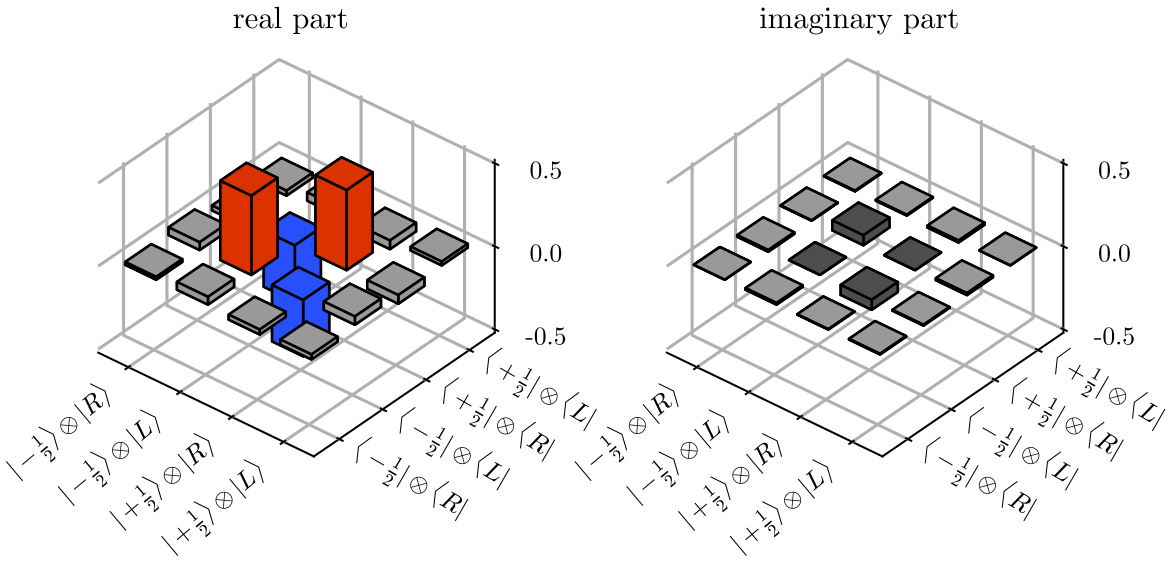

$$\begin{pmatrix} 0.017(5) & 0.047(7) & -0.03(1) & -0.03(1) \\ 0.047(7) & 0.478(5) & -0.34(1) & 0.05(1) \\ -0.03(1) & -0.34(1) & 0.483(5) & -0.052(7) \\ -0.03(1) & 0.05(1) & -0.052(7) & 0.023(5) \end{pmatrix} \quad \begin{pmatrix} 0 & -0.010(3) & -0.002(5) & -0.004(5) \\ 0.010(3) & 0 & 0.060(5) & 0.005(5) \\ 0.002(5) & -0.060(5) & 0 & -0.012(3) \\ 0.004(5) & -0.005(5) & 0.012(3) & 0 \end{pmatrix}$$

(a) First passage

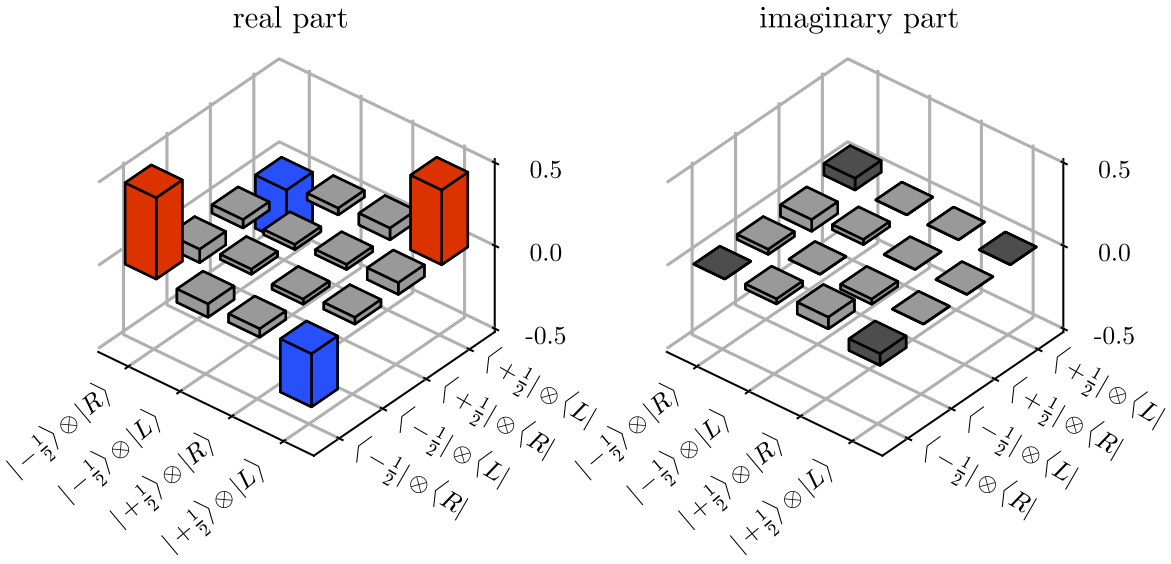

$$\begin{pmatrix} 0.49(2) & -0.08(3) & -0.05(9) & -0.32(5) \\ -0.08(3) & 0.03(2) & -0.03(5) & 0.04(9) \\ -0.05(9) & -0.03(5) & 0.03(2) & 0.07(3) \\ -0.32(5) & 0.04(9) & 0.07(3) & 0.45(2) \end{pmatrix} \quad \begin{pmatrix} 0 & -0.03(1) & -0.07(4) & 0.07(2) \\ 0.03(1) & 0 & 0.03(2) & 0.00(4) \\ 0.07(4) & -0.03(2) & 0 & -0.00(1) \\ -0.07(2) & -0.00(4) & 0.00(1) & 0 \end{pmatrix}$$

(b) Second passage

Figure C.7: Background corrected reconstructed atom-photon density matrix for the first and second passage, and the 393 nm projected onto $|V\rangle$.

C.3 Without conversion $|\Psi^i\rangle$

The measurements shown in 5.4.4 were also repeated for the $|\Psi^i\rangle = \frac{1}{\sqrt{2}}\left(|HV\rangle - i\,|VH\rangle\right)$ input state. We used an exposure window of 200 µs.

In contrast to a $|\Psi^-\rangle$ input state, we expect no oscillations in the $|D\rangle$ / $|A\rangle$ projection basis, but in the $|R\rangle$ / $|L\rangle$ projection basis. Additionally, for the measurement without an RF pulse, we expect the contrast to be in the $|D\rangle$ / $|A\rangle$ projection basis.

Table C.4: Phases and visibilities of the fringes for the data shown in fig. C.8 and C.9.

projector		first passage				second passage			
		with correction		w/o correction		with correction		w/o correction	
		Phase (°)	Vis	Phase (°)	Vis	Phase (°)	Vis	Phase (°)	Vis
$\|H\rangle$	$\|H\rangle$	173(2)	0.83(2)	173(2)	0.76(2)	173(10)	0.8(1)	172(11)	0.49(9)
$\|H\rangle$	$\|V\rangle$	351(3)	0.84(3)	351(3)	0.78(3)	341(10)	0.8(1)	343(12)	0.45(9)
$\|H\rangle$	$\|D\rangle$	349(11)	0.19(3)	349(11)	0.18(3)	4(25)	0.4(2)	4(25)	0.3(1)
$\|H\rangle$	$\|A\rangle$	213(25)	0.10(4)	213(25)	0.10(4)	194(45)	0.1(1)	194(51)	0.08(7)
$\|H\rangle$	$\|R\rangle$	82(2)	0.75(2)	82(2)	0.69(2)	273(10)	0.7(1)	273(9)	0.47(8)
$\|H\rangle$	$\|L\rangle$	263(5)	0.83(6)	262(5)	0.77(5)	77(15)	0.5(1)	76(16)	0.28(9)
$\|V\rangle$	$\|H\rangle$	354(3)	0.85(3)	354(3)	0.78(3)	1(12)	0.8(1)	360(12)	0.43(8)
$\|V\rangle$	$\|V\rangle$	178(3)	0.85(3)	178(3)	0.78(3)	180(14)	0.8(2)	177(16)	0.4(1)
$\|V\rangle$	$\|D\rangle$	181(19)	0.16(5)	181(19)	0.15(5)	185(29)	0.19(10)	185(28)	0.12(6)
$\|V\rangle$	$\|A\rangle$	349(33)	0.10(6)	349(33)	0.10(6)	111(52)	0.3(2)	111(49)	0.2(1)
$\|V\rangle$	$\|R\rangle$	268(4)	0.77(5)	268(4)	0.72(4)	97(11)	0.8(1)	98(11)	0.48(10)
$\|V\rangle$	$\|L\rangle$	90(3)	0.81(3)	90(3)	0.75(3)	250(10)	0.7(1)	251(11)	0.44(8)

The density matrices are shown in figure C.10 and fig. C.11 looks complicated but is as expected, and the fidelity achieved is comparable to the measurements shown in the main part. The achieved fidelities are summarised in table C.5.

Table C.5: Overview of the state fidelities and purities

passage		393 nm projection	with correction	w/o correction
first	fidelity	$\|H\rangle$	86(1)	81.5(10)
	purity		77(2)	70(2)
	fidelity	$\|V\rangle$	86(1)	81(1)
	purity		75(2)	68(2)
second	fidelity	$\|H\rangle$	78(4)	56(2)
	purity		69(8)	42(2)
	fidelity	$\|V\rangle$	83(5)	58(2)
	purity		74(9)	42(2)

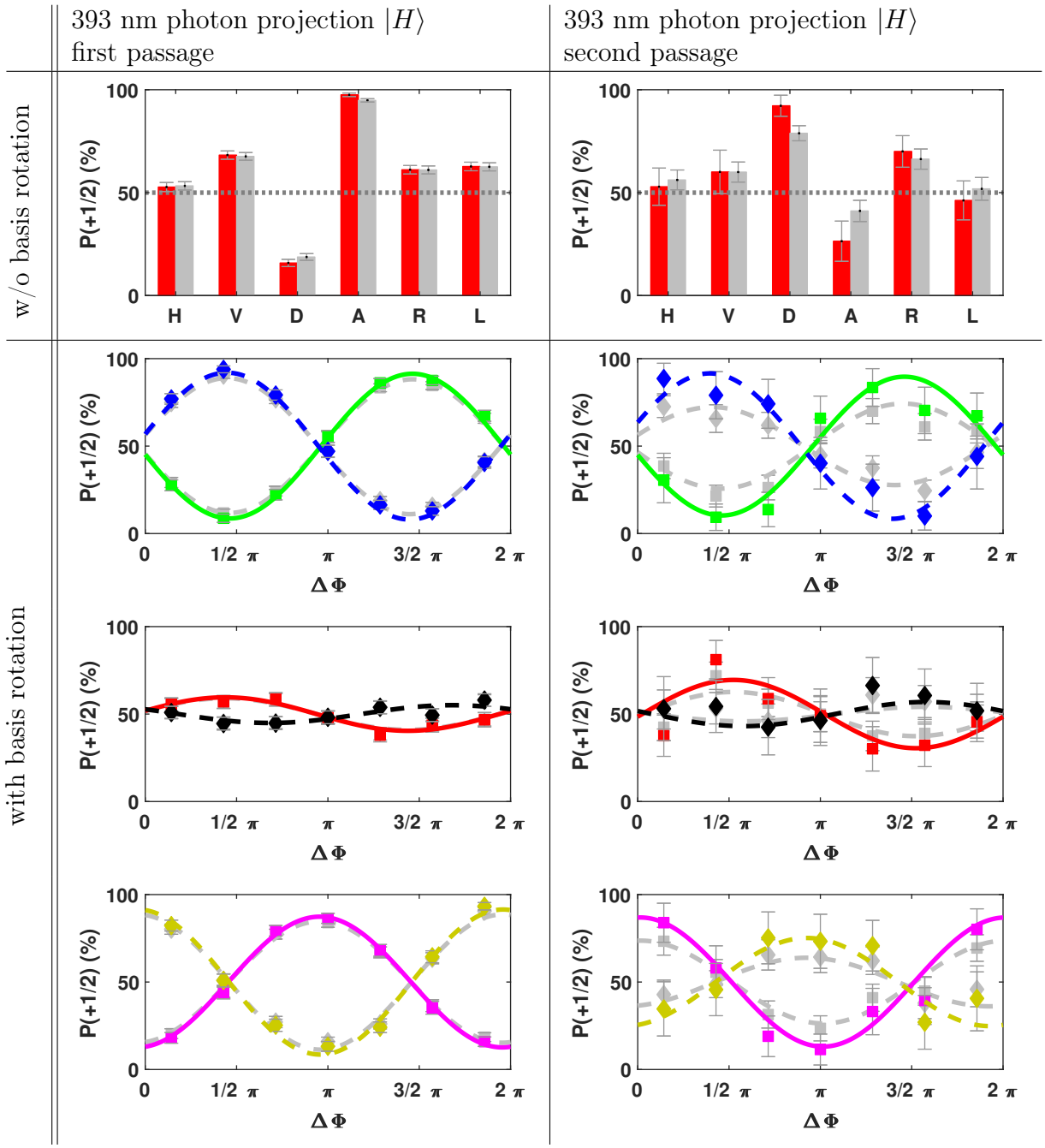

Figure C.8: Measurement results for the photon-photon to atom-photon entanglement transfer evaluated for a waiting time of 200 µs for the *first* and *second* passage. The 393 nm photon is projected to $|H\rangle$, and we use $|\Psi^i\rangle$ as the input state. The first row is without RF $\pi/2$-pulse. The other rows show oscillations due to the Larmor precession. Second row: green $|H\rangle$ / blue $|V\rangle$, third row: red $|D\rangle$ / black $|A\rangle$, last row: magenta $|R\rangle$ / yellow $|L\rangle$. Grey bars and lines show the data without background correction.

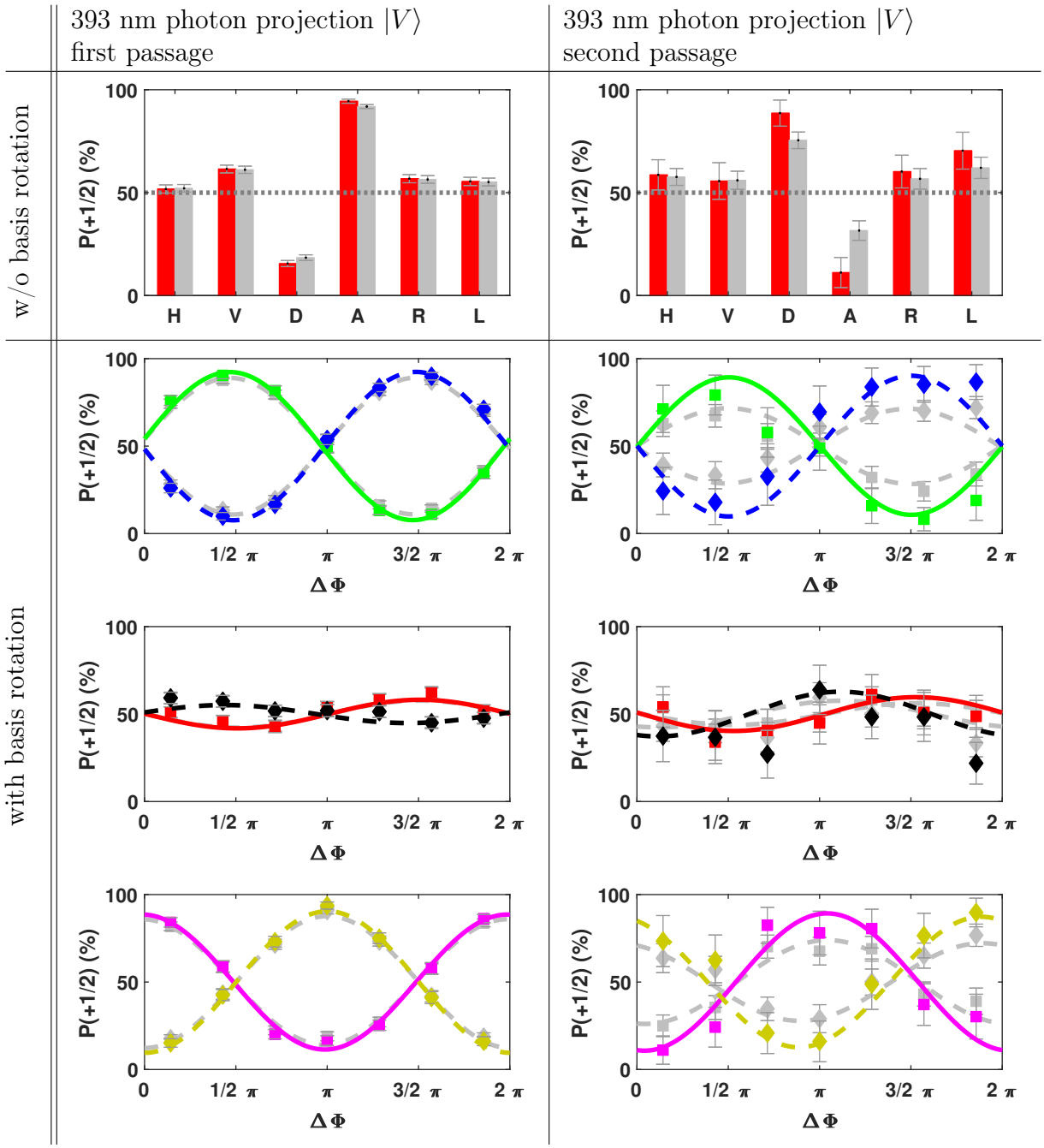

Figure C.9: Measurement results for the photon-photon to atom-photon entanglement transfer evaluated for a waiting time of 200 µs for the *first* and *second* passage. The 393 nm photon is projected to $|V\rangle$, and we use $|\Psi^i\rangle$ as the input state. The first row is without RF $\pi/2$-pulse. The other rows show oscillations due to the Larmor precession. Second row: green $|H\rangle$ / blue $|V\rangle$, third row: red $|D\rangle$ / black $|A\rangle$, last row: magenta $|R\rangle$ / yellow $|L\rangle$. Grey bars and lines show the data without background correction.

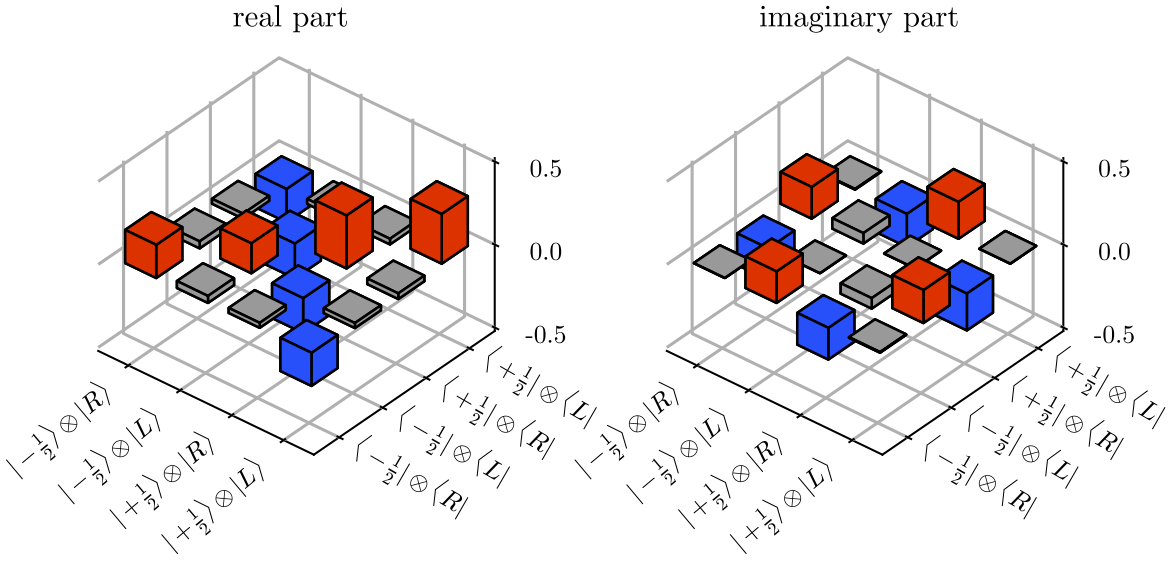

$$\begin{pmatrix} 0.20(1) & 0.042(8) & 0.03(1) & -0.20(1) \\ 0.042(8) & 0.18(1) & -0.21(1) & -0.03(1) \\ 0.03(1) & -0.21(1) & 0.32(1) & -0.034(8) \\ -0.20(1) & -0.03(1) & -0.034(8) & 0.30(1) \end{pmatrix} \quad \begin{pmatrix} 0 & -0.190(2) & 0.191(4) & -0.004(5) \\ 0.190(2) & 0 & 0.063(5) & -0.199(4) \\ -0.191(4) & -0.063(5) & 0 & 0.223(2) \\ 0.004(5) & 0.199(4) & -0.223(2) & 0 \end{pmatrix}$$

(a) First passage

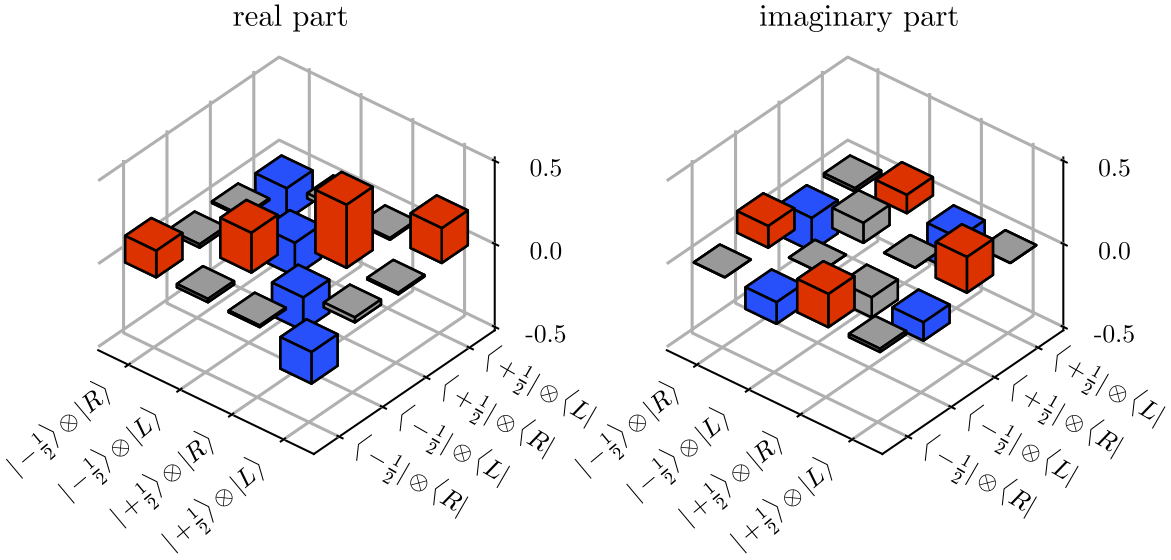

$$\begin{pmatrix} 0.16(4) & 0.02(4) & 0.01(4) & -0.19(4) \\ 0.02(4) & 0.24(4) & -0.20(4) & 0.03(4) \\ 0.01(4) & -0.20(4) & 0.38(4) & -0.01(4) \\ -0.19(4) & 0.03(4) & -0.01(4) & 0.21(4) \end{pmatrix} \quad \begin{pmatrix} 0 & 0.130(10) & -0.20(1) & -0.02(2) \\ -0.130(10) & 0 & 0.12(2) & 0.11(1) \\ 0.20(1) & -0.12(2) & 0 & -0.215(10) \\ 0.02(2) & -0.11(1) & 0.215(10) & 0 \end{pmatrix}$$

(b) Second passage

Figure C.10: Background corrected reconstructed atom-photon density matrix for the first and second passage, and the 393 nm projected onto $|H\rangle$. For an ideal density matrix, the red coloured bars should have a height of 0.25 and the blue coloured bars a height of -0.25.

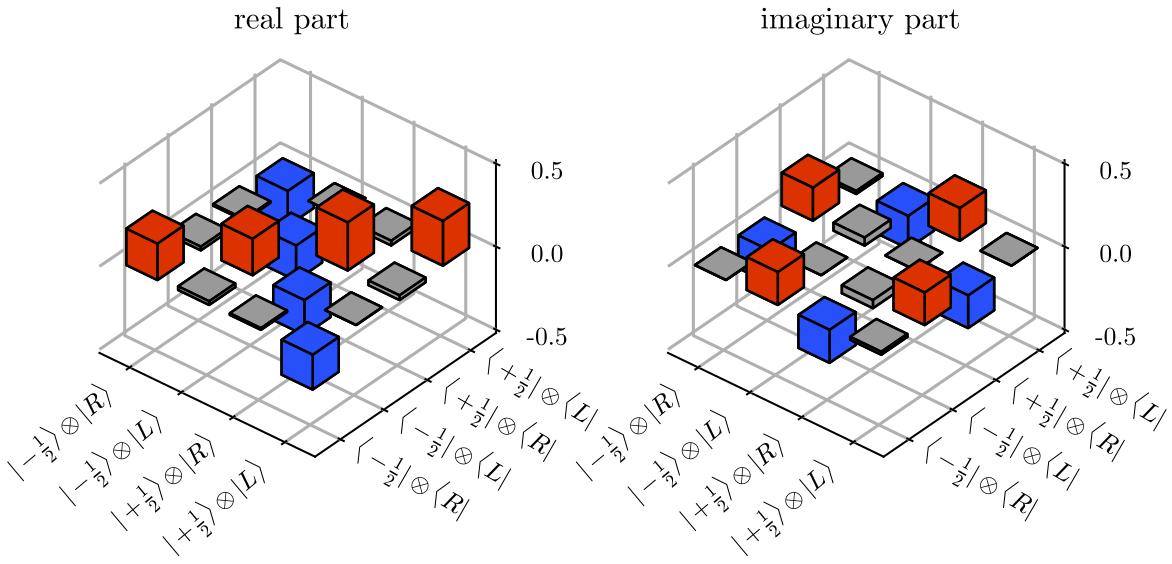

$$\begin{pmatrix} 0.22(1) & 0.022(8) & 0.01(1) & -0.21(1) \\ 0.022(8) & 0.22(1) & -0.21(1) & 0.00(1) \\ 0.01(1) & -0.21(1) & 0.29(1) & -0.028(8) \\ -0.21(1) & 0.00(1) & -0.028(8) & 0.27(1) \end{pmatrix} \quad \begin{pmatrix} 0 & -0.198(2) & 0.199(4) & -0.018(6) \\ 0.198(2) & 0 & 0.048(6) & -0.196(4) \\ -0.199(4) & -0.048(6) & 0 & 0.197(2) \\ 0.018(6) & 0.196(4) & -0.197(2) & 0 \end{pmatrix}$$

(a) First passage

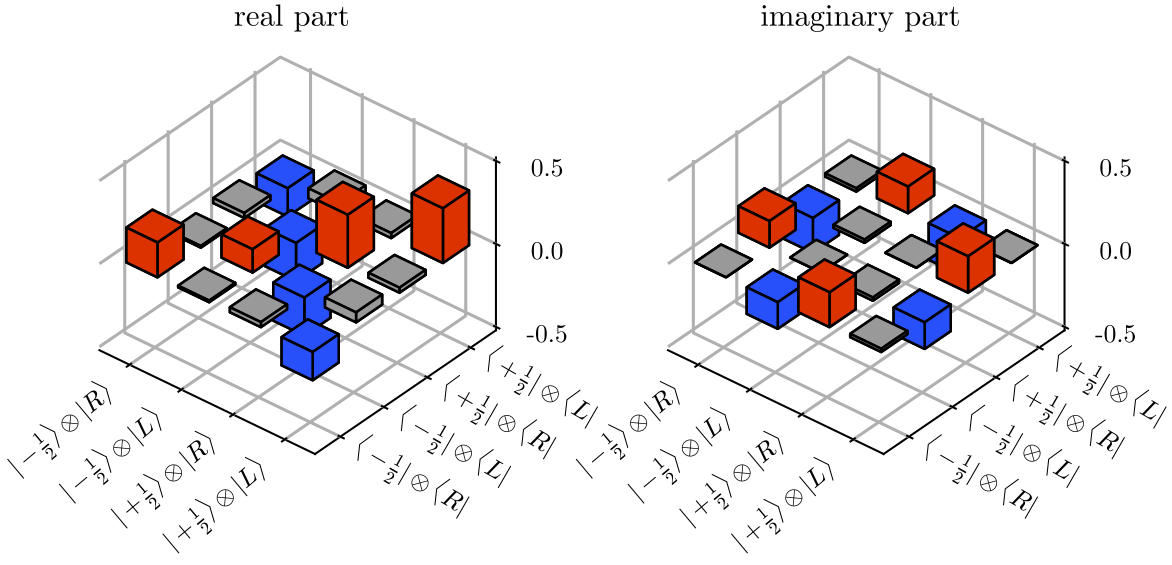

$$\begin{pmatrix} 0.21(4) & 0.01(3) & 0.03(4) & -0.17(5) \\ 0.01(3) & 0.14(4) & -0.23(5) & 0.06(4) \\ 0.03(4) & -0.23(5) & 0.32(4) & 0.03(3) \\ -0.17(5) & 0.06(4) & 0.03(3) & 0.33(4) \end{pmatrix} \quad \begin{pmatrix} 0 & 0.16(1) & -0.21(1) & -0.02(2) \\ -0.16(1) & 0 & 0.02(2) & 0.16(1) \\ 0.21(1) & -0.02(2) & 0 & -0.22(1) \\ 0.02(2) & -0.16(1) & 0.22(1) & 0 \end{pmatrix}$$

(b) Second passage

Figure C.11: Background corrected reconstructed atom-photon density matrix for the first and second passage, and the 393 nm projected onto $|V\rangle$. For an ideal density matrix, the red coloured bars should have a height of 0.25 and the blue coloured bars a height of -0.25.

C.4 With conversion

This section shows the evaluation of the entanglement transfer with conversion for each 393 nm detector separately. The phases and visibilities of the data shown in fig. C.12 and C.13 are summarised in table C.6.

The reconstructed density matrices for the *first* and *second* passages are shown in fig. C.14 and C.15. In table C.7, we summarise the purities and the fidelities of the entanglement transfer.

Table C.6: Phase and visibility of the sinusoidal fits of the data shown in figure C.12 and C.13.

projector		first passage				second passage			
		with correction		w/o correction		with correction		w/o correction	
		Phase (°)	Vis	Phase (°)	Vis	Phase (°)	Vis	Phase (°)	Vis
$\|H\rangle$	$\|H\rangle$	184(4)	0.77(5)	184(5)	0.71(5)	211(15)	0.7(1)	212(19)	0.3(1)
$\|H\rangle$	$\|V\rangle$	6(2)	0.77(2)	6(2)	0.71(2)	30(20)	0.6(2)	29(23)	0.3(1)
$\|H\rangle$	$\|D\rangle$	101(8)	0.67(8)	101(8)	0.62(8)	265(21)	0.6(2)	267(22)	0.3(1)
$\|H\rangle$	$\|A\rangle$	283(3)	0.72(3)	283(3)	0.66(3)	120(23)	0.4(1)	120(24)	0.18(7)
$\|H\rangle$	$\|R\rangle$	302(16)	0.22(6)	302(16)	0.21(6)	54(60)	0.1(1)	54(61)	0.07(7)
$\|H\rangle$	$\|L\rangle$	125(11)	0.17(3)	125(11)	0.16(3)	249(47)	0.2(1)	249(47)	0.10(9)
$\|V\rangle$	$\|H\rangle$	358(3)	0.76(3)	358(3)	0.69(3)	5(13)	0.8(2)	6(17)	0.4(1)
$\|V\rangle$	$\|V\rangle$	175(1)	0.74(1)	175(1)	0.67(1)	182(12)	0.8(1)	181(13)	0.39(8)
$\|V\rangle$	$\|D\rangle$	273(5)	0.71(5)	273(5)	0.65(5)	61(14)	0.7(1)	63(17)	0.37(10)
$\|V\rangle$	$\|A\rangle$	98(1)	0.71(2)	98(1)	0.65(2)	279(18)	0.6(2)	281(23)	0.3(1)
$\|V\rangle$	$\|R\rangle$	131(17)	0.20(6)	131(17)	0.19(6)	162(90)	0.2(3)	164(94)	0.1(1)
$\|V\rangle$	$\|L\rangle$	301(12)	0.20(4)	301(12)	0.19(4)	106(20)	0.5(2)	106(21)	0.3(1)

Table C.7: Overview of the state fidelities and purities

passage		393 nm projection	with correction	w/o correction
first	fidelity	$\|H\rangle$	84(1)	79(1)
	purity		82(2)	75(2)
	fidelity	$\|V\rangle$	84(1)	79.1(9)
	purity		78(2)	71(1)
second	fidelity	$\|H\rangle$	67(5)	47(3)
	purity		57(6)	35(2)
	fidelity	$\|V\rangle$	81(5)	54(3)
	purity		78(8)	39(2)

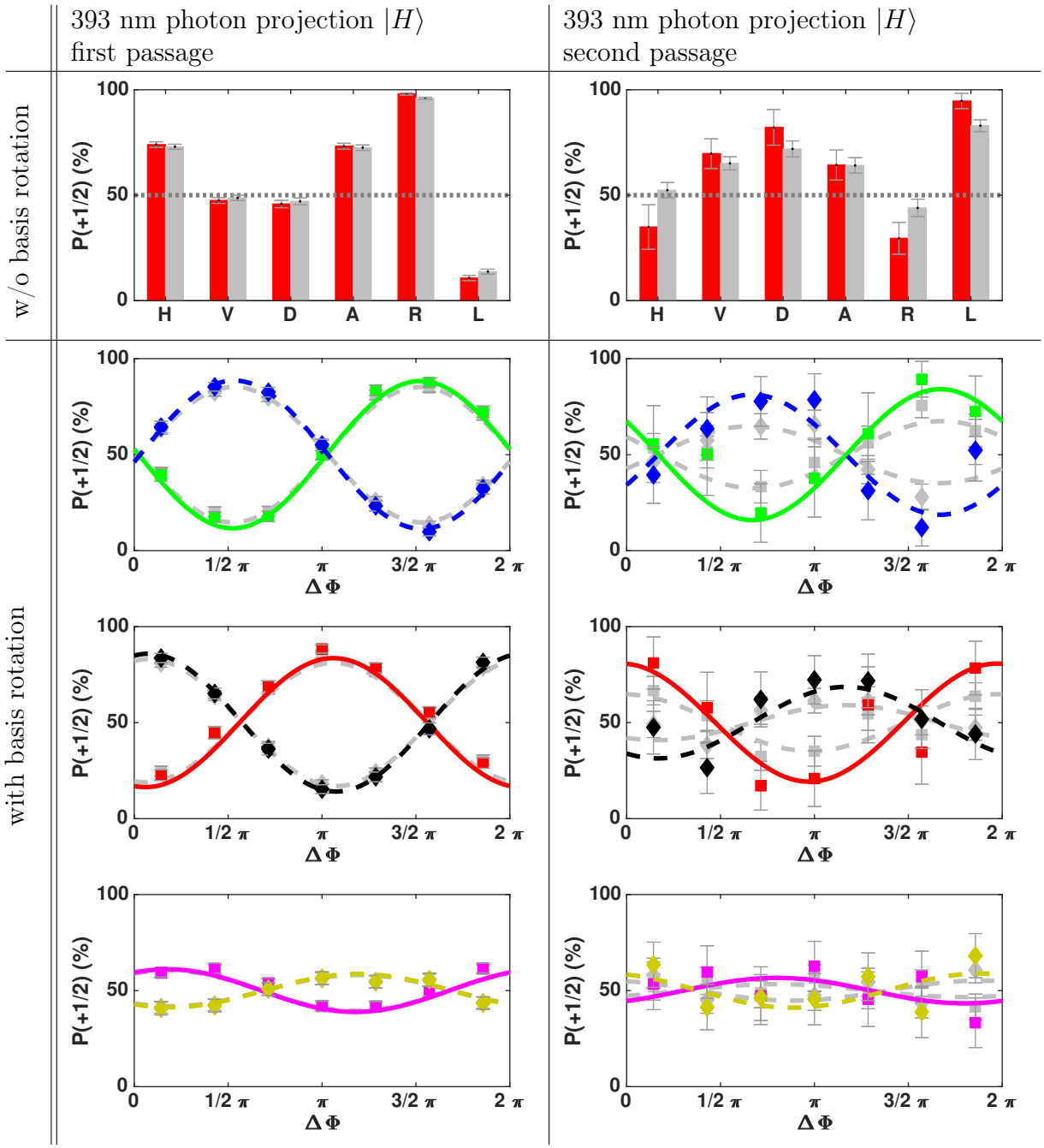

Figure C.12: Measurement results for the photon-photon to atom-photon entanglement transfer with conversion evaluated for a waiting time of 400 µs for the *first* and *second* passage. The 393 nm photon is projected to $|H\rangle$. The first row is without RF $\pi/2$-pulse. The other rows show oscillations due to the Larmor precession. Second row: green $|H\rangle$ / blue $|V\rangle$, third row: red $|D\rangle$ / black $|A\rangle$, last row: magenta $|R\rangle$ / yellow $|L\rangle$. Grey bars and lines show the data without background correction.

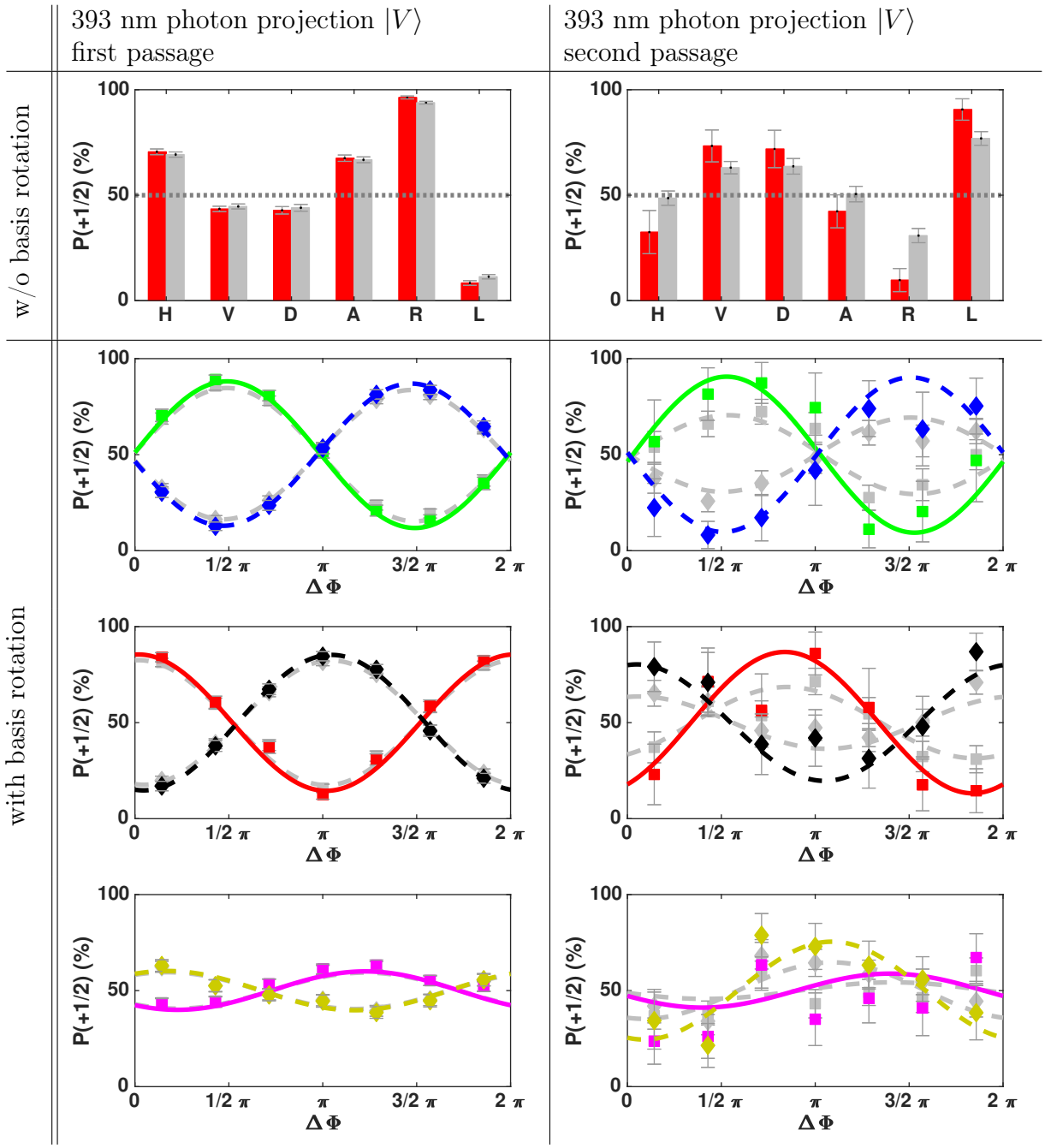

Figure C.13: Measurement results for the photon-photon to atom-photon entanglement transfer with conversion evaluated for a waiting time of 400 µs for the *first* and *second* passage. The 393 nm photon is projected to $|V\rangle$. The first row is without RF $\pi/2$-pulse. The other rows show oscillations due to the Larmor precession. Second row: green $|H\rangle$ / blue $|V\rangle$, third row: red $|D\rangle$ / black $|A\rangle$, last row: magenta $|R\rangle$ / yellow $|L\rangle$. Grey bars and lines show the data without background correction.

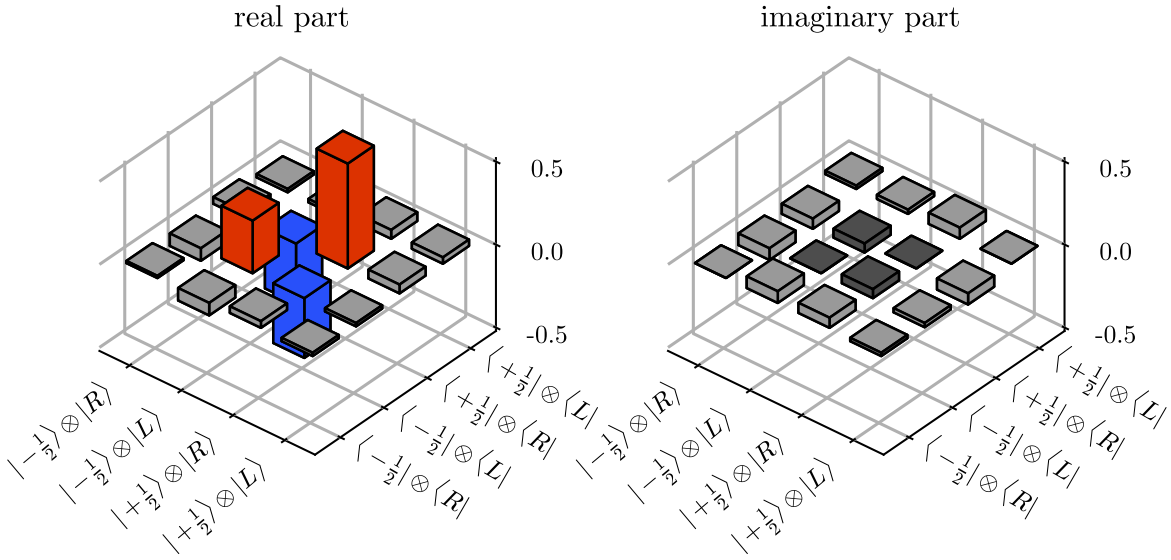

$$\begin{pmatrix} 0.020(5) & 0.050(6) & -0.01(2) & -0.033(9) \\ 0.050(6) & 0.511(5) & -0.350(9) & 0.04(2) \\ -0.01(2) & -0.350(9) & 0.442(5) & -0.045(6) \\ -0.033(9) & 0.04(2) & -0.045(6) & 0.026(5) \end{pmatrix} \quad \begin{pmatrix} 0 & -0.019(3) & -0.019(6) & -0.010(5) \\ 0.019(3) & 0 & 0.024(5) & 0.022(6) \\ 0.019(6) & -0.024(5) & 0 & 0.004(3) \\ 0.010(5) & -0.022(6) & -0.004(3) & 0 \end{pmatrix}$$

(a) First passage

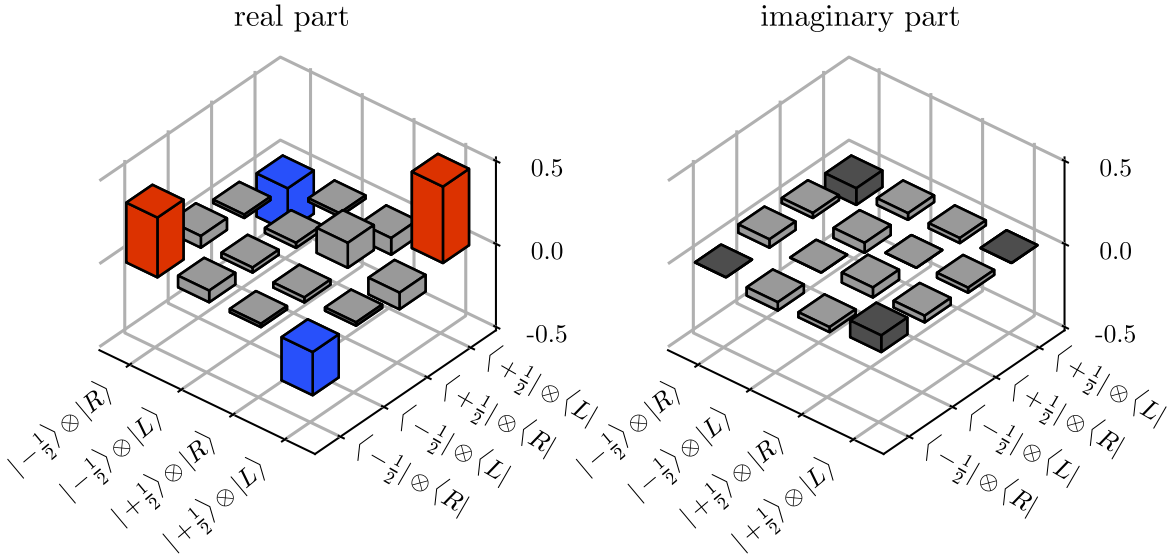

$$\begin{pmatrix} 0.42(3) & -0.08(3) & -0.03(8) & -0.33(4) \\ -0.08(3) & 0.07(3) & -0.09(4) & -0.03(8) \\ -0.03(8) & -0.09(4) & 0.11(3) & 0.05(3) \\ -0.33(4) & -0.03(8) & 0.05(3) & 0.40(3) \end{pmatrix} \quad \begin{pmatrix} 0 & 0.010(9) & 0.03(3) & 0.03(2) \\ -0.010(9) & 0 & 0.02(2) & -0.01(3) \\ -0.03(3) & -0.02(2) & 0 & -0.009(9) \\ -0.03(2) & 0.01(3) & 0.009(9) & 0 \end{pmatrix}$$

(b) Second passage

Figure C.14: Background corrected reconstructed density matrix between ion and the 1550 nm photon for the first and second passage and the 393 nm projected onto $|H\rangle$.

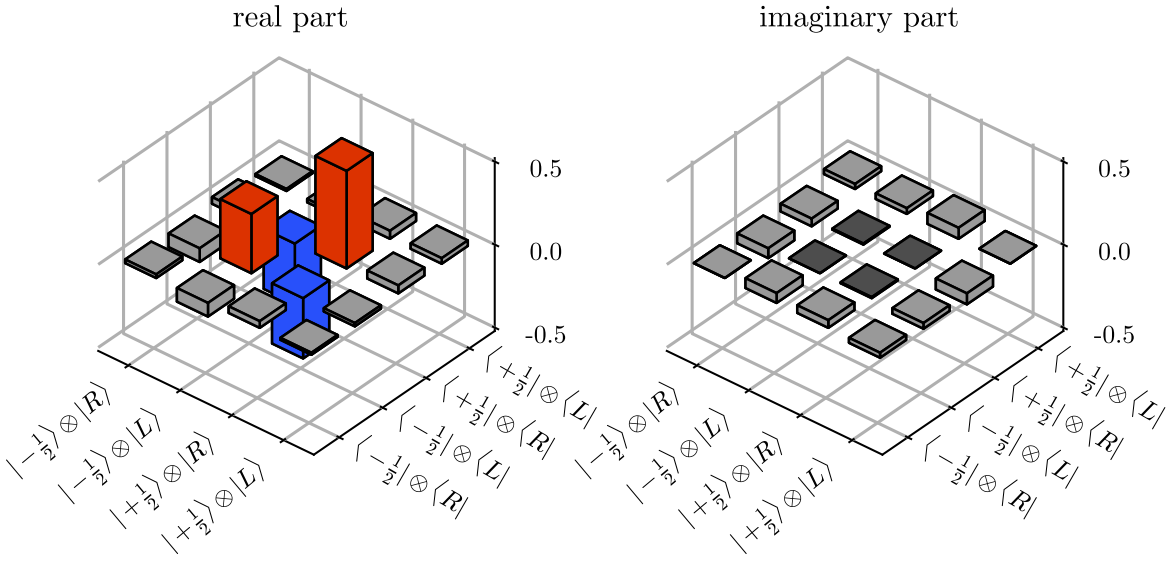

$$\begin{pmatrix} 0.017(5) & 0.047(7) & -0.03(1) & -0.03(1) \\ 0.047(7) & 0.478(5) & -0.34(1) & 0.05(1) \\ -0.03(1) & -0.34(1) & 0.483(5) & -0.052(7) \\ -0.03(1) & 0.05(1) & -0.052(7) & 0.023(5) \end{pmatrix} \qquad \begin{pmatrix} 0 & -0.010(3) & -0.002(5) & -0.004(5) \\ 0.010(3) & 0 & 0.060(5) & 0.005(5) \\ 0.002(5) & -0.060(5) & 0 & -0.012(3) \\ 0.004(5) & -0.005(5) & 0.012(3) & 0 \end{pmatrix}$$

(a) First passage

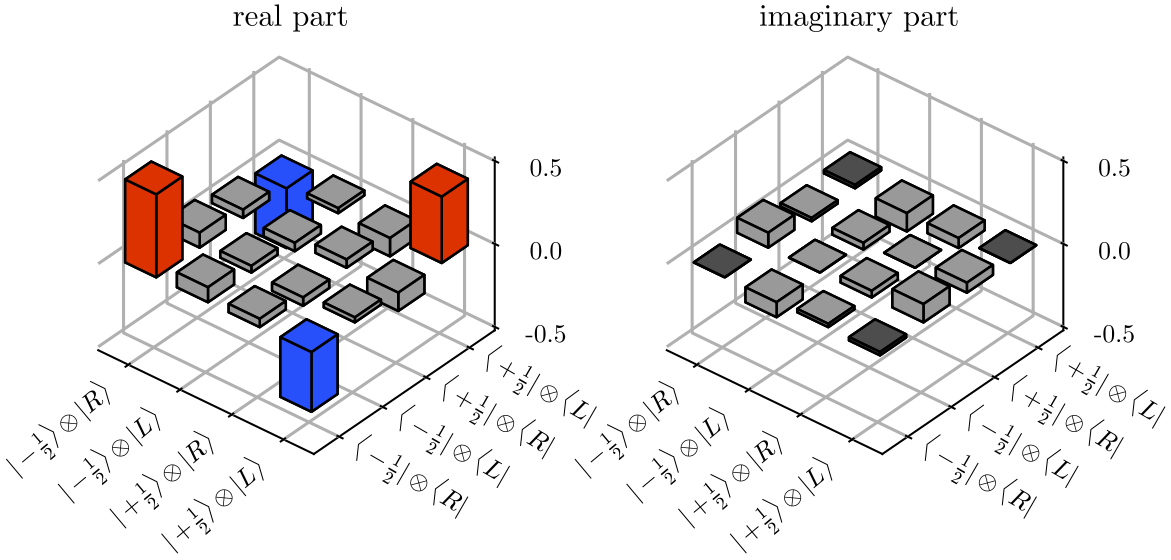

$$\begin{pmatrix} 0.49(2) & -0.08(3) & -0.05(9) & -0.32(5) \\ -0.08(3) & 0.03(2) & -0.03(5) & 0.04(9) \\ -0.05(9) & -0.03(5) & 0.03(2) & 0.07(3) \\ -0.32(5) & 0.04(9) & 0.07(3) & 0.45(2) \end{pmatrix} \qquad \begin{pmatrix} 0 & -0.03(1) & -0.07(4) & 0.07(2) \\ 0.03(1) & 0 & 0.03(2) & 0.00(4) \\ 0.07(4) & -0.03(2) & 0 & -0.00(1) \\ -0.07(2) & -0.00(4) & 0.00(1) & 0 \end{pmatrix}$$

(b) Second passage

Figure C.15: Background corrected reconstructed density matrix between ion and the 1550 nm photon for the first and second passage and the 393 nm projected onto $|V\rangle$.

C.5 With conversion and metropolitan fibre

This section separately evaluates the entanglement transfer with conversion and metropolitan fibre for each 393 nm detector. The phases and visibilities of the data shown in fig. C.16 and C.17 are summarised in table C.8.

For the data of the second passage, we reduce the number of bins to four to get a better signal. We see some oscillation in the $|H\rangle$ / $|V\rangle$ and $|D\rangle$ / $|A\rangle$ basis. However, the phase shift between them is wrong because of the calibration error. We do not try to reconstruct a density matrix for the mentioned reason.

The reconstructed density matrices for the first passage are shown in figure C.18. In table C.9, we summarise the purities and the fidelities of the entanglement transfer.

Table C.8: Phase and visibility of the sinusoidal fits of the data shown in figure C.16 and C.17.

projector		first passage				second passage			
		with correction		w/o correction		with correction		w/o correction	
		Phase (°)	Vis	Phase (°)	Vis	Phase (°)	Vis	Phase (°)	Vis
$\|H\rangle$	$\|H\rangle$	174(6)	0.90(6)	174(6)	0.84(6)	195(47)	0.2(2)	187(55)	0.3(3)
$\|H\rangle$	$\|V\rangle$	344(8)	0.63(8)	344(8)	0.57(7)	314(46)	0.5(3)	315(58)	0.6(4)
$\|H\rangle$	$\|D\rangle$	252(8)	0.79(8)	251(9)	0.72(9)	184(339)	0.1(3)	201(266)	0.1(5)
$\|H\rangle$	$\|A\rangle$	84(12)	0.7(1)	84(12)	0.6(1)	336(83)	0.5(6)	333(83)	0.5(6)
$\|H\rangle$	$\|R\rangle$	23(63)	0.2(3)	23(63)	0.2(2)			135(538)	0.1(10)
$\|H\rangle$	$\|L\rangle$	307(83)	0.1(2)	307(83)	0.1(2)	359(187)	0.1(3)	6(207)	0.1(5)
$\|V\rangle$	$\|H\rangle$	359(11)	0.7(1)	359(12)	0.7(1)	12(51)	0.4(3)	16(43)	0.6(4)
$\|V\rangle$	$\|V\rangle$	178(9)	0.8(1)	179(9)	0.7(1)	197(95)	0.2(4)	175(86)	0.4(6)
$\|V\rangle$	$\|D\rangle$	79(7)	0.71(7)	79(7)	0.65(7)	351(86)	0.2(3)	350(113)	0.2(3)
$\|V\rangle$	$\|A\rangle$	264(10)	0.9(1)	264(10)	0.8(1)				
$\|V\rangle$	$\|R\rangle$	232(40)	0.2(2)	232(39)	0.2(1)	208(82)	0.2(3)	216(60)	0.5(5)
$\|V\rangle$	$\|L\rangle$	123(38)	0.2(1)	124(38)	0.2(1)	337(23)	0.17(7)	335(35)	0.5(3)

Table C.9: Overview of the state fidelities and purities

passage		393 nm projection	with correction	w/o correction
first	fidelity	$\|H\rangle$	85(3)	81(3)
	purity		82(6)	75(5)
	fidelity	$\|V\rangle$	86(3)	82(3)
	purity		82(6)	74(5)

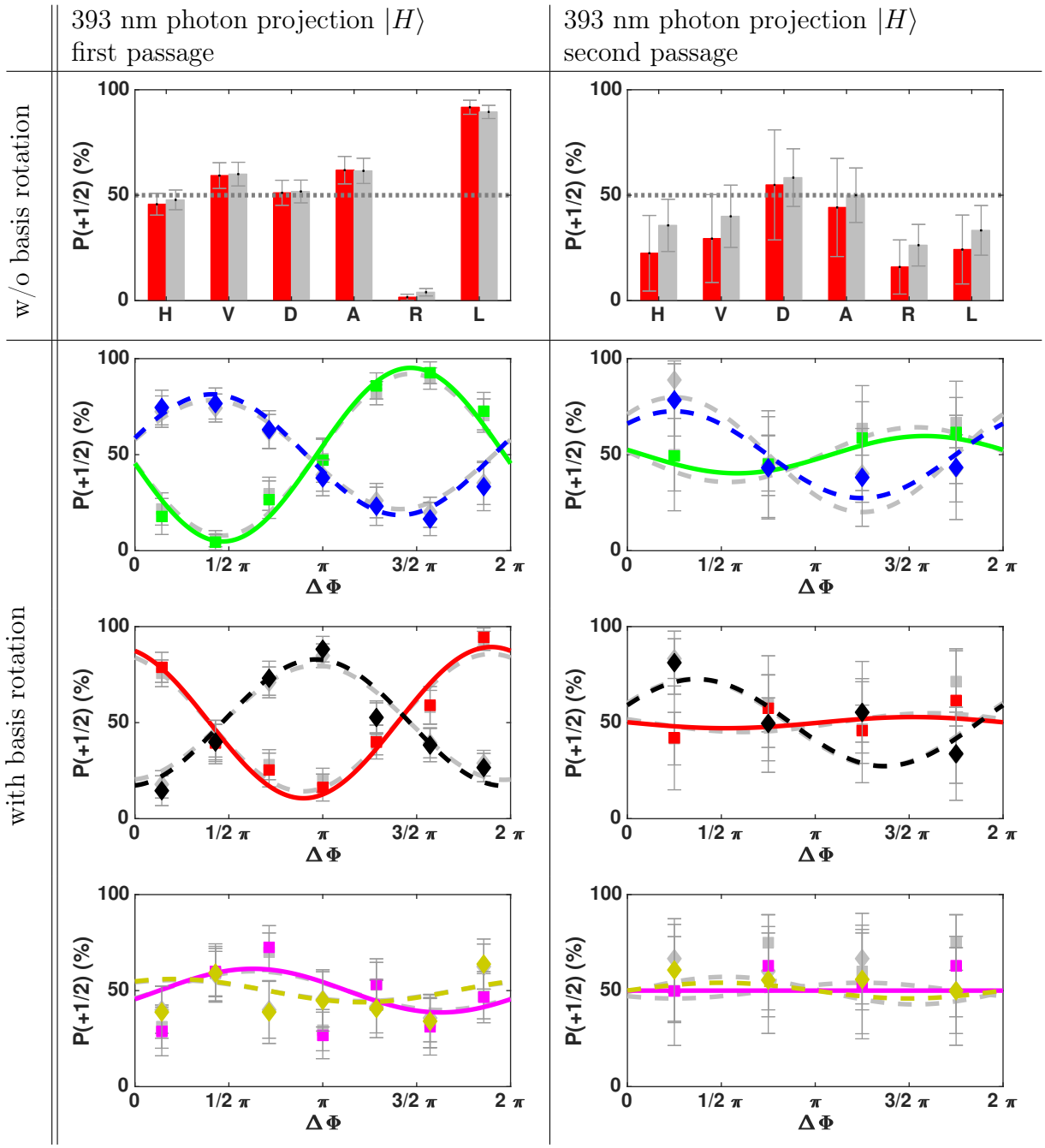

Figure C.16: Measurement results for the photon-photon to atom-photon entanglement transfer with conversion and metropolitan fibre evaluated for a waiting time of 400 µs for the *first* and *second* passage. The 393 nm photon is projected to $|H\rangle$. The first row is without RF $\pi/2$-pulse. The other rows show oscillations due to the Larmor precession. Second row: green $|H\rangle$ / blue $|V\rangle$, third row: red $|D\rangle$ / black $|A\rangle$, last row: magenta $|R\rangle$ / yellow $|L\rangle$. Grey bars and lines show the data without background correction.

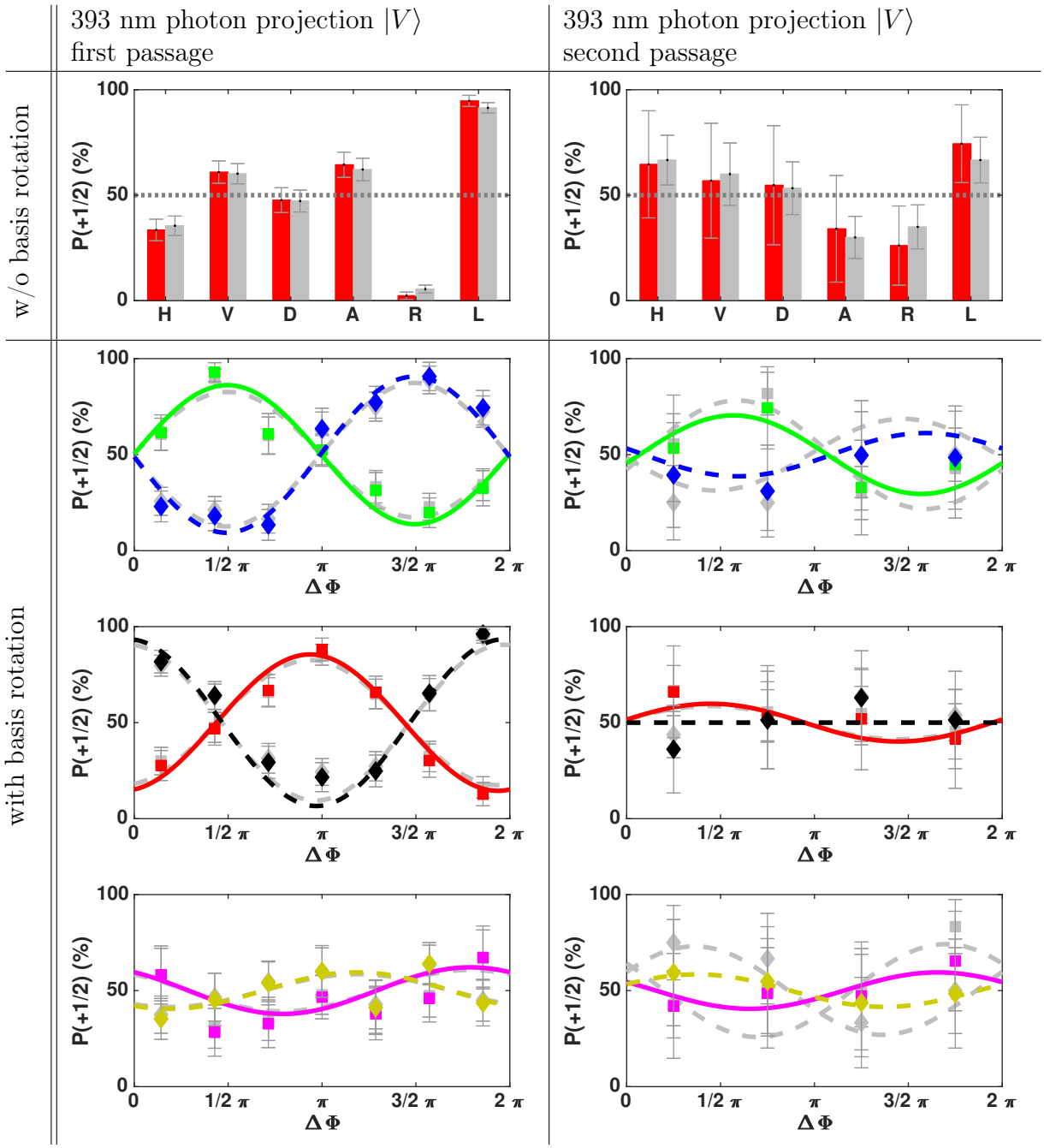

Figure C.17: Measurement results for the photon-photon to atom-photon entanglement transfer with conversion and metropolitan fibre evaluated for a waiting time of 400 µs for the *first* and *second* passage. The 393 nm photon is projected to $|V\rangle$. The first row is without RF $\pi/2$-pulse. The other rows show oscillations due to the Larmor precession. Second row: green $|H\rangle$ / blue $|V\rangle$, third row: red $|D\rangle$ / black $|A\rangle$, last row: magenta $|R\rangle$ / yellow $|L\rangle$. Grey bars and lines show the data without background correction.

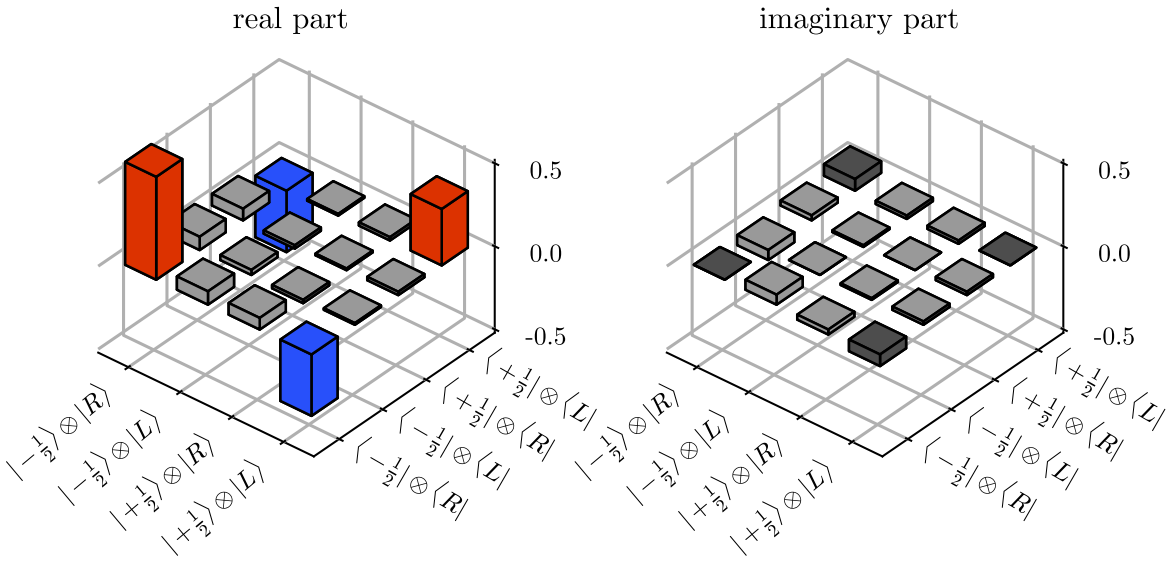

$$\begin{pmatrix} 0.62(2) & 0.08(2) & 0.07(7) & -0.37(3) \\ 0.08(2) & 0.03(2) & -0.02(3) & 0.01(7) \\ 0.07(7) & -0.02(3) & 0.01(2) & 0.02(2) \\ -0.37(3) & 0.01(7) & 0.02(2) & 0.34(2) \end{pmatrix} \quad \begin{pmatrix} 0 & -0.06(1) & 0.03(3) & 0.07(1) \\ 0.06(1) & 0 & -0.01(1) & -0.02(3) \\ -0.03(3) & 0.01(1) & 0 & -0.02(1) \\ -0.07(1) & 0.02(3) & 0.02(1) & 0 \end{pmatrix}$$

(a) First passage $|H\rangle$

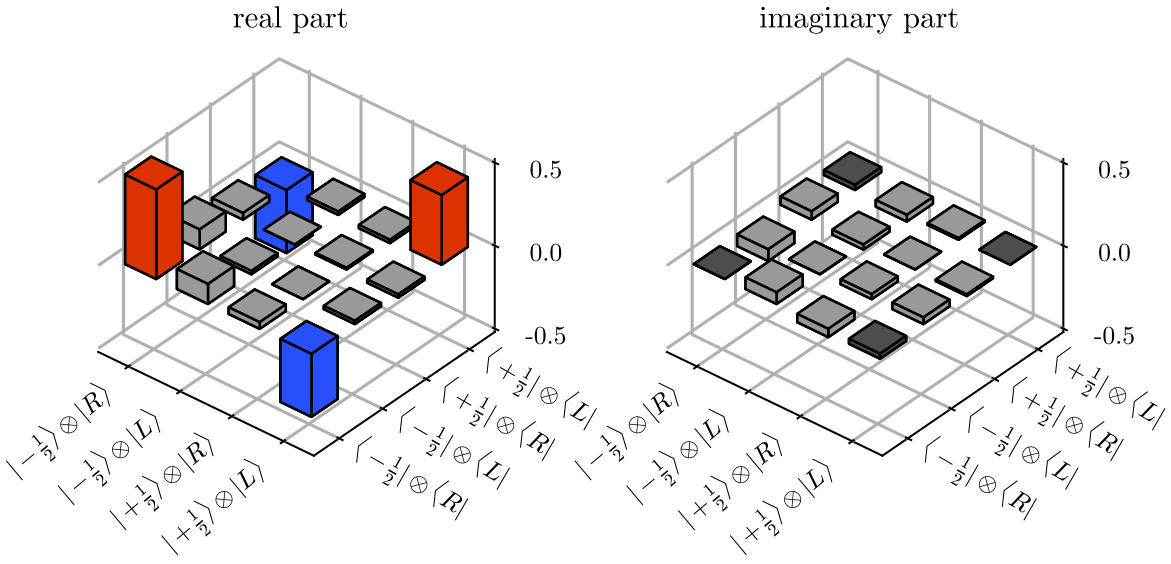

$$\begin{pmatrix} 0.54(2) & 0.12(2) & 0.04(4) & -0.38(3) \\ 0.12(2) & 0.02(2) & 0.00(3) & 0.02(4) \\ 0.04(4) & 0.00(3) & 0.01(2) & -0.02(2) \\ -0.38(3) & 0.02(4) & -0.02(2) & 0.42(2) \end{pmatrix} \quad \begin{pmatrix} 0 & -0.07(1) & 0.05(2) & 0.03(2) \\ 0.07(1) & 0 & -0.03(2) & -0.04(2) \\ -0.05(2) & 0.03(2) & 0 & 0.01(1) \\ -0.03(2) & 0.04(2) & -0.01(1) & 0 \end{pmatrix}$$

(b) First passage $|V\rangle$

Figure C.18: Background corrected reconstructed density matrix between ion and the 1550 nm photon for the first passage.

D Atom to photon quantum-state teleportation

In the following section, we show additional plots and evaluations for the teleportation measurements of the three settings of the main text. Additionally, we present the teleportation without conversion with another input state.

D.1 Without conversion $|\Psi^-\rangle$

In the following section, we will show the plots for the teleportation measurement without conversion evaluated for each of the 393 nm detectors separately. The phases and visibilities for the data shown in fig. D.21 and D.22 are summarised in table D.10. We use the $|\Psi^-\rangle$ Bell state as a photonic entanglement resource.

The reconstructed density matrices for the eight different projection combinations are shown in figure D.19 and D.20. The process fidelities are summarised in table D.11.

Table D.10: Phases and visibilities for the data shown in fig. D.21 and D.22.

projector		first passage				second passage			
		with correction		w/o correction		with correction		w/o correction	
393	854	Phase (°)	Vis	Phase (°)	Vis	Phase (°)	Vis	Phase (°)	Vis
$\|-\rangle_S \|H\rangle$	$\|H\rangle$	358(6)	0.72(6)	358(6)	0.67(6)	357(16)	0.8(2)	355(18)	0.4(1)
	$\|D\rangle$	266(4)	0.65(4)	266(4)	0.62(4)	80(24)	0.3(1)	80(24)	0.19(8)
	$\|R\rangle$	52(39)	0.13(9)	52(40)	0.12(9)	200(137)	0.1(3)	200(134)	0.1(1)
$\|+\rangle_S \|V\rangle$	$\|H\rangle$	354(4)	0.72(5)	354(4)	0.67(4)	1(8)	0.77(7)	4(12)	0.42(8)
	$\|D\rangle$	258(4)	0.66(4)	258(4)	0.62(4)	74(12)	0.7(1)	74(12)	0.38(8)
	$\|R\rangle$	20(7)	0.18(2)	20(7)	0.17(2)	311(86)	0.2(3)	314(99)	0.1(2)
$\|+\rangle_S \|H\rangle$	$\|H\rangle$	178(4)	0.81(5)	178(4)	0.75(4)	166(8)	0.88(10)	168(10)	0.48(8)
	$\|D\rangle$	81(5)	0.63(5)	81(5)	0.59(5)	272(13)	0.7(1)	271(14)	0.32(8)
	$\|R\rangle$	210(20)	0.12(4)	210(20)	0.11(4)	154(122)	0.1(2)	158(125)	0.1(1)
$\|-\rangle_S \|V\rangle$	$\|H\rangle$	169(4)	0.78(5)	169(4)	0.73(5)	158(7)	0.77(7)	158(8)	0.43(6)
	$\|D\rangle$	79(5)	0.63(5)	79(5)	0.60(4)	266(33)	0.4(2)	266(34)	0.3(1)
	$\|R\rangle$	163(19)	0.14(4)	163(19)	0.13(4)	255(57)	0.3(3)	250(61)	0.2(2)

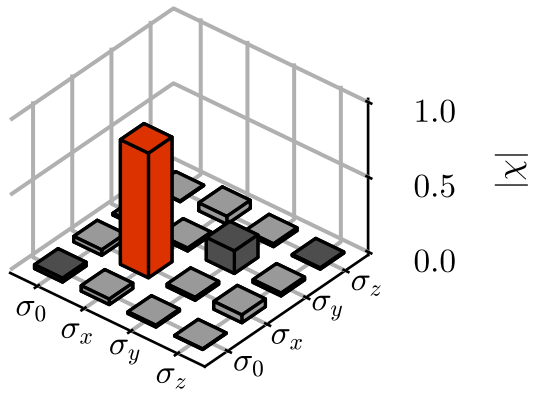

(a) Projection to $|\Phi^-\rangle = |-\rangle_S \otimes |H\rangle_{393}$

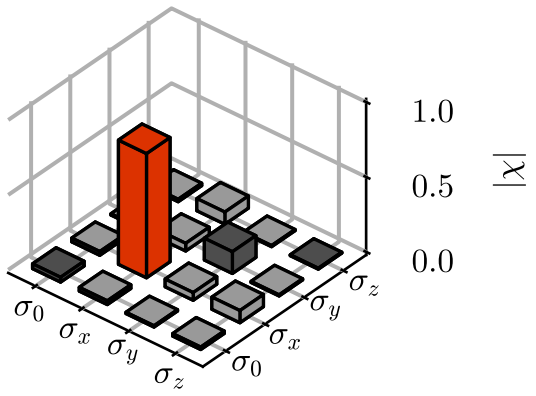

(b) Projection to $|\Phi^-\rangle = |+\rangle_S \otimes |V\rangle_{393}$

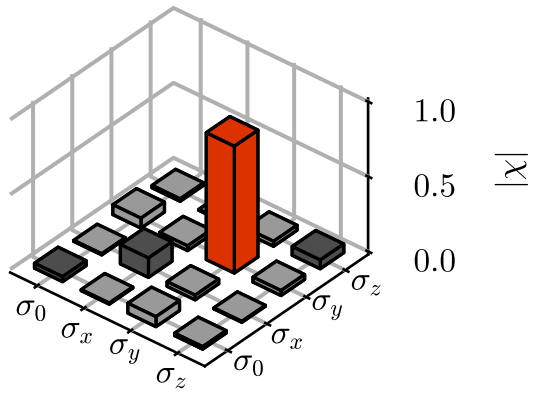

(c) Projection to $|\Phi^+\rangle = |+\rangle_S \otimes |H\rangle_{393}$

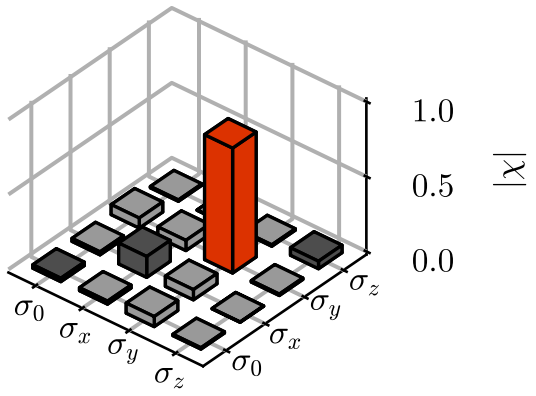

(d) Projection to $|\Phi^+\rangle = |-\rangle_S \otimes |V\rangle_{393}$

Figure D.19: Reconstructed process matrices of the quantum state teleportation without conversion. (a) and (b) show the result for a projection to the $|\Phi^-\rangle$-state and (c) and (d) for a projection to the $|\Phi^+\rangle$-state.

Table D.11: Summarised process fidelities for the 8 different measurement outcomes depicted in fig. D.19 and D.20.

Bell state	passage	state	fidelity w correction	fidelity w/o correction
$\|\Phi^-\rangle$	first	$\|-\rangle_S \otimes \|H\rangle_{393}$	87(7) %	85(7) %
$\|\Phi^-\rangle$		$\|+\rangle_S \otimes \|V\rangle_{393}$	87(7) %	85(6) %
$\|\Phi^+\rangle$		$\|+\rangle_S \otimes \|H\rangle_{393}$	88(6) %	86(6) %
$\|\Phi^+\rangle$		$\|-\rangle_S \otimes \|V\rangle_{393}$	87(7) %	85(6) %
$\|\Psi^-\rangle$	second	$\|-\rangle_S \otimes \|H\rangle_{393}$	78(16) %	65(9) %
$\|\Psi^-\rangle$		$\|+\rangle_S \otimes \|V\rangle_{393}$	86(7) %	71(6) %
$\|\Psi^+\rangle$		$\|+\rangle_S \otimes \|H\rangle_{393}$	88(10) %	70(7) %
$\|\Psi^+\rangle$		$\|-\rangle_S \otimes \|V\rangle_{393}$	80(14) %	67(9) %

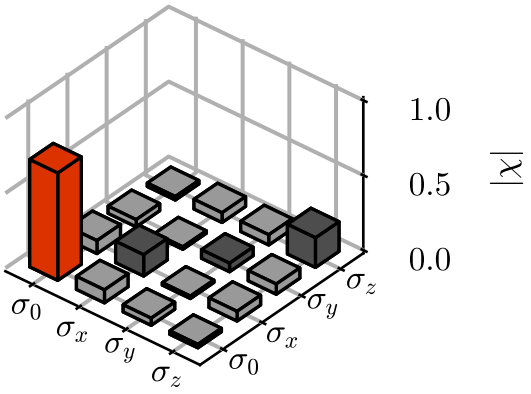

(a) Projection to $|\Psi^-\rangle = |-\rangle_S \otimes |H\rangle_{393}$

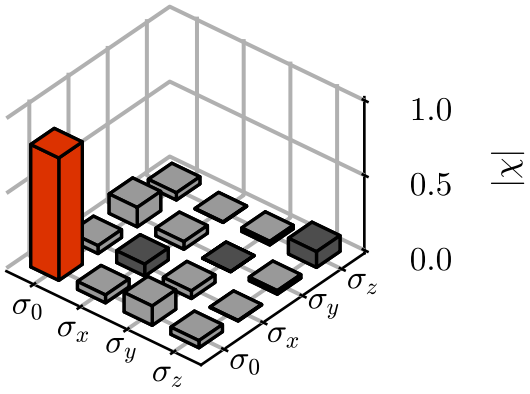

(b) Projection to $|\Psi^-\rangle = |+\rangle_S \otimes |V\rangle_{393}$

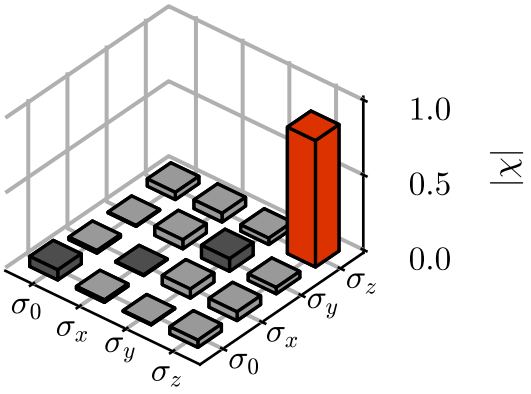

(c) Projection to $|\Psi^+\rangle = |+\rangle_S \otimes |H\rangle_{393}$

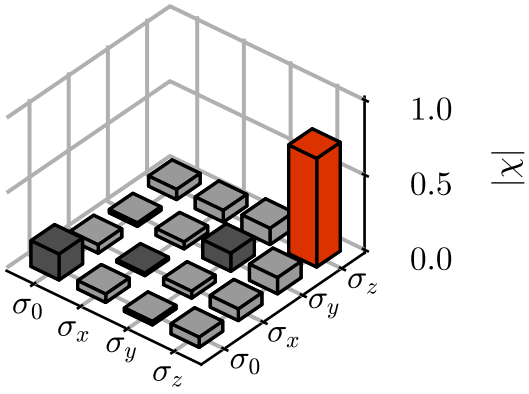

(d) Projection to $|\Psi^+\rangle = |-\rangle_S \otimes |V\rangle_{393}$

Figure D.20: Reconstructed process matrices of the quantum state teleportation without conversion. (a) and (b) show the result for a projection to the $|\Psi^-\rangle$-state and (c) and (d) for a projection to the $|\Psi^+\rangle$-state.

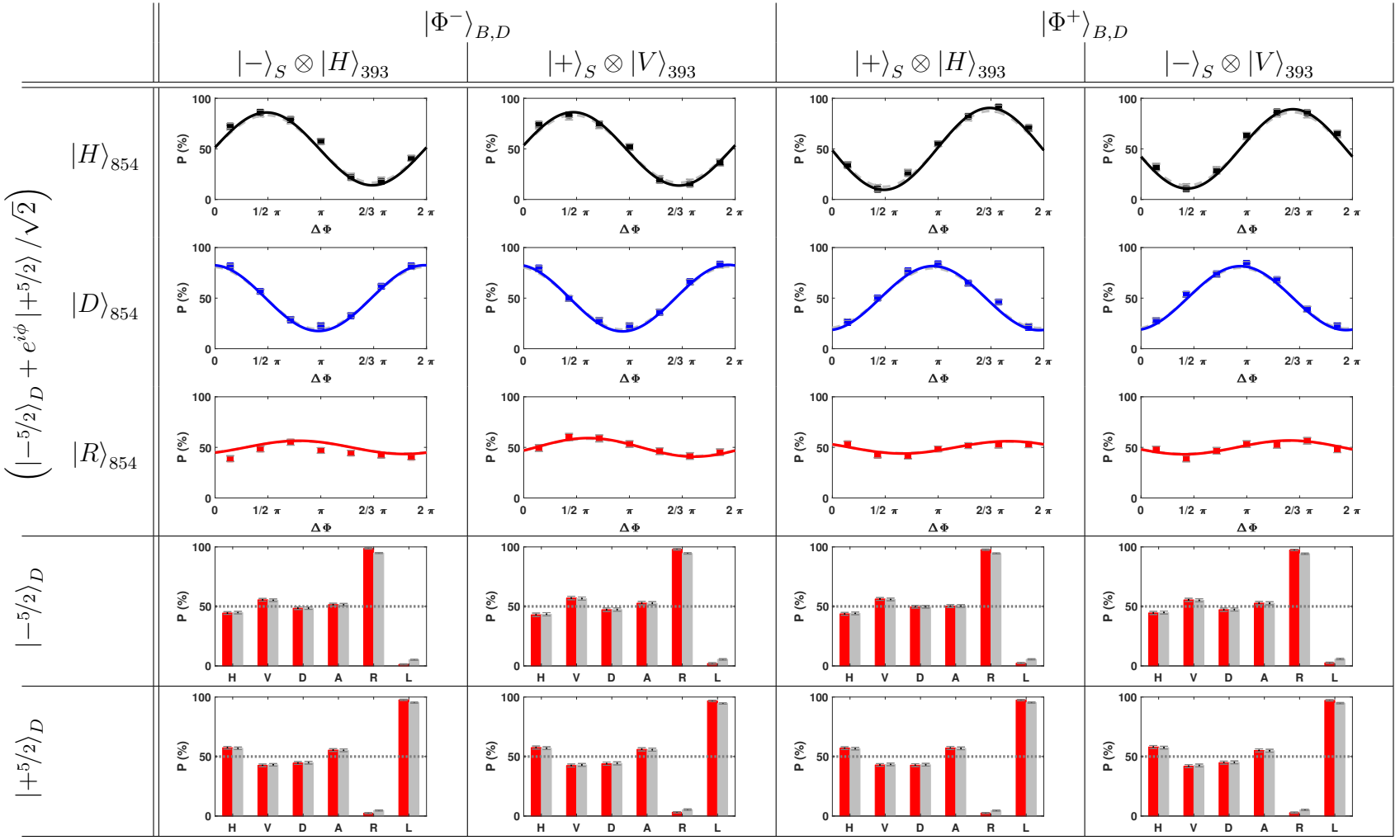

Figure D.21: Histograms and fringes for the three input states and the Bell state of the first passage. The data is evaluated for a waiting time of 350 µs. Grey bars and lines show the data without correction. The coloured ones with correction.

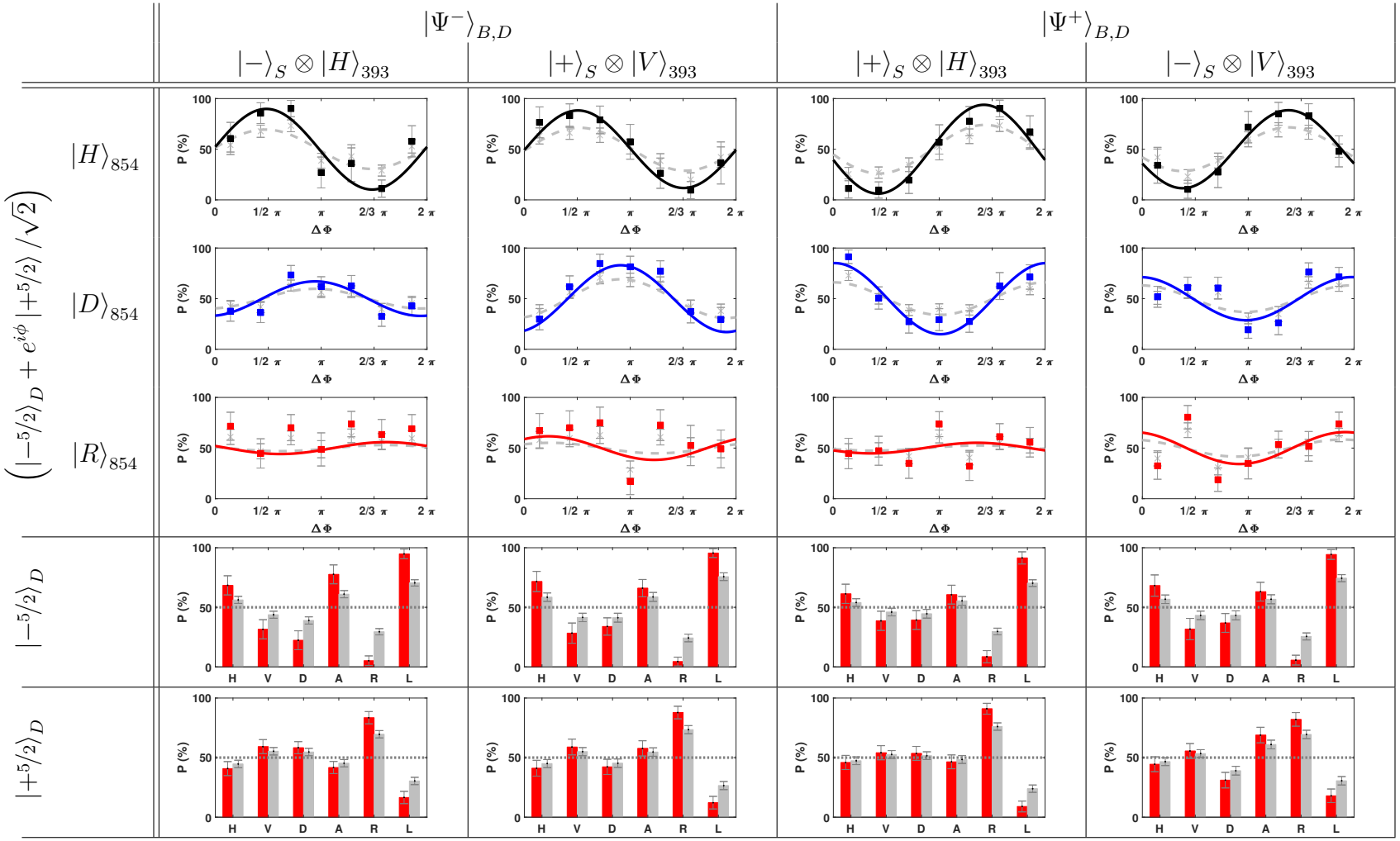

Figure D.22: Histograms and fringes for the three input states and the Bell state of the second passage. The data is evaluated for a waiting time of 350 µs. Grey bars and lines show the data without correction. The coloured ones with correction.

D.2 Without conversion $|\Psi^i\rangle$

Here, we present the results for the teleportation measurement with the $|\Psi^i\rangle$-state as a photonic resource of entanglement. The measurement is performed without conversion. The data is evaluated for each of the 393 nm detectors separately. The phases and visibilities for the data are shown in fig. D.25 and D.26 are summarised in table D.12.

The reconstructed density matrices for the eight different projection combinations are shown in figure D.23 and D.24. The process fidelities are summarised in table D.13. In contrast to process matrices with a Bell state as input, where we get a single Pauli matrix as a unitary operation, we get a combination of two for each projection. Therefore, we also must plot the real and imaginary parts of χ.

Table D.12: Phases and visibilities of the fringes for the data shown in figure D.25 and D.26.

projector		first passage				second passage			
		with correction		w/o correction		with correction		w/o correction	
393	854	Phase (°)	Vis	Phase (°)	Vis	Phase (°)	Vis	Phase (°)	Vis
$\|-\rangle_S \|H\rangle$	$\|H\rangle$	353(3)	0.84(4)	353(3)	0.77(3)	340(6)	0.81(6)	339(6)	0.46(4)
	$\|D\rangle$	172(26)	0.11(5)	172(25)	0.11(5)	226(41)	0.4(3)	224(46)	0.3(2)
	$\|R\rangle$	263(4)	0.83(5)	263(4)	0.77(5)	91(14)	0.7(2)	92(16)	0.4(1)
$\|+\rangle_S \|V\rangle$	$\|H\rangle$	355(2)	0.86(2)	355(2)	0.79(2)	7(8)	0.84(9)	5(7)	0.49(6)
	$\|D\rangle$	186(11)	0.12(2)	186(12)	0.11(2)	311(61)	0.2(2)	311(66)	0.1(1)
	$\|R\rangle$	266(2)	0.74(3)	266(2)	0.69(2)	83(7)	0.65(8)	84(8)	0.39(5)
$\|+\rangle_S \|H\rangle$	$\|H\rangle$	171(2)	0.83(2)	171(2)	0.77(2)	175(12)	0.8(2)	176(12)	0.5(1)
	$\|D\rangle$	14(19)	0.16(5)	14(19)	0.15(5)	324(29)	0.3(2)	323(31)	0.2(1)
	$\|R\rangle$	81(3)	0.75(4)	81(3)	0.70(3)	260(8)	0.62(8)	260(9)	0.36(6)
$\|-\rangle_S \|V\rangle$	$\|H\rangle$	177(4)	0.84(5)	177(4)	0.77(4)	172(19)	0.8(2)	169(22)	0.4(1)
	$\|D\rangle$	349(14)	0.15(4)	349(14)	0.14(4)	12(36)	0.3(2)	12(37)	0.2(1)
	$\|R\rangle$	91(3)	0.84(3)	91(3)	0.77(3)	266(12)	0.8(2)	267(12)	0.5(1)

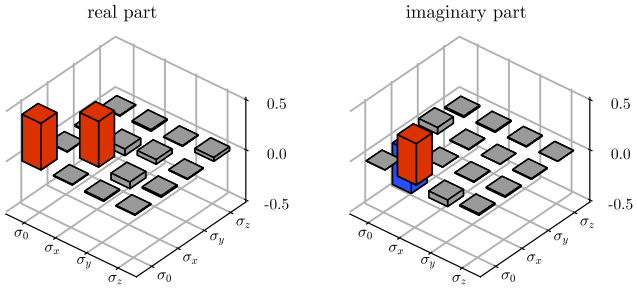

(a) Projection to $|\Phi^-\rangle = |-\rangle_S \otimes |H\rangle_{393}$

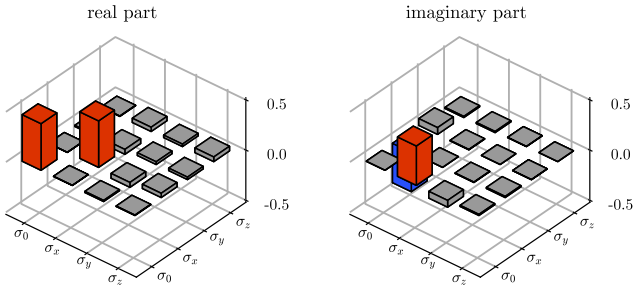

(b) Projection to $|\Phi^-\rangle = |+\rangle_S \otimes |V\rangle_{393}$

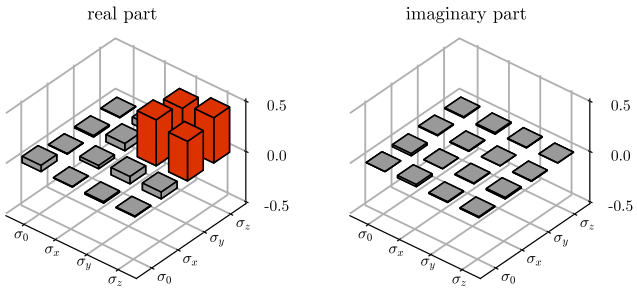

(c) Projection to $|\Phi^+\rangle = |+\rangle_S \otimes |H\rangle_{393}$

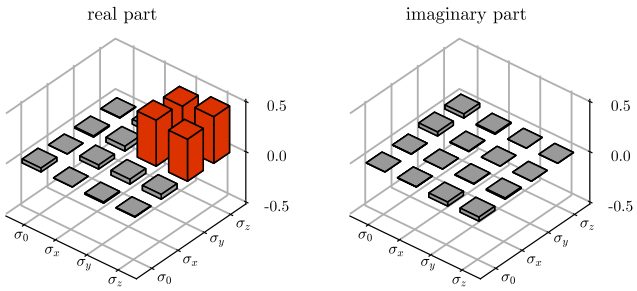

(d) Projection to $|\Phi^+\rangle = |-\rangle_S \otimes |V\rangle_{393}$

Figure D.23: Reconstructed process matrices of the quantum state teleportation without conversion. (a) and (b) show the result for a projection to the $|\Phi^-\rangle$-state and (c) and (d) for a projection to the $|\Phi^+\rangle$-state.

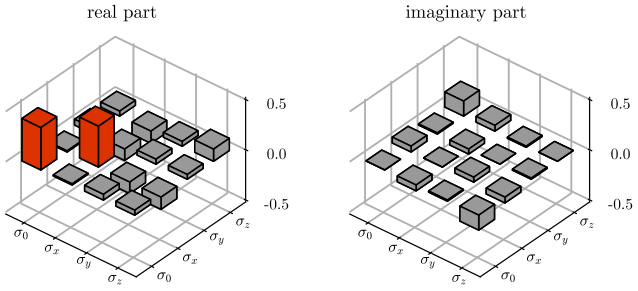

(a) Projection to $|\Psi^-\rangle = |-\rangle_S \otimes |H\rangle_{393}$

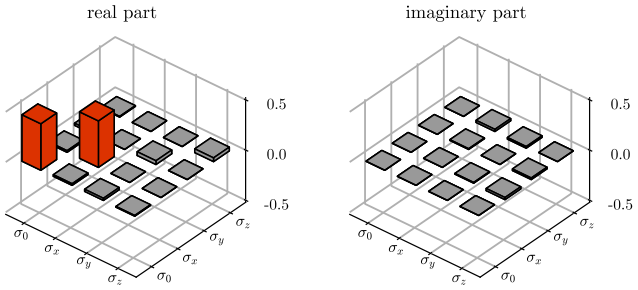

(b) Projection to $|\Psi^-\rangle = |+\rangle_S \otimes |V\rangle_{393}$

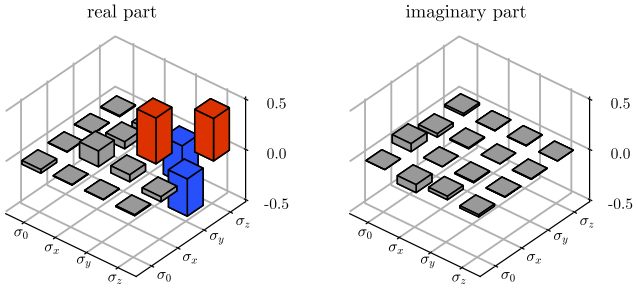

(c) Projection to $|\Psi^+\rangle = |+\rangle_S \otimes |H\rangle_{393}$

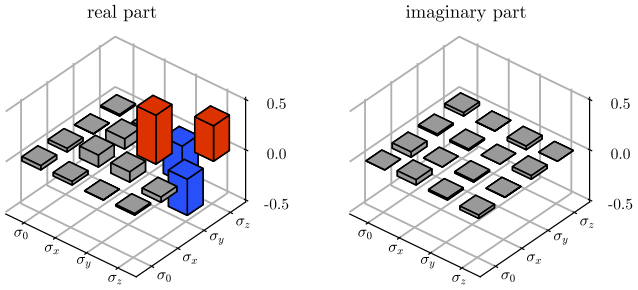

(d) Projection to $|\Psi^+\rangle = |-\rangle_S \otimes |V\rangle_{393}$

Figure D.24: Reconstructed process matrices of the quantum state teleportation without conversion. (a) and (b) show the result for a projection to the $|\Psi^-\rangle$-state and (c) and (d) for a projection to the $|\Psi^+\rangle$-state.

Table D.13: Summarised process fidelities for the 8 different measurement outcomes depicted in fig. D.23 and D.24.

Bell state	passage	state	fidelity w correction	fidelity w/o correction
$\|\Phi^-\rangle$	first	$\|-\rangle_S \otimes \|H\rangle_{393}$	91(3) %	88(3) %
$\|\Phi^-\rangle$		$\|+\rangle_S \otimes \|V\rangle_{393}$	90(3) %	87(3) %
$\|\Phi^+\rangle$		$\|+\rangle_S \otimes \|H\rangle_{393}$	90(3) %	87(3) %
$\|\Phi^+\rangle$		$\|-\rangle_S \otimes \|V\rangle_{393}$	92(3) %	89(3) %
$\|\Psi^-\rangle$	second	$\|-\rangle_S \otimes \|H\rangle_{393}$	81(14) %	68(8) %
$\|\Psi^-\rangle$		$\|+\rangle_S \otimes \|V\rangle_{393}$	85(6) %	71(4) %
$\|\Psi^+\rangle$		$\|+\rangle_S \otimes \|H\rangle_{393}$	86(7) %	72(5) %
$\|\Psi^+\rangle$		$\|-\rangle_S \otimes \|V\rangle_{393}$	85(11) %	70(6) %

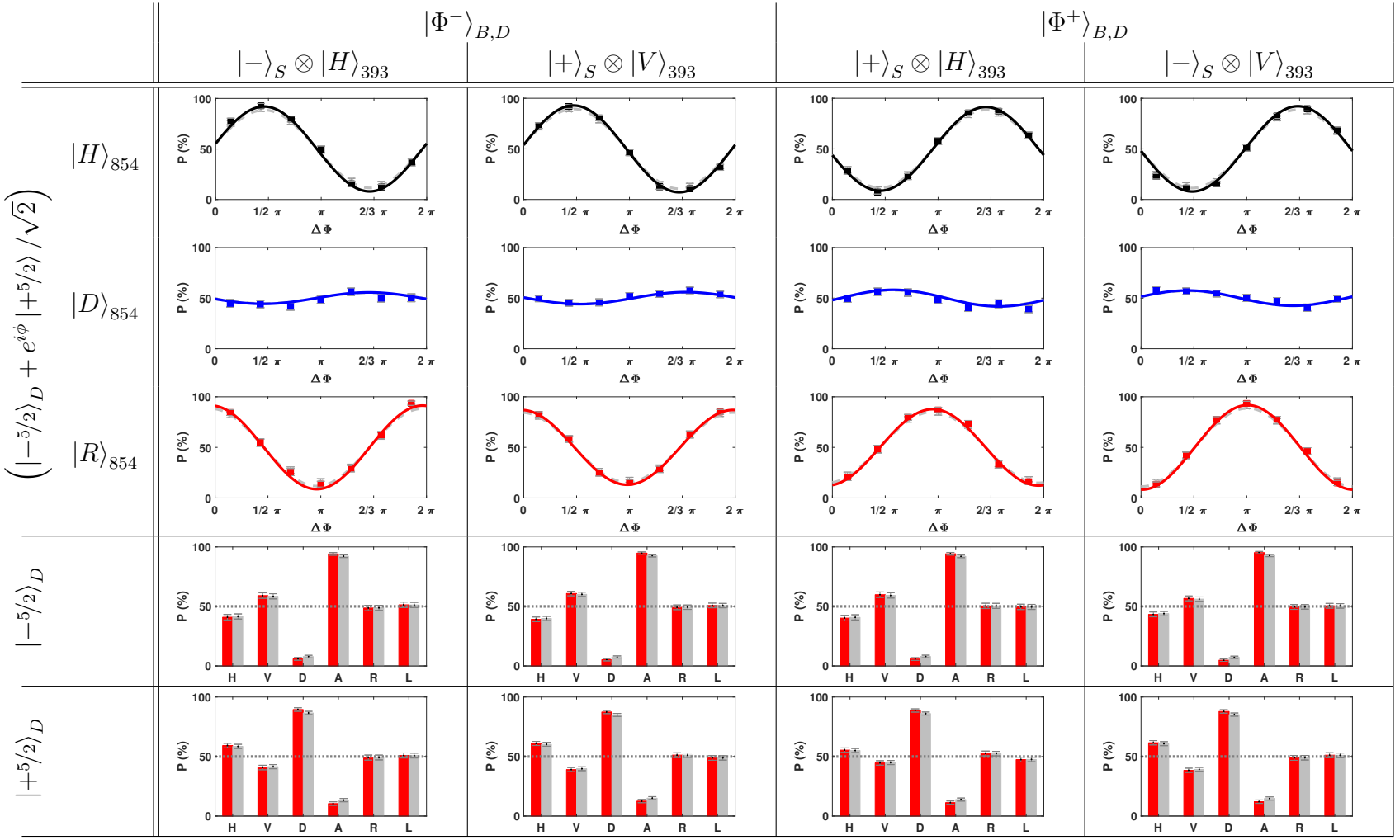

Figure D.25: Histograms and fringes for the three input states and the Bell state of the first passage. The data is evaluated for a waiting time of 200 µs. Grey bars and lines show the data without correction. The coloured ones with correction.

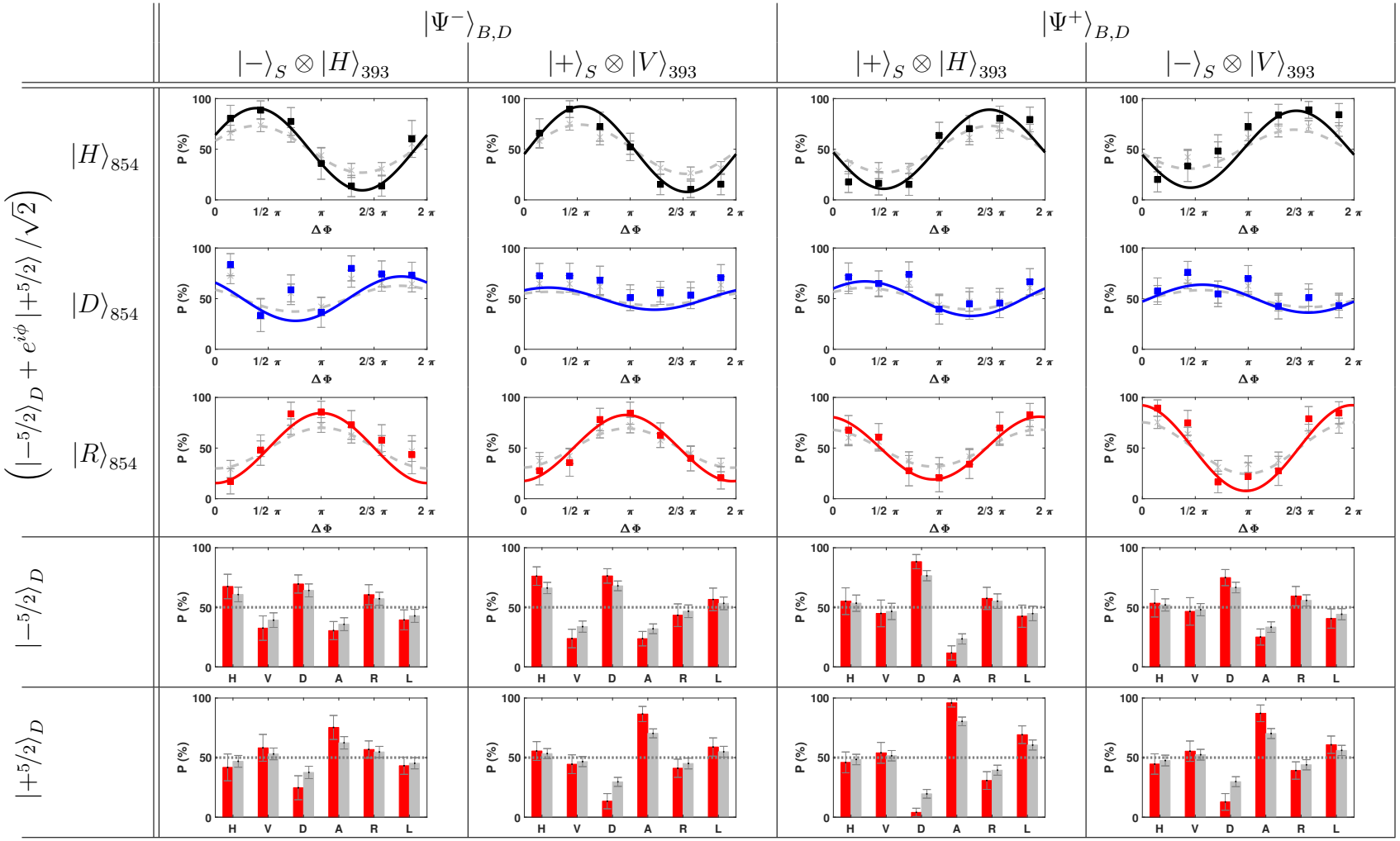

Figure D.26: Histograms and fringes for the three input states and the Bell state of the second passage. The data is evaluated for a waiting time of 200 µs. Grey bars and lines show the data without correction. The coloured ones with correction.

D.3 With conversion

This section presents additional results for the teleportation measurements with conversion to 1550 nm. The data shown here is evaluated for each of the 393 nm detectors separately. The phases and visibilities for the data shown in fig. D.29 and D.30 are summarised in table D.14.

The reconstructed density matrices for the eight different projection combinations are shown in fig. D.27 and D.28. The resulting process fidelities are summarised in table D.15.

Table D.14: Phase and visibility of the fringes for the teleporation measurment

projector		first passage				second passage			
		with correction		w/o correction		with correction		w/o correction	
393	854	Phase (°)	Vis	Phase (°)	Vis	Phase (°)	Vis	Phase (°)	Vis
$\|-\rangle_S \|H\rangle$	$\|H\rangle$	4(5)	0.79(6)	4(5)	0.72(5)	352(29)	0.5(3)	356(26)	0.21(10)
	$\|D\rangle$	278(4)	0.75(4)	278(4)	0.68(4)	81(13)	0.6(1)	80(12)	0.26(6)
	$\|R\rangle$	128(65)	0.2(2)	128(66)	0.2(2)	212(21)	0.3(1)	213(29)	0.16(8)
$\|+\rangle_S \|V\rangle$	$\|H\rangle$	355(4)	0.74(4)	355(3)	0.67(3)	0(10)	0.8(1)	358(8)	0.41(6)
	$\|D\rangle$	276(3)	0.71(3)	276(3)	0.64(3)	72(20)	0.7(2)	71(24)	0.3(1)
	$\|R\rangle$	130(56)	0.2(2)	130(57)	0.2(2)	293(25)	0.5(2)	294(32)	0.2(1)
$\|+\rangle_S \|H\rangle$	$\|H\rangle$	186(3)	0.77(3)	186(3)	0.70(3)	180(16)	0.7(2)	178(19)	0.3(1)
	$\|D\rangle$	107(8)	0.66(8)	107(8)	0.60(8)	241(31)	0.6(3)	244(30)	0.2(1)
	$\|R\rangle$	300(57)	0.3(3)	300(57)	0.3(3)	73(48)	0.2(2)	75(59)	0.1(1)
$\|-\rangle_S \|V\rangle$	$\|H\rangle$	177(6)	0.79(7)	177(6)	0.70(6)	190(14)	0.8(1)	190(14)	0.39(9)
	$\|D\rangle$	96(3)	0.72(3)	96(3)	0.65(3)	273(11)	0.65(10)	273(10)	0.31(5)
	$\|R\rangle$	303(41)	0.2(2)	303(42)	0.2(1)	21(82)	0.2(3)	21(100)	0.1(2)

Table D.15: Summarised process fidelities for the 8 different measurement outcomes depicted in fig. D.27 and D.28.

Bell state	passage	state	fidelity w correction	fidelity w/o correction
$\|\Phi^-\rangle$	first	$\|-\rangle_S \otimes \|H\rangle_{393}$	89(9) %	86(6) %
$\|\Phi^-\rangle$		$\|+\rangle_S \otimes \|V\rangle_{393}$	87(7) %	85(6) %
$\|\Phi^+\rangle$		$\|+\rangle_S \otimes \|H\rangle_{393}$	86(8) %	84(7) %
$\|\Phi^+\rangle$		$\|-\rangle_S \otimes \|V\rangle_{393}$	88(8) %	85(5) %
$\|\Psi^-\rangle$	second	$\|-\rangle_S \otimes \|H\rangle_{393}$	74(16) %	63(9) %
$\|\Psi^-\rangle$		$\|+\rangle_S \otimes \|V\rangle_{393}$	82(13) %	68(8) %
$\|\Psi^+\rangle$		$\|+\rangle_S \otimes \|H\rangle_{393}$	76(20) %	66(13) %
$\|\Psi^+\rangle$		$\|-\rangle_S \otimes \|V\rangle_{393}$	82(10) %	67(6) %

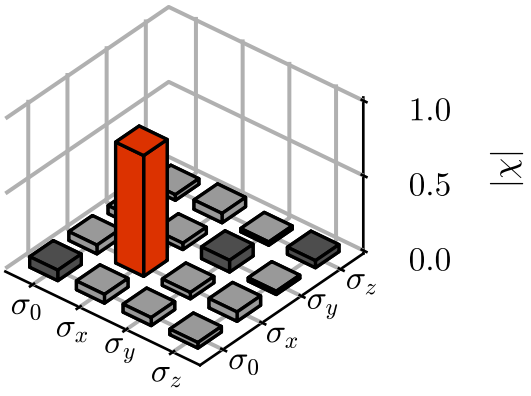

(a) Projection to $|\Phi^-\rangle = |-\rangle_S \otimes |H\rangle_{393}$

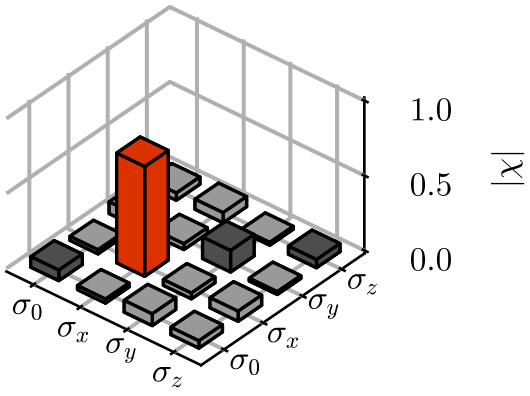

(b) Projection to $|\Phi^-\rangle = |+\rangle_S \otimes |V\rangle_{393}$

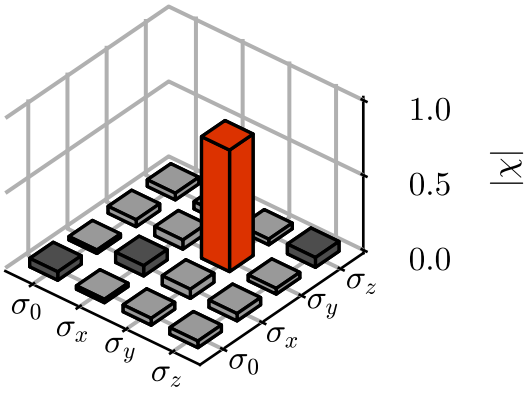

(c) Projection to $|\Phi^+\rangle = |+\rangle_S \otimes |H\rangle_{393}$

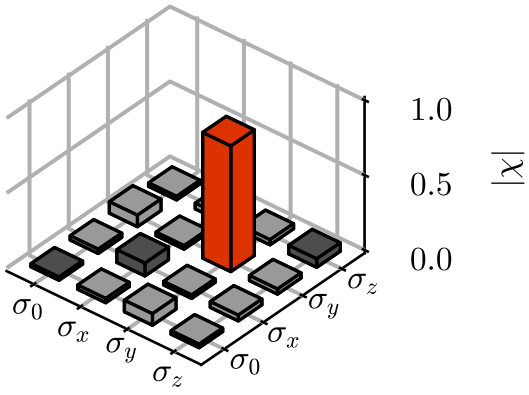

(d) Projection to $|\Phi^+\rangle = |-\rangle_S \otimes |V\rangle_{393}$

Figure D.27: Reconstructed process matrices of the quantum state teleportation with conversion. (a) and (b) show the result for a projection to the $|\Phi^-\rangle$-state and (c) and (d) for a projection to the $|\Phi^+\rangle$-state.

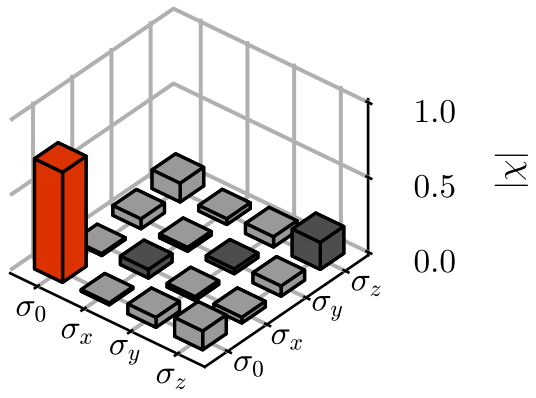

(a) Projection to $|\Psi^-\rangle = |-\rangle_S \otimes |H\rangle_{393}$

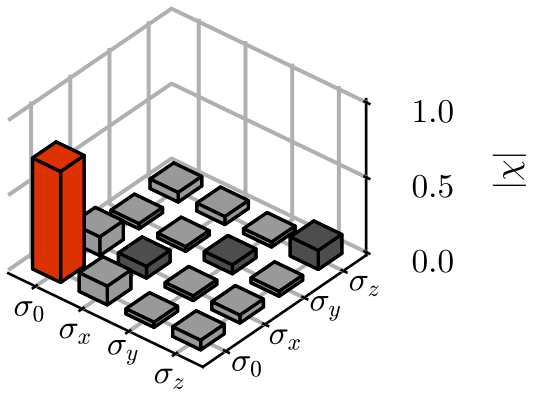

(b) Projection to $|\Psi^-\rangle = |+\rangle_S \otimes |V\rangle_{393}$

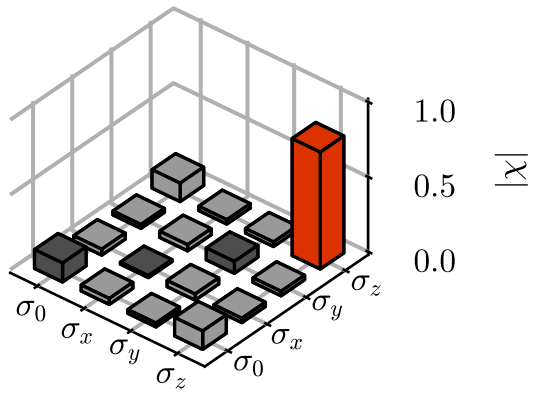

(c) Projection to $|\Psi^+\rangle = |+\rangle_S \otimes |H\rangle_{393}$

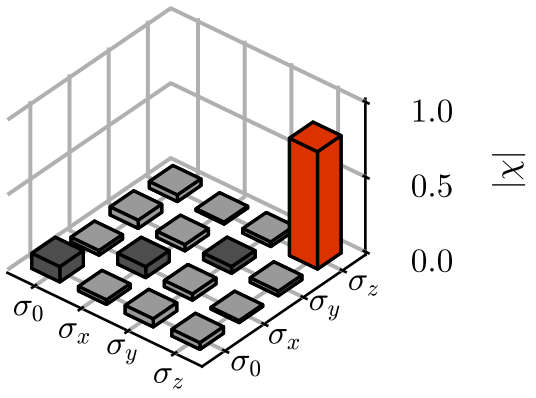

(d) Projection to $|\Psi^+\rangle = |-\rangle_S \otimes |V\rangle_{393}$

Figure D.28: Reconstructed process matrices of the quantum state teleportation with conversion. (a) and (b) show the result for a projection to the $|\Psi^-\rangle$-state and (c) and (d) for a projection to the $|\Psi^+\rangle$-state.

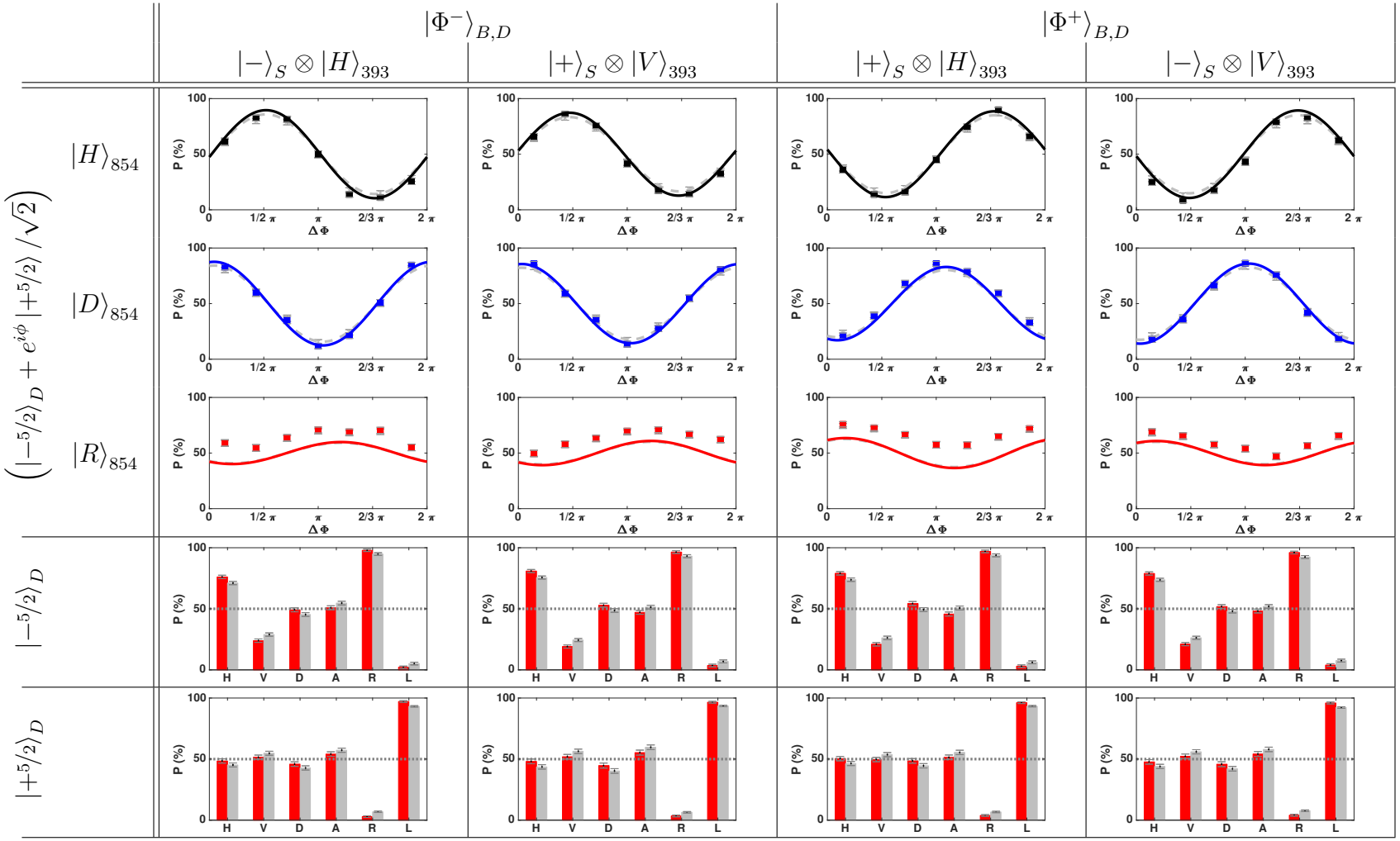

Figure D.29: Histograms and fringes for the three input states and the Bell state of the first passage for the measurement with conversion. The data is evaluated for a waiting time of 400 µs. Grey bars and lines show the data without correction. The coloured ones with correction.

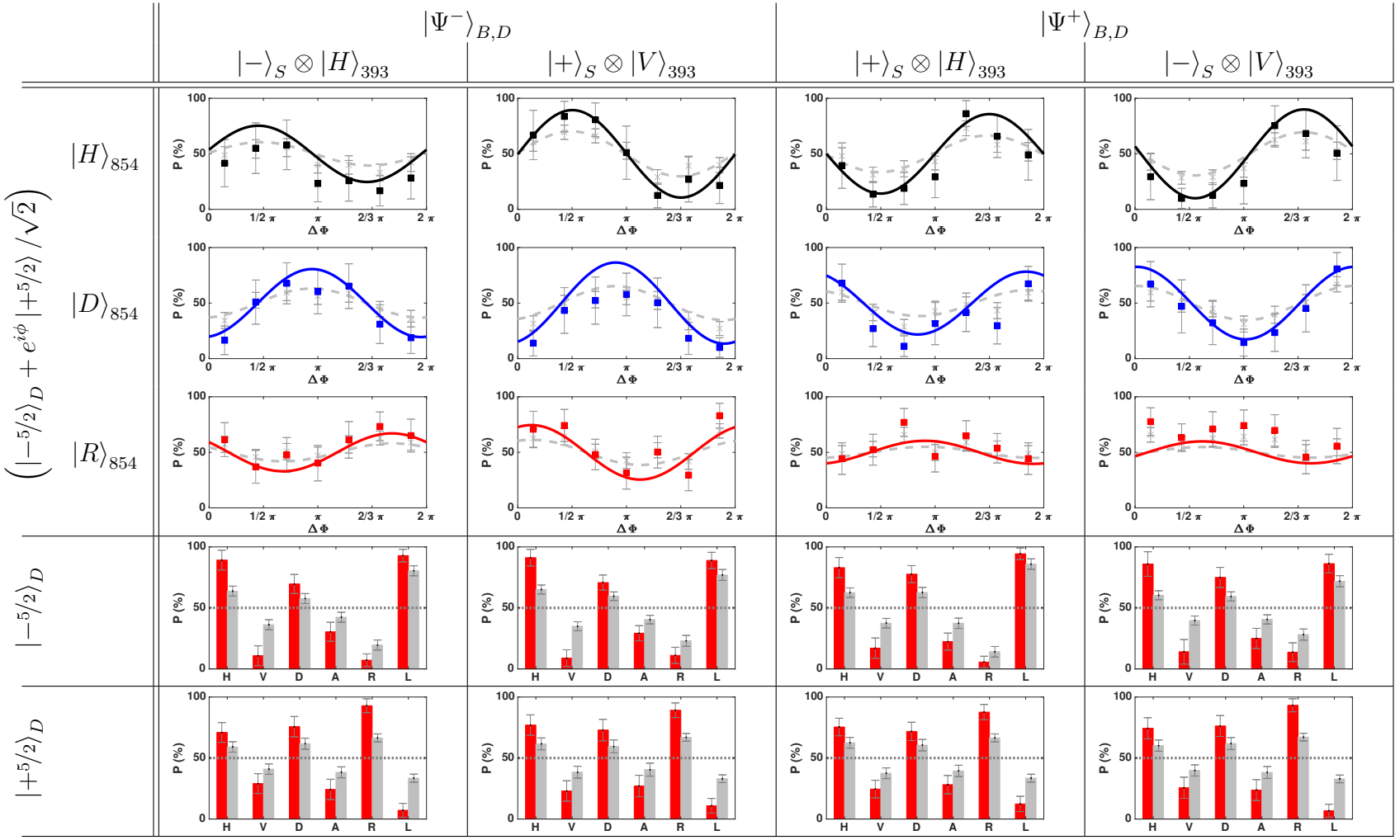

Figure D.30: Histograms and fringes for the three input states and the Bell state of the second passage for the measurement with conversion. The data is evaluated for a waiting time of 400 µs. Grey bars and lines show the data without correction. The coloured ones with correction.

D.4 With conversion and metropolitan fibre

In this section, we present additional results for the teleportation measurements with conversion to 1550 nm and the metropolitan fibre. The data shown here is evaluated for each of the 393 nm detectors separately. As mentioned in the main text, we have no usable data for the second passage. The phases and visibilities for the data shown in fig. D.32 are summarised in table D.16.

The reconstructed density matrices for the four different projection combinations of the first passage are shown in fig. D.31. The resulting process fidelities are summarised in table D.15.

Table D.16: Phase and visibility of the fringes for the teleporation measurment

projector		first passage			
		with correction		w/o correction	
393	854	Phase (°)	Vis	Phase (°)	Vis
$\|-\rangle_S \|H\rangle$	$\|H\rangle$	332(21)	0.17(6)	325(26)	0.3(2)
	$\|D\rangle$	358(520)	0.1(8)	357(354)	0.1(9)
	$\|R\rangle$	319(510)	0.0(2)	135(375)	0.1(5)
$\|+\rangle_S \|V\rangle$	$\|H\rangle$	26(48)	0.4(3)	10(51)	0.6(5)
	$\|D\rangle$	315(177)	0.1(3)	315(200)	0.1(2)
	$\|R\rangle$	10(88)	0.1(1)	4(79)	0.4(5)
$\|+\rangle_S \|H\rangle$	$\|H\rangle$	164(59)	0.3(3)	166(55)	0.4(4)
	$\|D\rangle$	160(33)	0.3(2)	164(36)	0.3(2)
	$\|R\rangle$	1(381)	0.1(4)	5(339)	0.1(7)
$\|-\rangle_S \|V\rangle$	$\|H\rangle$	163(135)	0.2(5)	165(124)	0.3(8)
	$\|D\rangle$	154(52)	0.4(3)	153(49)	0.3(2)
	$\|R\rangle$	178(114)	0.2(4)	184(93)	0.4(7)

Table D.17: Summarised process fidelities for the 8 different measurement outcomes depicted in fig. D.31.

Bell state	passage	state	fidelity w correction	fidelity w/o correction
$\|\Phi^-\rangle$	first	$\|-\rangle_S \otimes \|H\rangle_{393}$	86(9) %	83(9) %
$\|\Phi^-\rangle$		$\|+\rangle_S \otimes \|V\rangle_{393}$	85(5) %	82(6) %
$\|\Phi^+\rangle$		$\|+\rangle_S \otimes \|H\rangle_{393}$	89(8) %	85(7) %
$\|\Phi^+\rangle$		$\|-\rangle_S \otimes \|V\rangle_{393}$	88(9) %	85(9) %

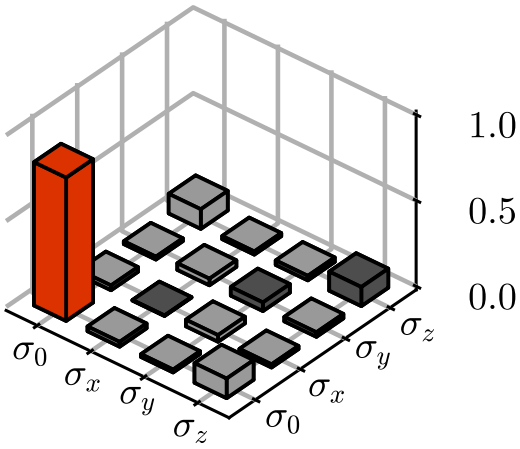

(a) Projection to $|\Phi^-\rangle = |-\rangle_S \otimes |H\rangle_{393}$

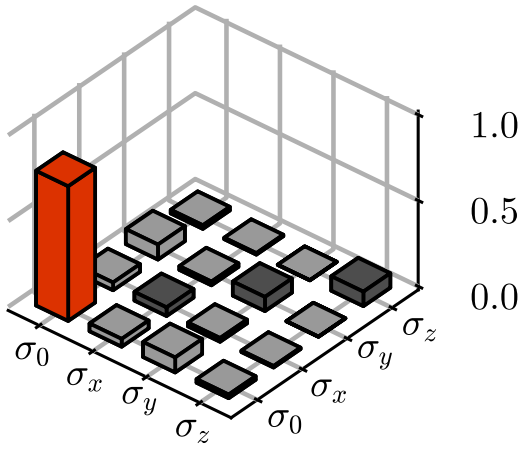

(b) Projection to $|\Phi^-\rangle = |+\rangle_S \otimes |V\rangle_{393}$

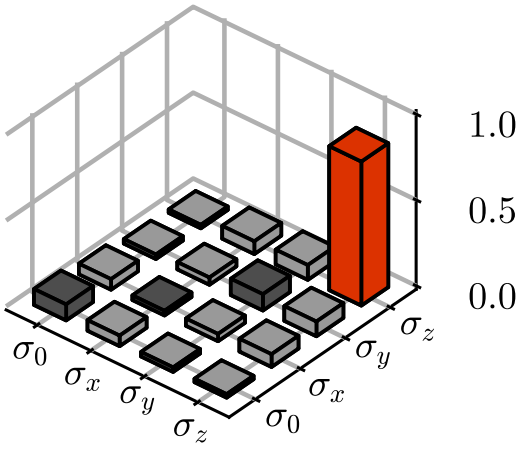

(c) Projection to $|\Phi^+\rangle = |+\rangle_S \otimes |H\rangle_{393}$

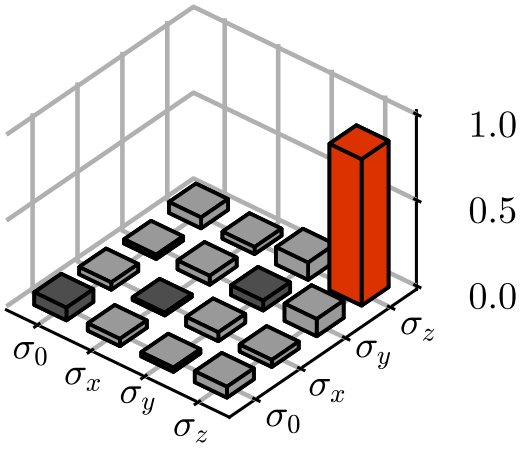

(d) Projection to $|\Phi^+\rangle = |-\rangle_S \otimes |V\rangle_{393}$

Figure D.31: Reconstructed process matrices of the quantum state teleportation with conversion and metropolitan fibre. (a) and (b) show the result for a projection to the $|\Phi^-\rangle$-state and (c) and (d) for a projection to the $|\Phi^+\rangle$-state.

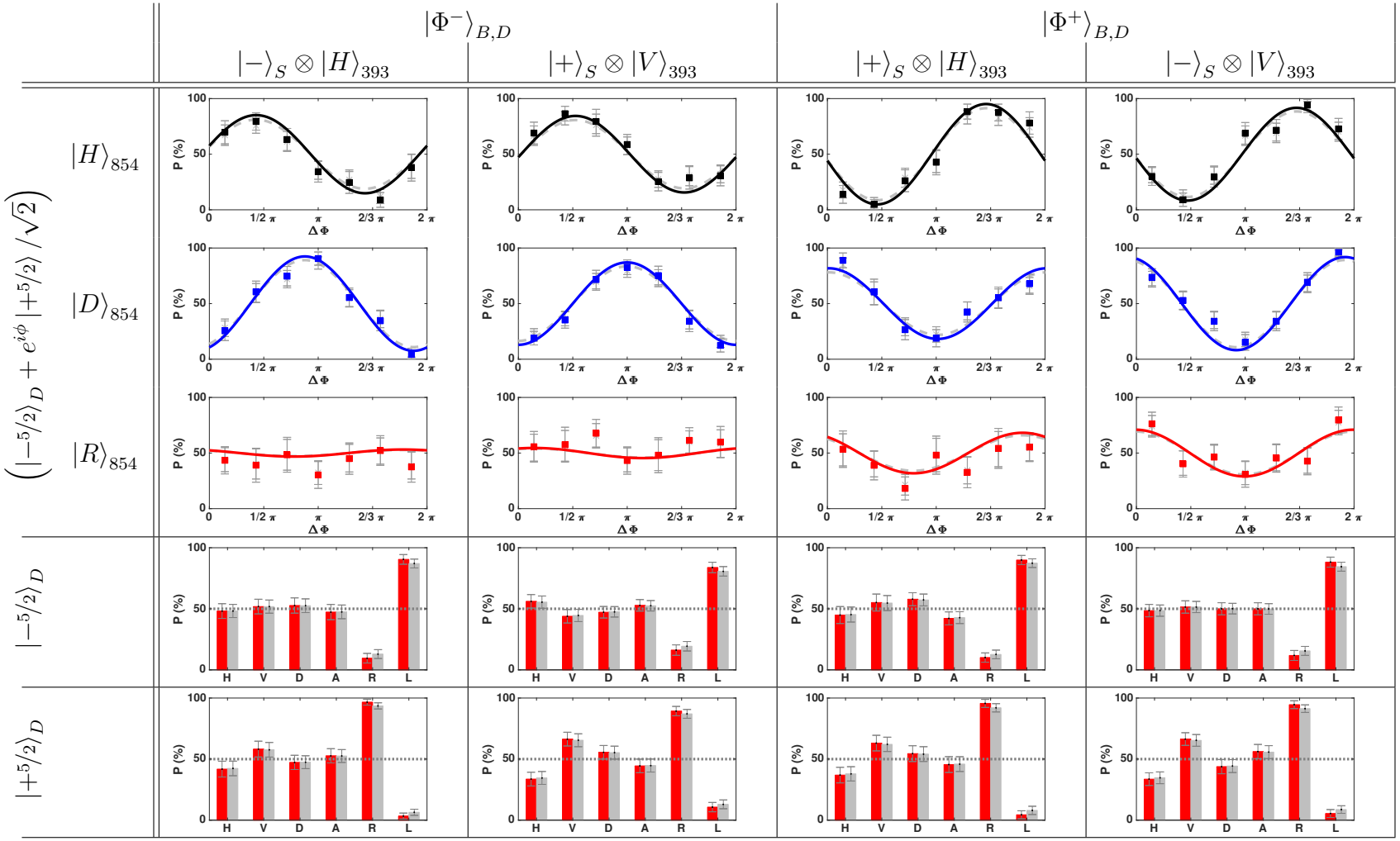

Figure D.32: Histograms and fringes for the three input states and the Bell state of the first passage for the measurement with conversion and metropolitan fibre. The data is evaluated for a waiting time of 400 µs. Grey bars and lines show the data without correction. The coloured ones with correction.

Danksagung

An dieser Stelle möchte ich mich bei allen Bedanken, die zum Gelingen dieser Arbeit beigetragen haben.

Ich möchte zunächst meinem Doktorvater, Jürgen Eschner, meinen Dank für seine Beratung, Ermutigung und Unterstützung während meiner gesamten Zeit am Lehrstuhl, sowohl während meiner Masterarbeit, als auch während meiner Promotionszeit aussprechen. Sein Fachwissen und seine Einsichten haben mir entscheidend dabei geholfen, meine Forschung zu gestalten und zum Erfolg zu führen.

Ich danke meinen Kollegen am Lehrstuhl für die Schaffung eines unterstützenden und kooperativen Forschungsumfeldes. Insbesondere möchte ich Stephan Kucera und Matthias Kreis für die hilfreichen Diskussionen und die Weitergabe ihres Wissens danken. Ohne die Hilfe der beiden wären die Messungen so nicht möglich gewesen. Danke auch an Omar Elshehy, Christian Haen und Max Bergerhoff für die Hilfe bei der Beaufsichtigung der wochenlangen Messungen und die Überwachung und Wartung des Ionenexperiments. Mein Dank gilt auch Tobias Bauer für die Überwachung und Wartung des Konverters. Ein weiterer Dank geht an Susanna Trampert für die Unterstützung in allen organisatorischen Dingen sowie den netten Gesprächen.

Schließlich möchte ich mich bei meiner Familie und meinen Freunden für ihre Liebe, Ermutigung und unermüdliche Unterstützung bedanken. Vor allem Kerstin, die wie eine Schwester für mich ist, möchte ich besonders hervorheben, die mich stets wieder aufgebaut und mich bei allem unterstützt hat. Ohne sie wäre diese Arbeit ebenfalls nicht möglich gewesen.